Investigating Correlations in Time Delay Interferometry Combinations of LISA Data

Jennifer Toher

Department of Physics and Astronomy
University of Glasgow

Presented as a Thesis for the degree of Ph.D.
at the University of Glasgow, University Avenue,
Glasgow, G12 8QQ.

Summary

The detection of Gravitational Waves using the Laser Interferometer Space Antenna (LISA) will open whole new areas of physics and astrophysics for exploration. The lower frequency signals detected by the antenna will allow us to probe gravitational wave sources that are inaccessible with current and future ground based detectors. However, the ability of LISA to detect gravitational wave signals is dependent on the removal of the laser frequency noise realisations from the optical bench measurements, that would otherwise dominate the signal data streams.

Time Delay Interferometry (TDI) provides a method for removing the laser noise contributions by time shifting the individual optical bench measurements. The cancellation of the noise is achieved by identifying the individual optical bench measurements that contain equal numbers of identical realisations of the laser noise but with opposing signs. Although the TDI combinations produce signal datastreams that are free from the laser frequency noise contributions, the time shifting of the optical bench measurements means that the TDI combination data streams defined at different time stamps will nevertheless contain identical realisations of the remaining detector noise terms. Independent TDI combinations (denoted A, E and T) can be constructed from the simpler laser-noise cancelling combinations by diagonalising the correlation matrix of the combination data streams at any given timestamp. This ensures that the optimal combinations are independent with respect to each other at this particular timestamp, but this result does not apply when the optimal combinations are compared at different timestamps. As the time shifting of the optical bench measurements introduces within them identically equal realisations of the remaining detector noise terms, the A, E and

T datastreams could therefore be correlated in time.

The presence, and potential impact, of these time correlations has been investigated for the first time within this thesis. This work has been carried out by identifying the time stamps and optical bench designations of the individual optical bench terms in the algebraic expression for each TDI combination. The resultant configuration of non-zero off-diagonal terms in the covariance matrix for the TDI combination data streams has been investigated for simplified models of the LISA constellation.

The presence of non-zero correlations between the combination datastreams could pose a serious problem to a number of signal parameter search methods that rely on the datastreams being independent. The effects on the parameter recovery for a gravitational wave signal containing two sinusoids has been investigated for a simplified LISA model and for the combination datastreams produced using the data from the second Mock LISA Data Challenge. In both cases, the presence of identically equal detector noise realisations in different time stamps of the signal datastreams introduces auto and cross correlations between the combinations. When the non-zero covariances were explicitly accounted for within the likelihood function, the confidence intervals, reflecting the uncertainty in our inference of the unknown parameters, were found to be significantly smaller - indicating significantly tighter constraints on the true signal parameters, in comparison to the results obtained with a likelihood function that assumed the data streams to be independent in time.

Declaration

This thesis describes the work undertaken between October 2004 and March 2008 in the field of Gravitational Wave Data Analysis. The work described within was carried out by the Author, with the help from her Primary Supervisor Martin Hendry and her Secondary Supervisor Graham Woan. References to work by other Authors have been clearly cited in the text.

Thesis Structure

The structure of this thesis is as follows. Chapter 1 presents a brief introduction to General Relativity and the wavelike solutions that indicate the presence of gravitational waves. It also includes a discussion on the nature of gravitational waves, possible astrophysical sources and the interferometric principles behind the detection of gravitational waves. This work is derived from the literature and the references are clearly cited within the text.

Chapter 2 provides a detailed overview of the LISA antenna, including descriptions of the individual spacecraft and the contributions to the LISA optical bench data streams. The sensitivity of the detector is also discussed and the cancellation criterion for the laser noise contributions, that would otherwise swamp the gravitational wave signals, is highlighted. Similarly to Chapter 1, the work discussed in this Chapter is derived from the literature and the references used are clearly cited in the text.

Chapter 3 introduces the principles and methodologies of Time Delay Interferometry (TDI). The different TDI combinations of the optical bench data streams, which cancel out the laser noise contributions, are introduced. The derivation of the TDI combinations provided in this Chapter, including the optimal combinations (A, E and T), is referenced from the literature and has been clearly cited in each case. The Author also introduces a new visualisation method for identifying the relevant optical bench measurements and the time delays required to be applied to each.

In the fourth Chapter, the existance of time correlations in the signal data streams of the TDI combinations is discussed and the Author presents her work on the identification of identically equal detector noise realisations at different time stamps of the combination data streams, for a simplified LISA model. From these results, the presence of the time correlations as non-zero values in the covariance matrices is discussed for the optimal TDI combinations (A, E and T) and the significance of the individual, and collective structure, of the non-zero terms is highlighted. This Chapter also contains an overview of the mathematical descriptions of covariance and correlation that are used extensively in the later Chapters. The references used in this Section are

clearly cited in the text.

Chapter 5 contains a brief overview of Bayesian Probability Theory and the analytical principles that can be used to recover signal parameters from observations. In this Chapter, the Author investigates the recovery of signal parameters for a gravitational wave data stream containing two sinusoidal signals and a simplified LISA model. The recovery of the unknown signal parameters using likelihood analysis is compared and discussed for signals that fully account for the presence of the time correlations, and for signals that are assumed to be independent. References used in the relevant Sections are clearly cited in the text.

In Chapter 6, the possibility of time correlations within the existing LISA data is investigated for the data sets created for the Mock LISA Data Challenges. The non-zero covariances between the optimal combination data streams at different time stamps, for the data provided by the LISA Simulator and Synthetic LISA, is presented and discussed in each case. The work in the Chapter was undertaken by the Author, with clear reference in the text to the use of the MLDC data sets.

The final Chapter includes a summary of the overall results for each Section and presents the overall conclusions on the work presented in the Thesis. The Author also discusses possible future work in this field.

Acknowledgements

Throughout my time as a PhD student at the University of Glasgow I have received help and support from a number of people that I would like to acknowledge in this Section.

I would like to thank my primary Supervisor Martin Hendry for all his help and continued support throughout my PhD. Thanks also to my secondary Supervisor Graham Woan, for his patience and encouragement. My heartfelt thanks to both of you for guiding my progress, providing valuable insights into the field of Gravitional Wave data analysis and for being able to answer all of my questions, sometimes with another question!

I would also like to thank the two Research Groups that I was part of; the Institute for Gravitational Research and the Astronomy and Astrophysics Group for making me feel welcome and for furthering my interest in the different fields of research. Thanks to PPARC (and now STFC) for providing the funding for my PhD and allowing me the opportunity to experience and contribute to cutting edge scientific research.

I would especially like to thank John Veitch and James Clark for being fantastic officemates; namely for providing encouragement and random chat in equal measures, for brewing coffee at a frightening strength and also for maintaining the office at a *comfortable* temperature. Thanks also to Matt Pitkin, Rejean Dupuis, Mikel Bastarrika and all of the other residents of R465 for keeping the reputation alive.

For in depth discussions on all manner of things and all round awesomeness I would like to acknowledge the talents of Bob Taylor, Jennifer Pollock, Peter Murray, Ross Galloway, Bryan Barr, Eleanor Chalkley, Hazel Bain, Richard Codling, Morag Casey,

David Crooks, Iain Hannah, Kerry O'Shea, Ed Bloomer, Chris Messenger, Siong Heng, Fiona Speirits and all the other members of the Lunchtime Slackers for keeping me highly entertained throughout my PhD. Thanks also to Robert McKay, Craig Stark, Iain Martin, Gordon Hill, Andy Gilston, Laura Reid and Helen Scott for fantastic Road Trips and Pub Wednesdays and also for appreciating and mocking the chip wrap in equal measures. As a group, your unfailng help and advice has been invaluable.

I would also like to thank McVities for making their Milk Chocolate Digestive Biscuits; one of the best Thesis Writing Companions a girl could ask for.

And finally, I would like to thank my parents, Susan and John Toher, and my sister Jacqui Toher for their continuous love and support throughout my Undergraduate and Postgraduate education. The success of my PhD and my continued interest in Physics and Science is the result of your continued encouragement.

Thank you.

Contents

List of Figures

List of Tables

Chapter 1

Introduction

The discovery and detection of *gravitational waves* will revolutionise our understanding of our Universe. The astrophysical electromagnetic signals collected by the current ground-based detectors provide information about our Universe in a wide range of frequencies. However the information contained in each signal is constrained by the last scattering interaction in which the waves participated. In many cases, the origin and nature of the signals is obscured by secondary scatterings close to the astrophysical source. Gravitational wave signals are relatively unaffected by the intervening matter and will therefore provide a way to directly probe the properties of sources that are completely invisible in electromagnetic wavelengths.

The information contained within the signals will shine light into a number of fields of physics, including cosmology and particle physics. The measurements will provide new data that may challenge our current understanding of how the Universe works and the current theories that we use to describe its properties and dynamics.

The prospect of detecting a gravitational wave signal is tremendously exciting but the expected amplitudes of the signals ($h \sim 10^{-21}$) and the comparable detector noise contributions are a challenging problem to overcome. Refined from the first detector design in the 1960s, the current ground based gravitational wave detectors are close to achieving the signal sensitivities that will allow confident detections of gravitational wave signals from the surrounding noise [6, 7].

In this Chapter, the Author will provide an introduction to Gravitational Wave Theory, including a brief overview of detection principles and methods used to date.

The full description of tensor mathematics that is necessary for a complete discussion of General Relativity has not been included in this thesis, but for further reading, the Author highly recommends the following references; [8, 9, 10].

The topics discussed within this thesis have numerous notational conventions and, for clarification, a Glossary has been provided in Appendix G as a reference for the differing usages and types of notation encountered in each field.

1.1 Introduction to General Relativity

General Relativity (hereafter GR) is a Theory of Gravity that combines the properties of Newtonian dynamics with the ideas on relative motion presented in Special Relativity (hereafter SR).

In mathematical terms, General Relativity represents the extension of the concepts formalised in Special Relativity in a globally flat spacetime to the more general case of curved spacetime geometry, that is locally flat. The pioneering work by Minkowski on the description of a *spacetime* structure, where the separate coordinates (t, x, y, z) used to define events in the reference frames of the observers were described as a four dimensional space, provided the necessary geometrical framework that led directly to the formation of General Relativity in 1914-16 [8].

Classical Newtonian and General Relativity have distinctly different descriptions of gravity. In the latter case, gravity is described in terms of the local geometric curvature of a global spacetime surface, while in the former case it is considered as the action of a force. The relative curvature of the surface is defined by the distribution of matter and energy. The local density of matter affects the geometry of spacetime, causing it to curve, while the curvature of spacetime in turn explains the motion of the mass within it. Thinking of this in terms of the Earth, the mass of the Earth distorts the surrounding spacetime by an amount determined by its gravitational mass, which crucially, is equivalent to its inertial mass. The orbits of smaller astronomical objects (e.g. asteroids) that do not measurably contribute to the curvature themselves, will follow the local spacetime curvature determined by larger masses (e.g. the Sun).

Within General Relativity, the gravitational field is described using *Einstein's Equations*, which directly relate the curvature of the spacetime to the distribution of the matter and energy, in the form of tensor expressions[1] [10].

$$G_{\mu\nu} = R_{\mu\nu} - \frac{1}{2} g_{\mu\nu} \mathcal{R} = 8\pi G T_{\mu\nu}$$

where G is the Newtonian Gravitational Constant. Note that in many cases [8, 11], simplified geometric units are introduced by defining $c = G = 1$. The convention for the index labelling follows that of [11]: indices from the greek alphabet (i.e. μ, ν) denote the four spacetime coordinates (i.e. $\mu = 0 - 3$), while the roman indices (i.e. a, b) describe only the spatial coordinates (i.e. $a = 1 - 3$).

The term in the right hand expression, $T_{\mu\nu}$ is the *Energy-Momentum tensor* which describes the distribution of matter and energy in the Universe. In astrophysics and cosmology, this matter distribution is commonly assumed to be a perfect fluid [2] [12, 13, 8]. The different components for the Energy-Momentum tensor, denoted by different index combinations, correspond to movements of energy or momentum across different coordinate surfaces.

The geometric curvature is described by the *Riemann Curvature Tensor* $R_{\beta\mu\nu}{}^{\alpha}$ and relates directly to the properties of the spacetime surface. Lowering the α index using a metric term, the Riemann tensor can also be written as,

$$R_{\alpha\beta\mu\nu} = g_{\alpha\lambda} R_{\beta\mu\nu}{}^{\lambda} = \frac{1}{2} \delta^{\delta}_{\alpha} (g_{\delta\nu,\beta\mu} - g_{\delta\mu,\beta\nu} + g_{\beta\mu,\delta\nu} - g_{\beta\nu,\delta\mu}) \tag{1.1}$$

where the comma subscript denotes partial differentiation over the following index terms. In the local inertial frame, this expression reduces to,

$$R_{\alpha\beta\mu\nu} = \frac{1}{2} (g_{\alpha\nu,\beta\mu} - g_{\alpha\mu,\beta\nu} + g_{\beta\mu,\alpha\nu} - g_{\beta\nu,\alpha\mu}).$$

[1] See References [10, 8] for a detailed discussion of tensor notation.

[2] A perfect fluid is a fluid that has no viscosity ($T^{ij} = 0$ for $i \neq j$) and no conduction of heat ($T^{0i} = T^{i0} = 0$) in the momentarily co-moving reference frame.

With this result, the symmetries between some of the index terms become apparent, and hence,

$$R_{\alpha\beta\mu\nu} = -R_{\beta\alpha\mu\nu} = -R_{\alpha\beta\nu\mu} = R_{\mu\nu\alpha\beta},$$

and,

$$R_{\alpha\beta\mu\nu} + R_{\alpha\nu\beta\mu} + R_{\alpha\mu\nu\beta} = 0.$$

Although these expressions have been derived in a local inertial frame, they are valid tensor expressions and are therefore applicable in all coordinate frames. They reduce the number of independent components from 256 to just 20.

As shown in equation 1.1, the Riemann tensor is described in terms of the second derivatives of the metric terms. The first order variations in the metric function are commonly expressed in terms of *Christoffel Symbols* $\Gamma^{\mu}_{\alpha\beta}$, where

$$\Gamma^{\mu}_{\alpha\beta} = \frac{1}{2} g^{\mu\sigma}(g_{\sigma\alpha,\beta} + g_{\sigma\beta,\alpha} - g_{\alpha\beta,\sigma})$$

The Riemann tensor can therefore be described in terms of the Christoffel symbols and their derivatives. Due to these definitions, the components of the Riemann tensor also satisfy the Bianchi identities, which constrain the differential properties of the tensor.

The Einstein Tensor, $G^{\mu\nu}$ and the Ricci Tensor, $R^{\mu\nu}$ are contractions of the Riemann tensor [8]. Note that $\mathcal{R}$ is a further contraction of the Ricci Tensor with the metric $g^{\mu\nu}$,

$$\mathcal{R} = g^{\mu\nu} R_{\mu\nu}.$$

This quantity is commonly referred to as the *Ricci Scalar* and provides a scalar measure of the global curvature.

The metric ($g_{\mu\nu}$) is a function that expresses the physical separation between events in spacetime in terms of the individual coordinates measured by observers in a particular reference frame [12]. For locally flat geometry, for example in Special Relativity,

a coordinate frame can be found in which the metric takes a very simple form,

$$g_{\mu\nu} = \begin{pmatrix} -1 & 0 & 0 & 0 \\ 0 & 1 & 0 & 0 \\ 0 & 0 & 1 & 0 \\ 0 & 0 & 0 & 1 \end{pmatrix}$$

where the first index denotes the time dimension and the remaining three describe the three spatial dimensions, x, y and z respectively. This metric description is termed the *Minkowski Metric* and can be used to relate the interval between two events to coordinates in the four dimensional spacetime structure. Note that the separation between the events can be infinitesimally small.

The extension of this framework globally for our Universe is made possible by applying the *Cosmological Principle*, the assumption that the Universe is homogeneous and isotropic. Different geometric frameworks are reflected in different metric descriptions, for example, the *Friedmann-Robertson-Walker metric* (FRW) is the most general form of the metric that describes a homogeneous and isotropic Universe. In this case, the metric takes a similar form as the Minkowski metric but with time dependent scale factor terms ($a(t)$) on the non-zero spatial coordinates; $g_{\mu\nu} = [-1, a^2(t), a^2(t), a^2(t)]$. Note that this form of the metric does not constrain the curvature of the Universe to being open, closed or static. The metric is just the mathematical framework that describes the separation due to the curvature; the matter distribution defines the type of curvature.

Solutions of the Einstein Equations correspond to unique descriptions of the properties and dynamics of gravity on the global matter distributions.

With the application of the Cosmological Principle, the solutions to the full form of the Einstein Equations involve solving ten independent nonlinear partial differential equations. The reduction in the number of independent solutions of the Equations is due to some terms reducing to zero in certain combinations and equivalences in the order of the indices due to the assumption of a homogeneous and isotropic Universe. The

validity of the simplification is independently supported by the large scale isotropy of the cosmic microwave background radiation and is itself an extension of the *Copernican principle* from which we observe that we occupy no special place within our Universe.

1.1.1 Cosmological Models

The solutions to GR provide the foundations for different *cosmological models*. The models describe the behaviour of the Universe in terms of physical properties and evolution. The models are built around the description of gravity provided by the Theory and are characterised by *cosmological parameters*, terms that quantify a particular property of the Universe. Examples include, the relative density of baryonic matter, the percentage of dark matter in the Universe or the speed at which the Universe is expanding. The individual values of these parameters will directly affect the properties of the Universe that are defined by them. For example, if the Universe expands too fast, small scale structure will have less time to form and therefore the value of the Hubble parameter, that characterises the expansion speed, will directly influence the matter distribution and hence the type of astronomical objects and the relative structures of the Universe that we see today.

Each model Universe has an unique combination of different cosmological parameters which will define the Universe at every stage of its evolution. By comparing our observed Universe with the predictions from different cosmological models, we can probe the constraints on the parameter values that the observations impose and thus identify the reduced number of models that are able to accurately describe our observable Universe.

Many of the current cosmological models use a simplified set of these equations that are based around the *Cosmological Principle*. With this assumption, the evolution of the Universe can be described by a single equation known as the *Friedmann Equation* [10],

$$H^2(t) = \frac{8\pi G}{3}\left[\rho(t) + \frac{\rho_{cr} - \rho_0}{a^2(t)}\right]$$

where $\rho(t)$ is the energy density of the Universe as a function of time and ρ_0 is the

current value. The critical density, which can be related directly to the curvature of the Universe, is given by the equation,

$$\rho_c = \frac{3H_0^2}{8\pi G}$$

where H_0 is the current value of the time dependent *Hubble constant* $H(t)$ and G is the Newtonian Gravitational Constant. From the recent results for the Wilkinson Microwave Anisotropy Probe (WMAP), the value of the H_0 is currently constrained to be 70.1 ± 1.3km/s/Mpc [14].

Note that cosmological models which are constructed around Equation 1.1.1 are known as *Friedmann Models*.

All of the cosmological models that incorporate General Relativity as a description of gravity will display some degree of common behaviour. For example, the incorporation of the description of Special Relativity constrains the speed of light in vacuum to be a universal constant for all model definitions. GR can be tested by investigating the global gravitational dynamics and properties of our observable Universe. The definition of the matter distribution and the curvature of spacetime using a metric framework leads to a interesting prediction: propagating perturbations in the metric itself, known as *gravitational waves*.

1.2 Introduction to Gravitational Waves

Gravitational waves can be seen in Einstein's theory of General Relativity, appearing as wavelike solutions in the mathematical metric description of the Field equations. They are often described as *ripples in spacetime*. This is a useful analogy and is usually accompanied with a clear picture of wavelike ripples on a two dimensional gridlike spacetime. These descriptions are very useful but are also misleading as the waves are perturbations in the four-dimensional spacetime metric. In contrast to the behaviour of scalar perturbations (e.g. longitudinal waves) which alter the geometric volume, gravitational waves cause a twisting distortion of the spacetime that does not affect

the volume. A passing gravitational wave therefore results in an alternate stretching and contracting of the spacetime itself. These perturbations propagate in the spacetime surface and will travel at the speed of light in vacuum [9, 12].

Gravitational waves are caused by the motion of large masses distorting the surrounding spacetime. Spacetime itself is relatively stiff as a medium and therefore the 'ripples' caused by such motions will be detectable only as a small perturbation in the geometric curvature of the surface. For an Earth-based detector, the predicted strain of an astrophysical gravitational wave source is typically about one part in 10^{22} [15]. Importantly, the waves are relatively unaffected by the presence of local matter distributions [8]. This unique property means that when the signals are detected and measured, they would contain unrivaled and unspoilt information about the sources themselves.

In this Section, the Author will present a brief introduction to the origin of the wave-like solutions in the Theory of General Relativity and discuss the properties of the waves and the possible astronomical sources that could generate them.

1.2.1 Gravitational Waves in Theory

Gravitational waves, generated by the motion of large matter densities, will affect the global spacetime surface and will result in a complex pattern of small-scale ripples in the spacetime surface. These ripples will interact with each other nonlinearly and the presence of global large-scale curvature will distort the wave fronts of the gravitational wave signals. It is, in general, extremely difficult to separate the individual contributions from a single gravitational wave source from the remaining metric terms [11].

Locally these interactions can be ignored and the gravitational waves viewed as propagating through a flat (or Lorentzian) spacetime. From this viewpoint, it is easier to distinguish between the metric terms and by using *Linearised Theory* it is possible to find solutions to the Einstein Equations that are able to be simplified as Wave

Equations[3].

Linearised Theory is a *weak-field approximation* to General Relativity, where spacetime is viewed as nearly Lorentzian, like Special Relativity. The waves can be viewed as local deviations from the underlying metric,

$$g_{\mu\nu} = \eta_{\mu\nu} + h_{\mu\nu} \tag{1.2}$$

where $\eta_{\mu\nu}$ is the Minkowski metric and $|h_{\mu\nu}| << 1$, following the notation and conventions of [11]. It can be shown that under a Lorentz transform Λ^{α}_{β}, $h_{\mu\nu}$ behaves like a tensor in SR[4]. Therefore within this description, the slightly curved spacetime can be separated out as flat spacetime with a 'tensor' perturbation $h_{\mu\nu}$ defined on it [8]. In the absence of gravity, spacetime is flat and therefore gravity itself is described as a symmetric, second rank tensor field $h_{\mu\nu}$, using the curved-space formalism of General Relativity [11, 16]. In simple terms, the spacetime description in Linearised Theory is curved, although the equations are solved as if it were not. Note that within the constraints of linearised theory, this metric description is correct to first order with General Relativity [8, 11]. The linearised wave descriptions are a simpler case of the more general *short-wave approximation*, where the waves are time-dependent perturbations on a smooth background which has a radius of curvature that is much larger than the wavelength of the waves themselves [9, 17].

From the mathematical description of the perturbation, the trace $h = h_{\alpha}{}^{\alpha}$ and thus the *trace reversed* form of the perturbation can be defined,

$$\bar{h}_{\mu\nu} = h_{\mu\nu} - \frac{1}{2}\eta_{\mu\nu}h$$

where $h = \eta_{\mu\nu}h^{\mu\nu}$. This equation relates the metric perturbation $h_{\mu\nu}$ to a description of the gravitational field $\bar{h}_{\mu\nu}$ [11].

Within the geometric descriptions of the curvature terms there is a certain amount

[3]See Appendix A for a detailed discussion of the wave like solution to the linearised Einstein Field Equations

[4]Note that $h_{\mu\nu}$ behaves like a tensor, provided that the Lorentz boost velocity described by the Lorentz transform is not close to the speed of light

of coordinate freedom, termed *Gauge freedom*, which enables the enforcement of the global *Lorentz gauge*,

$$\bar{h}^{\alpha\beta}{}_{,\beta} = 0,$$

where, as before, the comma subscript denotes differentiation over the adjacent index terms. It should be noted that the gauge conditions do not change the underlying system; they are self-imposed constraints on the existing coordinate freedom and are chosen as they simplify the mathematics. This freedom ensures that a coordinate frame can always be found that maintains the nearly Lorentzian description of the spacetime surface. With the enforcement of the Lorentz gauge, four out of the ten coordinate freedoms are constrained [17]. The remaining freedom relates to *infinitesimal Coordinate transforms* ξ_μ. These are tiny 'wiggles' in the coordinate system that do not affect the size of the perturbation $h_{\mu\nu}$ within the precision limits defined for Linearised Theory [11]. They are termed *residual gauge freedom*, which must also be constrained to,

$$\xi_{\mu,\alpha}{}^{\alpha} = 0$$

The enforcement of these Gauge conditions results in a simplified expression for the linearised Einstein Field Equations,

$$-\bar{h}_{\mu\nu,\alpha}{}^{\alpha} = 16\pi T_{\mu\nu}.$$

From this result, it can be shown that for empty space the propagation equations for the gravitational field reduce to,

$$-\bar{h}_{\mu\nu,\alpha}{}^{\alpha} = 0,$$

$$(-\frac{\partial}{\partial t^2} - \Delta^2)\bar{h}_{\mu\nu} = 0,$$

where

$$\nabla^2 = \left(\frac{\partial}{\partial x^2} + \frac{\partial}{\partial y^2} + \frac{\partial}{\partial z^2}\right).$$

On closer inspection, it can be seen that this result has taken the form of a wave equation - direct evidence for the presence of wavelike solutions of the metric perturbations.

The simplest solution for the wave equations are monochromatic plane waves [8, 11],

$$\bar{h}_{\mu\nu} = \mathcal{A} e_{\mu\nu} \exp(i k_\gamma x^\gamma) \tag{1.3}$$

where $\mathcal{A}$ is the wave amplitude, $e_{\mu\nu}$ is the polarisation tensor and k_γ is the wavevector. The form of the Field equations restricts the wavevector to be 'light-like', with the trace k^γ_γ equalling zero, while the gauge constraints on the gravitational field also ensures that the amplitude and wavevector must be orthogonal ($e^{\mu\nu} k_\nu = 0$). These two constraints on the gravitational waves themselves are commonly referred to as the *Transverse-Traceless Gauge*.

The application of this gauge reduces the remaining coordinate freedom for the wave terms and defines the amplitude tensor ($\mathcal{A} e_{\mu\nu}$) to be,

$$A^{TT}_{\mu\nu} = \begin{pmatrix} 0 & 0 & 0 & 0 \\ 0 & A_{xx} & A_{xy} & 0 \\ 0 & A_{xy} & -A_{xx} & 0 \\ 0 & 0 & 0 & 0 \end{pmatrix}$$

for a wave travelling in the z direction. In this case, the number of independent components of $A_{\mu\nu}$ has been reduced to two. From this analysis, it can be seen that gravitational waves are simple transverse waves, with two polarisations corresponding to A_{xx} and A_{xy} being non-zero respectively.

The effect of the gravitational waves on the surrounding matter, mentioned at the start of this Section, can be investigated by considering two particles separated by a small distance ϵ in the x direction. The particles are defined to be initially at rest relative to each other and hence the proper distance between them is defined to be

[8, 16],

$$\begin{aligned}\delta l &= \int |ds^2|^{1/2} \\ &= \int |g_{\alpha\beta} dx^\alpha dx^\beta|^{1/2} \\ &= \int_0^\epsilon |g_{xx}|^{1/2} dx \\ &\approx [1 + \frac{1}{2} h_{xx}^{TT}(x=0)]\epsilon\end{aligned}$$

where the perturbation term h_{xx}^{TT} can be thought of as the dimensionless strain of space; the ratio of the wave induced displacement of a free particle with the original displacement, both relative to the origin [9]. The TT superscript acts as a reminder of the applied gauge conditions and the nature of the gravitational waves.

As h_{xx}^{TT} is typically non-zero, the proper separation between the test particles in the x direction will change as the wave passes. The incoming gravitational wave will therefore change the physical distance between the two masses in the two directions for which the transverse-traceless perturbation is non-zero. An important distinction to note is that the coordinate distance between the masses is unaffected, the wave is changing the true separation between the two test particles.

Due to their transverse and traceless nature, gravitational waves will produce a *quadrupolar, divergence-free* force field,

$$F_j^{GW} = -mR_{j0k0}^{gw} x^k = \frac{1}{2} m \frac{\partial^2 h_{jk}^{TT}}{\partial t^2} x^k.$$

For a wave propagating in the z direction, as with equation 1.2.1, there are only four non-zero field components, relating to only two independent components. These give the gravitational waves two distinct polarisation states termed 'plus' and 'cross', shown in Figure 1.1, where,

$$h_+ \equiv h_{xx}^{TT} = -h_{yy}^{TT}$$
$$h_\times \equiv h_{xy}^{TT} = h_{yx}^{TT}$$

Hence, the full gravitational wave field can be reconstructed as,

$$h_{ij}^{TT} = h_{+}e_{jk}^{+} + h_{\times}e_{jk}^{\times}$$

where e_{ij} describe the polarisation tensor terms for the two polarisation states [9].

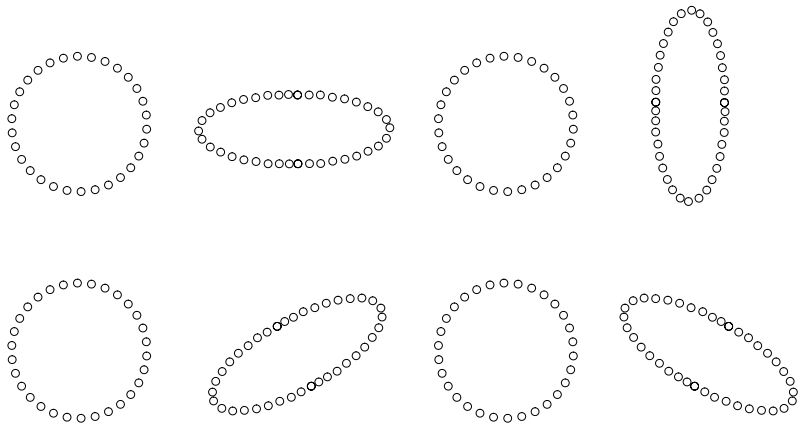

Figure 1.1: The Plus (top line) and Cross (bottom line) polarisations of a gravitational wave, with increasing time towards the right of the page [1].

In summary, gravitational waves are present as wave-like solutions to the Field Equations. From their origins as perturbations in the metric, they behave as TT entities, displaying a quadrupolar field with two distinct polarisations. The passage of a wave causes alternate stretching and contracting of the proper distance between the affected particles. The detection of a gravitational wave would confirm or at least colloborate the mathematical structure behind their prediction and provide a testbed for more detailed investigations in the limits of General Relativity and the sources themselves.

1.3 Gravitational Wave Sources

Gravitational waves are produced when the bulk movement of matter in the Universe affects the surrounding spacetime. The perturbations propagate outwards, carrying energy and angular momentum away from the originating source [18]. The waves are emitted most strongly in regions of spacetime where the local gravity is relativistic and

where the bulk motions of matter are moving at close to the speed of light [9].

Although there is a close relationship between matter distribution and spacetime curvature, gravitational waves are only produced by distinctive asymmetric bulk motions. For example, a spherically symmetric star collapse will not produce a gravitational wave, even if there is a large volume of mass, as there must be a deviation in the symmetry [18]. In this Section, the Author will introduce and discuss a range of astronomical sources that have the potential to be sources of gravitational wave signals.

1.3.1 Transient Sources

Astronomical objects that are only capable of producing gravitational waves for an extremely short period during their evolution are classified as *Transient sources*. They will emit a burst of gravitational waves, before fading rapidly.

To confidently detect a single burst source would require a high signal-to-noise ratio in a single detector or for the signal to appear as a simultaneous event in a number of detectors. The identification of solitary gravitational wave sources can be improved by utilising observations of the source in electromagnetic wavelengths. A number of gravitational wave sources are also highly visible in electromagnetic wavelengths and the information provided by these signals can be utilised to provide constraints on the signal parameters of the source. In many cases, the electromagnetic counterpart information providing a way to break degeneracies between the gravitational wave parameters (i.e. between mass and redshift) [19]. In this case, the combination of both sets of information could result in tighter constraints on the confidence intervals of the gravitational wave source parameters.

Supernovae

A core-collapse *supernova* is the result of the gravitational collapse of the inner degenerate core of an evolving star [17]. The available outward thermal pressure can no longer counter-balance the gravitational attraction and the inner core of the star collapses and rebounds. The collapse releases a large amount of energy (approximately

$0.15 M_{\odot} c^2$ [17]), most of which is converted into neutrinos. There is the possibility, however, that a small fraction could be converted to gravitational waves.

Dependent on the initial mass of the core, the remnant has the potential to become a neutron star or black hole. The gravitational waves could be produced from the dynamical instabilities in the rapidly rotating core as it evolves towards its end state. The rotation is due to the conservation of angular momentum and any asymmetry in the geometrical shape of the remnant could result in wave production [16].

Supernovae are (electromagnetically) among the brightest objects in the Universe and are well understood observationally. The detailed dynamics of the collapse are obscured by the outer layers of the star, even the neutrinos are secondary scattered by the intervening matter. As the propagation of the gravitational wave is mostly unaffected by the local matter; the signals could prove to be an invaluable way of probing the source itself.

1.3.2 Binary Systems

Binary systems have provided the best evidence for the reliability of General Relativity and the prediction of gravitational waves. Although there is still to be a direct observation of a gravitational wave signal there is conclusive indirect evidence. The most famous example of this is the binary pulsar PSR1913+16, discovered by Hulse and Taylor in 1974 [20].

The system contains two neutron stars with a combined orbit radius only marginally larger than the Sun's diameter [18]. The objects are caught in their communal gravitational attraction and are losing energy through gravitational radiation. As a direct result, the objects will move in a spiraling binary orbit. The increased orbital frequency of the binary translates into an increase in the power radiated as gravitational emission. The frequency and amptitude of the emitted wave increases over time, taking the form of a *chirp* like signal. The increase in signal frequency caused by the orbiting binary pair is limited to [9],

Until the final stage however ($f \geq 0.01$Hz [21]), the majority of the sources will emit

---

$f_{max} \simeq 1$ kHz for neutron stars

$f_{max} \simeq \frac{10 \text{ kHz}}{M_1/M_2}$ for BHBH, where M_1 is the larger object

---

an approximately monochromatic signal. The energy lost on each orbit can be predicted using General Relativity and has been independently collaborated observationally. This result secured Hulse and Taylor the 1993 Nobel Prize in Physics.

Our local galaxy contains billions of binary star systems; each with the potential to be a source of gravitational waves. A small subset of the population (approximately tens of millions) contain galactic compact objects such as white dwarfs, neutron stars and stellar black holes. Extra-galactic sources of detectable signals include *supermassive black holes* (SMBHs), with a total mass in the range of $10^4 M_\odot - 10^7 M_\odot$. The binaries will produce detectable continuous gravitational radiation as the orbits of the objects decay over time. The strength of the wave signal depends on the size of the orbiting masses. The low frequency gravitational wave spectrum ($10^{-4} - 10^0$Hz) is swamped by the large number of galactic compact binary signals. The individual signals are defined into two categories; *resolvable binaries* and *confusion foreground*; binaries that are unable to be confidently detected within the finite observation time.

The coalescing binary systems produce a distinctive gravitational waveform and can therefore be easily identified from background GW signals. The coalescence is characterised into three stages; firstly the previously mentioned *Inspiral* phase where the objects spiral towards one another releasing gravitational waves, the *Merger* when the objects interact and become one single object and finally the *Ringdown* waves released as the object relaxes into a Kerr black hole. In this final stage, the ringdown waves have a high frequency, relating to the monochromatic chirp-like nature of the inspiral phase, with a decaying amplitude. The properties of the waveform during the merger phase are not yet fully understood, although the two binary objects will continue to release gravitational waves during this phase [22, 19]. Note, that the waveform released during the final stages is sometimes referred to as the *coalescence waveform*, encompassing the

two final phases and last stage of the inspiral waveform when the tidal forces due to the masses of the objects has become noticeable. The timescale for the evolution is dependent on the initial masses of the binary components. The event rate for the neutron star and black hole binaries is estimated at $\sim$ (3/year)(distance/200Mpc)^3 [23, 24].

The binary waveforms for each stage are modelled theoretically using the *Post-Newtonian approximation* (PN) to General Relativity, a generalisation of Linearised Theory. In this approximation, the geometry of spacetime is described using Newtonian gravity in the lowest order but with a number of higher order corrections described by General Relativity [25]. As the binary objects enter the inspiral phase, the dynamics are well described using Newtonian gravity. As the frequency of the waveform increases towards f_{max}, the post-Newtonian corrections become more important.

Detecting Binary Systems

Combining these theoretical models with observations provides continuous tests of General Relativity and also a vast amount of information about the sources themselves. Modelling the evolution of the binary signal provides parameter information about the binary components; for example, the orbital period, eccentricity and individual masses.

Combining the observations also provides an estimate of the event rate of the different binary types, over the redshift range covered by the detector. As expected, there is a correlation between redshift distance and the prominence of a particular type of binary source (ie. NS-NS, NS-BH, BH-BH), peaked at a particular redshift range. Each binary system is composed from compact objects that are the end results of other astronomical processes and is therefore more probable in areas where the abundance and availability of each type is high [21].

The detectability of the binary is also dependent on the amplitude and frequency of the released GW signal. The initial frequency of the released gravitational wave is dependent on the properties of the binary components, i.e. separation, composition, initial velocites. This frequency will increase over the timescale of the evolution. In order for the signal to be detected, the signal must have sufficient *signal-to-noise* to be

identified from the surrounding background noise and must fall within the frequency band limitations of the detector. For a NS-NS binary, each with a mass of $1.4M_{\odot}$ and a signal-to-noise of 5, the estimated detection range for the current ground based detectors are shown in Table 1.3.2, [17], for a detection threshold of 5σ. For detection

Detector	TAMA300	GEO600	LIGO1	VIRGO	Adv LIGO
Range	3Mpc	14Mpc	30Mpc	36Mpc	500Mpc

purposes, binaries with masses greater than $1M_{\odot}$, that are radiating above 10^{-3}Hz, will always chirp within a one year time period [17].

It is therefore unsurprising that the signals from the smaller compact object binaries detectable by the current ground based gravitational wave detectors are galactic in source. These sources will radiate gravitational waves with a range of frequencies up to 0.1Hz. The number of sources, estimated from models of galactic population, predicts that there are approximately 10^5 binaries within the frequency band of 1mHz - 5mHz [26].

BHBH binaries

The ubiquity of black holes at the centre of galaxies and the inherent tendency of galaxies to combine together, means that there is a relative high event rate of BH-BH coalescences ($\sim 60-70$ events per year for space based detectors), in comparison to some of the larger SMBH-SMBH mergers [21]. This expectation has been confirmed kinematically by the discovery that galaxies with large central bulges host a massive $(10^6 - 10^9 M_{\odot})$ black hole [21]. Estimates from the high redshift quasar population also suggests that a large population of black holes has existed since early epochs [27].

This type of binary will produce strong gravitational wave amplitudes and will merge on timescales varying from hours to a few years, resulting in a Kerr black hole [22, 28].

There is an inherent *mass-redshift degeneracy* in the detection and measurement

of the sources, due to the inter-dependence of each term in the equations used to model signals. This implies that a system with total mass $5 \times 10^4 M_\odot$ at $z = 1$ will be indistinguishable from a binary with mass $2 \times 10^4 M_\odot$ at a redshift of 4. This degeneracy could be resolved using using collaboratory evidence from electromagnetic counterparts. This information can also be used to provide a pre-determined range of possible targets, increasing the possibility of a detection [19]. These sources are of extreme interest for detection as they are guaranteed sources for space based gravitational detectors due to the high numbers of extra-galactic sources and will provide a probe into relativistic gravitational regimes [9].

Extreme Mass Ratio Inspirals

If the binary is composed of a stellar mass compact object and a supermassive black hole, the stronger field of the SMBH results in complex orbits of the smaller mass object. Due to the disparity in the individual sizes, these type of binaries are termed *Extreme Mass Ratio Inspirals*. The timescale of the gravitational emission is directly related to the orbital time of the smaller mass, corresponding to approximately $10^4 - 10^5$ orbits.

An interesting property of the binary orbit is the *zoom-whirl behaviour*, where the smaller compact object completes many orbits around the BH ('whirls') as it 'zooms' in from apocenter to pericenter of the orbit [21, 27].

EMRIs are thought to be created due to the scattering processes with galactic cores. The compact object is brought within the gravitational influence of the black hole as the result of numerous multibody interactions with other objects. The resultant modulations caused by the orbiting binary encodes a large amount of information about the local spacetime. Tracing the individual orbits of the smaller companion would provide estimates of the spacetime properties with high precision. The parameters of the end state black hole could also be analysed without the assumption that it behaves as a Kerr black hole [21].

1.3.3 Stochastic Sources

Stochastic gravitational waves arise from the superposition of a number of discrete uncorrelated gravitational perturbations. They are often referred to as *random* waves and collectively form a background signal with a flat, or slightly peaked spectrum.

There are two main contributors to the stochastic background; the first are the galactic binary systems that are unable to be detected; termed the *confusion foreground*. These sources are emitting gravitational waves at frequencies lower than the detectable frequency band or over short timescales that result in the detector being unable to be resolve their position on the sky. The sources that fall into this category are viewed stochastically as a single spectrum, created from the superposition of the relevant sources. This foreground will contribute to the noise signal of a space based detector with lower frequency limits than the ground based detectors, swamping the instrumental curve below frequencies of approximately 1mHz.

The second main contribution is thought to be cosmological in origin; namely primordial fluctuations in the global spacetime structure introduced in the early stages of the Big Bang. These perturbations would have been parametrically amplified by *inflation*. These waves are estimated to have frequencies corresponding to a range of 10^{-16}Hz to 10^{10}Hz. The lower limit relates to the inverse Hubble scale when the Universe became matter dominated and the higher limit is determined by the timescale over which inflation ends and the Universe becomes hot and radiation dominated. The sources could therefore provide a direct probe for inflationary physics but unfortunately due to their small amplitudes are unable to be individually detected by any of the current gravitational wave detectors. Other cosmological sources include phase transitions due to matter density differences and cosmic strings in the early Universe [21].

1.4 Detection of Gravitational Wave Signals

The first dedicated gravitational wave detector was built in the 1960s by Joseph Weber to detect cosmic gravitational waves. At the University of Maryland, he constructed

the first *resonant bar detector*, which comprised of a large solid cylinder of aluminium with an approximate mass of 2×10^3kg. The concept was that a passing gravitational wave would cause the bar to excite at its resonant frequency, amplifying the signal and enabling it to be detected by electronics sensitive to the vibrations. Operating at room temperature, the resonant frequency of Weber's bar was approximately 1600Hz and was capable of detecting a length change of around 10^{-16} metres [17].

This sparked a global interest in the detection of gravitational wave signals. The sensitivities of the resonant bars were improved and new detector designs were built, capable of measuring the length change introduced by the wave using interferometry.

By the late 1970s, the achievable dimensionless strain that could be detected experimentally had improved by a factor of ten across the expected signal frequency range. For example, gravitational wave burst signals in the kilohertz frequency range with an incidence rate of three per year could now be detected at a dimensionless strain of $h \sim 10^{-16}$. This limit coincided with the maximum prediction for the signal amplitudes from theoretical calculations, indicating that a detection was possible, but unlikely.

In order to guarantee a confident detection, the noise sensitivities of $h \sim 1 \times 10^{-20}$, and ideally $h \sim 10^{-21} - 10^{-22}$, would need to be achieved [9]. This could be made possible by first identifying and then reducing the noise contributions in the signal frequency bands, which would improve the signal sensitivity of the detectors.

In this Section, the Author will first summarise the principles behind detecting an interferometric length change and then discuss some of the challenges facing the current detector designs.

1.4.1 Principles of Interferometry

Interferometry uses the wavelike nature of light to measure the properties of the waves themselves. The superposition of two or more waves creates an interference pattern that is directly related to the properties of the waves that are involved.

Commonly, the interferometer splits a single source of light into two coherent beams and directs them along different light paths before recombining the beam. This is an

example of *homodyne detection*, as the beams involved have the same wavelength. The resultant interference pattern is detectable as changes in the intensity levels of the beams on the detector.

If the properties of the light beams have been changed by their journey then the interference pattern will provide a measure of the variation, for example, of the relative phases of the light. The phase of a wave (θ) describes the completed fraction of a single repetition of the waveform from an initial reference point at t=0. For example, a cosine wave can be described in terms of a sine wave with a initial quarter wavelength phase shift ($\theta = 2\pi\frac{\lambda/4}{\lambda}$).

If two waves have the same frequency and phase then they will constructively interfere with each other to produce a single wave with a combined amplitude of the original waves. If the waves are exactly out of phase, then they will destructively interfere and cancel each other out, provided the amplitudes and frequencies are identical.

The length of the light paths will determine the outcome of the interference. An interferometer can therefore detect small changes in the light path by measuring the variations in the interference pattern. The changes in the pattern will be related to fluctuations in frequency or phase of the light. It is therefore important that the light source for the optical system is coherent. *Lasers* are often used as they produce monochromatic light beams that are coherent and also have small divergence angles making it easier for the light to be recombined.

Possible sources of the variations include the frequency variations of the light source, relative motions of the interferometer itself, variations in the refractive index or distortions in spacetime along the beam path, in other words, a passing gravitational wave.

A common optical configuration for interferometry is the *Michelson Interferometer*, made famous by Albert Michelson and Edward Morley when they used it to prove the non-existance of the aether [29]. As shown in Figure 1.4.1, within the Michelson Interferometer the light source is passed through a half silvered mirror which acts as a beam splitter, sending half of the light down each arm length toward the end mirrors.

The mirrors reflect each beam back along its original path, where the two beams are brought back together and directed into a detector to measure the interference pattern for the light. The end mirrors are placed perpendicular to each other at an equal distance from the beam splitter. This will ensure that the light path in each arm is the same [7].

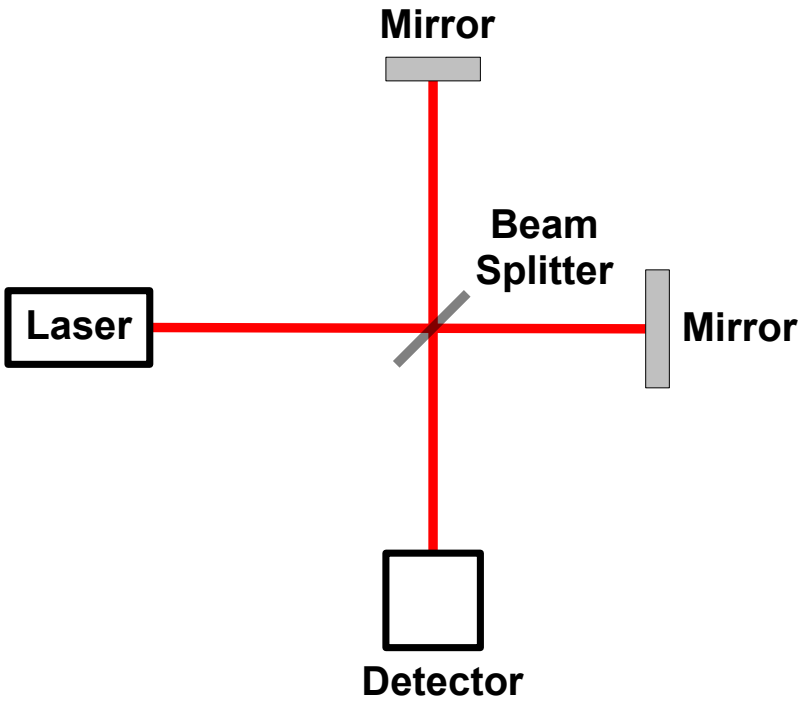

Figure 1.2: Diagram of Michelson Interferometer configuration. Within this framework, the laser beam from a single source is split by a half silvered mirror and travels down equal arm lengths towards the end mirrors. The beams are then reflected back along the arm length optical paths and are brought back together in the detector, producing an interferometric fringe pattern.

When the laser light is directed around the optical system, as opposite to travelling up and down two optical arms, the optical system is termed an *Sagnac* or *Ring Interferometer* [22]. Similar to the Michelson interferometer, the optical setup uses a single laser source that is divided in two by a beam splitter. The beams are directed in opposite directions around the optical bench, where reflective mirrors ensure that the beam paths cross again at the point of entry into the system. They are recombined to give an interference pattern and directed out of the ring system. Note that the total beam path must enclose an area.

The overall position of the interference fringes is dependent on the angular velocity

of the optical benches. If a bench is in motion then the entry/exit point will vary relative to the transit time of beams. This will result in unequal optical paths around the interferometer and will be detectable as a shift in the interference pattern.

In summary, the shape of the interference pattern is dependent on the frequency and phase of the laser light. Changes to the optical system will result in variations in the fringe pattern.

The data analysis implications of both types of interferometer are discussed in more detail in later Chapters, where the optical paths described in each case are utilised for recovering gravitational wave information from LISA.

1.4.2 Gravitational Wave Detection

The current ground based gravitational wave detectors use complex laser interferometry techniques to recover gravitational waves signals. The variation in the path length caused by a gravitational wave is of order $\frac{\Delta L}{L} \sim 10^{-20}$, which is approximately 10^{-5} smaller than the diameter of a proton, for an arm length (L) of 1 metre. This makes gravitational waves very difficult to detect and measure but sensitive measurements of the length change caused by an incident gravitational wave can be made using laser interferometry.

The phase stability of the laser light is approximately $\frac{\Delta\nu}{\nu} \sim 10^{-13}$ and therefore the *laser noise* contributions to the raw data stream will completely swamp the gravitational signal [30, 22, 5]. Fortunately during the interferometry the laser light is split into two coherent beams and therefore the laser noise contributions will be the same at each timestamp. If each beam experiences the same light travel time then the laser noise contributions will be cancelled out at the detector (for each timestamp). In other words, the laser noise can be removed as long as the optical system has arm lengths that are identically equal.

The passage of a gravitational wave through the location of the interferometer will alter the light path in each of the arms in a predicable way. The distortions in spacetime will cause the light travel time in one arm to shorten (contraction of the

spacetime) and simultaneously the other to lengthen (expansion of spacetime) for a tangental gravitational wave.

There are currently a number of gravitational detectors that use interferometry to search for gravitational wave signals. They provide a good coverage of possible source locations, enabling analysis to be done on the signals to recover the properties of the gravitational waves. These include the Laser Interferometry Gravitational wave Observatory (LIGO) [31] in America and the VIRGO interferometer in Italy [32], with equal arm lengths of 4km and 3km respectively. There are also smaller detectors, namely GEO600 [33] in Germany with arm lengths of 600m and TAMA [34] in Japan with 300m arm lengths. The individual configurations are variations on the classical Michelson interferometer design, where a slight variation in the length of the arms changes the intensity of the superimposed signal. The detectors have individual design solutions which improve the natural sensitivity of the interferometer to the gravitational wave strain. For example, the GEO600 system is kept seismically isolated from the surroundings by suspending the optical elements from pendulums. This ensures that they are kept in one-dimensional free fall. The pendulums have natural frequencies that are well below the sensitivity band for the detector and act as filters, removing the mechanical vibration noise that would affect the signal recovery [15].

The current gravitational wave detectors are sensitive to signals between approximately 10Hz and 10^3Hz. The achievable detectable strain with the current noise levels is approximately one part in 10^{22} (LIGO detector in frequency band = 50-1000Hz) [15].

The detectors operate in the *Long Wavelength Limit* (LWL), where the gravitational wavelength is much larger than the arm lengths of the detectors [35]. Note that the wavelength of the gravitational wave is $\frac{c}{f_0}$, where f_0 is the characteristic frequency of the wave. Due to the limitations on building a comparable sized detector on Earth, the detectors act like short antennas, restricting the sensitivity of the optical systems to the signals.

A number of the detectors are currently undergoing extensive upgrades that will improve their sensitivities to lower frequency gravitational waves. But the inherent noise

sources present on Earth and the practicalities in building large arm lengths place firm restrictions on the sensitivity of these detectors below the lower limit ($\sim$ 1Hz). However, there are a large number of interesting cosmological sources that emit gravitational waves but only below this frequency limit [22]. Probing these sources requires a new design of detector, one that is not limited to the same frequency constraints as the ground based detectors.

Chapter 2

Laser Interferometer Space Antenna

The *Laser Interferometer Space Antenna* (LISA) is a space based gravitational wave detector and will therefore be able to detect sources at lower frequencies than the existing ground based detectors [36, 22]. LISA will have good sensitivity in the $10^{-4} - 10^{-1}$ Hz band due to its unique design. A space based detector is free from the environmental noise that is responsible for the lower limits of the ground based detectors [37]. But also, there are fewer size constraints on the antenna, allowing LISA to operate outside of the long wavelength limit for most of its frequency band [22]. This will allow it to probe gravitational wave sources that are undetectable from earth.

LISA will complement the existing ground based gravitational wave detectors and also the results from other fields of astronomical research. Sources of strong gravitational waves are usually bright in the optical sense, termed in gravitational wave literature, the *electromagnetic counterpart*. Probing the source optically and with gravitational waves will provide two sets of complementary information about an astronomical object.

2.1 Antenna Design

The antenna design for LISA consists of three spacecraft, each forming one vertex of a near-equilateral triangle. Six laser beams connect the antenna together, two per

spacecraft, over a side length of 5 million kilometres. The antenna will be placed in an earth-like orbit, approximately 20° behind the Earth, with a one year orbital period and at a distance of 1AU from the Sun [38]. As shown in Figure 2.1, the plane of the antenna, described by the static configuration of the spacecraft, is orientated at a 60° angle towards the ecliptic. This helps to maintain the shape of the antenna, with respect to the Sun, throughout its orbit [37, 27]. The orbit of the antenna around the Sun, ignoring the individual motions of the spacecraft, is commonly referred to as *bulk motion*.

The three spacecraft also orbit clockwise around their common *centre-of-mass*, defined to be the point in space equidistant from each of the spacecraft. Note this point is also referred to as the guiding centre. To limit the acceleration noise (see later Sections for more information), the orbital paths of the individual spacecraft are chosen so that the two optical benches within each spacecraft are in *drag free orbits*. This means that the benches are in constant free fall, within the limitations of the orbital paths. The individual orbits are a compromise between maintaining the shape of the antenna and the drag free nature of the optical benches.

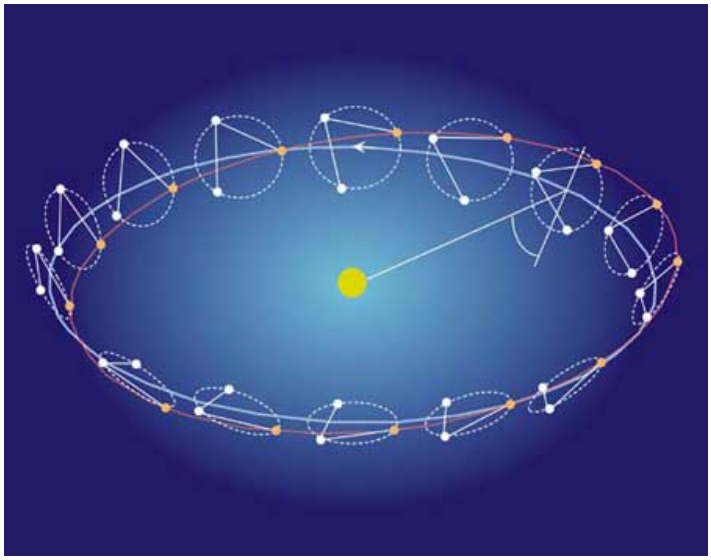

Figure 2.1: Diagram of the orbital path of LISA, showing the bulk motion around the Sun over the course of a year, and the individual orbits of each spacecraft. Picture Credit: Copyright NASA [2].

The motion of LISA, both tumbling and from bulk motion around the Sun, will result in modulations of the amplitude, phase and frequency of any gravitational wave

signal that is detected. The frequency modulation is sometimes also referred to as *Doppler modulation* and is mainly dominated by the bulk motions of the entire constellation in the low frequency limit. At higher frequencies the spiralling motions of the antennae themselves also has to be taken into account.

LISA is similar in many respects to the ground-based interferometric gravitational wave detectors; the changes in the laser path length caused by a passing gravitational wave are measured as changes in the interferometric fringe pattern within the detector. For a static detector, the largest change in the laser path will be seen when the polarisations of the signal and arm lengths of the detector are aligned. Due to the unique design, in terms of the shape of the antenna and the bulk and individual orbits, LISA is capable of detecting and measuring the length changes induced by signals with a large range of wave orientations. This will allow LISA to identify and probe gravitational wave signals coming from any direction on the sky. Note that the relative arm length difference measured by a 60° interferometer is precisely $\sqrt{3}/2$ times as large as the same difference measured by a 90° interferometer in the same location [37].

An important point to note is that the variations caused by the gravitational wave can be described by either the *phase modulation*, denoted notionally as s_{ij}, as is usually the case for interferometry, or the *frequency modulation* (y_{ij})[1] in terms of Doppler shifts. They are both functions of time describing the same fluctuations and can therefore be treated as equivalent measures [35]. As the gravitational wave itself is seen through the effect it has on the surrounding spacetime, the distortions h_{ij} are commonly described as *strains*.

Thinking of the Doppler fluctuations in terms of frequency modulations,

$$\delta f \simeq \left(\frac{v}{c}\right) f.$$

As the bulk motions have a period of one year, their corresponding frequency will be $f_m = 1/\text{yr}$. The centre-of-mass of the configuration will therefore have velocity $v/c = 0.994 \times 10^{-4}$. Using the above result, the frequency at which the Doppler shifts

[1] See Section 2.2 for a full discussion of the notation used for the inter-spacecraft modulation terms.

$(\delta f = (v/c)f)$ become measurable can be calculated using [38],

$$f_v = \frac{cf_m}{v}$$

where v describes the motion of the detector, f_v is the characteristic frequency and f_m is the frequency of the bulk motions.

Substituting in the speed of the guiding center gives a limiting frequency of $f_{gc} = 0.3$ mHz. Assuming that the arm lengths are 5×10^6km in length, each of the spacecraft will be moving with speed $v/c = 0.192 \times 10^{-5}$. This corresponds to a frequency of $f_{sc} = 16$ mHz. In summary, the bulk motions of LISA will have a measurable effect on the signal at frequencies higher than f_{gc}, while the cartwheel motion of the individual spacecraft will also become important above f_{sc} [38].

The limit (also known as the transfer frequency f_*) that marks the crossover between these regimes also happens to coincide with the point at which the gravitational wave wavelength is not precisely equal to the length of the detector arms. The transfer frequency is

$$f_* = \frac{c}{2\pi L}.$$

By substituting LISA's armlength into this relation, it can be seen that the crossover occurs at approximately 10 mHz [38]. Note that this frequency marks the point at which the long wavelength, and therefore the low frequency, limit begins.

2.2 Optical Bench Layout and Notation

LISA uses similar principles to ground-based Michelson Interferometers in order to detect and measure gravitational wave signals. In this Section, the Author will describe the optical layout for LISA and introduce one of the notation conventions used throughout the literature[2].

Independent lasers p_{ij} on each of LISA's six optical benches transmit narrowband beams toward the other spacecraft (S/C). There are six beams in total, travelling

[2]See Appendix C for further discussion of notation conventions

in both directions along the three arms of LISA. The individual spacecraft (S/C) are labelled 1,2 and 3 respectively, while the distances between them are denoted by L_1, L_2 and L_3, where L_i describes the arm length opposite the spacecraft with the same label ($S/C\ i$). Following the same labelling convention, the unit vectors between the spacecraft are described by $\hat{n}_i$, orientated anti-clockwise round the antenna, as shown in Figure 2.2.

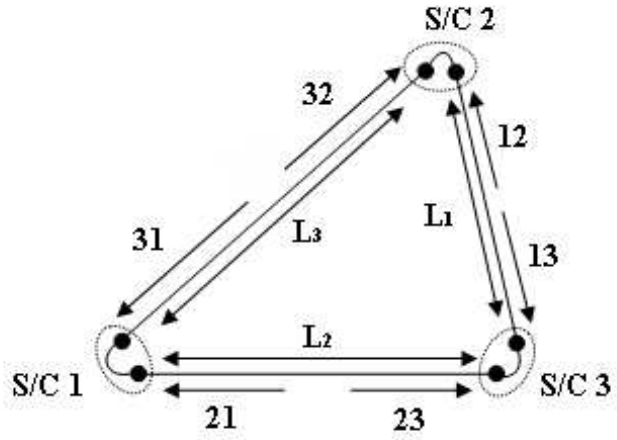

Figure 2.2: Optical bench notation for the three LISA spacecraft, in terms of spacecraft distances (L_i).

Instead of a single optical bench encapsulating the entire optical system as is the case for a Michelson Interferometer, each of the optical benches work together to conduct laser interferometry between the spacecraft.

The individual spacecraft are cylindrical in shape, approximately 2 metres in diameter and 50 centimetres high. The outer structure acts as a sun-shield and solar array, protecting the spacecraft from the light from the Sun. The internal structure is dominated by an articulated "Y" configuration which contains two optical systems[3] The articulation gives the optical benches good directional control which is extremely important as the orbits and therefore the relative positions of the spacecraft are not fixed [27].

[3]In this case, the LISA design discussed in this Section is a particular incarnation of the LISA design that is used in data analysis literature. This design is out-of-date with respect to the more recent LISA designs, where the current internal structure of LISA has been simplified to a "V" configuration but with similar properties.

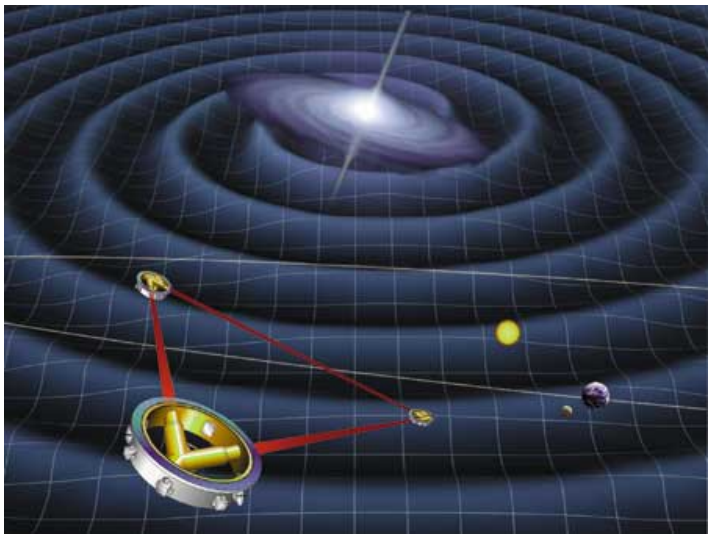

Figure 2.3: Diagram of LISA spacecraft. Picture Credit: Copyright NASA [2].

Each optical bench contains an independent laser source, a proof mass, beam splitters and photo receivers. When the laser light from one spacecraft (described as the *incoming light*), arrives at the front of a different bench, it is reflected off the local proof mass and mixed with the local laser light. The interference pattern is measured using the photodiode located at right angles to the initial path of the incoming light. This records measurements of the change of the phase s_{ij} between the two light sources. The *data stream* s_{ij} represents the one-way phase difference time series for the laser light traversing the arm length L_i. This inter-spacecraft laser light only interacts with one proof mass, the mass on the receiving spacecraft. Each proof mass is designed to be cubic in shape and constructed from an alloy of 90% gold and 10% platinum, to reduce the magnetic susceptibility of the mass [27].

The beam splitter located at the front of the optical bench splits the local laser light into two beams; the first interacts with the incoming light and is directed into the photodiode, the second is directed towards the other spacecraft, forming the *outgoing light* for the optical bench. Note that this outgoing light does not interact with the local proof mass.

Following the subscript notation conventions in Armstrong *et al.* [35][4], the inter-spacecraft measurement s_{ik} describes the change in phase measured by interfering light

[4]See Appendix C for discussion of different labelling conventions.

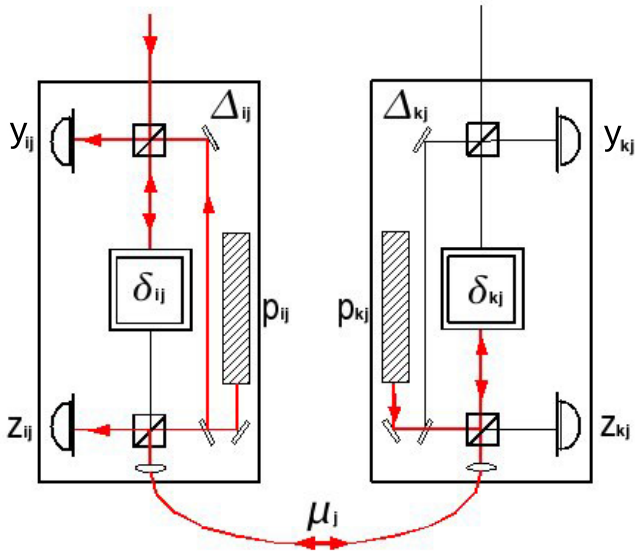

Figure 2.4: Simplified spacecraft optical bench layout. Each optical bench contains a single laser source (p_{ij}), and makes two measurements of the laser light beam, the inter-spacecraft measurement, y_{ij}, and the intra-spacecraft measurement, z_{ij}. The optical paths of the incoming and outgoing laser beams are created by beam splitters and mirrors. The movement of the optical bench is denoted by Δ_{ij} and the optical mass displacement by δ_{ij}. The large fibre noise in the optical fibres connecting the optical benches is denoted by μ_i.

on S/C k with the beam from S/C j. For example, the light from S/C 2, travelling down L_3 and mixing with light on S/C 1 is denoted by s_{31}. An important point to note is that all quantities related to the same bench use the same subscript notation as s_{ik}, shown in Figure 2.4.

Each optical bench has a second photodiode which provides a phase measurement τ_{ij} of the intra-spacecraft motion, the relative motion of the proof masses within each spacecraft. In this case the laser light is reflected off the rear side of the local proof mass and then transmitted to the other optical bench through fibre optics, where it mixes with the local laser light. Note that the intra-spacecraft laser light only interacts with the proof mass on the optical bench where the laser light originates.

In an ideal optical setup the laser beams would be perfectly coherent and collimated but unfortunately over the length of LISA's arms the beams begin to diverge, necessitating a 30cm Cassegrain telescope on each optical bench to transmit and receive the laser light. The optical power of the laser source is 1 W and thus over an arm length distance (L) of 5×10^9m, the incoming signals will be very faint, estimated at around

140 picowatts using equation 2.2 [27],

$$P_r = 0.5\frac{D^4}{\lambda^2 L^2}P_t,$$

where P_r and P_t are the received and transmitted laser powers respectively. D describes the telescope diameter (0.3m) and λ is the wavelength of the laser light, taken for this calculation to be 1064nm. Unlike the ground based interferometers which are able to create complex optical paths, as the received laser light for LISA is very weak, the phase differences between this light and the outgoing light is measured and full strength beams are retransmitted. The recovery of the gravitational wave signal is carried out at a later time using statistical algorithms on the data stream information.

In the absence of any noise contributions, the inter-spacecraft measurements will be modulated by a passing gravitational wave, which can then be detected and measured by combining the data stream information with the intra-spacecraft measurements.

2.3 Signal Data Stream

The optical system is subject to a number of different noise contributions that will affect the recovery of the gravitational wave signal from the data streams. The inter-spacecraft measurement is therefore the sum of the noise contributions and the gravitational wave modulation term. Note that these terms are commonly defined in either the frequency domain, denoted by y_{ij}, or equivalently in the phase domain with s_{ij}.

In the frequency domain, the inter-spacecraft measurements (y_{ij}) are therefore,

$$\begin{aligned} y_{ij}(t) &= y_{ij}^{GW} + y_{ij}^{noise} \\ &= y_{ij}^{GW}(t) + y_{ij}^{laser}(t) + y_{ij}^{op}(t) + y_{ij}^{accel}(t) \end{aligned} \tag{2.1}$$

where the noise contributions have been grouped into three main categories, describing modulations introduced by the lasers $y_{ij}^{laser}(t)$, the fluctuations in the optical path, $y_{ij}^{op}(t)$, and acceleration noise, $y_{ij}^{accel}(t)$. The phase data stream is described by the time

integral of the frequency data stream, multiplied by the central frequency of the lasers,

$$s_{ij}(t) = \nu_0 y_{ij}(t)$$

Note that the noise data stream $y_{ij}^{noise}(t)$ is commonly denoted by $n_{ij}(t)$.

2.3.1 Gravitational Wave Signal

The response of an optical bench data stream to a transverse, traceless plane gravitational wave is related to the unit wavevector ($\hat{k}$) [35, 36]. In the frequency domain, the inter-spacecraft modulation can therefore be described by,

$$y_{ij}^{gw} = \left[1 + \frac{1}{L_i}(\mu_j - \mu_k)\right][\Psi_i(t - \mu_k l - L_i) - \Psi_i(t - \mu_j l)].$$

Note that $\mu_i = \hat{k} \cdot \hat{p}_i$, where $\hat{p}_i$ describes the unit vector in the direction of spacecraft i, from the locations of the center-of-mass. The line-of-sight distance between each spacecraft and the guiding centre is denoted by l. Note that $L_i \hat{k} \cdot \hat{n}_i = l(\mu_j - \mu_k)$ and Ψ_i are the scalar functions, [35],

$$\Psi_i(t) = \frac{1}{2}\left[\frac{\hat{n}_i \cdot h(t) \cdot \hat{n}_i}{1 - (\hat{k} \cdot \hat{n}_i)^2}\right]$$

The gravitational wave, in terms of a first-order spatial metric perturbation ($h(t)$) at the guiding centre, is described by $(h_+(t)e_+ + h_\times(t)e_\times)$, where $h_{+,\times}$ are the polarisations of the wave and $e_{+,\times}$ are 3-tensors that are tranverse to $\hat{k}$ and traceless. In an orthonormal propagation frame $(\hat{i}, \hat{j}, \hat{k})$, they have components,

$$e_+ = \begin{pmatrix} 1 & 0 & 0 \\ 0 & -1 & 0 \\ 0 & 0 & 0 \end{pmatrix}, \quad e_\times = \begin{pmatrix} 0 & 1 & 0 \\ 1 & 0 & 0 \\ 0 & 0 & 0 \end{pmatrix}$$

In terms of the LISA data streams, note that compression of the armlength is represented by a positive h_{ij}.

2.3.2 Laser Noise

The six lasers in the LISA configuration are independent, implying that the laser light is coherent and monochromatic. As there is a laser source on each optical bench, each laser beam will have a different central frequency (ν_{ij}) and individual random fluctuations around this value. A nominal central frequency (ν_0) can be defined by taking the average of the six central frequencies. The variation in the central frequencies could be as large as several tens of megahertz [39].

The fluctuations in the frequency of the lasers, $y_{ij}^{laser}(t)$, or the *Laser noise*, will contribute the largest amount to the spacecraft noise. The frequency fluctuations are denoted as $C_{ij}(t)$, where the instantaneous frequency is described by,

$$\nu_{ij}(t) = \nu_0[1 + C_{ij}(t)],$$

where the subscript ij denotes the local optical bench number. Hence, the laser noise (y_{ij}^{laser}) relates directly to the optical bench from which the laser light originates.

The laser noise contribution that enters the data stream measurements for a particular time stamp will be the instantaneous difference between the frequencies of the light from the transmitting and receiving spacecraft. In other words,

$$y_{ij}^{laser} = C_{ik}(t - L_i) - C_{ij}(t) = C_{ik,i}(t) - C_{ij}(t) \tag{2.2}$$

or in terms of phase,

$$s_{ij}^{laser} = p_{ik}(t - L_i) - p_{ij}(t) = p_{ik,i}(t) - p_{ij}(t) \tag{2.3}$$

where p_{ij} are the fluctuations in the phase of the laser light, defined as the time integral of $\nu_0 C_{ij}$. Note that, the time series of the laser phase data stream s_{ij}^{laser} is defined as the time integral of the central frequency (ν_0) and the frequency fluctuation data stream, $y_{ij}(t)$.

The notation for the laser noise terms follows a simple pattern. There are only

3 possible subscripts and therefore the number that does not appear in the Doppler stream subscript (in this case k) relates to the transmitting spacecraft number. The laser light travels down the arm denoted by the first number in the Doppler subscript (i), relating to a delay operator of i. The laser light is mixed with the light on the receiving space craft, denoted by the second subscript in the Doppler term (j).

The comma subscript notation ($_{,i}$) is a *delay operator* denoting the time delay of light from travelling down the arm i [35].

$$a_{ij,k}(t) = a_{ij}(t - L_k), \tag{2.4}$$

where the length L_k has units of time, or $\frac{L_k}{c}$, when c is the speed of light in vacuum. Note that negative time stamps correspond to measurements that were taken in the past. A time delay of L_k references the measurement in the data stream for the optical bench that was taken at the current time stamp minus L_k stamps. The time taken for the light to travel down the arms can be described in terms of the number of timestamps taken by the detectors. In other words the length of the arms can be defined in terms of a number of discrete timestamps. To prevent confusion with the notation, if the current time stamp is $t = 1$ and a time delay of "$,3$" is applied, this does not correspond to the $1 - 3 = -2$ measurement but the $1 - L_3$ measurement.

In terms of the laser light, the $y_{32,3}$ describes the measurement of the light received at optical bench 32 at time $t - L_3$. This corresponds to the light measured at optical bench 31 at time t, as the separation between the optical benches is exactly equal to L_3 timestamps. By comparing the same timestamp of the laser beam as it leaves the first optical bench, $y_{32,3}$, and on arrival at the next optical bench, y_{31}, the inter-spacecraft measurement will have the same noise contribution terms and therefore provide a direct measure of any gravitational wave modulation of the signal.

Impact of the Laser Noise Contributions

As previously discussed, the laser frequency fluctuations related directly to the optical bench of the laser source (y_{ij}^{laser}). For an interferometer configuration with a single laser

source, and for equivalent optical paths around the system, the same realisation of the laser noise will be present in the laser beams at superposition and will therefore will exactly cancel. The motion of LISA introduces variation in the individual optical paths of the arms, which will result in the incomplete removal of the laser noise contributions.

The impact of the laser frequency fluctuations can be estimated by considering the simple case for a single Michelson Interferometer with unequal arm lengths of L_1 and L_2 respectively. The returning laser phase noise term in one arm, $C(t)$, corresponds to the laser phase noise term at a previous timestamp, $C(t - 2L_i)$, where i denotes the respective arm length. Therefore the difference between the laser phase noise terms will be,

$$\begin{aligned} \Delta C(t) &= [C(t - 2L_1) - C(t)] - [C(t - 2L_2) - C(t)] \\ &= C(t - 2L_1) - C(t - 2L_2). \end{aligned}$$

In frequency space, the equivalent strain due to the fractional frequency fluctuations can be approximated to first order [36], as,

$$|\Delta\tilde{C}(f)| \simeq |\tilde{C}(f)|\frac{4\pi f}{c}|(L_1 - L_2)|,$$

where $\tilde{C}(f)$ denotes the Fourier Transform of the laser phase measurements $C(t)$.

Using the above equation, the approximate size of the effect of the frequency fluctuations can be estimated. Note that the fractional frequency fluctuations of a stabilised laser is about $10^{-13}/\sqrt{\text{Hz}}$, in the millihertz band. If the time difference between a round trip in each of the arms is 0.5 seconds, corresponding to a relative arm length differences of a few percent, then in this frequency band, the equivalent strain due to the uncancelled frequency fluctuations will be approximately $6.3 \times 10^{-16}/\sqrt{\text{Hz}}$ [36].

Note that the target LISA strain sensitivity in the millihertz frequency range is around $10^{-20}/\sqrt{\text{Hz}}$ and therefore these relative frequency fluctuations will have a serious impact on the sensitivity of LISA over the frequency range, unless they can be removed. Hence an important challenge for LISA is the removal or reduction of these

laser noise contributions to allow detection and measurements of the gravitational wave signals.

2.3.3 Acceleration Noise

Unlike the static ground based detectors, the optical setup for LISA uses a single proof mass on every optical bench, defining the end points for the arm lengths of the antenna. It is extremely important that the proof masses are kept in free fall or as close to free fall as the chosen orbital paths are able to achieve, to reduce the individual displacement of the masses ($\vec{\delta}_{ij}$) and of the entire optical bench, denoted by $\vec{\Delta}_{ij}$, following the spacecraft notation convention. The optical benches are not assumed, in general, to be rigidly connected ($\vec{\Delta}_{ij} \neq \vec{\Delta}_{kj}$). This means that the movement of an optical bench does not induce or reflect similar motions in the other optical bench within the same spacecraft. Note that the displacement quantities are described in terms of vector components along the arms, denoted by the arrow superscript ($\vec{}$). They are commonly defined to be normalised and positive in the direction of the other spacecraft. In terms of frequency modulations,

$$\begin{aligned} y_{ij}^{pm} &= 2\hat{n}_i \cdot \vec{\delta}_{ij}, \\ y_{ij}^{ob} &= -\hat{n}_i \cdot \vec{\Delta}_{ij} - \hat{n}_i \cdot \vec{\Delta}_{ik,i}, \end{aligned}$$

where superscripts *pm* and *ob* denote the proof mass and optical bench terms respectively.

The individual motion of the optical system (sometimes referred to as *shearing* [40]) results in changes of the distances between the spacecraft and therefore of the phase (and also frequency) of the incoming light. They can therefore be described in terms of the variations in the arm lengths with time or the relative velocities of the arm lengths ($\dot{L}_i(t) = \frac{dL_i}{dt}$). These slow varying modulations are sometimes termed Doppler shifts and the variations are predicted to be of order of tens of megahertz [39]. As the forces acting on the system when the spacecraft are not in freefall result

in accelerations of the optical components, importantly the proof mass, this source of noise is termed *acceleration noise* and can be estimated from the individual motions of the optical benches. Note that, in simple data analysis models, the acceleration noise is commonly described as being spacecraft dependent rather than optical bench dependent.

From the LISA Pre Phase Report A [41], the acceleration noise spectrum for a single proof mass is expected to be 3×10^{-15}m sec^{-2}Hz$^{-1/2}$ at around 10^{-4}Hz. Note that the spectrum is described in units of the acceleration per root hertz and therefore must be converted to an expression in terms of fractional frequency fluctuations. Note that the acceleration of the proof mass is the second time derivative of the individual displacements. Therefore, if $x(t)$ denotes the displacements over time, then the Fourier Transform of the velocity ($\frac{d\tilde{x}}{dt}$) relates to $2\pi i f\tilde{x}(f)$ in frequency space, where $x(t)$ and $\tilde{x}(f)$ are the Fourier Transform pair. The power spectrum of the velocity noise is therefore equal to the power spectrum of the acceleration divided by $4\pi^2 f^2$ [36]. In other words, the power spectrum for the fractional frequency fluctuations is,

$$\begin{aligned} S_y^{accel} &= \frac{(3 \times 10^{-15}\text{m sec}^{-2}\text{Hz}^{-1/2})^2}{(4\pi^2 f^2 c^2)} \\ &= 2.5 \times 10^{-48}[f/1\text{Hz}]^2\text{Hz}^{-1}. \end{aligned}$$

In this case there is an inverse square frequency dependence, producing a power spectrum that corresponds to red rather than white noise. White noise describes noise that is uncorrelated over time, with a uniform power density in the time domain. This means that instead of a flat power spectrum in frequency space, the spectrum is sloped, denoting higher intensity (higher energy) at lower frequencies. In simple terms, the spectrum is shifted towards the red end of the spectrum (i.e. towards lower frequencies). In terms of the acceleration noise contributions, it will have the largest effect at low frequencies [35, 42].

2.3.4 Optical Path and Shot Noise

Due to the design of LISA, the discretised nature of the laser light is detectable at low signal-to-noise, resulting in a *shot noise* contribution $y_{ij}^{shot}(t)$ to the signal [39]. As the laser beam is composed of individual photons, the total number of photons detected by the photodiode will vary with time as the intensity of the light will randomly fluctuate over time. Thus, the laser noise contribution is related to a single optical bench and can be described as white phase noise [35]. The amplitude of the noise spectrum for an individual laser link (y_{ij}) is taken as,

$$S_y^{shot} = 5.3 \times 10^{-38} (f/1\text{Hz})^2 \text{Hz}^{-1}.$$

Note that the shot noise power spectrum is proportional to f^2, where f is the fourier frequency [35, 4].

The shot noise term is combined with the beam pointing noise to create an aggregate *optical path noise*, describing the fluctuations in the laser path [5]. These variations are denoted by y_{ij}^{op} in terms of frequency and s_{ij}^{op} in units of phase. The combined noise term is expected to have a spectrum of $20 \times 10^{-12}\text{m Hz}^{-1/2}$ [36, 40]. It is assumed that the aggregate optical path noise has the same transfer function as pure shot noise. The *transfer function* describes a mapping between the input and output frequencies, in other words the response of the antenna as a function of frequency [27, 43]. Employing the same Fourier transform procedure as before, the above spectrum can be converted to a velocity spectrum by multiplying by $(4\pi^2 f^2)$. The spectrum for the fractional frequency fluctuations in the optical path is equivalent to the velocity spectrum divided by the speed of light squared, and therefore,

$$S_y^{op} = 1.8 \times 10^{-37} (f/1\text{Hz})^2 \text{Hz}^{-1}.$$

Note that the optical path and acceleration noises constrain the lower frequency sensitivity for LISA, in the absence of the laser noise contributions. The achievable *strain sensitivity level* is therefore set at $h \simeq 10^{-21}/\sqrt{\text{Hz}}$ [30].

2.3.5 Other Contributions

Phase modulations to the signal are also introduced as the laser light travels between the optical benches on the same spacecraft. The laser light is passed through optical fibres that introduce a large *fibre noise*, μ_i. The subscript follows the same notation conventions as the spacecraft labelling. Here, the phase change is assumed to be independent of propagation direction. This noise contribution can be removed by describing the intra-spacecraft measurements in terms of the differences between the benches $(z_{ij} - z_{kj})$.

The Doppler shifts due to relative velocities in LISA's arm lengths $(\dot{L}_i)$ and the variations in the laser central frequencies (ν_i) will result in a large fringe rate or *beat note* frequency in the photodetectors. This must be accounted for before measurements of the gravitational fluctuations can be made. In the literature, the method used to accomplish this is termed frequency *down conversion* or *tracking* of the fringe rates [39]. Each optical bench is equipped with an onboard clock in the form of a *UltraStable Oscillator* (USO), which produces a tracking or base-banded frequency f_i. The addition of these clocks is a trade off between cancelling the noise contributions without the addition of a tracking mechanism and the introduction of a new noise source in the form of phase fluctuations in the USO (q_i). A current state-of-the-art USO has a frequency stability of approximately 10^{-13} in the millihertz frequency band and therefore will introduce frequency variations $(\frac{\dot{q}_i}{\nu_i})$ of order 10^{-20} [39].

Note that for *first generation* LISA configuration the beat note frequencies are not present in the data streams as the spacecraft are defined to be stationary with respect to each other $(L_1 = L_2 = L_3)$ and therefore $\dot{L}_i = 0$. The lasers are also assumed to have the same central frequency $(\nu_{ij} = \nu_0)$, removing the other source of the large fringe rate.

2.4 Optical Bench Data Streams

Using the information from the previous Sections, the inter-spacecraft measurements can now be defined in terms of the contribution terms rather than the noise categories. For the static LISA configuration, the six inter-spacecraft measurements can be described as,

$$y_{ij_{RHS}} = y_{ij}^{GW} + y_{ij}^{op} + C_{ik,i} - C_{ij} + [2\hat{n}_i \cdot \vec{\delta}_{ij} - \hat{n}_i \cdot \vec{\Delta}_{ij} - \hat{n}_i \cdot \vec{\Delta}_{ik,i}] \quad (2.5)$$

$$y_{ij_{LHS}} = y_{ij}^{GW} + y_{ij}^{op} + C_{ik,i} - C_{ij} + [-2\hat{n}_i \cdot \vec{\delta}_{ij} + \hat{n}_i \cdot \vec{\Delta}_{ij} + \hat{n}_i \cdot \vec{\Delta}_{ik,i}] \quad (2.6)$$

where the subscripts range from $1 \rightarrow 2 \rightarrow 3 \rightarrow 1$ and the expressions for the respective benches can be found by cyclic permutation of the indices [22, 4, 44]. The RHS and LHS designations relate to the relative positions of the optical benches with respect to the spacecraft orientation. For example, optical benches $21, 32$ and 13 are all RHS benches, while $31, 12$ and 23 are described as LHS benches. The different labels are needed as the data stream expressions are slightly different in terms of the signs of the optical bench vectors. For example,

$$y_{21} = y_{21}^{GW} + y_{21}^{op} + C_{23,2} - C_{21} + [2\hat{n}_2 \cdot \vec{\delta}_{21} - \hat{n}_2 \cdot \vec{\Delta}_{21} - \hat{n}_2 \cdot \vec{\Delta}_{23,2}] \quad (2.7)$$

$$y_{31} = y_{31}^{GW} + y_{31}^{op} + C_{32,3} - C_{31} + [-2\hat{n}_3 \cdot \vec{\delta}_{31} + \hat{n}_3 \cdot \vec{\Delta}_{31} + \hat{n}_3 \cdot \vec{\Delta}_{32,3}]. \quad (2.8)$$

Note that the proof mass displacement is multiplied by a factor of two, reflecting the total change in the optical path caused by a single displacement of the mass. The corresponding inter-spacecraft measurements for the rotating LISA configuration are described in [39].

The six intra-spacecraft measurements z_{ij} describing the phase change within a spacecraft, are always defined in terms of differences in order to cancel out the large

fibre noise. In other words, the individual terms are described as,

$$z_{ij_{RHS}} = C_{kj} - C_{ij} + 2\hat{n}_k \cdot (\vec{\delta}_{kj} - \vec{\Delta}_{kj}) + \mu_j \tag{2.9}$$

$$z_{ij_{LHS}} = C_{kj} - C_{ij} - 2\hat{n}_k \cdot (\vec{\delta}_{kj} - \vec{\Delta}_{kj}) + \mu_j. \tag{2.10}$$

Following the same procedure and permutations as the inter-spacecraft measurements,

$$z_{21} = C_{31} - C_{21} + 2\hat{n}_3 \cdot (\vec{\delta}_{31} - \vec{\Delta}_{31}) + \mu_1 \tag{2.11}$$

$$z_{31} = C_{21} - C_{31} - 2\hat{n}_2 \cdot (\vec{\delta}_{21} - \vec{\Delta}_{21}) + \mu_1. \tag{2.12}$$

The differences are always defined in the same direction, in other words; $z_{21} - z_{31}$, $z_{32} - z_{12}$ and $z_{13} - z_{23}$.

Note that equations 2.5 describe the phase change between the laser light leaving the outgoing space craft and the proof mass on the receiving spacecraft. Equations 2.9 describe the relative motion of the optical benches. By combining the results from these equations, the true optical path length can be determined.

An important point to note is that due to LISA's unique shape, the six data streams can be treated collectively as a ring interferometer but they can also be combined to reconstruct the output from *two perpendicular Michelson interferometers* oriented at 45^o to each other, denoted by I and II [19]. In this situation, LISA can be viewed as two separate detectors that can measure both polarisations of a gravitational wave signal simultaneously.

2.5 LISA Data Stream

The data stream ($y_{I,II}(t)$) measured by each optical bench can be described simply in terms of a noise term $n_{I,II}(t)$ and a possible gravitational wave signal. This signal is the product of the polarisations of the gravitational wave, denoted by $h_{+,\times}(t, \vartheta)$ and

the respective detector response functions $F^{+,\times}_{I,II}(t)$. Notationally,

$$y_{I,II}(t) = H_{I,II}(t;\vartheta) + n_{I,II}(t),$$

where,

$$H_{I,II}(t;\vartheta) = \frac{\sqrt{3}}{2}[F^{+}_{I,II}(t)h_{+}(t,\vartheta) + F^{\times}_{I,II}(t)h_{\times}(t,\vartheta)].$$

Note that the detector response functions, denoted by $F^{+,\times}_{I,II}(t)$, are discussed in Section 2.6. The optical bench noise terms are described by equation 2.1 and correspond to the sum of the realisations of the different noise contributions. The $n_{I,II}(t)$ term describes the data stream composed from individual noise contributions for the reconstructed Michelsons. The noises on each bench are assumed to be uncorrelated random gaussian processes, in other words the combined expectation value is $< n_i(t)n_j(t) >= 0$.

Note that the $\frac{\sqrt{3}}{2}$ factor corresponds to the conversion of the relative armlength change from a 60° to a 90° interferometer [37].

To prevent any notational confusion, note that $h_{+,\times}(t,\vartheta)$ corresponds to the polarisation of the source gravitational wave signal with source parameters ϑ, and is commonly written just as $h_{+,\times}(t)$. In the previous Section, the term h_{ij} describes the phase modulation induced along one of the laser arm lengths caused by a passing gravitational wave.

The sensitivity of the detector to a particular angular position and source orientation is time dependent, related to the orbit and individual movement of LISA. These effects are encapsulated into the detector response functions $F^{+,\times}_{I,II}$ and are discussed in more detail in Section 2.6.

The gravitational waveform is time dependent but is also characterised by a set of parameters ϑ, relating to the angular position and stage of binary coalescence. These include the masses of the binary objects, the speed of their orbit around each other and the distance to the binary.

2.6 LISA Antenna Patterns

The detector response function describes the sensitivity of the detector to a particular source direction. The recovery of a signal from a particular direction of the sky is directly related to the sensitivity of the detector to that direction.

Due to LISA's shape and design, it is not just sensitive to one direction but will be able to detect signals from all directions, at the same time. When LISA is operational, this range of sensitivity will pose a problem as every measurement will contain information from all the gravitational wave sources that are within range. This will result in *source confusion noise*, where there are too many signals with similar sky locations, orientations and parameter values, that the information provided by signal data is not sufficient to distinguish between them, in the parameter space. Recovering a single signal from the data streams will therefore require the statistical techniques that are discussed in Section 5.2. Note that the location of the source would be an unknown parameter and would be recovered during the parameterised search over the data.

Due to LISA's motion, the exact sensitivity of the antenna to a particular source direction will vary with time. The sensitivity of LISA to any particular direction will depend on the orientation of the detector, the frequency of the signal itself and also the polarisation of the signal. In the low frequency limit, the Doppler modulation of LISA comes from the orbit of the guiding center, in other words, the bulk motion of the whole antenna round the Sun. In this situation the sensitivity of the antenna, its antenna pattern, is well understood and can be approximated as a quadrupole.

Above the transfer frequency, the sensitivity of the detector to a particular direction is complicated by the relative amplitudes and phases of the signal polarisations, the Doppler shifts resulting from the periodic motions of the antenna and the further modulations caused by the individual motions of the spacecraft. This will result in an antenna pattern that is notably non-quadrupolar.

When the data streams for LISA are used to construct the response from a Michelson detector, the antenna pattern can be reconstructed to describe the sensitivity of the detector in this situation.

There are two polar Cartesian coordinate systems that can be used to describe the motion of the source and the detector. The first is described as *unbarred* coordinates, relating to (x, y, z) and tied to the detector's frame. In this coordinate system the detector is static while the antenna rotation is described in terms of the motion of the sky. In other words, the detector lies in the $x - y$ plane and the $x - y$ coordinates rotate with the detector.

In the *Long Wavelength Limit* (LWL), following Cutler [37], the detector beam pattern coefficients can be calculated in terms of the source coordinates (θ_S, ϕ_S),

$$F_I^+(\theta_S, \phi_S, \psi_S) = \frac{1}{2}(1 + \cos^2\theta_S)\cos 2\phi_S \cos 2\psi_S - \cos\theta_S \sin 2\phi_S \sin 2\psi_S \quad (2.13)$$

$$F_I^\times(\theta_S, \phi_S, \psi_S) = \frac{1}{2}(1 + \cos^2\theta_S)\cos 2\phi_S \sin 2\psi_S + \cos\theta_S \sin 2\phi_S \cos 2\psi_S \quad (2.14)$$

where $(+, \times)$ describe the two polarisations of the gravitational wave and where F_I^i described the sensitivity of the 60° LISA detector to a gravitational wave with polarisation i, reconstructed for the 90° Michelson configuration. Note also that ψ_S is the polarisation angle of the wavefront. In this case, the detector plane rotates through the observation of the fixed polarisation source.

By evaluating the above functions for all source angles, the features in the antenna patterns for the plus polarisation can be seen in Figure 2.5. Note that the Figure is plotted in polar coordinates and therefore the limits on each axis correspond to theta $= [-\Pi, \Pi]$ and phi$=[-\frac{\Pi}{2}, \frac{\Pi}{2}]$.

The above Figure describes the instantaneous sensitivity of LISA in terms of source angle to a particular polarisation $(h_+, h_\times)$ of the signal. The beam pattern coefficients correspond to values between -1 and 1.

The second set of spherical polar coordinates, the *barred* $(\overline{x}, \overline{y}, \overline{z})$, defines the system in terms of the frame of the ecliptic. In other words the bulk motions of the detector are removed, leaving the individual rotations of the spacecraft. In this case, the $\overline{x} - \overline{y}$ plane is defined to be the ecliptic, the plane of the Earth's motion around the Sun.

In the barred coordinate system, the trajectory of the antenna's centre-of-mass can

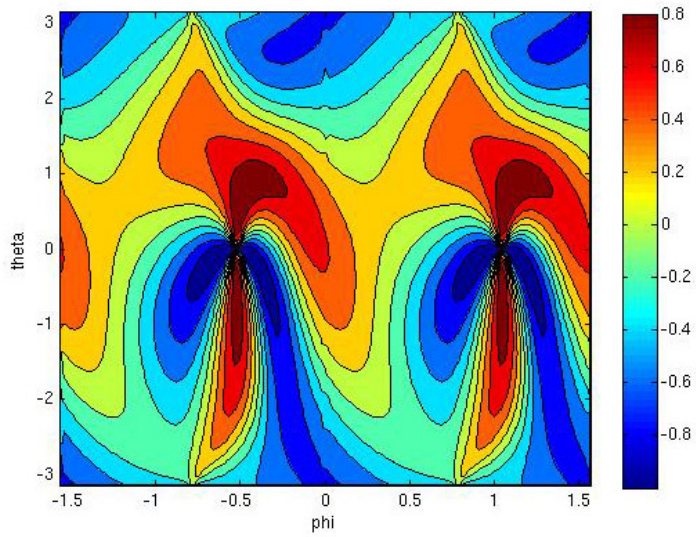

Figure 2.5: Sensitivity Antenna pattern for the plus polarisation F_I^+ for source orientation angles denoted by theta (θ_S) and phi (ϕ_s). The relative sensitivity to a particular source direction is described by the corresponding values in the colour bar.

therefore be defined as,

$$\begin{aligned} \overline{\theta}(t) &= \frac{\pi}{2}, \\ \overline{\phi}(t) &= \overline{\phi}_0 + \frac{2\pi t}{T}, \end{aligned}$$

where T is the orbital period, defined as one year, and $\overline{\phi}_0$ is a constant defining the initial location of the detector [37].

2.7 The Main Challenge for LISA

In summary, the problems that are solved by moving the detector into space, namely the frequency limitations on ground based interferometric gravitational wave detectors, introduce other difficulties that could be easily overcome on Earth. The signal measured at the front of the optical bench of each spacecraft contains a number of noise contributions (laser, optical path, acceleration) that will swamp the gravitational wave signals.

The shot noise and optical path noise levels contribute to the LISA sensitivity curve but the largest contribution comes from the fluctuations in the laser frequencies. This

noise term is removed easily during the direct recombination of the beam for an equal arm length interferometer. However, the motion of LISA introduces a light travel time down each of the arms that varies by a few percent and therefore direct recombination of the light will no longer remove the laser noise [22, 36].

In order to detect gravitational wave signals and achieve LISA's sensitivity goal of $10^{-20}/\sqrt{\text{Hz}}$, another method must be found that will give exact cancellation of the laser noise contributions. A promising analytical solution termed *Time Delay Interferometry* removes the laser noise terms by combining together mulitple timestamps of the laser light that have the same realisations of the noise. This method is discussed in more detail in Chapter 3.

2.8 LISA Signals

The LISA dataset is expected to contain a large number ($\approx 10^4$) of resolvable overlapping sources. These gravitational wave sources will range in strength from galactic binary systems that are smaller than our Sun to high-redshift Supermassive Black Holes [45]. Due to its design, the inter-spacecraft measurements for LISA will be modulated by every gravitational source that is within range. The ability of the detector to resolve these sources will be dependent on the orientation of the antenna, the strength of the gravitational wave signal and the total observation time. An overview of possible gravitational wave sources was given in Section 1.3. In this Section, the Author will briefly discuss the resolvability of each of the sources within the LISA band $10^{-4} - 1$ Hz [27].

In contrast to the source populations detectable by the current ground based detectors, LISA is able to detect gravitational wave signal that have much lower frequencies. Figure 2.8 shows the predicted sensitivity curve, generated using the Online Sensitivity Curve Generator created by Shane Larson [3, 46]. The curve corresponds to a signal-to-noise of 1, equal arm-lengths of 5×10^9m and a laser wavelength of 1064 nanometers. The limits on the sensitivity floor are determined by the position noise budget and there is assumed to be individual white dwarf (relating to the blue line on the Figure)

and instrumental noises. Note that the root spectral density ${h^L}_f$ is also termed the *spectral amplitude*.

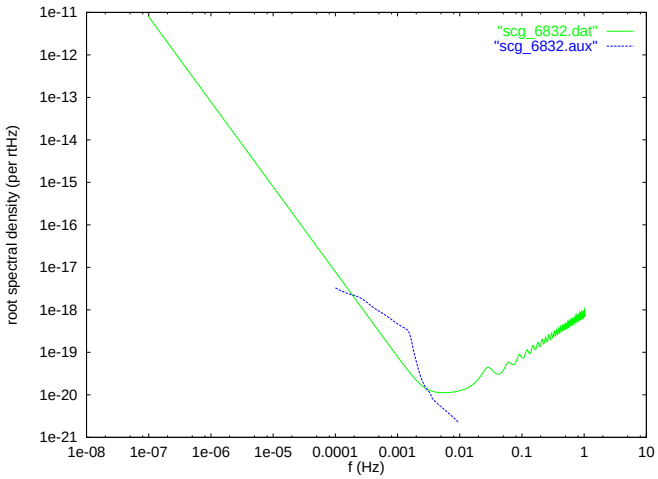

Figure 2.6: Standard LISA sensitivity, generated by the Online Sensitivity Curve Generator [3] using the default settings (equal arms, all-sky, SNR = 1), with an estimate for the confusion limited galactic binary background.

The low frequency rise shown in Figure 2.8 is due to acceleration noise in the system and relates to the point where the acceleration noise begins to dominate over position noise.

The high frequency structure is the direct result of corresponding high frequency structure in the gravitational wave transfer function. Note that the high frequency "knee" which marks the start of the decrease in sensitivity at higher frequencies occurs at approximately $f = 1/(2\Pi\tau) = 10^{-2}$Hz, where τ is the armlength of the antenna (and is assumed at these frequencies to be comparable to the wavelength of the gravitational wave). From the above Figure, it can be seen that LISA has greatest sensitivity between $10^{-3} - 10^{-2}$Hz, which is referred to as a mid-frequency "floor". The width of this "floor" is related to the acceleration noise level and the arm length of the antenna. The corresponding sensitivity of the detector to signals with frequencies within this range is determined by the size of the position noise [43].

The strongest signals in the LISA band are thought to be Supermassive Black Hole Binary coalescences, typically with a total mass limit of approximately $4 \times 10^7 M_\odot$. A binary corresponding to this upper limit will spend approximately zero time in the

LISA band, but less massive binaries will emit detectable signals for longer timescales.

The detectability of the chirping binaries is dependent on the total observing time (T_{obs}) of the mission and is therefore related directly to the frequency resolution of the observations. As the frequencies of the binary signals is increasing with time, detection estimates can be made using the *stationary frequency*. Signals with this frequency will cross a frequency bin in exactly the observation time,

$$f_s \simeq [\frac{8}{3}\frac{\kappa}{T_{obs}^2}]^{3/11},$$

where κ is constant, relating to the chirp mass of the binary. Using the above equation for a SMBD binary with individual masses of $10^6 M_\odot$ and a total observation time of 1 year, the stationary frequency is calculated to be 8.14×10^{-6}Hz [27].

Chirping binaries in the LISA signal are predicted to have total mass range of $10^4 - 10^7 M_\odot$ with mass ratio of 0.05:1. They are calculated to spend approximately a few months to years in the LISA band, corresponding to thousands of wave cycles and therefore it will be possible for even high redshift sources to be detected with high SNR. Small supermassive black holes with mass ranges of $10^5 - 10^6 M_\odot$ are predicted to have an event rate of 10 per year, in a redshift range of $2 \leq z \leq 6$. In addition there should also be one high mass supermassive black hole merger at high redshift [19, 21]. There are also thought to be at least one EMRI event a year with a 1:10^5 mass ratio and a few hundred with 10:10^5 mass ratios [27]. Note that in contrast to the black hole coalescences, most detectable EMRI events will be relatively close, limited to redshift of less than 1 [21].

Chapter 3

Time Delay Interferometry

The detection of gravitational wave signals using laser interferometry is dependent on the removal of the laser noise contributions that would otherwise dominate the optical bench measurements. Ground based interferometers use equal length detector arms and beam splitters to ensure that the light beams have the same realisation of the laser noise at each time stamp. When the two beams are interfered together in the detector, the laser noise realisations present in each beam are cancelled out.

The laser noise components for LISA are offset from each other by the small changes in the armlengths introduced by the motion of the individual spacecraft. LISA is therefore dependent on data analysis techniques to identify and remove the laser noise contributions and to reconstruct the signal data streams from the armlength data.

Time Delay Interferometry (TDI) utilises the discretised nature of the datastream measurements to identify the time stamps that have the same laser noise realisations and hence provides solutions to the laser noise problem by linearly combining and time-shifting the appropriate armlength data to cancel the laser noise component.

3.1 TDI Generations

Achieving the laser frequency cancellation for the full LISA configuration is an extremely challenging task. The motions of the antenna as a whole and of the individual spacecraft compound the difficulties for recovering the gravitational wave signal.

Valuable insight can be gained by tackling the laser noise cancellation for simpler

models of the full configuration. This allows each of the interferometry challenges with the LISA configuration to be tackled incrementally, analysing the laser noise cancellation for simpler models of LISA and building on the solutions for each stage.

In the simplest case, termed *First Generation TDI*, the cancellation criterion has been investigated for a stationary static array [35]. In this situation, the distances between the spacecraft are defined to be unequal but constant in time. For example, for the laser light traveling down the arm opposite spacecraft 1, denoted using the spacecraft notation to be L_{13} and L_{12}, directional independence[1] means that $L_{12}(t)$ is equal in length to $L_{13}(t)$ (i.e. $L_{ij} = L_{ik}$). Each arm length is defined to be the same length for the laser light traveling in both directions and the modulations of the arm lengths due to the motion of the spacecraft are ignored. The LISA model for this TDI generation most closely resembles the interferometric framework for the ground based detectors and as such can utilise common interferometric solutions for the laser noise cancellation. See Section 3.2.1 for further discussion of the First Generation TDI combinations.

Building on the initial TDI combinations, the solutions for the static case can be adapted and modified to a rotating LISA configuration, commonly refered to as *TDI 1.5* and *Modified TDI* [47, 40, 39]. In this model, the bulk motions of the antenna around the Sun are present but the individual motions of the spacecraft are ignored. The rotation introduces directional dependence on the armlengths ($L_{ij} \neq L_{ik}$). A number of the first generation combinations can be easily applied to the rotating array, specifically the eight pulse combinations discussed later in this Chapter. The datastreams and time delays used in their construction will still include identical equal laser noise terms with the time dependance. The optical paths in this case can be described as *vanishing areas*, as they are reflected back along their original paths in each case. By contrast, the Sagnac combinations $(\alpha, \beta, \gamma, \zeta)$ discussed in Section 3.2.1, which utilise an optical path similar to that of a Sagnac interferometer, enclosing a finite area and as mentioned in Section 1.4.1, will therefore be more sensitive to the rotation of the optical bench.

[1]Note that the directional dependence relation is $L_{ij} = L_{ik}$ rather than $L_{ij} = L_{ji}$ as would be conventionally expected, due to the labelling conventions applied to the arm lengths.

The movement of the entry/exit point for the interferometry introduces an additional phase difference in the laser light. The Sagnac combinations will therefore need more complex modifications to ensure that the laser noise cancellation criterion is met [48].

The LISA configuration that accounts for the movement of the whole antenna and the individual spacecraft is termed *Second Generation TDI*. These models will be, by necessity, more complicated than those for First Generation. The motion of the antenna introduces direction dependance and also time dependance on the armlengths. Building on the First Generation combinations, the removal of the laser noise terms requires the careful modification of the simpler time delay solutions [48, 47].

An important point to note is that the sensitivity of the solutions in each case to an incident gravitational wave is the same. The corrections introduced to adapt the stationary array solutions to the second generation case are important for the cancellation of the laser frequency noise but have only small effects on the gravitational wave signal and the other noise contributions. Therefore, a datastream that is free from the laser noise contributions for the rotating and orbiting case will only differ by small amounts from the static case and therefore at any frequency f, the gravitational response with respect to the remaining noises (also termed the secondary noises) will be unchanged [22, 40].

In later Chapters, the LISA configuration is described in terms of a rotating-static array. To simplify the data analysis model, the following assumptions have been made:

- The first order frequency fluctations introduced by the motion of the spacecraft from the optical bench datastream ($\dot{L}(t)$) are able to be removed [39].
- The laser noise contribution due to the lasers having different central frequencies can be compensated for [39].
- The LISA configuration can be treated as a stationary array ($L_i = L_{ij} = L_{kj}$) [4].
- The phase modulations introduced by the ultra stable oscillators can be removed from the datastreams [39].

In each case, the laser fluctuations and phase modulations are able to be removed either analytically or by the hardware.

3.2 Types of Combinations

Thinking of LISA in terms of the entire optical system, a beam travelling between the spacecraft in a clockwise direction would have the same optical path as an anticlockwise beam, assuming that the arm lengths are constant in time. The optical setup on each bench provides a measure of the phase difference between the incoming and local light (inter-spacecraft measurement), and also the differences between the local light on the two benches within each spacecraft (intra-spacecraft measurement). Note that both of the optical benches within each spacecraft simultaneously transmit and receive laser beams. Therefore, if the lasers have the same central frequency, the phase differences between an incoming beam and outgoing beam for a particular spacecraft could be accounted for during the data analysis by including the appropriate intra-spacecraft measurements.

3.2.1 Sagnac Six Pulse Combinations (α, β, γ)

A TDI combination constructed from the datastream values for a clockwise path will have the same laser fluctuation terms as an anti-clockwise path for a static antenna, as the optical benches are measuring the same timestamp of the laser beam. The path around the antenna can be identified by following a timestamp of the beam down each of the arms or by correctly timeshifting the relevant measurements related to a single optical bench.

The individual optical bench measurements also acquire phase measurements (Δ_{ij}) that account for Doppler shifts caused by the non-inertial motions of the optical bench [35]. These can be ignored when assuming a rigid rotation case, which ensures that the up- and down-link time delays are equivalent (ie. $L_{ij} = L_{ik} \equiv L_i$).

Applying the Sagnac framework to the entire LISA configuration, the laser fre-

quency fluctuation noise can be cancelled out by subtracting two complete optical paths in opposite directions.

$$\begin{aligned}\alpha =& y_{21} - y_{31} + y_{13,2} - y_{12,3} + y_{32,12} - y_{23,13} \\ &- \frac{1}{2}(z_{13,2} + z_{13,13} + z_{21} + z_{21,123} + z_{32,3} + z_{32,12}) \\ &+ \frac{1}{2}(z_{23,2} + z_{23,13} + z_{31} + z_{31,123} + z_{12,3} + z_{12,12})\end{aligned} \tag{3.1}$$

where $y_{13,2}$ describes the inter-spacecraft measurement taken at optical bench 13 at a timestamp of $(t - L_2)$, where t is the current time stamp. In this case, the TDI combination α is constructed from optical paths are defined with reference to spacecraft 1 [36, 30].

The datastream produced by the α combination is constructed from the instantaneous realisations of the signal and noise contributions. In order to successfully remove the laser noise realisations, the optical paths in terms of the inter- and intra-spacecraft measurements introduce identical noise terms with equal and opposite signs that cancel out within the combination. In this case, due to the shape of the combination and the particular optical bench measurements that are used, both the laser noise and optical bench terms cancel out. See Appendix E for a detailed proof of the noise cancellation for α. Note that the remaining noise terms only appear once in each optical bench datastream and therefore are unable to be cancelled out by an identically opposite term. Two similar combinations (β, γ) can be found by cyclical permutation of the indices for the optical bench subscript designations $(1 \rightarrow 2 \rightarrow 3 \rightarrow 1)$. This relationship can be seen more clearly in Figures 3.1 and 3.2. The diagrams describe the inter- and intra-spacecraft terms present in the combination respectively. Each figure contains six LISA representations in Tinto [35] notation. In Figure 3.1 the top line describes the positive terms in the combination, the negative forming the second line. The intra-spacecraft measurements have been organised by respective spacecraft differences in Figure 3.2. The two types of spacecraft measurement have been separated to highlight the inherent similarities in the structures for each case. Describing the

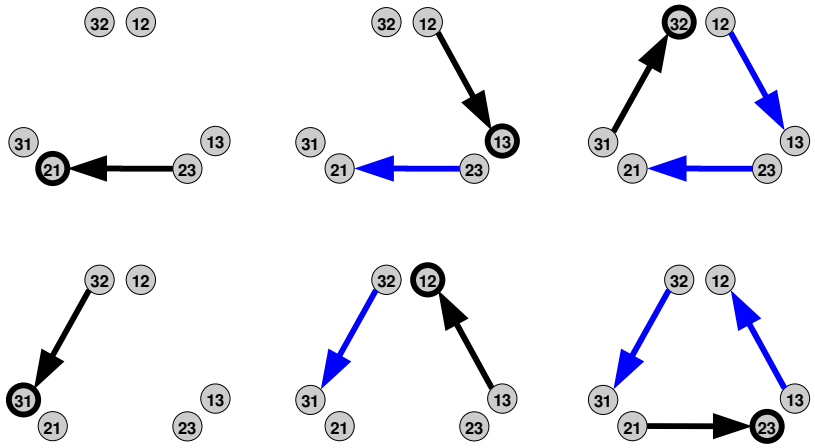

Figure 3.1: Diagram of the optical bench measurements present in the First Generation TDI combination α. The top row denotes the clockwise optical path/positive terms in the Sagnac combination, while the second row describes the respective anti-clockwise optical paths relating to the negative terms in the TDI combination expression. Black arrows denote the location of the optical bench measurements, the blue arrows denote the timeshifts applied to the optical bench terms.

time stamps visually allows the patterns in the structures to be seen more clearly. For example, by comparing the timestamp arrows on each of the antenna diagrams in each figure, it can be clearly seen that the equivalent intra-spacecraft measurement has also acquired the same time delay operators.

The inter-spacecraft measurements for the combination at the current time stamp, are denoted by a black arrow. The direction of the arrow describes the light travelling from the transmitting spacecraft to the receiving spacecraft. The optical bench that measures the arriving laser light is denoted by a black ring round the bench number. This can be seen, for example, in the diagram in the top middle of Figure 3.1 which denotes the combination term $y_{13,2}$. The black arrow is pointing towards the receiving optical bench which measures y_{31}. The blue arrows describe the timeshifts that are applied to the optical bench measurements. The location of the arrow describes the armlength delay applied to the term, in this case, a time shift of L_2 denoted by the arrow on armlength 2 and relating to $y_{,2}$. Hence the combination of the arrows describes the full combination term $y_{13,2}$.

Note that the armlengths are assumed to be free from directional dependence ($L_{ij} \neq L_{ik}$), but the directions of the timeshifts have been maintained in the figures to preserve

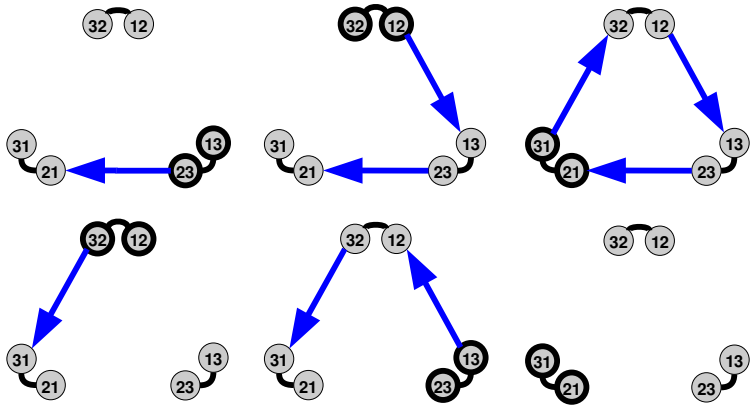

Figure 3.2: Diagram of the intra-spacecraft measurements that relate to the corresponding inter-spacecraft measurements in Figure 3.1, for the α combination. Black arrows denote the location of the optical bench measurements, the blue arrows denote the timeshifts applied to the optical bench terms.

the structure of the overall combination. Note also that by tracing the path of each of the arrows (both black and blue) on each diagram in Figure 3.1, it can be seen that the end point for each coincides with one of the optical benches on spacecraft 1.

In Figure 3.2, the intra-spacecraft measurements for the current time stamp are denoted by the highlighted pair of optical benches. Note that the diagrams relating to these measurements are represented by benches that are joined together. The intra-measurements are timeshifted in a similar way to their corresponding inter-spacecraft datastreams, denoted by blue arrows.

Looking at the individual noise contributions on each optical bench, the laser fluctuations that appear in the inter-spacecraft measurement s_{ji} are related to the laser source on the transmitting optical bench. The movement of this bench can be characterised by the intra-spacecraft measurement $(z_{jk} - z_{ik})$ that occured at a timestamp related to the length of the arm the light traveled down. Hence any timeshifts that are applied to the s_{ij} terms will also be applied to the z_{ij} terms of the outgoing spacecraft, with the addition of the time shift along the direction of travel for the laser beam.

Looking at the arrows for the top line diagrams from right to left, the black arrows describing the inter-spacecraft measurements correspond to the laser beams reaching the righthand optical bench on each spacecraft at the same time. In other words,

they are instantaneous measurements of the light in the antenna for a particular time stamp. If the optical paths between the LISA spacecraft were considered to be two directional laser beams, a single optical path would correspond to a laser timestamp leaving the front of an optical bench on spacecraft 1, traveling through the other benches and arriving again at the back of the same optical bench. The individual LISA measurements can be reconstructed to create this optical path by time shifting the relevant measurements by particular time stamp values.

For clarity, only the terms with no timeshifting will enter the combinations with a timestamp taken at the current time, the other terms relate to their respective optical benches but for past time stamps.

The combinations described in this section are termed Sagnac Combinations as they utilise datastream information from every optical bench, reflecting the optical setup for a ring interferometer. This method for recombining the datastream information is described as *Six-pulse combinations* as a δ-gravitational wave signal will result in a six-pulse response in the combination datastream. In other words the signal will appear at six different times in the full datastream; the exact time stamps will be dependent on the arrival direction of the wave and the configuration of the detector [35].

3.2.2 Fully Symmetric Sagnac Combination (ζ)

The above optical paths of the Sagnac datastream combinations correspond to clockwise and anti-clockwise trips around the antenna with respect to a single spacecraft. Following Prince *et al* [30], there is a similar combination (ζ) termed the *Fully Symmetric Sagnac Combination*, that satisfies the laser noise cancellation criterion and utilises single time delays along a neighbouring arm.

$$\begin{aligned}\zeta =& y_{32,2} - y_{23,3} + y_{13,3} - y_{31,1} + y_{21,1} - y_{12,2} \\ &+ \frac{1}{2}(-z_{13,21} + z_{23,12} - z_{21,23} + z_{31,23} - z_{32,13} + z_{12,13}) \\ &+ \frac{1}{2}(-z_{32,2} + z_{12,2} - z_{13,3} + z_{23,3} - z_{21,1} + z_{31,1})\end{aligned} \tag{3.2}$$

In this case, every datastream term is time shifted along the previous arm in the direction of travel of the armlength data. For example, the time shifted data stream measurement $y_{32,2}$ is travelling clockwise along arm 3 and is time delayed along arm 2. The corresponding anticlockwise term is $y_{23,3}$, which travels along armlength 2 and is timeshifted by L_3.

If the armlengths are equal ($L_i = L_j = L_k$), then the individual terms, corresponding to one part of the optical path, are the identical opposites of the respective terms for the other direction. This can be seen more clearly in Figure 3.3. The top line of the antenna diagrams represents the positive terms (clockwise) in the combination expressions, the second line the anticlockwise terms (similar to Figures 3.1 and 3.2). Comparing the individual antennas in each column of Figure 3.3, the arrows in each case describe the same optical path shape, although in different directions.

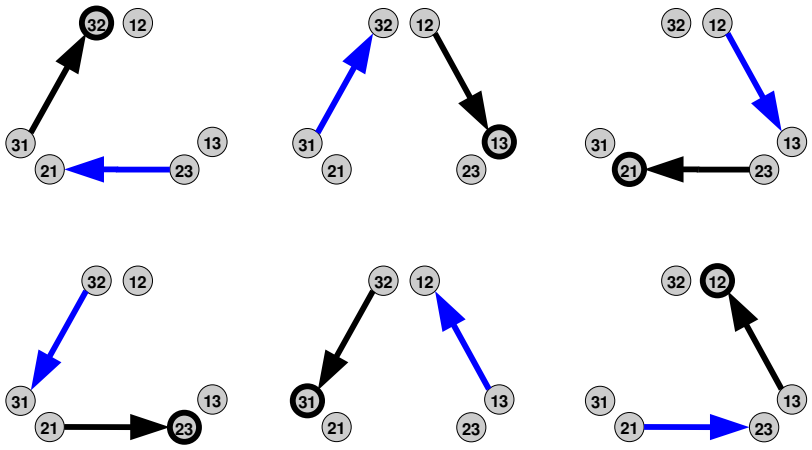

Figure 3.3: Diagram of the inter-spacecraft optical bench measurements present in the First Generation TDI combination ζ. Black arrows denote the optical bench measurements, while the blue arrows relate to the time delay operator applied to the term.

On closer inspection of the intra-spacecraft diagrams in Figure 3.4, it can be seen that the antenna diagrams only contain blue arrows. These correspond to the different time delays applied to the inter-spacecraft terms, with the addition of the timeshift for the laser light travel time down the arm, similar to the construction of the intra-spacecraft terms for α.

Similar to the previous combinations, a δ-gravitational wave signal will result in a

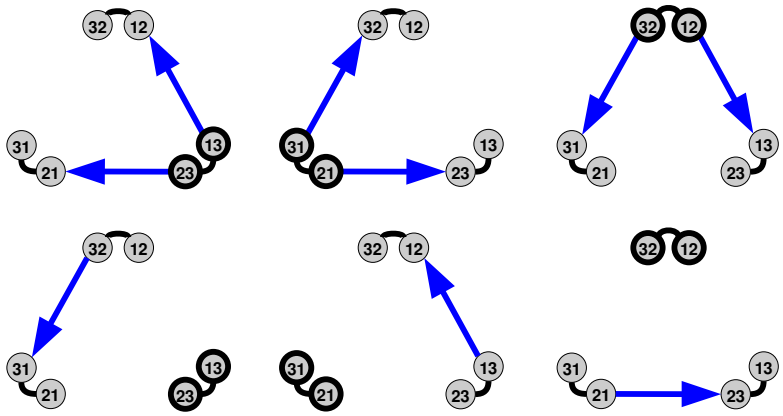

Figure 3.4: Diagram of the intra-spacecraft optical bench measurements present in the First Generation TDI combination ζ.

six-pulse response in the datastreams. The identically symmetrical antenna paths will acquire the same laser noise terms that can then be cancelled out during the analysis.

Note that the similarity between the two types of Sagnac combinations, enables the Symmetric Sagnac expression to be defined in terms of the α, β and γ,

$$\zeta - \zeta_{,123} = \alpha_{,1} - \alpha_{,23} + \beta_{,2} - \beta_{,31} + \gamma_{,3} - \gamma_{,12}$$

The ζ expression, as described above, has only one time delay term applied to the individual terms. The α, β and γ expressions have equal numbers of terms with zero, one and two time shifts applied. The time shifting of these terms increases the range of the time delays by one; the expressions are now timeshifted by up to four time delays. As the Sagnac combinations use similar datastream terms, when they are combined together in the above expression they introduce identically equal and opposite terms, removing the expressions with two and three timeshifts, leaving an expression which contains the correct single and double timeshifts. This results in a description of the difference in ζ in terms of α, β and γ.

3.2.3 Eight Pulse Combinations (X, Y, Z)

Thinking of the individual laser noise contributions from the optical benches, the above combinations were derived by applying an existing interferometric shape onto the datastreams, one that would be able to cancel the laser noise terms. In a similar way, a 30° unequal arm Michelson combination would also introduce identical noise terms into the reconstructed datastream. Instead of the Sagnac optical paths, the combination is constructed using information from only four optical benches, analogous to the light beam travelling in both directions down two of the arms.

$$\begin{aligned} X \;=\; & y_{32,322} - y_{23,233} + y_{31,22} - y_{21,33} + y_{23,2} - y_{32,3} + y_{21} - y_{31} \\ & + \frac{1}{2}(-z_{21,2233} + z_{21,33} + z_{21,22} - z_{21}) \\ & + \frac{1}{2}(z_{31,2233} - z_{31,33} - z_{31,22} + z_{31}) \end{aligned}$$

Similar to the α combination, X is constructed around spacecraft 1, utilising datastreams from optical benches 31 and 21 on S/C 1 itself and benches 32 and 23 on the other spacecraft [36, 30]. This method restricts the available time delays but also the sources of laser noise. There are two variations of this combination shape, termed Y and Z, which can be derived by cyclic permutation of the indices $(1 \to 2 \to 3 \to 1)$. These combinations are termed *Eight Pulse Combinations* as they display an eight pulse response to a δ-gravitational wave, directly related to the number of inter-spacecraft terms [35]. The structure of the X combination can be seen more clearly in Figures 3.5 and 3.6.

A method that can achieve the laser noise cancellation without using information from the entire antenna is extremely useful. For example, if the communications between two of the spacecraft went offline, then information about the gravitational wave signals could still be recovered using the Michelson combinations.

Following the colour scheme for the time delay arrows introduced in Figure 3.1, the black arrows denote current time datastream values, measured on the optical bench indicated by the arrow direction. The blue arrows describe time shifts of the optical

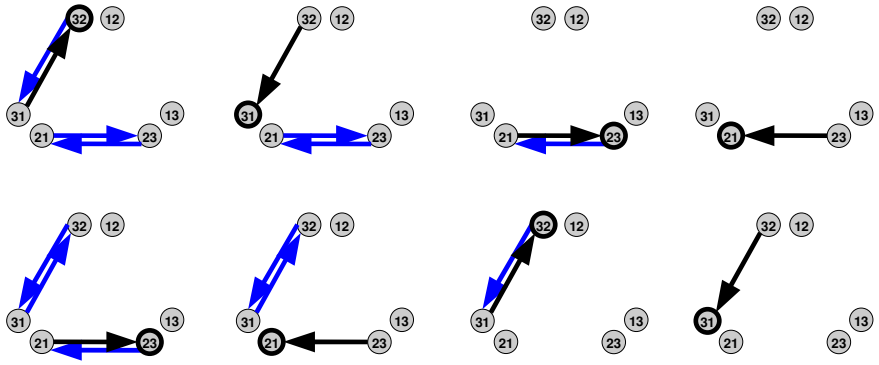

Figure 3.5: Diagram of the inter-spacecraft optical bench measurements present in the TDI combination X. Black arrows denote the optical bench measurements, while the blue arrows relate to the time delay operator applied to the term.

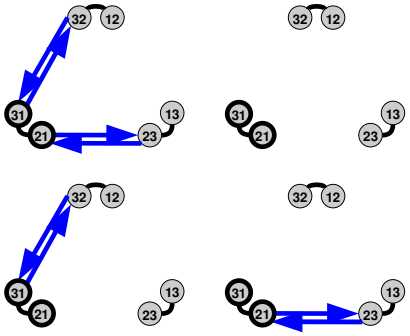

Figure 3.6: Diagram of the intra-spacecraft optical bench measurements present in the TDI combination X. Black arrows denote the optical bench measurements, while the blue arrows relate to the time delay operator applied to the terms.

bench measurements which are direction independent for the rigid rotation approximation. Note that the eight optical bench measurements correspond to laser beams emitted by spacecraft 1 at timestamp $(2L_2 + 2L_3)$ and the measurements of this beam as it travels along each of the arms (L_2, L_3) in both directions. In other words, the datastreams reconstruct two Michelson optical paths.

The number of intra-spacecraft measurements is reflected by the nature of the reconstruction. There are only four terms needed, due to the fewer laser noise terms.

The z_{ij} measurements correspond to the current motion of the spacecraft and the intra-spacecraft measurement that occurred at the same time as the initial laser light was transmitted by spacecraft 1, shown in the top line of Figure 3.6. The other diagrams

describe the intra-spacecraft measurements for S/C 1 when the light is received at the other optical benches. Crucially the intra-optical bench measurements all relate to the original spacecraft. The reason for this is that the inter-spacecraft measurements are either measured on S/C 1 or are subject to time delays to relate the light back to the original light from the spacecraft. Note that the term $y_{32,3}$ describes the light measured by bench 32 with a time delay 3 - a measurement of the light received when the light that became y_{31} was transmitted.

Note that the 30° Michelson combination and the 45° Michelson detector mentioned in Section 2.4 are two possible configurations of LISA. The second interferometric framework uses the datastream information to algebraically reconstruct the output from a 45° detector, similar in shape to many of the current ground based detectors. Due to the design of the LISA antenna and the inherent flexibility provided by measuring each of the laser arm lengths separately, there are three other eight pulse combinations that satisfy the laser noise cancellation criterion, termed the Beacon (P, Q, R), Monitor (E, F, G) and Relay (U, V, W) responses [22, 30, 36]. They require the same number of datastreams as the Unequal Arm Michelson, but they use different interferometric forms, for example, the Beacon utilises information from two spacecraft, while the other two require all three. The relative structures of the combinations, with respect to the Unequal Arm Michelson are shown in Figure 3.7.

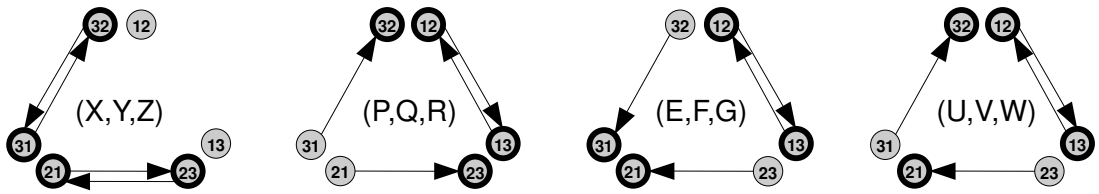

Figure 3.7: Diagrams of the Unequal Arm Michelson (X,Y,Z), Beacon (P,Q,R), Monitor (E,F,G) and Relay (U,V,W) Eight Pulse Combinations. The arrows describing the optical paths described by each of the combinations respectively.

Due to their structure and the time delay terms involved, the eight pulse combinations can be described in terms of the six pulse Sagnac Combinations (α, β, γ), the relevant datastream measurements provided by the time shifted sum of the smaller

combinations [35]. For the Unequal Arm Michelson combinations,

$$\begin{aligned} X_{,1} &= \alpha_{,32} - \beta_{,2} - \gamma_{,3} + \zeta \\ Y_{,2} &= \beta_{,13} - \gamma_{,3} - \alpha_{,1} + \zeta \\ Z_{,3} &= \gamma_{,32} - \alpha_{,2} - \beta_{,3} + \zeta. \end{aligned} \tag{3.3}$$

Note that as the six pulse combinations are free from the laser noise contributions, it follows directly that the eight pulse combinations constructed from them will inherit the same property

The appropriate datastreams terms can be constructed from the Sagnac combinations with the addition of the Fully Symmetric Sagnac combination (ζ). As previously discussed, the ζ combination can in turn be described in terms of α, β, γ, its inclusion in the above expressions highlights the relative structure of the reconstruction to be seen. In other words, the eight pulse combinations have the same time stamp measurements as the time shifted Sagnac combinations constructed around each spacecraft in turn and the fully symmetric optical path combination [48]. Note that the eight pulse combinations that correspond to the construction from the smaller combination descriptions are timeshifted versions of X, Y and Z, not X, Y, Z at the current time stamp of the data. This is the direct result of the individual time stamps of the optical bench measurements present in the six pulse combinations.

3.3 Uncorrelated Noise Combinations (A, E, T)

The TDI combinations discussed in the previous chapter are defined to be free from laser noise contributions but in general will be strongly correlated with each other as they contain similar terms from a number of optical benches. This is a potentially serious issue for parameter estimation. For example, it will result in inefficient Markov Chain Monte Carlo sampling of the Likelihood Function, as in most cases the TDI combination terms are assumed to be uncorrelated [49].

It is possible to utilise the properties of the simpler combinations to construct three

new combinations (A, E, T) that will not only cancel the laser noise terms but are orthogonal in the TDI space at any timestamp of the measurement data.

3.3.1 Derivation of the Optimal TDI Combinations

Each of the First Generation combinations describes a configuration of the datastreams y_{ij} that will remove the laser frequency noise and allow the gravitational wave signals to be detected. Within the framework of TDI, each datastream is individually accounted for, which allows the construction of numerous laser noise cancellation combinations (α, ζ, X). The sensitivity of a combination to a particular signal will be dependent on the individual structure of the combination and the orientation of the antenna at the time of the measurement. LISA could, therefore, be described as a multi-detector array that contains every laser noise cancellation combination. In other words, LISA can be viewed simultaneously as many different detectors constructed from every possible combination of the data stream that achieves laser noise cancellation.

With different methods for detecting the gravitational wave signal, there must be an optimal way to combine the different combinations to maximise LISA's sensitivity to the signal. In other words, a single combination of the datastream measurements that maximises the *signal-to-noise ratio* (SNR).

An important point to note is that within the TDI space defined by the combinations, there will be solutions that are scalar multiples and recombinations of simpler TDI streams. For example, as seen in the previous section, the First Generation eight pulse combinations can be described in terms of the six pulse Sagnac combinations. The six pulse combinations providing the simplest foundations for describing the possible laser noise cancellation criterion, for a static and stationary LISA configuration. The Sagnac combinations can therefore be described as spanning the space for the First Generation Time Delay Interferometry variables [48]. Maximising the SNR for the datastreams constructed from these combinations should therefore provide the highest sensitivity to a gravitational wave signal.

Following the approach in Prince *et al* [30], the six pulse combinations $\alpha, \beta, \gamma,$ and ζ

can be expressed in terms of a linear combination in Fourier space ($\tilde{}$),

$$\eta(f) = a_1(f, \vec{\lambda})\tilde{\alpha}(f) + a_2(f, \vec{\lambda})\tilde{\beta}(f) + a_3(f, \vec{\lambda})\tilde{\gamma}(f) + a_4(f, \vec{\lambda})\tilde{\zeta}(f),$$

where $a_i(f, \vec{\lambda})_{i=1}^{4}$ are complex functions of the Fourier frequency f and vector $\vec{\lambda}$, relating the contribution of each combination to the linear relation $\eta(f)$. The $\vec{\lambda}$ terms are characterised by the properties of the gravitational wave signal (ie. the source location, waveform parameters, etc) and the properties of the noise terms that affect $\alpha, \beta, \gamma, \zeta$. For a given realisation of the functions, η will appear as an element within the combination space. Therefore the configuration that will have the highest sensitivity to a given gravitational wave signal can be found by identifying the $a_i(f, \vec{\lambda})_{i=1}^{4}$ function values that maximise the signal-to-noise ratio for $\eta(f)$.

3.3.2 Defining the Signal-to-Noise Ratio

As discussed in Section 3.2.2, the Fully Symmetric combination ζ can be described in terms of the other combinations α, β, γ and therefore only these combinations truly span the space. Redefining $\eta(f)$ in these terms gives a signal-to-noise expression of,

$$SNR_{\eta}^{2} = \int_{f_l}^{f_u} \frac{|a_1\tilde{\alpha}_s + a_2\tilde{\beta}_s + a_3\tilde{\gamma}_s|^2}{\langle |a_1\tilde{\alpha}_n + a_2\tilde{\beta}_n + a_3\tilde{\gamma}_n|^2 \rangle} df \tag{3.4}$$

where f_l and f_u correspond to the frequency limits on the LISA band and subscripts denote the signal (s) and noise (n) components of α, β, γ respectively.

To help clarify the notation, two vectors are defined for the signal and noise components, $\vec{x}^{(s)}$ and $\vec{x}^{(n)}$, equal to $(\tilde{\alpha}_s, \tilde{\beta}_s, \tilde{\gamma}_s)$ and $(\tilde{\alpha}_n, \tilde{\beta}_n, \tilde{\gamma}_n)$ respectively. The functions $a_i(f, \vec{\lambda})_{i=1}^{3}$ can be similarly described as $\vec{a}$. The correlation matrix $(\mathcal{C})$ for the vector random processes $\vec{x}_n$ will be 3-by-3, describing the collective permutations of the three combination terms. Note that the auto-correlation of the combinations will form the diagonal entries of the matrix. The matrix itself is defined to be Hermitian[2] and

[2] A Hermitian matrix is a square matrix where the complex entries are equal to its own conjugate transpose (i.e. $a_{ij} = a_{ji}^{*}$)

non-singular, and hence,

$$\mathcal{C}_{rt} = \langle \vec{x}_r^{(n)} \vec{x}_t^{(n)*} \rangle.$$

This is a reasonable assumption as the correlation of α, β, γ with themselves will be non-zero in each case. The components of the Hermitian matrix for the signal are represented as $\mathcal{A}_{ij}$, equal to $\vec{x}_i^{(s)} \vec{x}_i^{(s)*}$. Rewriting the SNR relation gives,

$$SNR_\eta^2 = \int_{f_l}^{f_u} \frac{\vec{a}_i \mathcal{A}_{ij} \vec{a}_j^*}{\vec{a}_r \mathcal{C}_{rt} \vec{a}_t^*} df, \tag{3.5}$$

where the repetition of the indices indicates the application of the summation convention for those terms. Note that the star superscript (*) denotes the complex conjugate of the expression. Examining the above equation, it can be clearly seen that the signal-to-noise ratio is formed from the descriptions of the signals in the frequency domain, divided by the corresponding noise descriptions.

In the TDI space, the optimal combinations of the α, β, γ expressions will correspond to stationary values of the SNR and therefore of the integrand. This relationship can be described via the equations,

$$\frac{\partial}{\partial \vec{a}_k} \left[\frac{\vec{a}_i \mathcal{A}_{ij} \vec{a}_j^*}{\vec{a}_r \mathcal{C}_{rt} \vec{a}_t^*} \right] = 0, \quad \text{k=1,2,3.}$$

And therefore, by taking the partial derivatives, the expression can be rewritten as,

$$\mathcal{C}_{ir}^{-1} \mathcal{A}_{rj} \vec{a}_j^* = \left[\frac{\vec{a}_p \mathcal{A}_{pq} \vec{a}_q^*}{\vec{a}_l \mathcal{C}_{lm} \vec{a}_m^*} \right] \vec{a}_i^*$$

where the indices vary over the range (1,2,3). Note that, at this stage the above expression has taken the form of an eigenspace description ($A\vec{x} = \lambda \vec{x}$). Hence, the above equation shows that the complex relation involving the function terms $\vec{a}$ can be expressed directly in terms of the matrix $\mathcal{C}^{-1} \cdot \mathcal{A}$. In terms of the stationary points in the TDI space, the independent vectors that describe the space can be found by diagonalising the correlation matrix.

In mathematical notation, the signal component matrix $\mathcal{A}$ can be described as *Rank*

1, as the matrix contains only one linearly independent row [50]. Therefore, the matrix product $\mathcal{C}^{-1} \cdot \mathcal{A}$ will also only have one non-zero eigenvalue, which can be identified by taking the trace of the matrix. This result will correspond to the sum of its three eigenvalues or more accurately the single non-zero result. Therefore, putting the above results into Equation 3.5, the optimal signal-to-noise ratio can be described as,

$$SNR^2_{\eta \text{opt}} = \int_{f_l}^{f_u} \vec{x}_i^{(s)} \mathcal{C}_{ij}^{-1} \vec{x}_j^{(s)*} df.$$

In summary, an optimal configuration of combination terms can found for the LISA datastreams by using the signal-to-noise ratio that involves the inverse of the correlation matrix and the signal vector components.

3.3.3 Diagonalising the Correlation Matrix

The structure of the correlation matrix will depend on the properties of the noise terms in each combination and also the approximations applied to the LISA configuration. For stationary arms, defined to be $L = 16.67$ sec in length, the laser frequency noise terms are perfectly removed by the construction of the First generation combinations. The remaining noise terms, described in equation 2.1, are the optical path and proof mass noises. Following Prince *et al* [30], the optical path noises are assumed to be equal and uncorrelated with each other, and similarly for the proof mass noise contributions. In this situation the correlation matrix is defined as,

$$C = \begin{pmatrix} S_A & S_{AB} & S_{AB} \\ S_{AB} & S_A & S_{AB} \\ S_{AB} & S_{AB} & S_A \end{pmatrix}$$

Note that the correlation is a measure of the covariance of the measurements divided by their individual standard deviations (See Section 4.1.5 for further discussion). The diagonal terms of the correlation matrix, relating to the auto correlation of the combinations, assumed to be equal to each other and are denoted by the real function

S_A. The cross correlation terms are described in a similar way and are represented by S_{AB}. In other words, the entries in the correlation matrix are described by only two values; either S_A or S_{AB}. Note that this is a simplification of the true structure in the correlation matrix and is designed to make the diagonalisation easier.

Uncorrelated TDI combinations can therefore be constructed by diagonalising the correlation matrix; computing its eigenvalues and eigenvectors and thus identifying which linear combinations of the Sagnac variables will have a diagonal covariance matrix. The eigenvalues are found to be [51],

$$\mu_1 = \mu_2 = S_\alpha - S_{\alpha\beta}, \quad \mu_3 = S_\alpha + 2S_{\alpha\beta}$$

Note that two of the eigenvalues are equal to each other, as expected due to the properties of the combination A, this implies that the third eigenvector (μ_3) will be orthogonal to the two-dimensional space defined by the eigenvector μ_1. Note that due to this property the degenerate eigenvectors (μ_1, μ_2) associated with this space are not necessarily orthogonal to each other. This can be overcome by directly orthogonalising the set of results. The ortho-normalised eigenvectors are therefore,

$$\begin{aligned} \vec{v}_1 &= \frac{1}{\sqrt{2}}(-1, 0, 1) \\ \vec{v}_2 &= \frac{1}{\sqrt{6}}(1, -2, 1) \\ \vec{v}_3 &= \frac{1}{\sqrt{3}}(1, 1, 1) \end{aligned}$$

In the combination space these correspond to,

$$\begin{aligned} A &= \frac{1}{\sqrt{2}}(\tilde{\gamma} - \tilde{\alpha}) \\ E &= \frac{1}{\sqrt{6}}(\tilde{\alpha} - 2\tilde{\beta} + \tilde{\gamma}) \\ T &= \frac{1}{\sqrt{3}}(\tilde{\alpha} + \tilde{\beta} + \tilde{\gamma}). \end{aligned} \tag{3.6}$$

In summary, these combinations[3] are described in terms of the First Generation Sagnac Combinations defined in the frequency domain. The method of their construction ensures that the laser noise contributions will be removed but also that the remaining noises terms will be uncorrelated for any given time stamp [30, 22].

3.3.4 Analysis of Laser Noise Cancellation for A

As discussed in the previous sections, the construction of α, β and γ combinations from the raw optical bench measurements ensures the cancellation of the laser noise terms for a single timestamp. The TDI combinations A, E and T are scalar compositions of these variables and therefore further combinations directly constructed from the combination terms should also be free from the laser noise contributions. In this Section, the Author will investigate the assumption of the laser noise cancellation for the optimal combination A by analysing the individual terms introduced by the time shifted optical bench measurements.

Using the definition of laser noise from equation 2.2, the individual optical bench terms within the combinations can be identified. To simplify the analysis the LISA configuration is assumed to be static and stationary, and hence the laser noise is spacecraft rather than optical bench dependent.

[3]The designation of A, E, T for these combinations relates to the initial letters of Armstrong, Estabrook and Tinto.

Writing out the laser noise terms explicitly for A, using the equation (4.10), gives

$$\begin{aligned} A_{ds}^{laser} &= [C_2(t-L_1) - C_3(t)] - [C_1(t-L_2) - C_3(t)] \\ &\quad -[C_3(t-L_2) - C_1(t)] + [C_2(t-L_3) - C_1(t)] \\ &\quad +[C_1(t-L_3-L_1) - C_2(t-L_1)] \\ &\quad -[C_2(t-L_3-L_2) - C_1(t-L_2)] \\ &\quad -[C_2(t-L_1-L_3) - C_3(t-L_2)] \\ &\quad +[C_3(t-L_1-L_3) - C_2(t-L_3)] \\ &\quad +[C_3(t-L_2-L_1-L_3) - C_1(t-L_1-L_3)] \\ &\quad -[C_3(t-L_1-L_2-L_3) - C_2(t-L_2-L_3)] \\ &\quad -[C_1(t-L_3-L_1-L_2) - C_2(t-L_1-L_2)] \\ &\quad +[C_1(t-L_2-L_1-L_3) - C_3(t-L_1-L_3)] \end{aligned} \tag{3.7}$$

where $C_i(t)$ is the laser noise realisation on spacecraft i at time t. The laser noise is spacecraft dependent and this can be denoted by the single subscript in the laser noise terms. This equation can be simplified, as before, by setting the arm lengths to be equal. As the current question is whether or not the laser noise is always removed, the terms will remain unsimplified in the following analysis to ensure that the conclusions are applicable to the general case.

In order to cancel the laser noise, the expressions must have equal numbers of terms with the same spacecraft numbers and times, with opposing signs. To help with this identification, the terms in equation (3.7) can be re-arranged, grouping together the

terms with similar numbers of time shifts,

$$\begin{aligned} A_{ds}^{laser} &= C_3(t) - C_3(t) + C_1(t) - C_1(t) \\ &\quad + C_2(t - L_1) - C_2(t - L_1) - C_3(t - L_2) + C_3(t - L_2) \\ &\quad - C_1(t - L_2) + C_1(t - L_2) + C_2(t - L_3) - C_2(t - L_3) \\ &\quad + C_1(t - L_3 - L_1) - C_1(t - L_1 - L_3) \\ &\quad - C_2(t - L_3 - L_2) + C_2(t - L_2 - L_3) \\ &\quad - C_2(t - L_1 - L_3) + C_2(t - L_1 - L_2) \qquad (3.8) \\ &\quad + C_3(t - L_1 - L_3) - C_3(t - L_1 - L_3) \\ &\quad + C_3(t - L_2 - L_1 - L_3) - C_3(t - L_1 - L_2 - L_3) \\ &\quad - C_1(t - L_3 - L_1 - L_2) + C_1(t - L_2 - L_1 - L_3). \\ &= 0 \qquad (3.9) \end{aligned}$$

This re-arrangement allows us to see that there are identically equal numbers of negative terms for every positive laser noise term and this ensures that each line in the equation will be cancelled out. Therefore the total laser noise for A at time t, and hence for all time stamps of the data, will be zero. See Appendix F for a detailed analysis of the cancellation of optical bench dependent laser noise.

3.3.5 Discussion of A, E, T in the Time Domain

In terms of the optical bench measurements, the optimal datastreams are constructed from linear combinations of the Sagnac expressions. As the six-pulse combinations are permutations of each other, they will therefore contain similar optical bench terms. The structure of the optimal combinations ensures that each time stamp of the data streams produced using the combination expressions will be independent with respect to each other, defined by the diagonalisation the covariance matrix for the Sagnac variables. This property removes the possibility of covariance between the datastreams.

The derivation described in Prince *et al* [30] was constructed in the frequency

domain. But importantly, the definitions of the covariance matrix and signal-to-noise ratio can also be made in the time domain. In this case the equivalent analysis can be applied to the time domain combination terms. In other words, the definitions of the optimal combinations A, E, T can be made consistently in both domains.

3.3.6 Optimal Combinations using X, Y, Z

The optimisation procedure described in Section 3.3.1 can be easily extended to different structures of covariance matrices and initial choice of combinations. In terms of the eight-pulse combinations, with an identical assumed structure for the covariance matrix, substituting the positions of α, β, γ for X, Y, Z in Equation 3.4, a different set of independent combinations (a, e, t) can be defined as [52],

$$\begin{aligned} a &= \frac{1}{\sqrt{2}}(Z - X) \\ e &= \frac{1}{\sqrt{6}}(X - 2Y + Z) \\ t &= \frac{1}{\sqrt{3}}(X + Y + Z) \end{aligned} \tag{3.10}$$

Comparing equations 3.6 and 3.10, it can be seen that the algebraic structure of the equations is the same in both cases. In mathematical terms, as the structure of the covariance matrices are the same, the eigenvectors are defined by the same set of orthogonalised vectors.

An important point to note is that although the two sets of independent combinations take the same form, the original combinations used to define them are different and therefore they define different optimal expressions. The eigenvectors that span the combinations space take the same form but are different vectors in the full TDI space. Note that the eight-pulse combinations can be described in terms of the Sagnac expressions and therefore the optimal combinations (a, e, t) could be redefined in terms of α, β, γ using the definitions in equations 3.3.

Variation of Optimal Combinations (a, e, t)

The diagonalised covariance matrix for the combinations X, Y, Z has two identically equal eigenvalues, corresponding to a two dimensional plane in the eigenspace. Mathematically, there should be a single solution for every eigenvalue but in this situation any set of orthogonal vectors, that are also orthogonal to the third eigenvector, will be able to span this space. There is therefore some inherent freedom about the choice of the corresponding ortho-normalised eigenvectors that can be used to generate the optimal combinations. In this section, I will introduce one of the other possible combinations discussed in the literature and compare it to the A,E and T independent combinations, introduced by Prince *et al* [30].

The combination expressions A and E in Section 3.3.1 describe one possible choice of eigenvectors. Another commonly used definition is [53, 54],

$$\begin{aligned} a &= \frac{1}{3}(2X - Y - Z) \\ e &= -\frac{1}{\sqrt{3}}(Z - Y) \\ t &= -\frac{\sqrt{2}}{3}(X + Y + Z) \end{aligned} \tag{3.11}$$

The above expressions appear at first glance to be different from the definitions described in Prince *et al* [30], but on closer inspection, the structure of the combinations are similar and can be rewritten in the form of equations 3.6 by interchanging the labels A and E and re-scaling.

Starting with the definitions of the optimal combinations from Prince *et al* [30], this procedure involves replacing the positions of the combinations α, β, γ with the equivalent term in X, Y, Z. Unlike the combinations in Section 3.3.6, the individual combination terms do not relate linearly to their equivalent term, but instead relate to,

$$\alpha \to Y \quad \beta \to X \quad \gamma \to Z$$

The combinations themselves, can be related by,

$$A \to -\frac{\sqrt{2}}{\sqrt{3}}\, e \quad E \to -\frac{\sqrt{2}}{\sqrt{3}}\, a \quad T \to -\frac{\sqrt{2}}{\sqrt{3}}\, t.$$

In summary, by diagonalising the correlation matrix description of the data stream components, optimal combinations can be constructed that describe independent reconstructions of the LISA datastreams at each time stamp of the data.

Chapter 4

Detailed Analysis of Time Correlations within LISA data

Time Delay Interferometry describes methods for combining the optical bench terms to construct new data streams that are not subject to the laser noise contributions. The time shifting of the inter-spacecraft measurements ensures that the laser noise terms present in the combination data streams are cancelled out due to the additional presence of equivalent noise realisation with the opposing sign. The new data stream will, however, contain timeshifted components of the other inter-spacecraft contributions; namely the remaining noise terms and the gravitational wave signal. The construction of the optimal combinations A, E and T generates reconstructed data streams that are orthogonal to each other for any given timestamp. These relate to linear expressions of the Sagnac combinations and as the six-pulse combinations are permutations of each other, the optimal orthogonalised combinations will contain similar optical bench terms.

But as the Sagnac data streams are constructed by timeshifting the optical bench measurements, the current time stamp of the optimal combinations will also contain terms that were measured at previous timestamps. There is the possibility that due to the time shifting applied to the terms that an individual noise realisation term will appear more than once in any data stream. In other words, as the time delays are applied in discrete units of arm length size, the reconstructed data streams corresponding to the different optimal combinations could utilise the same realisation of the noise. For

example, the optical bench terms $n_{ij}(t_a)$ and $n_{ij}(t_b - L)$ will describe the same noise realisation when $t_a = t_b - L$. It is therefore possible that the time delay operators introduced to remove the laser noise contributions could result in the same realisations of the detector noise terms contributing to different timestamps of the data stream.

Although the construction of the optimal combinations ensures that there is zero covariance between the combinations at any given time, the ambiguity introduced by timeshifting the non-laser noise terms means that the data streams could be correlated in time.

In this Chapter, the Author will briefly provide an overview of the mathematical descriptions of correlations and covariances within signal measurements, and then using the properties of the LISA data stream, investigate the individual terms that appear in the combination data streams and the possible correlations between them at different timestamps.

4.1 Mathematical Overview of Covariance and Correlation

The signal measured at each of the LISA optical benches contains laser noise and detector noise contributions. Each type of noise is described by an underlying probability distribution and therefore the individual noise contributions to the LISA signal relate to realisations of the associated distributions. In this Section, the Author will briefly introduce the mathematical concepts required to investigate, in the current and later Chapters, the statistical properties of the LISA data stream.

4.1.1 Expectation Value

As the realisations of the noise contributions are from known distributions (see Section 2.3 for further discussion), the average value of a single noise contribution can be found by determining the *expectation value* (or expected value) of the noise measurements.

The expectation value expresses the average value of a set of measurements when

the variation of the values comes from an underlying distribution. Notationally, the expected value for a function ($f(X)$) of the single continuous variable X is $E\left(f(X)\right)$.

$$E\left(f(X)\right) = \langle f(X) \rangle = \int f(X) P(X) dX$$

where $P(X)$ is the probability density function of X. The expectation value is the sum of each value multiplied by its probability of occurring, based on the underlying distribution.

Note that if the shape of the underlying distribution is not known, the expectation value can be estimated by the *sample mean*, calculated from the normalised sum of the measurements. As the individual noise contributions to the LISA data stream are known and the noise distributions are well understood, any references in later Sections to the mean of signal measurements refers to the expectation value of the underlying distribution.

4.1.2 Population Variance

The variation in the individual realisations of the LISA noise contributions can be described by comparing each value to the expected value for the distribution. This provides a measure of the *population variance* (σ^2) and describes the spread in the measurement values. For a variable X, the expression for the population variance is,

$$\mathrm{var}(X) = \sigma^2 = \left\langle (X - \mu)^2 \right\rangle$$

where μ is the expectation value of the distribution ($E(X)$). In terms of a continuous distribution, this relation can be expanded as,

$$\sigma^2 = \int P(X)(X - E(X))^2 dX,$$

taking into account the probability density distribution of the variable X. Note that for measurements that are known to be drawn from a well defined probability distribution,

the population variance is commonly referred to as the *variance* of the values.

4.1.3 Covariance

Relationships between two variables can be quantified in terms of their *covariance*.

$$\mathrm{cov}(X, Y) = E((X - \mu)(Y - \nu)),$$

where μ is the expected value of X, $E(X)$ and ν is the expected value of data set Y, $E(Y)$. In this notation, the variance is a special case of the covariance where the two variables X and Y are identical. This is an extremely important relation for parameter estimation as it provides a measure of how one might expect two data sets which sample the variables X and Y to vary with respect to each other.

In simple terms, if the variables X and Y are sampled by different sets of observed data, then their covariance will be a measure of how the individual values in each data set vary with respect to each other. Moreover, if the data sets were used to infer the values of the two parameters of interest, then their covariance provides an indication of how well each data set was able to constrain the parameters, and the degree of interdependence of the parameter constraints which each data set provides.

4.1.4 Covariance matrices

For our signal, the measurement data set corresponds to a series of measurements taken over a defined time period, with a specified time interval between each measurement. Therefore, each measurement relates to the same source but not the same point in the waveform. Each of the observations can be considered individually, identified by its specified timestamp. One can then, for example, form a *covariance matrix* (C) describing the data values measured at different time stamps. This matrix can be

written as,

$$C = \begin{bmatrix} \sigma_{11}^2 & \sigma_{21}^2 & \sigma_{31}^2 \\ \sigma_{12}^2 & \sigma_{22}^2 & \sigma_{23}^2 \\ \sigma_{13}^2 & \sigma_{23}^2 & \sigma_{33}^2 \end{bmatrix},$$

where the subscripts denote different timestamps; σ_{ij}^2 is a measure of the covariance between an observation taken at time stamp i and one taken at time j.

If there is no covariance between the data sets, the signal value at one time stamp is not dependent on the value at a different time. In such a situation the measurements are described as *independent*. Mathematically, two events (A,B) are defined to be independent if and only if,

$$P(AB) = P(A)P(B).$$

The above expression indicates that the joint probability for both events is equal to the product of the individual probabilities for each event.

Consider the simple example of a noise signal composed of *white gaussian noise*. White gaussian noise describes a random noise signal, drawn from a gaussian distribution that has an uniform power spectral density. This means that the noise signal has equal power in equally sized frequency bands, in other words, each realisation reflects an equal probability based in the frequency domain. If the LISA noise signal was entirely composed of white gaussian noise then the the covariance would be zero across all time stamps. The random nature of the signal would ensure that no prediction can made about the signal at a later time, based on the current values. Due to this property, if a noise signal is found (or assumed) to be white, then there are no correlations between the data at different timestamps. For a signal composed of white Gaussian noise, therefore, the covariance matrix takes the form,

$$C = \begin{bmatrix} \sigma^2 & 0 & 0 \\ 0 & \sigma^2 & 0 \\ 0 & 0 & \sigma^2 \end{bmatrix},$$

for a noise signal drawn from a gaussian distribution with variance of σ^2. In this example, as there is only a single noise signal, sampled at different timestamps, the covariance matrix describes the covariance of the signal with itself over the time measurements, denoted by the column and row numbers. The only non-zero terms in the covariance matrix are therefore the variances of the signal values at each timestamp. Note that, for this simple example, the variance of the underlying gaussian distribution is defined to be constant over time ($\sigma_i^2 = \sigma^2$). The absence of any non-zero covariance terms between the measurements means that the signal values are *independent* with respect to each other over time.

If the noises are independent but the variance is changing with time, in this case the covariance matrix would take the form,

$$C = \begin{bmatrix} \sigma_1^2 & 0 & 0 \\ 0 & \sigma_2^2 & 0 \\ 0 & 0 & \sigma_3^2 \end{bmatrix},$$

where σ_i^2 is the variance of the signals at time stamp i.

4.1.5 Correlation

Correlation is a measure of the departure of two variables from independence. It is closely related to the description of the covariance, and is in fact a scaled measure of the covariance between two variables.

The *Pearson Product-Moment Correlation Coefficient* (ρ) defines the correlation as the covariance of the variables (X,Y) divided by the product of their standard deviations.

$$\rho_{X,Y} = \frac{\mathrm{cov}(X,Y)}{\sigma_X \sigma_Y} = \frac{\sigma_{XY}^2}{\sigma_X \sigma_Y},$$

Expanding the expression for the Pearson product-moment correlation coefficient in

terms of the signal data streams gives,

$$\begin{aligned} \rho_{X,Y} &= \frac{E((X-\mu)(Y-\nu))}{\sigma_X \sigma_Y} \\ &= \frac{E(XY) - E(X)E(Y)}{\sqrt{E(X^2) - E^2(X)}\sqrt{E(Y^2) - E^2(Y)}} \end{aligned}$$

where μ and ν are the expectation values of variables X and Y respectively.

The value of the correlation coefficient indicates the strength of the linear relationship between the variables. If the variables are *independent* then, as there is zero covariance between the data stream values, the correlation coefficient will return a value of zero. If there is strong correlation between the variables, the graph of one variable against the other will show a strong linear relationship, in other words, the data values, when plotted against one another, will lie close to a diagonal straight line. The gradient of the straight line is related to whether the relationship is a positive or negative correlation. A negative correlation is also termed an anti-correlation. If there is no correlation, then the plot will show no structure at all.

In most cases, the returned correlation value will be somewhere between -1 and 1, which denote the extremes of the correlation values and describe high positive and high negative correlations respectively. The exact value of the correlation describes the strength and form of the linear correlation.

4.2 Identifying Non-Zero Covariance Terms in the LISA Data Stream

Following the approach in Romano and Woan [55], the correlations present in the LISA data streams can be investigated by identifying the individual noise contributions that will have non-zero correlation. In this Section, the Author will present a detailed analysis of the covariances for the independent TDI combinations A, E and T.

The correlations between the combination data streams can be investigated by comparing the individual components of the reconstructed signal at each timestamp. From

equation 2.1, it can be seen that the data streams y_{ij}, in the absence of a gravitational wave signal, are the sum of three noise terms; laser, optical path (containing shot noise) and acceleration noise. In this simple example, it is assumed that there are just two types of noise: laser noise (p_{ij}) and detector noise (n_{ij}). The detector noise term describes the remaining noise contributions in the measurement signal that are associated with the detector. The laser noise contributions will be removed from the reconstructed data streams by the structure of the TDI combinations.

In this analysis, both types of noises were assumed to be mutually uncorrelated and Gaussian distributed with variances σ_p^2 and σ_n^2. This implies that the expectation value of the variables, denoted by angled brackets ($\langle\rangle$), will be zero unless the noise realisations are identical. The expectation value can therefore be described in terms of two Kronecker Delta functions,

$$\langle n_a[t_c] n_b[t_d] \rangle = \delta_{ab}\delta_{cd}\sigma_n^2 \tag{4.1}$$

$$\langle p_a[t_c] p_b[t_d] \rangle = \delta_{ab}\delta_{cd}\sigma_p^2 \tag{4.2}$$

$$\langle n_a[t_c] p_b[t_d] \rangle = 0 \tag{4.3}$$

where the subscripts a and b are the bench numbers for the two variables respectively and the subscripts c and d denote the different time stamp values for the individual data streams. Note that the above conditions only hold when the random processes in question have white spectra, non-white noise spectra will mean that there is non-zero auto-correlations at all LISA time stamps.

The Kronecker Delta function for the bench numbers takes the form

$$\delta_{ab} = \begin{cases} 1, \text{ if a = b} \\ 0, \text{ if a} \neq \text{b} \end{cases}$$

and similarly for δ_{cd}. Each term in the data stream (p_{ij}, n_{ij}) will correspond to a realisation of the noise drawn from the corresponding Gaussian distribution with appropriate choice of variance. See Section 2.3 for a discussion of the noise distributions.

The above constraints imply that the detector noises can only be correlated when they occur on the *same bench* and at the *same timestamp*. To investigate whether A, E and T have any correlated noise, the individual optical benches and times are associated which each of the TDI combinations must be identified.

4.3 Identification of Individual Bench Terms

For a static and stationary antenna, the data streams can be described in terms of the inter-spacecraft measurements [35]. The absence of the rotation and flexing motion of LISA ensures that the laser noise contributions will be precisely removed and therefore can be described as spacecraft dependent, rather than optical bench dependent ($p_{ij} \equiv p_j$). The LISA data stream for an optical bench in the time domain is defined as,

$$s_{ij} = p_k(t - L_i) - p_j(t) + n_{ij}(t) + h_{ij}(t)$$

where $h_{ij}(t)$ is the phase modulation introduced to the signal by the incident gravitational wave. Note that the optical bench dependent terms are denoted by two subscript indices, relating to the labeling of the individual optical benches. The single subscript denotes spacecraft dependence. For example, the data stream measured at time t on optical bench 31 is described as,

$$s_{31} = p_2(t - L_3) - p_1(t) + n_{31}(t) + h_{31}(t),$$

where the laser frequency noise contributions are denoted by the realisations of the laser noise as the light is transmitted by spacecraft 2 and when it is received at spacecraft 1.

The Sagnac Combinations are constructed from particular optical bench measure-

ments, that correspond to different optical bench designations and time stamp values,

$$\alpha = s_{21} - s_{31} + s_{13,2} - s_{12,3} + s_{32,12} - s_{23,13} \tag{4.4}$$

$$\beta = s_{32} - s_{12} + s_{21,3} - s_{23,1} + s_{13,23} - s_{31,21} \tag{4.5}$$

$$\gamma = s_{13} - s_{23} + s_{32,1} - s_{31,2} + s_{21,31} - s_{12,32} \tag{4.6}$$

where $s_{ij,k}$ is the data stream measured at spacecraft ij, at time $t - L_k$ [35]. This notation makes the discussion and analysis of a large number of time stamps manageable but for clarification, the equations in terms of the time shifts are,

$$\alpha = s_{21}(t) - s_{31}(t) + s_{13}(t - L_2) - s_{12}(t - L_3) + s_{32}(t - L_1 - L_2) - s_{23}(t - L_1 - L_3)$$

$$\beta = s_{32}(t) - s_{12}(t) + s_{21}(t - L_3) - s_{23}(t - L_1) + s_{13}(t - L_2 - L_3) - s_{31}(t - L_1 - L_2)$$

$$\gamma = s_{13}(t) - s_{23}(t) + s_{32}(t - L_1) - s_{31}(t - L_2) + s_{21}(t - L_1 - L_3) - s_{12}(t - L_2 - L_3).$$

From the above expressions, it can be seen that the time delay operators required to remove the laser noise terms relate to measurements that occur at earlier timestamps. These measurements are already present in the LISA data streams. Note that for the initial timestamps of the combination data streams, the required timeshift measurements in the optical bench data streams are not present.

From Prince *et al* [30], the secondary combinations are described as,

$$A = \frac{1}{\sqrt{2}}(\tilde{\gamma} - \tilde{\alpha}) \tag{4.7}$$

$$E = \frac{1}{\sqrt{6}}(\tilde{\alpha} - 2\tilde{\beta} + \tilde{\gamma}) \tag{4.8}$$

$$T = \frac{1}{\sqrt{3}}(\tilde{\alpha} + \tilde{\beta} + \tilde{\gamma}) \tag{4.9}$$

where $\tilde{\alpha}$ denotes the Fourier Transform of the α combination, from phase into frequency space. The derivation of these equations by Prince *et al* [30] was discussed in Section 3.3. These combination descriptions can be used to construct a list of the optical bench and spacecraft terms that are utilised for an individual timestamp of the reconstructed

optimal data streams. The individual terms will have different signs (i.e. +ve or -ve) and timestamp values. Due to the structure of the combinations, there is a maximum time delay of three armlengths, which will constrain the required dataset length needed for each measurement to be within $(L_1 + L_2 + L_3)$ of the current time stamp. In other words, there must be a minimum number of time stamps, corresponding to the total number of measurements taken while the beam travels down three of the arms, before the optimal combinations can be constructed.

Using the above equations, we can now identify the individual data streams associated with the independent combinations and the times at which they occur. In this situation,

$$\begin{aligned} A_{ds} &= s_{13}(t) - s_{23}(t) - s_{21}(t) + s_{31}(t) \\ &\quad + s_{32}(t - L_1) - s_{31}(t - L_2) - s_{13}(t - L_2) + s_{12}(t - L_3) \\ &\quad + s_{21}(t - L_1 - L_3) - s_{12}(t - L_2 - L_3) - s_{32}(t - L_1 - L_2) + s_{23}(t - L_1 - L_3). \end{aligned} \tag{4.10}$$

The subscript (ds) is a reminder that A is described in terms of the data streams in the time domain, while equations (4.7)-(4.9) are the ortho-normalised combinations in the frequency domain. The algebraic relationships between the components of the uncorrelated noise combinations are the same in either domain (See Section 3.3.5 for further discussion of this point). The above expression can be further simpified by defining the arm lengths to be equal $(L_1 = L_2 = L_3 = L)$.

$$\begin{aligned} A_{ds} &= s_{13}(t) - s_{23}(t) - s_{21}(t) + s_{31}(t) \\ &\quad + s_{32}(t - L) - s_{31}(t - L) - s_{13}(t - L) + s_{12}(t - L) \\ &\quad + s_{21}(t - 2L) - s_{12}(t - 2L) - s_{32}(t - 2L) + s_{23}(t - 2L). \end{aligned} \tag{4.11}$$

Investigating the individual optical bench terms for the other combinations, relates to,

$$\begin{aligned} E_{ds} &= s_{21}(t) - s_{31}(t) - 2s_{32}(t) \\ &\quad +2s_{12}(t) + s_{13}(t) - s_{23}(t) \\ &\quad +s_{13}(t-L) - s_{12}(t-L) - 2s_{21}(t-L) \\ &\quad +2s_{23}(t-L) + s_{32}(t-L) - s_{31}(t-L) \\ &\quad +s_{32}(t-2L) - s_{23}(t-2L) - 2s_{13}(t-2L) \\ &\quad +2s_{31}(t-2L) + s_{21}(t-2L) - s_{12}(t-2L) \end{aligned}$$

And for T,

$$\begin{aligned} T_{ds} &= s_{21}(t) - s_{31}(t) + s_{32}(t) \\ &\quad -s_{12}(t) + s_{13}(t) - s_{23}(t) \\ &\quad +s_{13}(t-L) - s_{12}(t-L) + s_{21}(t-L) \\ &\quad -s_{23}(t-L) + s_{32}(t-L) - s_{31}(t-L) \\ &\quad +s_{32}(t-2L) - s_{23}(t-2L) + s_{13}(t-2L) \\ &\quad -s_{31}(t-2L) + s_{21}(t-2L) - s_{12}(t-2L) \end{aligned}$$

Note that due to the adoption of equal arm lengths, the combination A is described by optical bench measurements specified at only three time stamps, namely t, $t-L$ and $t-2L$.

4.4 Covariance in the TDI expressions

The presence of time correlations in the reconstructed data streams can be determined by investigating the covariance between the TDI combinations. The data streams y_{ij} are a series of timestamped measurements and therefore can be investigated by analysing the auto- and cross-covariances for A, E and T.

The *cross-covariance* describes the covariance between the different combinations at

different times, while *auto-covariance* is the covariance between the same combinations that have been time shifted with respect to each other. In other words,

$$\text{cross-covariance} = \text{cov}[X(t_a)Y(t_b)]$$
$$\text{auto-covariance} = \text{cov}[X(t_a)X(t_b)]$$

where t_a and t_b are the different time stamps and X and Y are the different TDI combinations. Note that the auto-covariance defined for the same timestamp value is a measure of the *variance*.

Concentrating on the general noise terms and comparing A with itself, the auto-covariance is given by,

$$\begin{aligned} C_{ab} &= \text{cov}[A(t_a), A(t_b)] \\ &= \langle A(t_a)A(t_b)\rangle - \langle A(t_a)\rangle\langle A(t_b)\rangle \\ &= [\langle A_1(t_a)A_1(t_b)\rangle + \langle A_2(t_a)A_2(t_b)\rangle + \dots] \\ &\quad -[\langle A_1(t_a)\rangle\langle A_1(t_b)\rangle + \langle A_2(t_a)\rangle\langle A_2(t_b)\rangle + \dots] \end{aligned}$$

where C_{ab} denotes the entry in the covariance matrix for A, corresponding to time stamps of t_a and t_b, and A_i denotes the ith term in the A combination.

The cancellation of the laser noise terms at any timestamp, by the introduction of equal and opposite terms, will also ensure that there are no laser noise correlations in time. Any covariance between two individual laser noise terms will be cancelled out by the presence of a laser covariance term corresponding to the same bench and time stamp but with the opposite sign. However, the noise terms n_{ij} are present in the same abundance as the data stream terms and therefore could be correlated in time.

4.4.1 Worked Example for $\text{cov}[A(2)A(7)]$ with $\sigma_n = 1$

The time correlation of the combinations can be investigated by identifying the presence of any non-zero auto- and cross-covariances of the individual noise terms. The

introduction of a timeshift might allow different terms to be correlated over time. In this simple example, the covariance of A has been calculated for equal arm lengths (L) of 5 and we assume that the variances of the noises are identical and of value $\sigma_n^2 = 1$. By introducing two time shifts of $t_a = 2$ and $t_b = 7$, the covariance takes the form,

$$C_{A(t_a)A(t_b)} = \mathrm{cov}[A(t_a), A(t_b)],$$

where $A(t_a) = A(2)$ is described by

$$\begin{aligned} A(2) &= n_{13}(2) - n_{23}(2) - n_{21}(2) + n_{31}(2) \\ &\quad + n_{32}(-3) - n_{31}(-3) - n_{13}(-3) + n_{12}(-3) \\ &\quad + n_{21}(-8) - n_{12}(-8) - n_{32}(-8) + n_{23}(-8), \end{aligned}$$

and

$$\begin{aligned} A(7) &= n_{13}(7) - n_{23}(7) - n_{21}(7) + n_{31}(7) \\ &\quad + n_{32}(2) - n_{31}(2) - n_{13}(2) + n_{12}(2) \\ &\quad + n_{21}(-3) - n_{12}(-3) - n_{32}(-3) + n_{23}(-3). \end{aligned}$$

For $t = 2$, the time stamps of the optical bench measurements are 2, -3 and -8, as a result of the time delay operators. The negative time stamps correspond to measurements of the data stream that occurred at time stamps earlier that the initial timestamp. For $t = 7$, the timestamp measurements occur at 7, 2 and -3. From equation 4.1, it can be seen that the expectation value of terms with time stamps of -8 and 7 will be zero, as they are only present in one of the combinations. For the expectation value to be non-zero, the data stream value must have been measured at the same bench and at the same time. The terms that meet this criterion for $A(2)$ and $A(7)$ are $[-n_{13}(2)n_{13}(7-5)]$, $[-n_{31}(2)n_{31}(7-5)]$, $[-n_{32}(2-5)n_{32}(7-10)]$ and

$[-n_{12}(2-5)n_{12}(7-10)]$. Hence, the nonzero covariance expression is,

$$\begin{aligned}\mathrm{cov}[A(2)A(7)] &= [-\langle n_{13}(2)n_{13}(2)\rangle - \langle n_{31}(2)n_{31}(2)\rangle - \\ &\quad \langle n_{32}(-3)n_{32}(-3)\rangle - \langle n_{12}(-3)n_{12}(-3)\rangle] - \\ &\quad [-\langle n_{13}(2)\rangle^2 - \langle n_{31}(2)\rangle^2 - \langle n_{32}(-3)\rangle^2 - \langle n_{12}(-3)\rangle^2].\end{aligned}$$

In this case, the non-zero cross-covariance terms present in the data streams are removed by equal and opposite noise expressions due to the assignment of identical noise variances for each optical bench. Note that as the noise terms are defined to be white gaussian noise to simplify the analysis, the cross terms in the above expressions will be zero as only the same bench, same time stamp terms will be non-zero. The true LISA noise spectra is non-white but by highlighting the terms that are definitely going to correlate with time (i.e. the ones that are the reappearances of the exact same terms), we can more easily determine analytically if any of these terms appear. If any these terms are present in the data stream, then they should result in non-zero covariances for both white and non-white noise spectra.

Grouping the similar bench terms together gives,

$$\begin{aligned}\mathrm{cov}[A(2)A(7)] &= -(\langle n_{13}(2)n_{13}(2)\rangle - \langle n_{13}(2)\rangle^2) \\ &\quad -(\langle n_{31}(2)n_{31}(2)\rangle - \langle n_{31}(2)\rangle^2) \\ &\quad -(\langle n_{32}(-3)n_{32}(-3)\rangle - \langle n_{32}(-3)\rangle^2) \\ &\quad -(\langle n_{12}(-3)n_{12}(-3)\rangle - \langle n_{12}(-3)\rangle^2).\end{aligned}$$

Hence, using equation 4.1,

$$\begin{aligned}\mathrm{cov}[A(2)A(7)] &= -\sigma_n^2 - \sigma_n^2 - \sigma_n^2 - \sigma_n^2 \\ &= -4\sigma_n^2.\end{aligned}$$

This result has been evaluated computationally using a MATLAB[56] code that follows the same identification procedure. For reference, the MATLAB script has been

provided in Appendix H. Note that as the variances of the noises are defined in this example to be the same for every optical bench, and the laser noise covariances are cancelled out, the covariances of the combination data streams can be expressed in terms of the detector noise variance σ_n^2. In other words, the strength of the covariance can be described in terms of the multiplication factor of the detector noise variance, equal to -4 in the above worked example. The results can therefore be denoted simply as an image plot, where the covariance between the individual TDI combinations is denoted by a coloured square, the shade of which is dependent on the strength of the covariance in units of σ_n^2.

The auto-covariance for combination A between timestamps $1-3$ and $6-8$ can be seen in detail in Figure 4.1. The gridlines distinguish between the different time stamp blocks, each corresponding an auto-covariance of A for particular time stamp values. For example, the block in the second row and seven columns along corresponds to the covariances between the combination data stream when the first variable in the covariance expression is at time 2 and the second is at time 7. The tile denoting $\mathrm{cov}[A(2)A(7)]$ is the top left corner of the matrix block and using the colour bar information it can be seen that the covariance is $-4\sigma_n^2$, matching the result from the above analysis. Interestingly, only the diagonal terms within this image plot are non-zero, describing the auto-covariance for timestamp pairs; (1,6),(2,7) and (3,8).

To investigate this effect, the computational analysis is extended to 30 timestamps, resulting in the 30-by-30 covariance matrix shown in Figure 4.2. From this plot, it can be seen that the non-zero structure in Figure 4.1 forms part of a larger diagonal structure in the covariance matrix. The image plot shows non-zero diagonal terms on and around the main diagonal of the matrix. Using the colour bar information as before, it can be seen that, within the defined time ranges, there are only four possible values for the auto-covariance; $12\sigma_n^2$, 0, $-2\sigma_n^2$ and $-4\sigma_n^2$. The largest values correspond to the variances of the combination on the main diagonal.

The non-zero terms follow the main diagonal but at a distance of 5 and 10 blocks from it respectively. Looking at Figure 4.2 in more detail, the non-zero terms are

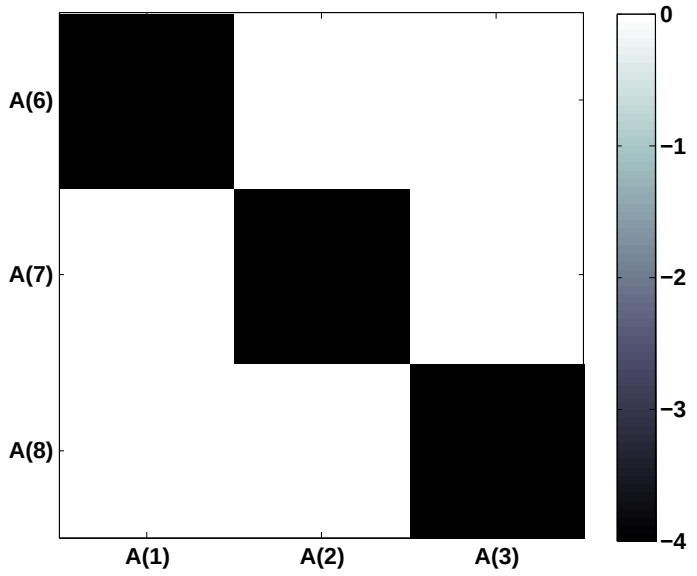

Figure 4.1: Covariance matrix for the A optimal combination data streams for timestamps surrounding $A(2)$ and $A(7)$ for noise distributions with $\sigma_n = 1$. The colour of each tile describes the strength of the correlation between the measurements at time stamps indicated by the location of the block in the matrix

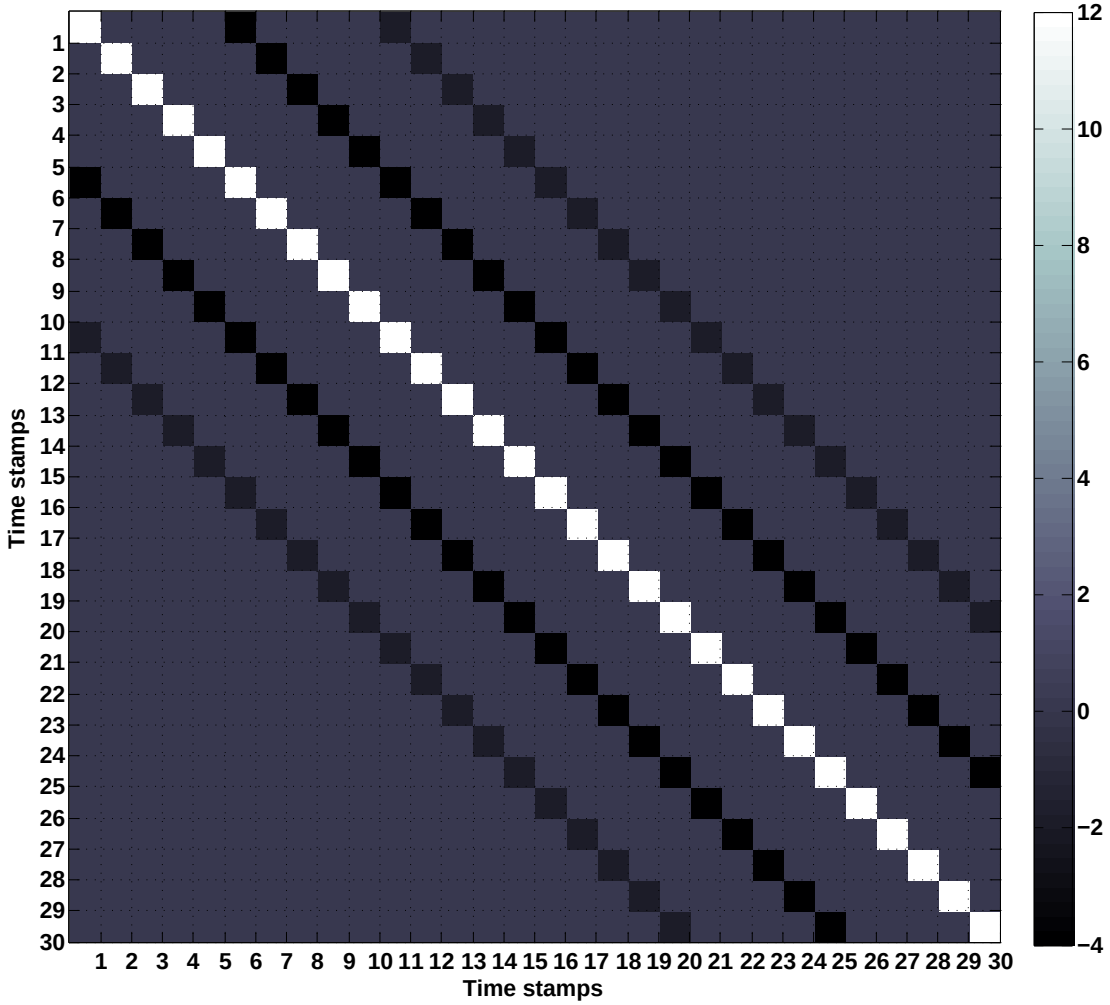

Figure 4.2: Covariance matrix for A optimal combination data streams for noise distributions with $\sigma_n = 1$, over 30 time stamps. The colour of each tile describes the strength of the correlation between the measurements at time stamps indicated by the location of the block in the matrix

located at the time stamp intersections that are a single or double multiple of the LISA armlength. In this case, the armlengths are defined to be static and equal to $L = 5$, in units of optical bench measurements, and therefore the non-zero terms occur at time stamp blocks that have a difference of 5 or 10 between their time stamp values. For example, for the matrix block at the intersection of timestamps 2 and 7, the time stamp difference between them is 5, which is equal as the first multiple of the arm length size. The block at this intersection should therefore be non-zero. Looking back at Figure 4.1, it can be clearly seen that this is in fact the case. From Figure 4.2 it can clearly be seen that all the non-zero terms also exhibit this pattern; the non-zero values occurring when the difference between the time stamps in the covariance expression is a single or double multiple of the LISA armlength.

Discussion

The non-zero auto-covariances appear in the covariance matrix for the combination data streams due to the time delays applied to the optical bench terms during the generation of the A combination. The main constraint for a non-zero covariance is the availability of a term in the other expression that has the same timestamp and bench number. Each term will have between zero and three time delays applied to it by the construction of the Sagnac combinations, in units of arm lengths and therefore only the time shifts that identically equal the arm length size will meet the covariance constraint. In other words, the optical bench term $n_{ij,k}$ will align with a n_{ij} term, when the second term is subject to a time shift exactly equal to L_k. This limits the number of times a data stream term can align with a similar term with the same bench numbers.

To clarify, the terms that initially had the same optical bench number but different time stamps will align only when the time shift is a multiple of the armlength. Note that the A combination at the current timestamp has four different time stamp values and therefore if a term is shifted more than three times it will be unable to have non-zero covariance with any other term apart from itself. The presence of two off-diagonal

covariance diagonals in Figure 4.2 implies that the similar optical bench terms are at a maximum of two time delays apart.

The value of the non-zero covariances will be dependent on the total number of terms within the combination that, once timeshifted, will have the same time stamp value and optical bench number. It is unsurprising, therefore, that the variances of the combination displays the strongest covariance values, as in this situation all of the terms within the expression are timeshifted by the same amount and therefore they all meet the criteria shown in Equation 4.1.

Conclusions

In summary, the A combination is generated from two of the Sagnac Combinations that introduce different optical bench noise terms while cancelling the laser noise contributions. These terms are optical bench dependant but the timeshifting applied to the whole expression will result in the A combination having non-zero time covariances. The presence of the time covariances in the A data streams are the result of the noise terms utilising the same realisations of the noise. Unfortunately, as E and T are constructed in the same manner, they could also be subject to noise correlation terms.

4.4.2 Worked Example for $\mathbf{cov}(A(2)E(7))$ with $\sigma_n = 1$

Following a similar procedure as the previous example, we can investigate the strength of the covariance between the TDI combinations, for example, for $A(2)$ and $E(7)$ with equal arm lengths corresponding to 5 time stamps. The optical benches associated with $A(2)$ have been previously discussed and are described in equation 4.12. The individual detector noise contributions to the data streams for $E(7)$ can be calculated from equation 4.12, and hence,

$$\begin{aligned} E(7) \;=\; & n_{21}(7) - n_{31}(7) - 2n_{32}(7) + 2n_{12}(7) + n_{13}(7) - n_{23}(7) \\ & + n_{13}(2) - n_{12}(2) - 2n_{21}(2) + 2n_{23}(2) + n_{32}(2) - n_{31}(2) \\ & + n_{32}(-3) - n_{23}(-3) - 2n_{13}(-3) + 2n_{31}(-3) + n_{21}(-3) - n_{12}(-3). \end{aligned}$$

Hence, the non-zero terms $(A(2)E(7)_{nonzero})$ are,

$$n_{13}(2)n_{13}(2), \quad n_{21}(2)2n_{21}(2), \quad -n_{23}(2)2n_{23}(2), \quad -n_{31}(2)n_{31}(2),$$
$$n_{32}(-3)n_{32}(-3), \quad n_{13}(-3)2n_{13}(-3), \quad -n_{31}(-3)2n_{31}(-3), \quad -n_{12}(-3)n_{12}(-3)$$

Therefore the covariance is,

$$\begin{aligned} \mathrm{cov}[A(2)E(7)] &= \sigma_n^2 + 2\sigma_n^2 - 2\sigma_n^2 - \sigma_n^2 + \sigma_n^2 + 2\sigma_n^2 - 2\sigma_n^2 - \sigma_n^2 \\ &= 6\sigma_n^2 - 6\sigma_n^2 \\ &= 0 \end{aligned}$$

As there are an equal number of terms corresponding to each sign of σ_n^2, any covariance between the noise terms is cancelled out. This result was corroborated computationally using the same MATLAB code as the previous example expanded to the full A, E, T expression. In this case, each block in the matrix corresponds to a 3-by-3 matrix describing the auto- and cross-covariances of the combinations at each time stamp. As before, the covariance between the combinations, for a particular time stamp, is measured in terms of the variance of the detector noise distribution σ_n^2.

In terms of structure within the image plot, the diagonal of each matrix block contains the individual auto-covariances of the combinations, while the off-diagonal entries denote the cross-covariances for the timestamp values described by the location of the matrix block. This structure can be seen explicitly in Table 4.1 for the matrix block corresponding to timestamps 2 and 7.

A(2)A(7)	A(2)E(7)	A(2)T(7)
E(2)A(7)	E(2)E(7)	E(2)T(7)
T(2)A(7)	T(2)E(7)	T(2)T(7)

Table 4.1: Diagram of the block matrix present, at each time stamp, in the covariance matrices for the A, E, T TDI combination data streams.

Note that the individual tiles on the diagonal of the entire matrix describe the variance of the combinations; the auto-covariance for the same combination at the

same timestamp. Due to the structure of the matrix block, the image plot should be symmetric about the diagonal of the entire matrix, as the covariance for timestamps i and j should be identical to the result for j and i.

Figure 4.3 represents the computational analysis of the combinations terms for timestamps 2 and 7 respectively. Within this matrix block, $A(2)E(7)$ corresponds to the tile in the second row and the first column. From the colour bar, it can be seen that the MATLAB code comes to the same result for $A(2)E(7)$ as the above analysis. It can also be seen that for the time values represented by the matrix block, all of the cross-covariances are zero. From the image plot, only the auto-covariances are non-zero and are described in terms of $-4\sigma_n^2$, $-12\sigma_n^2$ and $12\sigma_n^2$ respectively. Note that the value for the auto-covariance of A, within this time range, is identical to the result from Section 4.4.1 and therefore implies that all of the auto-covariance terms are non-zero due to the absence of identical noise terms.

Expanding this analysis to timestamps varying from 1 to 30, Figure 4.4 displays the results of the computational analysis for combinations $A, E,$ and T. Similar to Figure 4.2, the image plot shows clear diagonal structure on and around the main diagonal. Comparing these results with the results in the previous Section for A, the strength of the individual non-zero covariance terms for A, E, T displays a larger range of values, corresponding the total number of noise terms present in each combination. For example, the variance of the combinations corresponds to $12\sigma_n^2$ for A, $36\sigma_n^2$ for E and $18\sigma_n^2$ for T, with 12, 18 and 18 optical bench dependent noise terms in each case. Note that the evaluation of $36\sigma_n^2$ for E from 18 noise terms is the result of the factor of 2 introduced by the β combination during the reconstruction of the combination. The location of the secondary diagonals follow the same pattern discussed for Figure 4.2, the non-zero covariance values are located at the 3-by-3 matrix blocks corresponding to the time shift differences that are the first and second multiples of the arm length size.

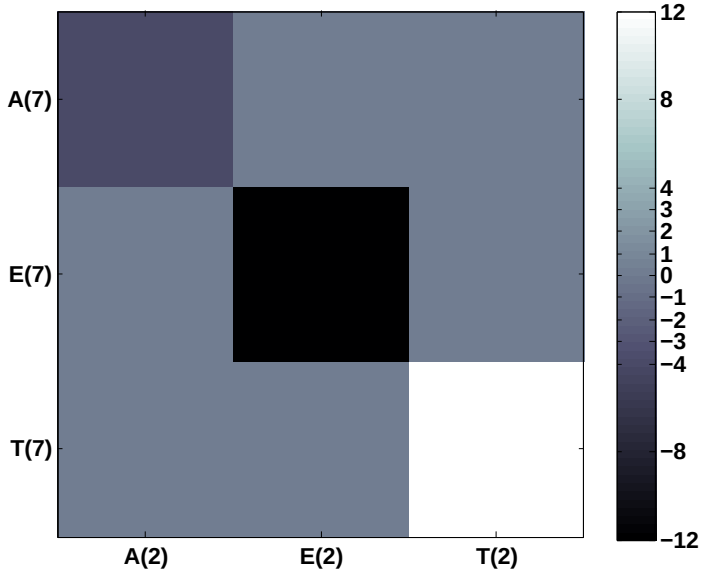

Figure 4.3: Image Plot of the covariance between $A, E,$ and T combination data streams with $\sigma_n = 1$, for the matrix block corresponding to timestamps 2 and 7.

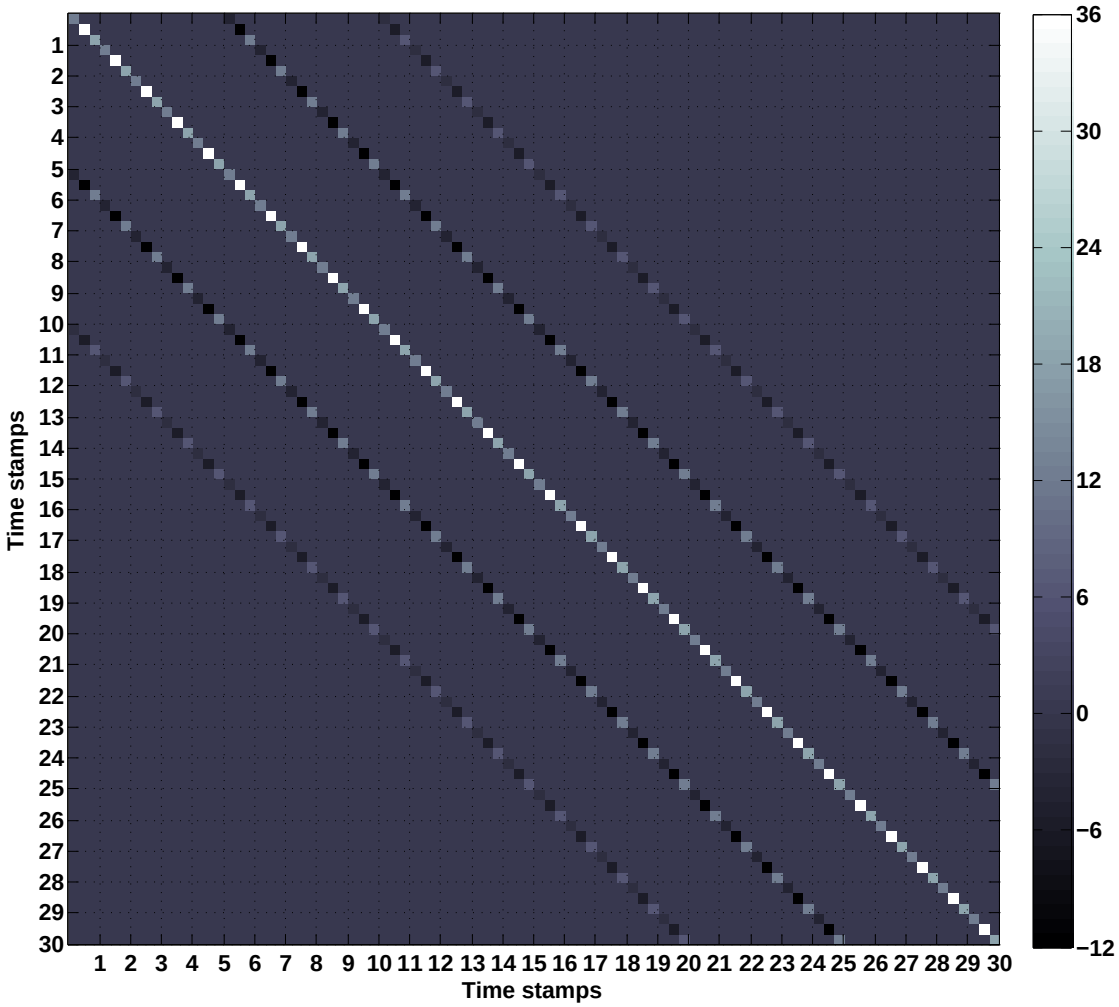

Figure 4.4: Colour Bar Plot of the covariance between $A, E,$ and T combination data streams with $\sigma_n = 1$, over 30 timestamps. The colour of each tile describes the strength of the correlation between the measurements at time stamps indicated by the location of the block in the matrix. Each 3-by-3 block denotes a single time stamp of the data stream, while each square within each block describes the covariance between two of the combinations, from the top left: (A, A), (A, E), (A, T), (E, A), (E, E), (E, T),(T, A), (T, E) and (T, T).

Conclusions

As predicted by the results in Section 4.4.1, the other optimal combinations E and T display the same behaviour within the covariance matrix; they are both subject to auto-covariances at multiples of the arm length size. The reason for this behaviour is due to the introduction of similar optical bench terms during the construction of the A, E, T expressions from the Sagnac combinations. It is therefore probable that they will contain terms with the same time stamp and optical bench number and that will therefore be able to meet the non-zero covariance criterion. The auto-covariances describe the timeshifting of a combination with respect to itself and are non-zero at multiples of the LISA armlength. There are also non-zero cross-covariance terms present in the data streams but due to the assignment of identical noise variances for each optical bench, the non-zero terms are removed by equal and opposite noise expressions. This cancellation is the direct result of the choice of noise variance.

4.4.3 Worked Example for cov$[A(2)E(7)]$ with σ_n varying from $(0.8 - 1.3)$

In the previous examples, it has been assumed that the variance of the detector noise distribution σ_n^2 is identical for each of the optical benches. In the above example this allowed perfect cancellation of the covariances between the combinations. An interesting question is, therefore, if the variances of the noise distributions are optical bench dependent, are the non-zero auto-covariances seen in the previous Sections still present in the data streams?

To investigate whether the choice of σ_n^2 will affect the strength of the covariance between the combinations, each of the optical benches was assigned a value of the detector noise variance linearly from 0.8 to 1.3.

$$\sigma_{n_1}^2 = 0.8, \sigma_{n_2}^2 = 0.9, \sigma_{n_3}^2 = 1.0, \sigma_{n_4}^2 = 1.1, \sigma_{n_5}^2 = 1.2, \sigma_{n_6}^2 = 1.3$$

Using the same combination pair (A, E) as the previous Section, with the same

timeshifting, the cross-covariance can be rewritten as:

$$\begin{aligned}\mathrm{cov}[A(2)E(7)] &= \sigma^2_{n_4} + 2\sigma^2_{n_6} - 2\sigma^2_{n_5} - \sigma^2_{n_1} + \sigma^2_{n_2} + 2\sigma^2_{n_4} - 2\sigma^2_{n_1} - \sigma^2_{n_3} \\ &= 1.1 + (2 * 1.3) - (2 * 1.2) - 0.8 + 0.9 + (2 * 1.1) - (2 * 0.8) - 1.0 \\ &= 1\end{aligned}$$

In this case, although the individual optical bench terms are identical to those in Section 4.4.2, the variation in the detector noise variances results in a non-zero cross-covariance.

Figure 4.5 shows the results for the MATLAB code with the new noise variances. As expected, the presence of differing noise variances introduces some correlation between the TDI combinations. Interestingly, only the blocks containing the relatively timeshifted combinations for the arm length time stamps were affected. In other words, only the blocks that in Section 4.4.2 contained non-zero auto-covariances are now displaying non-zero cross-covariances. This confirms the reasoning in the previous Section that these terms were reliant on the exact cancellation of the noise terms to produce zero cross-covariance. The time shifting of the expressions creates the cross-covariances which are not perfectly cancelled out, describing the alignment of similar optical bench terms that at the current time stamp contain different time shifts. The other covariance terms are still perfectly cancelled out, implying that they are composed of exactly equal and opposite realisations of the optical bench detect noise data streams.

Examining the results for the non-zero cross-covariances more closely, Figure 4.6 describes a subset of the covariance matrix corresponding to time stamps 2 horizontally and 7 vertically, with respect to Figure 4.5. In the previous example, Figure 4.3 showed that the net covariance for the off diagonal terms was zero for the same time stamps, but in this case there are small covariances between the combinations; the quantitive values are shown in Table 4.2.

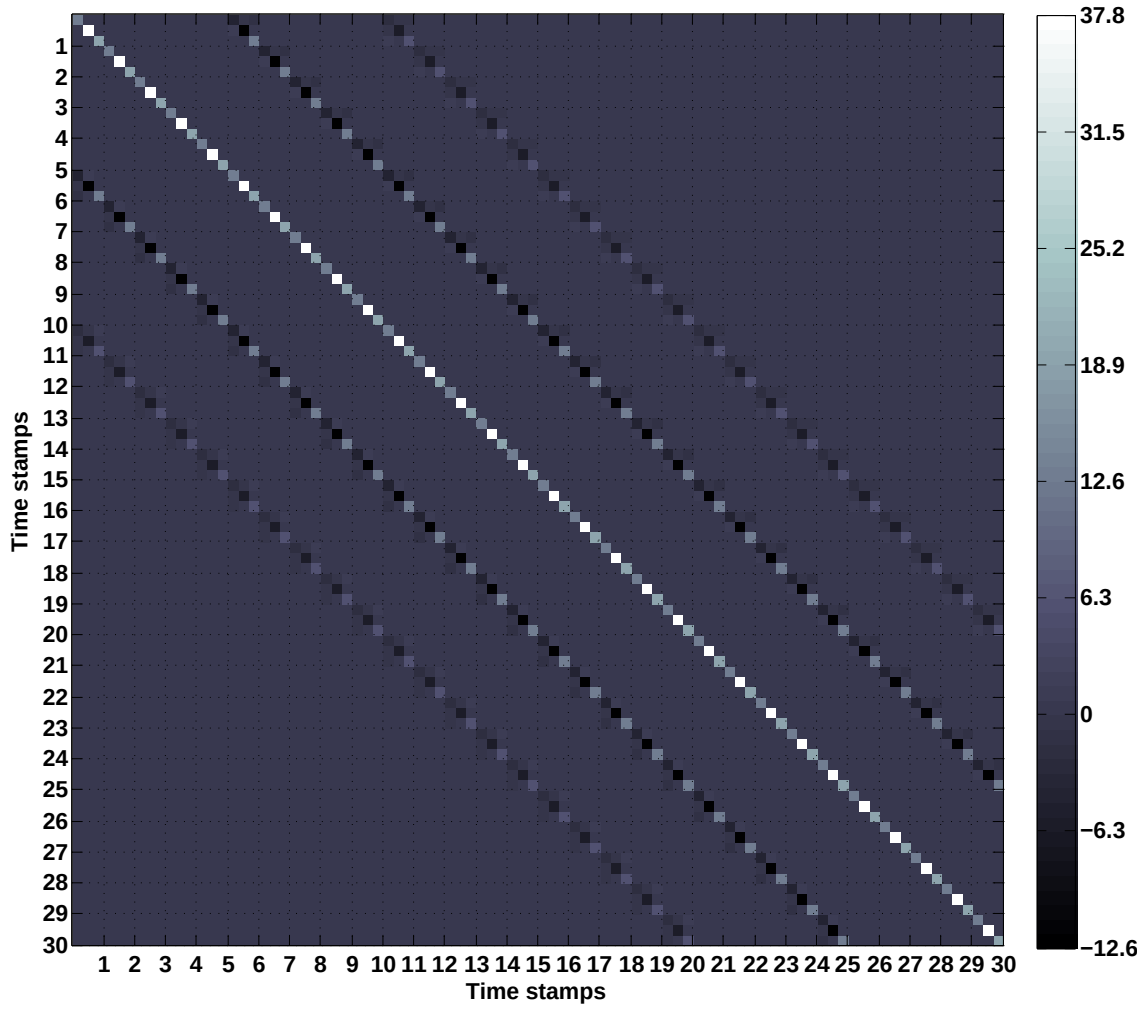

Figure 4.5: Covariance matrix for A, E, T at time stamps 1 to 30, $\sigma_n = 0.8 - 1.3$. The colour of each tile describes the strength of the correlation between the measurements at time stamps indicated by the location of the block in the matrix

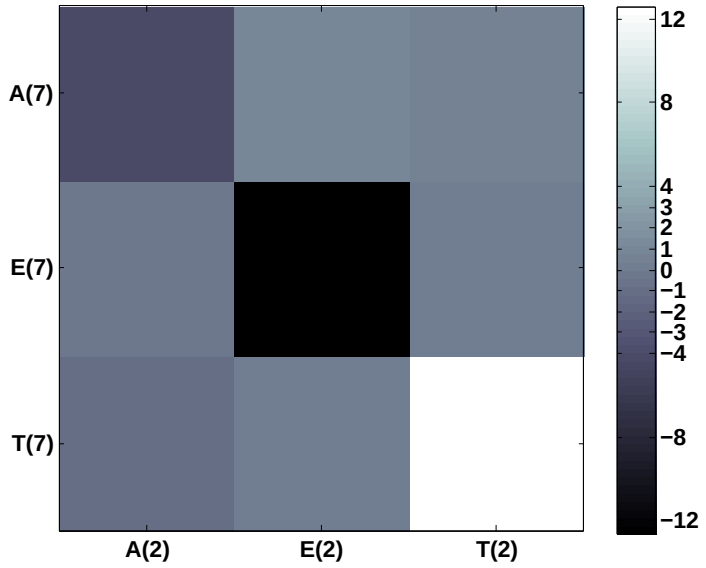

Figure 4.6: Covariance matrix for A, E, T at timestamp 2 and 7, $\sigma_n = 0.8 - 1.3$. The strength of the covariance between the time stamps of the combination data streams is denoted by the colour of the tile, the corresponding value described by the colour bar at the right hand side of the plot.

	$A(2)$	$E(2)$	$T(2)$
$A(7)$	-4.2	1	0.4
$E(7)$	-0.2	-12.6	0
$T(7)$	-0.8	0	12.6

Table 4.2: Covariance matrix for A, E and T at time stamps 2 and 7.

Conclusions

The variation in the values assigned for the variances of the optical bench detector noises σ_n^2 has introduced non-zero cross-covariance terms that are relatively small compared to the auto-covariances for the same timestamp. As expected, the variation in the noise variance values has not removed the auto-covariances seen in the previous Sections, but resulted in the addition of non-zero cross-covariance terms. In this case, the covariances that were removed due to the presence of the equal and opposite terms are no longer perfectly removed, resulting in non-zero cross-correlation terms at multiples of the LISA arm length. As shown in Figure 4.5, the covariances between A and E and A and T are non-zero for time shift values equal to the first and second multiples of the arm lengths.

4.4.4 Conclusions

The optimal TDI combinations A, E, T are defined from the Sagnac Combinations (α, β, γ) and are constructed in such a way as to be uncorrelated at any given time stamp. The removal of the laser noise (p_{ij}) from the data streams is possible by combining different optical bench data streams with different time stamps values. The resultant data stream for an optical bench dependent detector noise (n_{ij}) contribution will therefore contain different bench numbers and realisations of the noise at each timestamp. The combination data streams therefore display non-zero covariances and therefore correlations between the combinations when there are terms present in the expressions that have the same optical bench number and time stamp value, corresponding to the same realisation of the detector noise. The work in this Chapter investigated the possibility of the recombinations of the data streams containing time

correlations, by analysing the individual noise terms that could appear in the covariance matrix for the combinations, for independent optical bench noise streams.

The covariance matrix for A is described in terms of the variance and auto-covariances of the combination. For equal noise variances, as expected, the variance of the combination was non-zero over time. The results also showed that the auto-covariance terms were also non-zero when the size of the time shift within the covariance matrix corresponded to a single or double multiple of the LISA arm length. The reason for this is due to the size of the time delay operators applied during the construction of the Sagnac combinations. The time delays are discretised into units of arm length size and therefore only time shifts corresponding to these units have a possibility of being correlated.

This property was also seen when the analysis was expanded to the full A, E, T covariance matrix. Varying the size of the individual noise variance values introduced non-zero cross-covariance terms within the same matrix blocks that contain non-zero auto-covariance terms. This result uncovered an underlying property of the entire covariance matrix; the absence of cross-covariance terms with the equal noise variances was not due to the absence of noise terms that met the covariance criterion, described in Equation 4.1, but rather the presence of equal and opposite numbers of terms that were perfectly cancelled out.

In summary, the combinations A, E and T have non-zero variances, as expected by the presence of identically equal terms. The equal terms in each combination also ensure the cancellation of the non-zero covariance terms at every time stamp. For all timestamp values, except those with a separation equivalent to the arm length size, there are no auto- or cross-covariances of the combinations. Due to the time delays applied to the combination components, when the difference of the time stamps is equal to one or two armlengths, the combinations contain terms that, when timeshifted, relate to non-zero auto-covariances. There are also non-zero cross-covariances present at these time stamps. But the structure of the combinations themselves results in the complete cancellation of the cross-covariances between E and T in every situation

and the presence of non-zero cross-covariances for (A, E) and (A, T) unless the noise variances are identical, as seen from Figures 4.5 and 4.6. The combination data streams contain non-zero cross-covariance terms for every time stamp but the presence of equal and opposite noise realisation terms will remove the overall effect for most timestamps.

In conclusion, the optimal combinations A, E, T are uncorrelated at any given timestamp but unfortunately they are subject to auto- and cross-covariances and therefore will be correlated in time.

4.5 Covariances in a LISA Model

In the previous examples, the armlengths of LISA were defined to be $L = 5$ to facilitate the analysis for a number of armlengths within a manageable number of timestamps. The non-zero covariance terms were identified at the first and second multiples of the LISA armlength. For a more realistic LISA armlength of $L = 15$, the non-zero terms would be expected to occur at time stamp intersections with differences of 15 and 30. For example the first auto-correlation terms would be predicted to be within the matrix block at timestamps 1 and 16. Figure 4.7 describes the result of the MATLAB analysis for equal noise variances of $\sigma_n^2 = 1$, for 30 timestamps.

Comparing Figures 4.4 and 4.7, it can be seen that the values of the auto-covariances are the same in each case. As expected, the extension of the analysis to the larger armlength size has moved the secondary diagonals to the matrix blocks at a distance of 15 from the main diagonal. Note that the auto-covariances corresponding to the second multiple of the armlengths are not present in the covariance matrix as they would appear at timestamps outside the current timestamp range displayed.

As the time shifts applied to the optical bench terms are defined in terms of armlength units, the same optical bench terms that have non-zero correlation at the current time stamp, will also have non-zero correlation values at a later time stamp or different definition of LISA arm lengths. In other words, the same optical bench terms will remain correlated in time for a static LISA configuration (i.e. TDI 1). The identification of the non-zero covariance terms is therefore consistent with the analysis for different

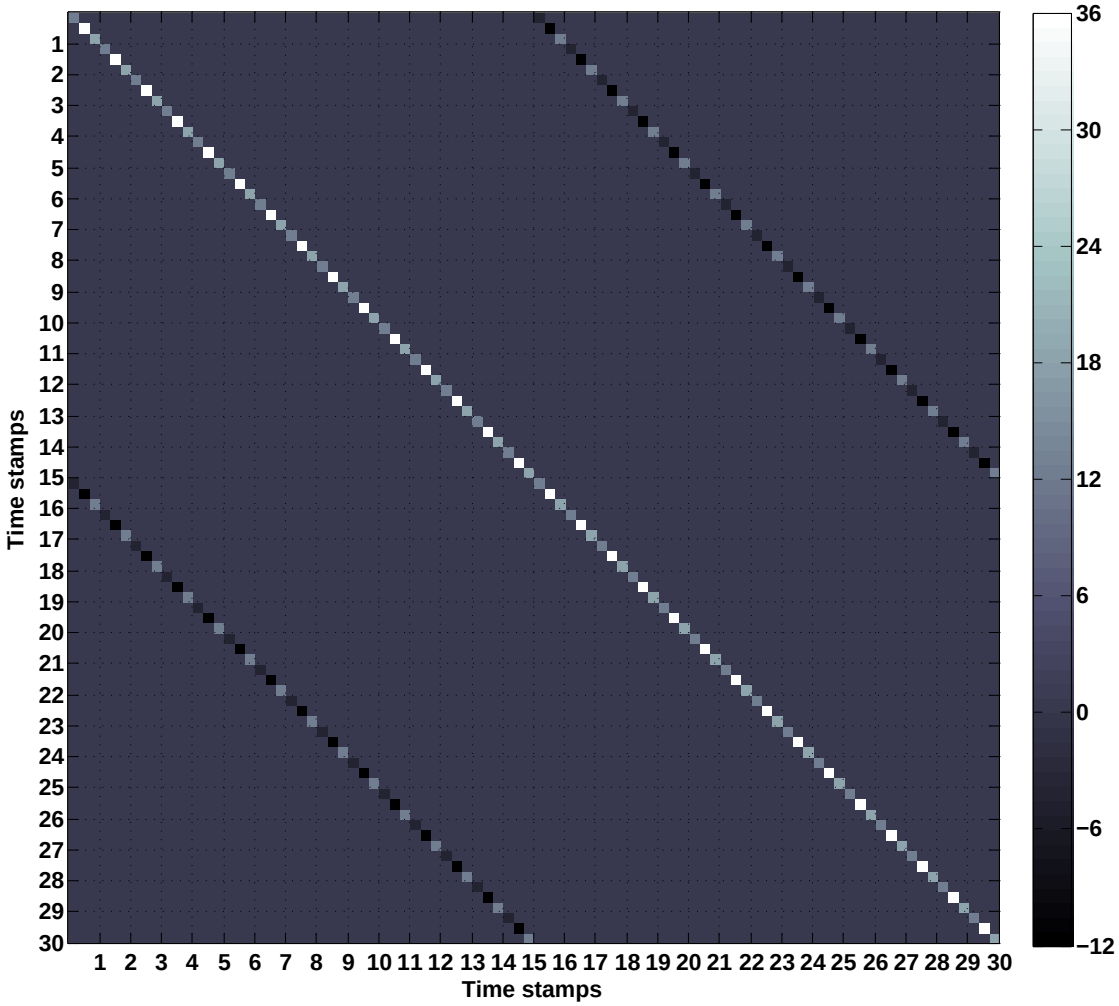

Figure 4.7: Covariance matrix for A, E, T with LISA armlength of 15 and $\sigma_n^2 = 1$

arm length sizes, as the same terms will correlate irrespective of the size of the arm length - the only constraint is that the arm length size does not vary with time.

In other words, throughout the above analysis the LISA armlengths were assumed to be static throughout the defined timestamp range. An interesting application of the analysis would be to investigate the effect of varying the armlengths over time. For more sophisticated LISA models, the rotation of the antenna and movement of the optical benches will affect the instantaneous length of the antenna arms. The covariances that appear in the previous examples describe alignment between terms in different data streams that have the same optical bench number and timestamp value. If the armlength size is time dependent, many of the zero covariance terms appearing in Figures 4.4 and 4.5 that are due to the presence of equal and opposite terms will be unable to meet the conditions for non-zero covariance. Hence, variations in the size of the arm length could therefore result in more non-zero terms appearing in the covariance matrix.

To investigate the effect of the unequal armlengths on the covariance matrix, the MATLAB analysis was applied to the LISA model with noise variances of $\sigma_n^2 = 1$ and the collective armlengths varying discretely between 16 and 14 with every time stamp. For example, the first four armlength distances are therefore 16, 15, 14 and 15. The resultant covariance matrix is shown in Figure 4.8. The introduction of time dependent armlength information has introduced new structures to the covariance matrix. There are now non-zero auto-covariances in time stamp matrix blocks surrounding the central diagonal.

An important point to note, at this stage, is that the extension of the analysis to more realistic LISA models (e.g. with variable arm lengths) is achievable with the existing form of the MATLAB code. The identification of the identical time stamps and optical bench labels is not dependent on the simplifications adopted by the idealised LISA models. This is in marked contrast to the "classical" TDI analysis, where the inclusion of the variable arm lengths makes the expressions for the TDI variables much more complicated.

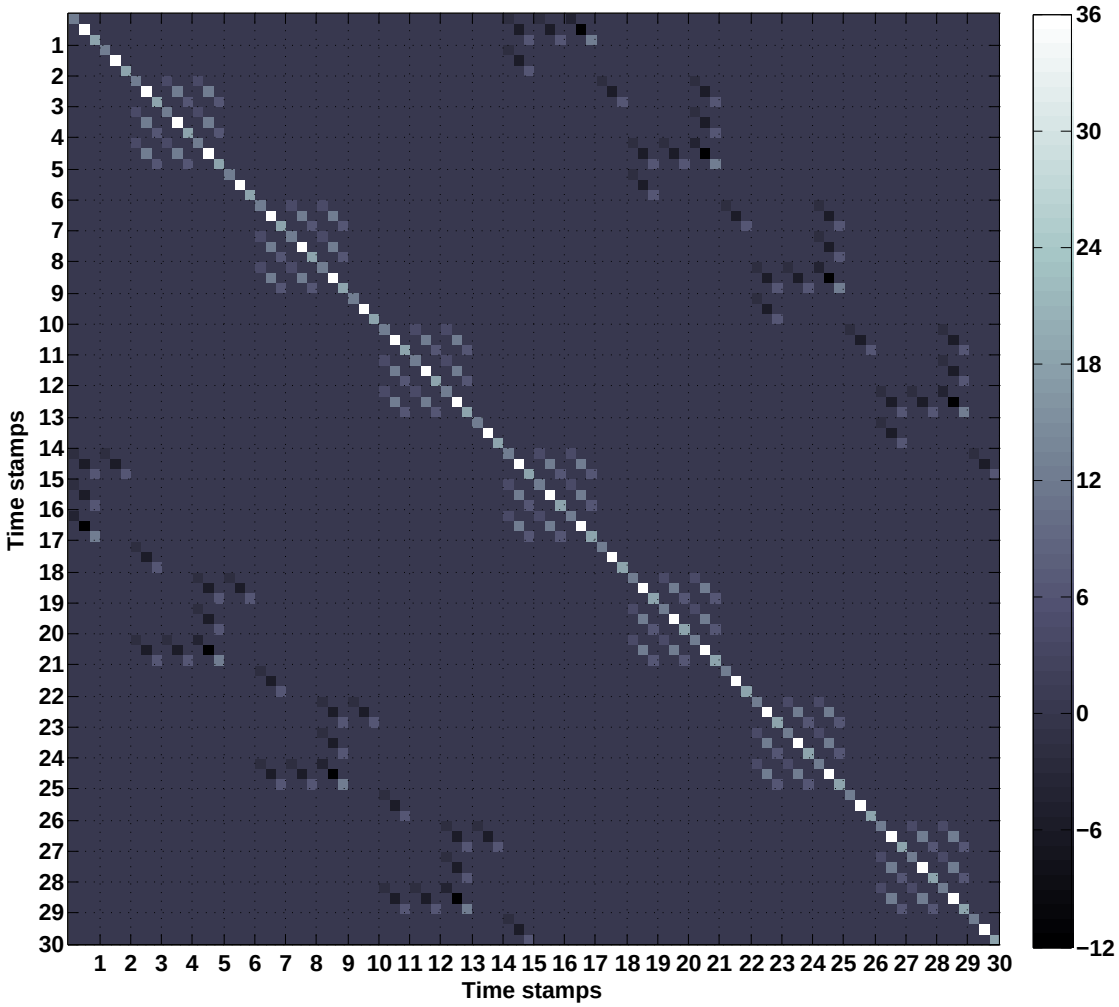

Figure 4.8: Covariance matrix for A, E, T with a varying LISA armlength around 15 and $\sigma_n^2 = 1$. The colour of each tile describes the strength of the correlation between the measurements at time stamps indicated by the location of the block in the matrix and referenced by the colour bar at the right of the Figure. It can be seen that the variation in the LISA arm length has introduced non-zero auto-covariances at time stamps relating to a first or second multiple of the current arm length at the time stamp value.

The timestamps of the individual optical bench measurements are the sum of the armlength size at that timestamp and the time shift applied by the covariance matrix. Therefore the structure of the non-zero auto-covariances around the central diagonal are the direct result of the pattern in the size of the armlengths. As the pattern repeats every four time stamps and the values are at most two units apart, the similar optical bench terms present in the combinations will be able to correlate when the time stamp values of the individual terms are the same. For example, the auto-covariance for A may contain a detector noise term $n_{ij}(t-L(t))$ which at timestamp 3 has an armlength size of $L(3) = 14$, and hence the timestamp of the term is -11. At a later timestamp ($t = 4$), the armlength is now $L(4) = 15$ and the same term still has a timestamp of -11. Therefore, the same realisation of the noise will appear in the data stream at more than one timestamp, and will correlate with time.

The important point to note about these non-zero auto-covariances is that they are the direct result of the time dependent differences in the armlengths. The individual optical bench terms that are currently non-zero in the covariance matrix are present in the data streams of the previous examples but as the timestamps were not the same, they did not meet the non-zero covariance criterion. Their appearance in the current covariance matrix provides a measure of the variations in the armlengths.

Comparing the results with those in Figure 4.4, it can be seen that only some of the matrix blocks have been affected by the variation in armlengths. The variance of the terms remains the same, as expected, as the armlengths are varying coherently and therefore the instantaneous realisations of the data stream will be unchanged. An interesting effect of the time-dependent armlengths is to introduce non-zero auto-covariances for time stamp blocks surrounding the main diagonal. In other words, the spread in the armlength values results in a similiar spread in auto-covariance blocks that are non-zero. The non-zero auto-covariances only appear in matrix time stamp blocks around the diagonal where the variations in the armlengths are able to compensate for differences in time stamps associated with the time delay operators.

This effect is easier to see in the structure of the secondary diagonals, the variations

in the armlength have introduced a spread in the non-zero auto-covariances, related directly to the spread in the armlength values. The terms still relate to the multiples of the armlength size, but this value is now directly influenced by the arm length size for the individual timestamps.

4.5.1 Conclusions

As discussed in the previous Section, the combinations A, E, T are correlated in time, relating to non-zero covariances at timestamp intersections equal to single and double multiplies of the LISA armlength. The combinations contain a number of terms with the same optical bench designation but different time stamp values. The current timestamp of the data streams will have non-zero covariance if they each contain at least one term relating to the same realisation of the noise. The time shifting applied during the construction of the covariance matrix results in some of the terms corresponding to the same realisations of the noise and therefore appearing as non-zero covariances.

The inclusion of time dependent arm length information will directly affect the location of the terms that appear in the covariance matrix. The time stamps of the individual terms relate directly to the current time stamp value and the time delays introduced during the construction of the Sagnac Combinations. As the time delays are defined in units of arm lengths, the resultant timestamp of the optical bench terms is very sensitive to changes in the arm length size. This introduces non-zero auto-covariances at timestamps surrounding the central diagonal of the covariance matrix and variations in the structure of the secondary diagonals, reflecting the differences in the arm length size. In other words, the differences in the separation between the spacecraft over time introduces variation to the existing non-zero structure in the covariance matrix. Hence, the shape of the structures in the covariance matrix provide a direct measure of the relative armlengths of the antenna.

The impact of the time correlations discussed in this Chapter on the recovery of signal parameters from LISA data streams is investigated in Chapter 5, for a simple, illustrative model.

Chapter 5

Investigations of Correlations in LISA data

The analysis of the combination data streams for A, E and T uncovered non-zero auto- and cross-covariances as a result of the utilisation of the same realisation of the detector noise at different time stamps. It is currently assumed that the construction of the A, E and T combinations ensures that the corresponding signal data streams are independent for any given time stamp. However, the method of constructing these TDI conbinations [30] only ensures that they are uncorrelated with respect to each other, for the current time stamp of the measurement data.

An important application of the time correlation results, established in the previous Chapter, is to evaluate their impact on LISA parameter estimation. For example, one would like to understand the extent to which time correlations may pose a problem for likelihood based searches and Markov Chain Monte Carlo analysis [57, 45, 16]. The current strategies for searching for gravitational wave signals do not take account of the time correlations, treating the combination datastreams at different time stamps as statistically independent. An important step therefore is to determine quantitatively the effect of the time correlations on the recovery of signal parameters, firstly with the combination datastreams assumed to be independent and then with the time correlations explicitly and fully accounted for in our model.

In this Chapter, the Author will first introduce the key concepts of Bayesian Probability Theory and then discuss how, in general, *signal analysis* techniques can be used

to recover parameter information relating to the gravitational wave sources using the data stream measurements. The Author will then investigate the recovery of the source parameters using two simplified LISA models where the presence of the time correlations in the signal data streams is correctly modelled in the first case but is absent in the second set of model templates. Investigating the recovery of the signal parameters for a simplified LISA model provides valuable insight into the possible effect of the time correlations on the full LISA data stream, isolated from unrelated data analysis problems, for example, the absence of missing signal measurements or problems with the free fall properties of the individual spacecraft.

5.1 Introduction to Bayesian Probability Theory

Probability Theory is extremely important in data analysis as it provides mathematical frameworks for evaluating how likely a measurement or parameter value is, based on the data. In this Section, the Author will introduce the notation used throughout this field and then discuss how Probability Theory can be applied to parameter recovery.

5.1.1 Probability Laws and Notation

Probability is something that we use in our everyday lives: it appears implicitly in banking, insurance and even undisguised in the form of gambling websites. When you place a bet, there is a probability that you will win, there is also usually a larger probability that you will lose. The value assigned to each outcome is a measure of how likely the particular outcome is. The probability of an outcome (A) is usually written as $P(A)$.

Certainties are assigned the highest probability value, denoted as 1 or 100%. Unsurprisingly, the events which have no possibility of occurring are assigned values of 0. Uncertainties will correspond to a value between these limits, describing the *degree of belief* in the outcome. Within the probability framework of Bayesian Probability Theory, this definition is very important and denotes, in this case, how much you believe

that the proposition A is true. Note that by defining the degree of belief in the outcome of A being true, it also places a limit on the probability of A being false, denoted by $\overline{A}$. The total probability of any situation must always equal 1 and therefore,

$$P(A) + P(\overline{A}) = 1.$$

This is a requirement of Probability Theory known as the *Sum Rule*. It implies that if there are a number of different outcomes then the total probability will be split between each, based on its relative probability defined by the individual degree of belief in the occurrance of each outcome.

Conversely, if you define how much you believe in A and also in B *given* A, denoted $P(B|A)$, then you have also defined your degree of belief in both of the outcomes together,

$$P(A, B) = P(B|A)P(A).$$

In other words, the joint probability of A and B occurring is the product of the individual probability that A will occur and the probability that B will occur, given that A has already occurred. This is commonly known as the *Product Rule*.

If the probabilities relate to more than one parameter $P(A, B)$, the probability for a single outcome can be found by *marginalising* over the other parameters,

$$P(B) = \int_{-\infty}^{\infty} P(A, B) dA.$$

This process involves integrating over the probabilities related to the other parameters, to isolate the probabilities relevant to the outcome in question. In the above example, marginalisation flattens the two dimensional probability space into one dimension. Within signal analysis, marginalisation is often employed to remove *nuisance parameters*, variables that are present in the analysis that hold little information about the signal or are related to other sources other than those of primary interest. For example,

the raw signal could contain background noises or instrumentation parameters that are not particularly interesting compared to the sources themselves.

Note that this formalism assumes that the probabilities are described in terms of a continuum limit, where there is a continous distribution of outcomes, within a defined range. This would apply to situations such as recovering signal parameters from data. The exact value of physical variables could have any precision between the expected limits. This means that each must be considered and assigned a appropriate probability value. This *probability density function* can be described in terms of a mathematical distribution. If the distribution is normalised, the area under the curve (for a two dimensional distribution) is defined to be one. The shape of the normalised distribution describes the relative probabilities of each of the values.

Gaussian noise is noise that has a probability density function that conforms to the normal distribution. For the gaussian curve, the values that are in close proximity to the true value will be highly probable, with the true value having the highest probability. Note that the density function is not itself a probability; it only describes the relative distributions of the probability over a small range. The probability can be recovered from the pdf using,

$$P(A, b_1 \leq B \leq b_2) = \int_{b_1}^{b_2} \mathrm{pdf}(A, B) dB.$$

This relates to a situation where both A and B are true and that B lies within values b_1 and b_2.

5.1.2 Introduction to Bayes Theorem

In a similar manner to Frequentist Probability Theory[1], *Bayesian Probability Theory* (BPT) describes uncertainty in terms of mathematical distributions. However, in this case, the measurements of a random experiment are viewed as reflections of an underlying distribution, in contrast to the frequentist interpretation where the probability

[1]In Frequentist Probability Theory, the probability of an event occurring is described in terms of the limit of the relative frequency of a large number of trials.

of an event is defined in terms of the frequency of occurrance.

Due to the way in which Bayesian probabilities are assigned, the Theory directly encapulates the concept of learning. In this case, a probability is defined as the product of other probabilities that define the state of belief about different aspects of the situation.

BPT is commonly used in signal analysis as it provides a framework which can be used to quantitatively determine which of the possible theoretical models provides the best fit to the existing data. The Theory itself is neatly encapsulated by *Bayes' theorem*,

$$P(\text{hypothesis}|\text{data}, I) = \frac{P(\text{data}|\text{hypothesis}, I).P(\text{hypothesis}|I)}{P(\text{data}|I)}. \tag{5.1}$$

It comes from rearranging the Sum and Product Rules of Probability Theory, mentioned in the previous Section, and can be used to assign values to how likely your model is, given the existing data.

Each term in the above equation represents a probability related to the model and the data:

$$\begin{aligned} P(\text{hypothesis}|\text{data}, I) &= \left\{ \begin{array}{l} \text{Probability of the hypothesis, given the} \\ \text{data and the background information } I. \end{array} \right. \\ &= \text{Posterior Probability} \end{aligned}$$

$$\begin{aligned} P(\text{data}|\text{hypothesis}, I) &= \left\{ \begin{array}{l} \text{Probability of the data, given your model} \\ \text{and the background information } I. \end{array} \right. \\ &= \text{Likelihood function} \end{aligned}$$

$$\begin{aligned} P(\text{hypothesis}|I) &= \left\{ \begin{array}{l} \text{Probability of your hypothesis, in the} \\ \text{context of the background information } I. \end{array} \right. \\ &= \text{Prior Probability} \end{aligned}$$

$$P(\text{data}|I) = \begin{cases} \text{Probability of the data, in the context} \\ \text{of the background information } I. \end{cases}$$
$$= \text{Evidence}$$

Each of the terms is also given a formal name highlighting what it represents. For example, the probability that the model (hypothesis) is true, on the basis of the existing information, is called the *prior* as it describes the prior state of knowledge before the addition of the new information (data). The quantity of interest is termed the *posterior*, as it represents the state of knowledge once the new information has been included. The probability that the observations in the data were seen, based on your model, is termed the *likelihood*. Note that the likelihood itself is not a probability, it is a function that modifies the prior probability on the basis on the data. And finally, the probability of observing the data on the basis of the background information is called the *evidence*. This term is commonly described by a uniform distribution and, in this case, will not affect the shape of the related posterior distribution. Note that in many cases, the evidence term is not incorporated into the analysis and Bayes' theorem is re-defined in terms of a proportional relation rather than an equality [58].

Bayes Theorem provides the analysis framework for model selection and parameter estimation by relating the quantity of interest, the posterior, which is a measure of how likely the model is given the data, to terms that are easier to assign, namely the likelihood and the prior.

An important point to note is that in Bayesian Probability Theory the probabilities that you would assign to an particular event are dependent on your state of knowledge. If two people are presented with the same information they should assign the same probabilities but if one person is given additional information then the probabilities would differ from each other. See Appendix B for a detailed example of using Bayesian Probability Theory to determine the bias on a coin.

A word of caution though; if constraints are placed on the limits of the parameters and the true value is excluded, then the parameter estimates from the data mea-

surements will never be able to reflect the true value. Also, if you assign a highly constrained gaussian to an incorrect parameter value but the true value is still present in the parameter space, then you will need a large sample of data before the location of the maximum peak in the posterior coincides with the true value.

In summary, the values that are assigned for the probabilities are described in terms of mathematical distributions over a region in the parameter space. The shape and limits on the probabilities are dependant on individual knowledge about the event, encapsulated by the prior probability distribution. The posterior describes the probability of a particular outcome based on the measurements and any prior information and can be defined in terms of the likelihood and prior probability that are easier to assign.

5.2 Recovery of Information from LISA Signals

Each of the LISA data streams will, in principle, contain information from a number of gravitational wave sources and realisations of the different detector noises. The *source confusion* noise, discussed in Section 2.6, complicates the task of recovering the parameters from a single source. The TDI combinations further complicate the gravitational wave responses during the construction of new data streams that are free from the laser noise contributions. Each gravitational wave signal is described in terms of its signal parameters, related to the physical properties of the source. An expected signal can be expressed in terms of a *model template*, describing the realisation of the signal over the length of the data stream. Each model template is described in terms of particular values of the source parameters. The recovery of the signal can therefore be regarded as a multi-parameter estimation problem.

The task for the signal analysis is to correctly identify the model template that best-fits the data stream; in other words, the set of parameters that most accurately model the signal measurements. The definition of the best-fit model depends upon the method used to algebraically describe the goodness of fit. Using Bayesian Probability Theory, we can provide a quantative measure of the fit in terms of the relative posterior

probabilities of the signal parameters, based on the individual model templates.

5.2.1 Likelihoods

By thinking of Bayes theorem in vectorial form, it is easier to see how it can be used to infer parameter information from a large amount of data. Consider the case of a signal which is a simple sinusoid; the variables in the algebraic waveform and therefore, the possible searchable parameters are the amplitude, frequency and phase of the signal. Each parameter has an expected range of values corresponding to the prior constraints on each unknown. The limits on the parameters collectively define the size of the parameter space, which in the case of the sinusoid signal is three dimensional. The true parameter values will appear as a point in this space.

In order to recover an unknown sinusoidal signal, the observational data (D_k) are compared to noiseless data (F_k) created from model templates which are generated for particular values of the parameters (X) within the parameter space at discrete timestamps. If the model parameters exactly match the true signal parameters, then the ($D_k - F_k$) data stream only contains background noise signals. Therefore the best fit model can be identified by searching over the parameter space for the parameter values that correspond to model templates that will minimise the ($D_k - F_k$) data stream [58].

For example, for gaussian noise the likelihood function (L) takes the form,

$$L = \text{prob}(D|X,\sigma) = \prod_{k=1}^{N} \frac{1}{\sigma_k\sqrt{2\pi}} \exp\left(-\frac{(D_k - F_k)^2}{2\sigma_k^2}\right), \tag{5.2}$$

where σ is the standard deviation and σ^2 is the variance of the gaussian background noise. Note that, in many cases, the measurements are assumed to have the same underlying variance for the noise terms $\sigma_k = \sigma$ and hence, the likelihood expression can be simplified as,

$$L = \left(\frac{1}{\sigma\sqrt{2\pi}}\right)^N \exp\left(-\sum_{k=1}^{N} \frac{(D_k - F_k)^2}{2\sigma^2}\right),$$

where the $(D_k - F_k)/\sigma$ terms are the *normalised residuals* of the data, which provide a quantified measurement of how well the individual observations fit the expected results [58].

In this case, the likelihood expression assumes that the data measurements are independent and therefore that the *joint pdf probability*, $\text{prob}(D|X,\sigma)$ is the product of the probabilities of the individual measurements,

$$\text{prob}(D|X,\sigma) = \prod_{k=1}^{N} \text{prob}(D_k|X,\sigma).$$

In equation 5.2, the right hand expression containing the sum of the squares of the normalised residuals is termed the χ^2 relation,

$$\chi^2 = \sum_{k=1}^{N} \frac{(D_k - F_k)^2}{\sigma^2}. \tag{5.3}$$

Using this definition, the likelihood expression can be redefined simply as,

$$L = \frac{1}{(\sigma\sqrt{2\pi})^N} \exp\left(-\frac{\chi^2}{2}\right).$$

The likelihood describes the probability of obtaining the observations given a particular set of model data (F_k), corresponding to one evaluation of the model parameters (X). The likelihood is therefore a function of the parameters related to the models (i.e. $L(a,b)$ for unknown parameters a and b). For a simple gw signal composed of two sinusoids of unknown frequencies, the likelihood values can be plotted as a surface within a two dimensional frequency space. The most likely values of the parameters for the data can be recovered by finding the location of the maximal peak in the likelihood, in other words, where the *maximum likelihood* $(L_{\max})$ occurs.

5.2.2 Log-Likelihoods and Chi Squared

The *Log-Likelihood* ($\mathcal{L}$) of the likelihood expression for gaussian noise is defined as,

$$\begin{aligned} \mathcal{L} &= \ln(L) && (5.4)\\ &= \ln\left(\frac{1}{\sigma\sqrt{2\pi}}\right)^N - \left(\sum_{k=1}^{N}\frac{(D_k - F_k)^2}{2\sigma^2}\right) && (5.5)\\ &= N\ln\left(\frac{1}{\sigma\sqrt{2\pi}}\right) - \frac{\chi^2}{2} && (5.6) \end{aligned}$$

This form of the likelihood is very useful as it separates, into a simple linear sum, the expressions that are related to the data stream from the terms that are constant over the parameter space. We can see immediately that the maximum likelihood occurs for the parameter values that minimise the chi-squared relation, where

$$\mathcal{L}_{\max} = N\ln\left(\frac{1}{\sigma\sqrt{2\pi}}\right) - \frac{\chi^2_{\min}}{2}.$$

Note that the size of the chi-squared relation is directly related to the difference between the observations and the predicted model data. Note that the operation of the natural logarithm does not affect the shape of the parameter surface described by the likelihood expression and therefore the location of the maximum likelihood in L and $\mathcal{L}$ relates to the same parameter values for each unknown.

In this form, comparisons between the models can be drawn more easily as the constant term is the same in each case and therefore would cancel out in a direct comparison between two likelihoods with two different sets of parameters (i.e. comparing the residuals with $F_k(X)$ against those with $F_k(Y)$). Once the location of the maximal peak has been identified then the shape of the likelihood surface can be explored quantatively by evaluating,

$$\Delta\chi^2 = 2(\mathcal{L}_{\max} - \mathcal{L}) \quad (5.7)$$

This is an extremely useful measure as it describes the variations in the *goodness of fit*

for the models. In other words, the expression quantifies the change in how well each of the models fits the data with respect to the best fit model. The most likely model will correspond to the minimum, and hopefully zero, value of $\Delta\chi^2$ and a *maximum peak* in the corresponding likelihood plot.

5.2.3 Confidence Intervals

Finding the maximum likelihood value only returns a set of best fit parameters but it does not provide a measure of how well these values are constrained. It is therefore important to know not only the location of the maximum likelihood but the shape of the likelihood surface in its vicinity.

For the special case of a bivariate gaussian distribution, confidence intervals can be determined from the $\Delta\chi^2$ values, related to the shape of the probability curve [59, 60],

$$\begin{aligned} 1\sigma &= 2.3 \\ 2\sigma &= 6.17 \\ 3\sigma &= 11.8 \end{aligned} \tag{5.8}$$

The standard deviations values (σ) relate to the underlying volumes in the probability space; 1σ denoting the limits that contain approximately 68% of the probability density, while 3σ encloses 99.7%. In Bayesian probability theory, the maximum of the distribution is not as important as the location of the bulk of the probability, indicated by the regions of the confidence intervals.

An important point to note is that the evaluation of the likelihood and the best fit value that is recovered is dependent on the prior limits of the parameters and how well sampled the parameter space is. If the true value of a parameter is outside the prior range of the parameter or the space is poorly sampled, then the best fit values of that parameter might only correspond to a local maximum of the likelihood, rather than the overall best fit value for the data. On the other hand, oversampling the model parameter space is computer intensive and may not return an answer that is

substantially different from a smaller sample size. The trick is to find the optimal balance between these constraints, carefully choosing model limits and sample sizes.

5.3 Application of the Time Correlations to a Sinusoidal Signal

In a likelihood analysis, the signal parameters are estimated by identifying the model template that best fits the current data. The template waveforms take the form of the type of signal that you are expecting to recover from the data. They are characterised by a number of model parameters, each with a predefined range. The best fit template will therefore correspond to the best estimate for the true signal parameters. Within this framework, the effect of the time correlations in the TDI variables can be evaluated by comparing the recovery of the signal parameters from a source using two different types of model signal. In the first case, the presence of the time correlations in the observed signal is ignored while in the second case, the time correlations are taken into account.

To simplify the analysis, the gravitational wave source can be modelled, for example, as a simple signal composed of two sinusoids with defined frequencies (f_1,f_2),

$$\text{signal}(i) = A_1 \sin(2\pi f_1 t(i)) + A_2 \sin(2\pi f_2 t(i)).$$

Here the signal data stream is composed of N measurements, corresponding to observations at times $t(1)$ to $t(N)$. Using signals that can be easily determined will allow us to investigate the true effect of the covariances, isolated from any other problems with the data stream. The time correlations can be introduced through correlated noise terms constructed from one of the TDI combinations, chosen to be A in this case. Following the same procedures in the Section 4.4, the noise data streams for A are constructed from the individual noise data streams from the six optical benches. These are defined to be gaussian noise streams of length N, each with a mean of zero and a specified

variance (σ^2).

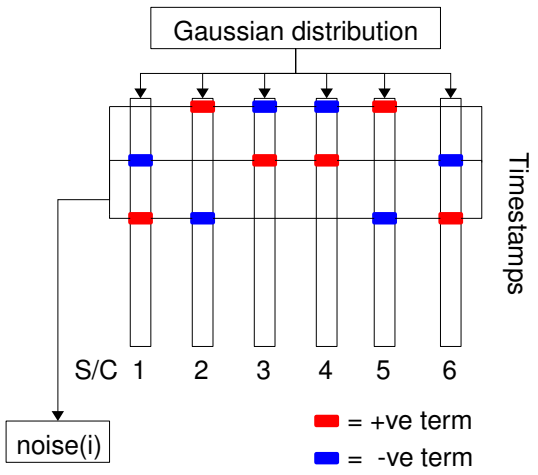

Figure 5.1: Flow diagram of the creation of the noise data stream for combination A, from the six optical bench data streams. The current time noise incorporates a number of noise realisations with different timestamp values and optical bench terms. The relevant terms are denoted by the red (+ve) and blue (-ve) boxes.

In this simplified example model, the signal produced by the model templates (data(i)) measured by LISA, is therefore

$$\text{data}(i) = A_1 \sin(2\pi f_1 t(i)) + A_2 \sin(2\pi f_2 t(i)) + \text{noise}(i), \tag{5.9}$$

where data(i) is defined for the same number of measurements as the noise signal (N), which we have specified as being spaced evenly in the time domain.

Following the method described in Section 5.2, estimates of the best fit model parameters can be inferred using Bayesian Probability theory. In this case there are two unknown parameters, corresponding to the frequencies of the sinusoidal signals. As the noise is gaussian, the likelihood expression can be written as

$$L(a,b) = \left(\frac{1}{\sigma\sqrt{2\pi}}\right)^N \exp\left[-\sum_{i=1}^{N} \frac{(\text{data}(i) - \text{model}(i,a,b))^2}{2\sigma^2}\right] \tag{5.10}$$

where σ is the standard deviation of the noise and $L(a,b)$ describes the likelihood function for a particular set of model parameters. For example, consider the case

where the model data, model(i, a, b), is described by a single data stream containing two sinusoidal signals calculated using equation 5.9 (for known signal amplitudes) and two frequency estimates for the unknown parameters (a, b). This type of signal is a simplification of the signals received from a binary object; two astrophysical bodies that are orbiting round one another and releasing gravitational waves. It could also be thought of as a small subset of the white dwarf binaries that are within our own galaxy; resolvable signals that are close in sky position and are releasing gravitational wave signals, modelled simply as two sinusoidal signals.

Note that for the sinusoidal signals, there are four unknown parameters; the frequency and amplitude of each source, but to simplify this specific example, the amplitudes of the signals are assumed to be known and therefore reducing the model to a two parameter problem.

In the model parameter space, the unknown frequencies have a defined range, determined from the known or predicted constraints on the true values. Note that the above form of the likelihood expression is only valid when the noise component of the signal is free from correlations (i.e. is independent). The total number of models is related to the sample number of each parameter in the frequency space. For example, if there are M_1 discrete possible values of the first sinusoid frequency and M_2 discrete estimates of the second frequency parameter, then the total number of models corresponds to the combined number of combinations of each parameter value. In other words, the total number of models, and hence the number of likelihood values is calculated by M_1 multiplied by M_2. Note that in this type of analysis, there are degenerate solutions in the likelihood, as there are no constrictions made on the properties of the signal components (e.g. that the frequency of a is larger than b), hence both the (a, b) and (b, a) solutions should be equally likely.

Covariance matrices in the Likelihood expression

The above likelihood expression can also be defined in terms of the *covariance matrix* (C) for the measurements,

$$L(a,b) = \frac{1}{(2\pi)^{\frac{N}{2}}|C|^{\frac{1}{2}}} \exp\left[-\frac{1}{2}\sum_{i=1}^{N} A(i,a,b)\right], \tag{5.11}$$

where,

$$A(i,a,b) = (\text{data}(i) - \text{model}(i,a,b))^T [C^{-1}](\text{data}(i) - \text{model}(i,a,b)).$$

The first and third factors in $A(i,a,b)$ are vectors defining the differences between the measured and predicted signals, while the superscript T describes the vector transpose, changing a row vector into a column vector, or vice versa.

The elements of the covariance matrix C_{ij} relate to the covariances between the different timestamps of the signal. For example, the element in the covariance matrix at row i and column j is σ_{ij}; the covariance between the signal measurement at times i and j. Note that for independent measurements, only the diagonal elements of the covariance matrix are non-zero, as there are no covariances between the time stamps of the signal.

Comparing equations 5.10 and 5.11, it can be seen that the individual variance terms in the first equation have been collectively defined in terms of the covariance matrix in the second expression. Note that the covariance matrix appears twice in the new form; the inverse covariance matrix replaces the individual variances in the χ^2 expression, while the standard deviations in the scale factor have been replaced collectively by the square root of the determinant of the covariance matrix. The *determinant* of a matrix is denoted by $\det C$ or $|C|$, which for a diagonal (or nearly diagonal) matrix will be (approximately) the product of the variances for each time stamp.

The time correlations in the TDI combinations of the LISA data stream relate directly to the non-zero covariance terms in the covariance matrix. Therefore, the above likelihood expression can be extended to samples that are correlated in time by adopt-

ing a covariance matrix with non-zero cross- and auto-covariance terms. The covariance matrix for the TDI expressions can be calculated using the method described in Section 4.4. Following the procedures discussed in Section 5.2.2, the effect of the time correlations can therefore be investigated by comparing the likelihood functions computed by adopting (incorrectly) a diagonal covariance matrix and also by incorporating the correct time correlated signal description. This will provide a quantitative indication of how the likelihood surface is modified by the inclusion of the time correlations, or in other words, how the surface is affected by ignoring the time correlations when they are present.

5.3.1 Amplitude Parameter Search

For a data stream containing two sinusoidal signals with unknown amplitudes ($A_1(a)$, $A_2(b)$), the model template can be defined as,

$$\text{model}(i, a, b) = A_1(a)\sin(2\pi f_1 t(i)) + A_2(b)\sin(2\pi f_2 t(i)). \tag{5.12}$$

Note that, as before, the model data stream is dependent on three variables; the time stamps (time(i)) of the measurements ($i = 1, N$), the model amplitudes ($A_1(a), A_2(b)$) which, following the same definitions as the previous example, are sampled at M_1 and M_2 values respectively. The frequencies of the individual sinusoidal waveforms are similarly defined to be f_1 and f_2.

In this case, the frequencies of the respective data stream components are assumed to be known and equivalent to the true frequencies of the signal ($f_i^{signal} = f_i^{model}$). The time dependent components of the model templates are well defined by the measurements and therefore the amplitude search has been reduced to evaluating two unknown scalars, equal to the amplitudes of the signal. The expected amplitude range corresponding to a detectable LISA signal is determined by the sensitivity of the antenna to the individual binaries and the signal-to-noise ratio for the data streams. In this simple example, the limits on the amplitude range can be defined using the predicted

sensitivities to be 1×10^{-22} and 1×10^{-20}, to allow optimal sampling across the amplitude range of the data stream signal containing the two sinusoids. As before, the total number of model templates relates to $M_1 \times M_2$ possible combinations of the unknown amplitude parameter values for the individual signal components.

Analysis

Similar to the previous Chapter, the LISA data stream is described in terms of a gravitational wave signal, taken in this case to be sinusoidal, and a noise term that is in turn defined by laser and optical bench noise contributions (See Section 2.3 for a detailed discussion of the noise terms). The laser noise contribution is assumed to have been removed for the data stream during the construction of the TDI combinations, and therefore the remaining noise contributions are a function of the optical bench dependent detector noise realisations. The noises are modelled as Gaussian distributions with specified variances (σ^2) and zero means.

The time dependent covariance matrix for the optimal TDI combination A can be investigated, for the illustrative case of a data stream containing two sinusoidal signals, by incorporating the properties of the model and the covariance matrix into the likelihood expression shown in equation 5.11. The analysis relating to the situation where the time correlations are unaccounted for in the model templates can be modelled using the same likelihood expression but with a diagonal covariance matrix with the same non-zero diagonal terms as the time correlated covariance matrix. This will ensure that the respective variances of the data streams are assigned the same values.

As mentioned in the previous Section, the best-fit model template can then be identified by determining the location of the minimum in the $\Delta\chi^2$ relation. In each case, the recovery of the individual sinusoidal signal amplitudes, determined from the confidence regions of the likelihood surface, can be computed using the $\Delta\chi^2$ surface, describing the relative changes in the χ^2 values.

Results

To accurately model the LISA data streams, the amplitude values and the model template frequencies were chosen with reference to the predicted limits from the signal sensitivities of LISA [17]. The armlengths of the antenna are measured in units of time, related to the discrete number of optical bench measurements taken during the light travel time down a single arm. In this case, this value is defined to be 15 time stamps and the LISA configuration is assumed to be static and stationary. Table 5.1 contains a detailed list of the parameter values used in this analysis. Note that the MATLAB code used for this analysis is provided in Appendix H.

Variable	Value
Amplitude (A_1)	2×10^{-21}
Amplitude (A_2)	8×10^{-21}
Arm Length	15
Frequency (f_1)	2×10^{-4}
Frequency (f_2)	5×10^{-4}
Length of data stream	1000
Model Amplitude Ranges	$[1 \times 10^{-22}, 1 \times 10^{-20}]$
Number of Models (M_1, M_2)	500, 500
Variance of Detector Noise	1×10^{-42}

Table 5.1: Quick Reference for true signal properties and analysis parameters for the amplitude search.

The resultant likelihood surfaces, shown in terms of $\Delta\chi^2$, can be seen in Figures 5.2. The features on the likelihood surface are represented as image plots, relating the size of the variations in $\Delta\chi^2$ to a colour scale shown in the figures. As the exact location of the minimum peak is difficult to determine from the slowly varying likelihood surfaces, two further image plots (Figures 5.3 and 5.4) describe the confidence intervals relating to the values shown in equation 5.8. Note that Figure 5.4 provides an enlarged view of the features shown in Figure 5.3 around the true parameter values of the signals.

It can be clearly seen that both confidence intervals are elliptical in shape reflecting positive correlation between the signal parameters. The inclusion of the time correlations to the analysis has resulted in a substantially smaller confidence interval, reflecting a tighter constraint on the minimal peak in the $\Delta\chi^2$ surface. The true parameters of the signal are contained within both confidence intervals and are located

within the first standard deviation (σ) of the mean with the independent covariance matrix. Due to the granularity of the confidence intervals relating to the discretised likelihood analysis with the time correlations, the corresponding interval contain the true values are harder to see, but are at least within the outer confidence region. This could be a reflection on the length of the data stream and the total number of model templates.

The recovery of the signal parameters by marginalising over the surface is shown in Figure 5.5. In this case, the features on the likelihood surface have been translated into a one dimensional plot by summing the likelihood values along each dimension of the surface in turn. For example, as there are two unknown parameters, the likelihood surface is two dimensional and therefore the line on the surface along a particular dimension relates a single value of one parameter to every model value of the other parameter. By summing over each parameter dimension in turn, the marginalisation plots allow the features of likelihood surface relating to changes in the other parameter value to be seen more clearly. Note that the marginalisation values have been normalised to facilitate the comparisons between the results.

From Figure 5.5 and with reference to the true signal parameters defined in Table 5.1, it can be clearly seen that the true values of the signal parameters have been recovered in each case, but as predicted from the shape of the confidence intervals, the proper inclusion of the time correlations in the covariance matrix leads to a significantly narrower constraint on the best-fit parameter values.

5.3.2 Frequency Parameter Search

Applying the above analysis to the more complex recovery of the frequency parameters from the data stream containing two sinusoidal signals, the model templates take the form,

$$\text{model}(i, a, b) = A_1 \sin(2\pi f(a)t(i)) + A_2 \sin(2\pi f(b)t(i)). \tag{5.13}$$

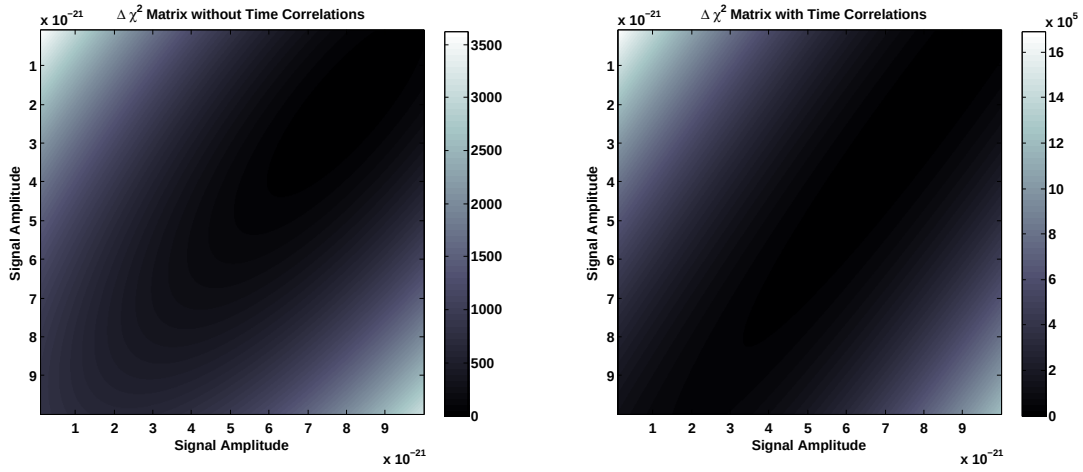

Figure 5.2: $\Delta\chi^2$ Surfaces for the Amplitude Parameter Search, for independent and time correlated covariance matrices.

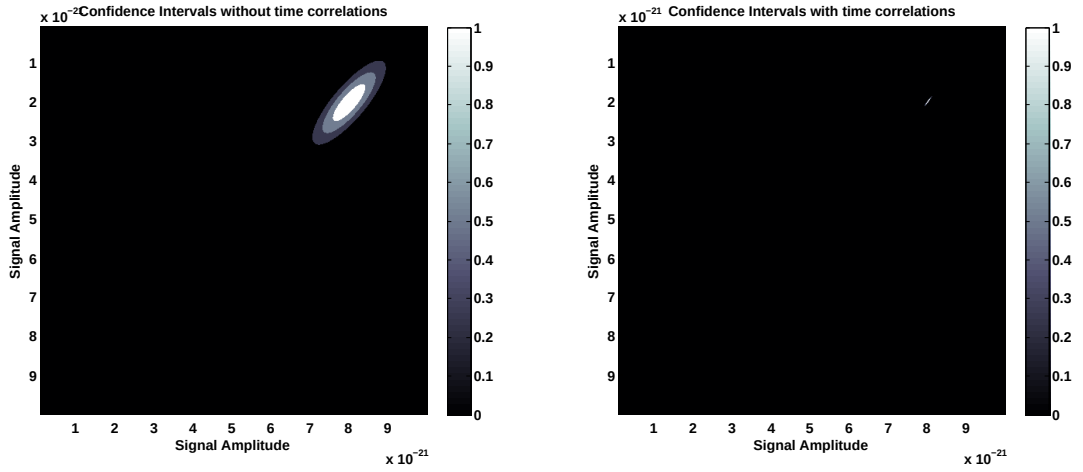

Figure 5.3: Plots of Confidence Intervals for the Amplitude Parameter Search, for independent and time correlated covariance matrices. The colour bands showing the areas enclosed by the $1\sigma, 2\sigma, 3\sigma$ confidence regions.

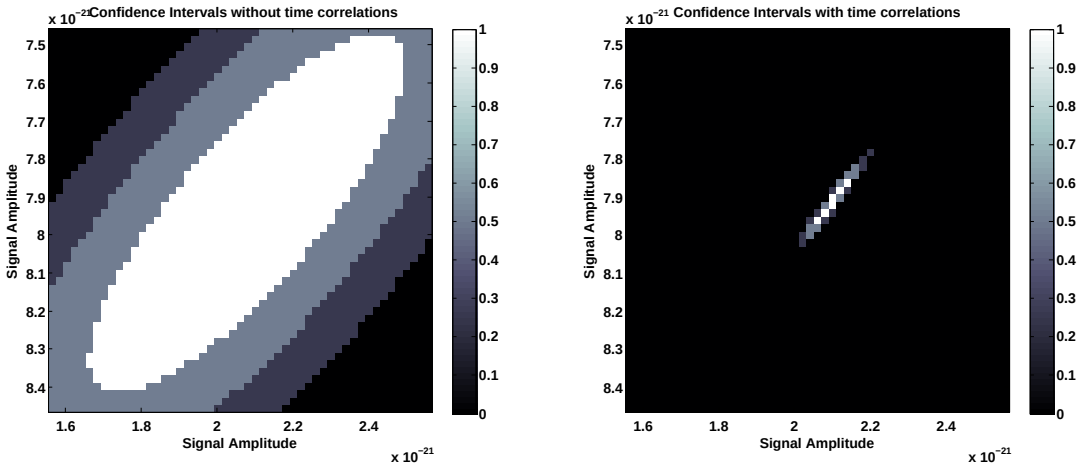

Figure 5.4: Plots of Confidence Intervals for the Amplitude Parameter Search, for independent and time correlated covariance matrices, around true values of Signal Parameters. The colour bands showing the areas enclosed by the $1\sigma, 2\sigma, 3\sigma$ confidence regions.

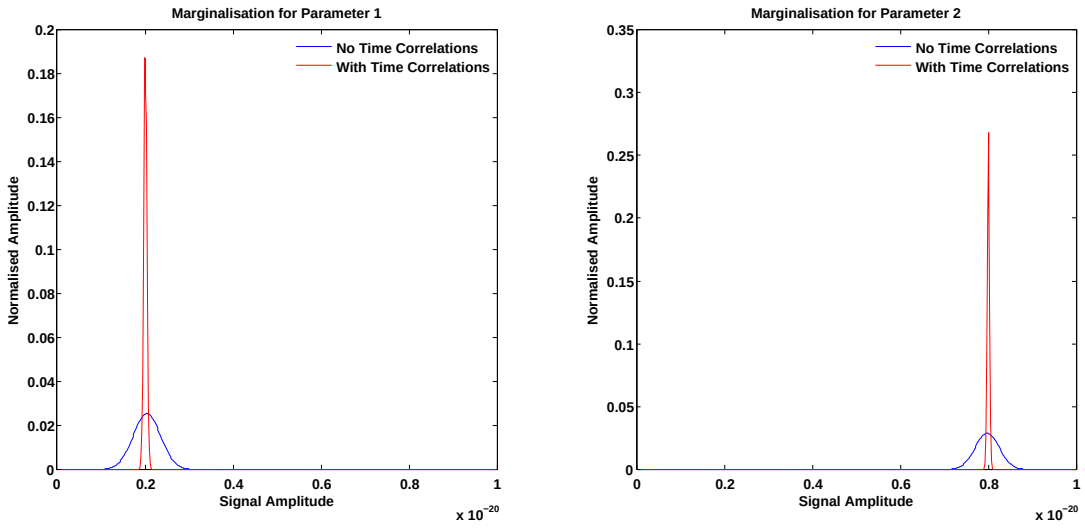

Figure 5.5: Marginalisation Plots for the Amplitude Search, for independent and time correlated covariance matrices, describing the recovery of the two unknown amplitude parameters.

where in this case, the amplitude parameters are known and therefore M_1 and M_2 denote the total number of discrete frequency values $(f(a), f(b))$ in each case. The frequency limits on a detected signal are determined by LISA's sensitivity. LISA will be able to detect gravitational wave sources once they reach a particular signal-to-noise ratio threshold. This threshold corresponds to a particular separation of the binary participants, in the case where the gravitational wave signals are emitted from an inspiralling binary. The limit will also place constrictions on the size, age and strength of the source. The upper limit is determined by the total number of measurements that LISA makes. In this simple toy example, the amplitude of the binaries and the frequency range can be assumed to be reasonably well known, perhaps due to additional information from the existence of an electromagnetic counterpart.

Results and Discussion

Following a similar analysis as discussed in the previous Example, a series of model templates were generated corresponding to the true values of the signal amplitude but with discrete model frequencies ranging between 1×10^{-3} and 5×10^{-3}. Each model template corresponds to a point in the two dimensional parameter space, relating to the intersection of two sampled values of the different model frequencies. The density of the points reflects the choice of the number of templates for each frequency (M_1, M_2). The sampled likelihood surface computed from the data stream for the model templates will therefore reflect the same density of points. Using the parameter values shown in Table 5.2 and the MATLAB code in Appendix H, the relative shape of the surface was investigated using the $\Delta\chi^2$ relation, and is presented here as image plots, shown in Figure 5.6. The relative amplitudes of the features are described by different colours, the related frequency values can be determined from the color bar.

In contrast to Figure 5.2, the surfaces show peaks relating to regions of sharply defined changes in $\Delta\chi^2$. Interestingly, both $\Delta\chi^2$ surfaces show similar features in the same locations. In other words, the surface structure, i.e. the location of the maximum and minimum peaks on both surfaces occur in the same regions of the parameter space.

Variable	Value
Amplitude (A_1)	1×10^{-21}
Amplitude (A_2)	1.1×10^{-21}
Arm Length	15
Frequency (f_1)	2×10^{-3}
Frequency (f_2)	4.5×10^{-3}
Length of data stream	1000
Model Frequency Ranges	$[1 \times 10^{-3}, 5 \times 10^{-3}$
Number of Models (M_1, M_2)	200,200
Variance of Detector Noise	1×10^{-42}

Table 5.2: Quick Reference for true signal properties for the Frequency Search.

Comparing the two plots in Figure 5.6 and using the information from the colour bars for each plot, it can be seen that although the structure of the surfaces is similar, the addition of the time correlations results in a sharper minimum peak in the $\Delta\chi^2$ surface at the location of the true parameter values. From Figure 5.7 and the enlarged version provided by Figure 5.8, the above conclusion can be corroborated by noting that the locations of the confidence intervals for the surface encompass the true frequency values. This means that with the inclusion of the time correlations, which account for similar realisations of the noise signal occuring at different timestamps, the predicted model signals in the region of the parameter space close to the true values show a larger change in the $\Delta\chi^2$ value. Hence by accurately modelling and accounting for the time correlations in the true signal, the model estimates of the signal are closer to the true values.

As previously mentioned, due to the structure of the likelihood analysis there is the possibility of degenerate peaks occurring on the surfaces. They correspond to the correct values of the frequencies but for the incorrect signal component. In other words, if the true frequencies relate to point (a, b) in the two dimensional space, there could be a similar minimal peak at (b, a). This type of feature can be seen in the left hand plot in Figure 5.7, corresponding to the likelihood analysis with the diagonal covariance matrix. In this case, the points in the parameter space corresponding to the degenerate combinations of the parameter values are computed to have similar likelihood values. The likelihood surface is therefore similar in structure about the

diagonal. In this situation, the information provided by comparing the signal and model data streams was not sufficient to remove the degeneracies. By contrast, the results with the time dependent covariance matrix only display a single peak. The addition of the time correlation information allows the likelihood analysis to distinguish between the degenerate peaks.

Figure 5.8 shows the structure of the minimal peaks in more detail. In both cases, the confidence intervals are spherical and place the true values of the signal parameters at the center of the confidence intervals. As expected from the results in Section 5.3.1, the confidence intervals describing the recovery with the addition of the time correlations are much narrower, reflecting a sharper defined peak in the likelihood.

From the normalised marginalisation plots shown in Figure 5.9, it can be seen that the true values of the signal parameters are recovered in both cases but as before, the inclusion of the time correlations results in a narrower peak, related to a tighter constraint on the parameter values.

5.3.3 Comparable Frequency Parameter Search

In the above examples, the unknown signal parameters were specially chosen to be clearly defined and separate in the parameter space. This allowed the parameter recovery to be easily computed with a reasonable number of signal measurements and parameter sample sizes. By incorporating the time correlations into the likelihood analysis, the above results for the recovery of the unknown frequency parameters show tighter constraints on the parameter values. The ability to recover the signals with a narrower peak in the parameter space could be extremely useful when determining signal parameters that are close in frequency. In other words, does the inclusion of the time correlations into the model analysis allow the recovery of frequency parameters that are unable to be determined using the independent model?

In order to investigate the recovery of two signals that are close in frequency space, the analysis discussed in the previous Section was repeated but for signals that are much closer in the parameter space.

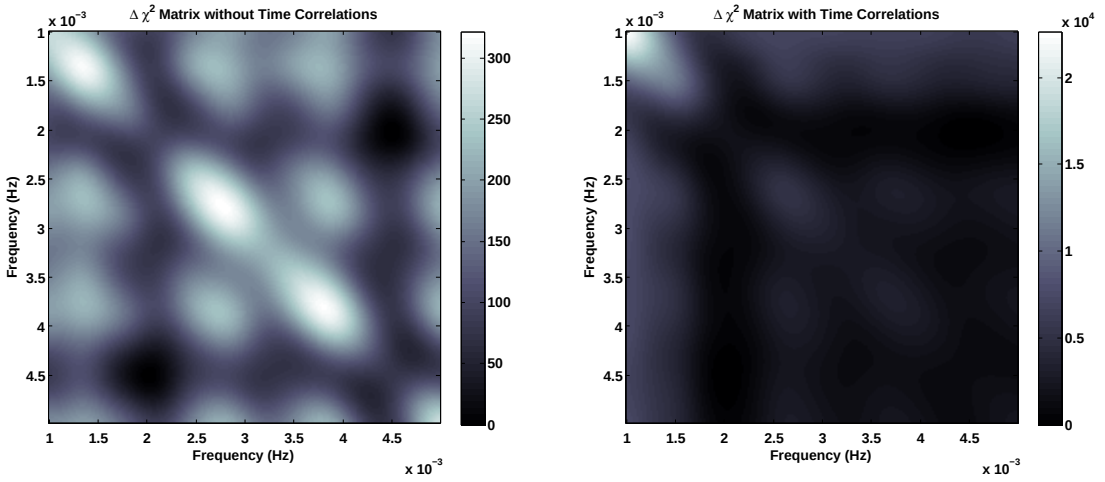

Figure 5.6: $\Delta\chi^2$ Matrices for the Frequency Parameter Search, for independent and time correlated covariance matrices.

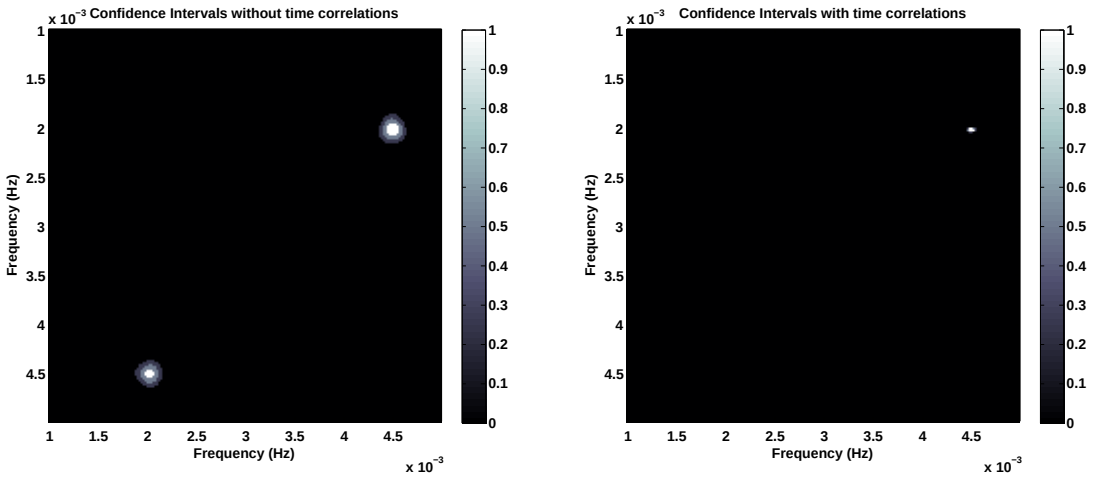

Figure 5.7: Confidence Invervals Plots for the Frequency Parameter Search, for independent and time correlated covariance matrices. The colour bands showing the areas enclosed by the $1\sigma, 2\sigma, 3\sigma$ confidence regions.

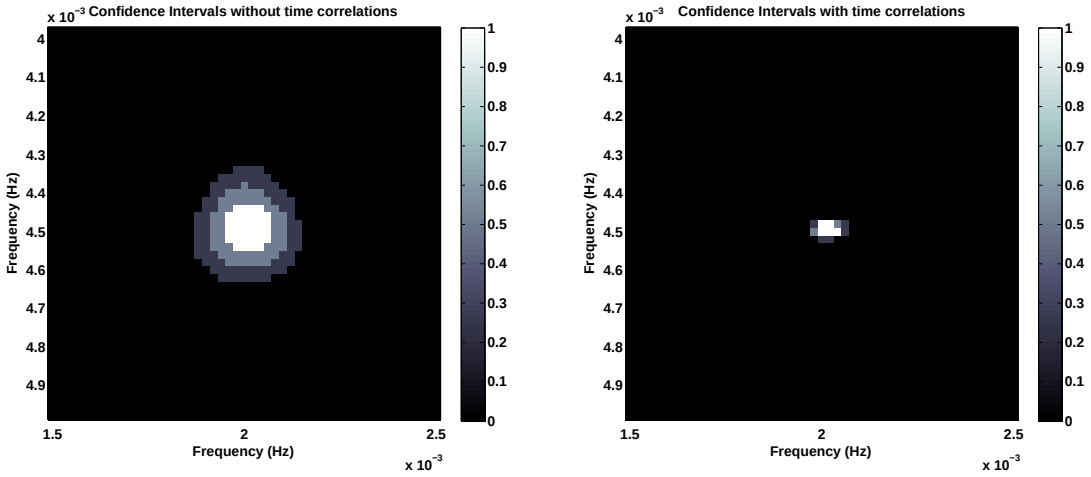

Figure 5.8: Confidence Interval plots for the Frequency Parameter Search, for independent and time correlated covariance matrices, around the true values of the signal parameters (2×10^{-3}Hz, 4.5×10^{-3}Hz). The colour bands showing the areas enclosed by the $1\sigma, 2\sigma, 3\sigma$ confidence regions.

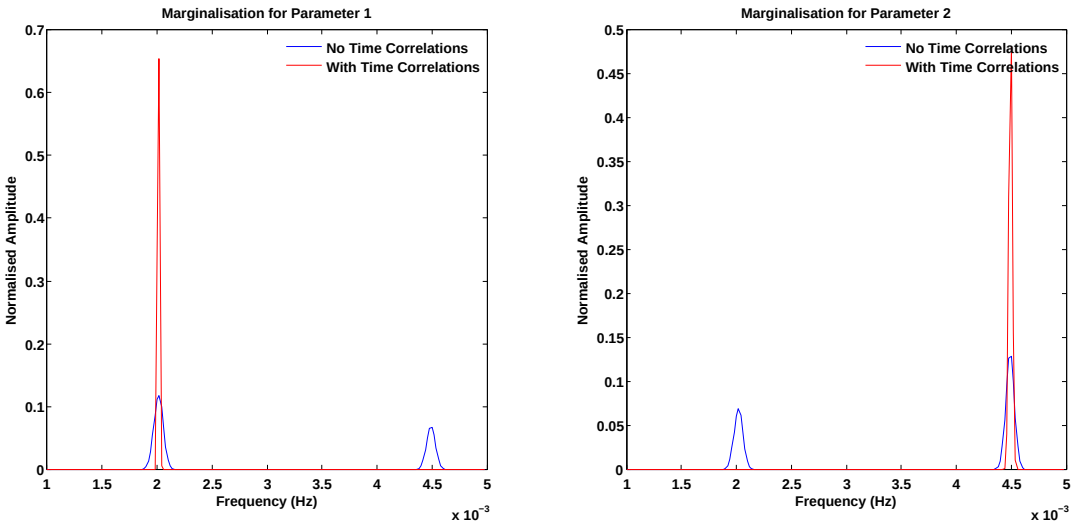

Figure 5.9: Marginalisation Plots for the Frequency Parameter Search, for independent and time correlated covariance matrices, describing the recovery of the two unknown frequency parameters. The true values of the frequency parameters are 2×10^{-3}Hz and 4.5×10^{-3}Hz.

Variable	Value
Amplitude (A_1)	1×10^{-21}
Amplitude (A_2)	1.1×10^{-21}
Arm Length	15
Frequency (f_1)	2×10^{-3}
Frequency (f_2)	2.01×10^{-3}
Length of data stream	1000
Model Frequency Ranges	$[1 \times 10^{-3}, 5 \times 10^{-3}]$
Number of Models (M_1, M_2)	400, 400
Variance of Detector Noise	1×10^{-42}

Table 5.3: Quick Reference for true signal properties for the Comparable Frequency Search.

The results of the analysis for the $\Delta\chi^2$ surface are shown in Figure 5.10, using the same model template as the previous example but for the ranges of values shown in Table 5.3. In this case, the frequency values are only separated by a difference of 1×10^{-5} in the parameter space.

Figures 5.11 and 5.12 relate the features in the $\Delta\chi^2$ plot to volumes in the probability spaces, describing the confidence intervals for the parameter recovery. The true structure of the intervals can be seen more clearly in Figure 5.12. From these plots, we can see that the confidence intervals in each case have overlapped, creating a single elongated confidence interval. The shape of the confidence intervals reflect the difficulties in recovering signals that are close in the parameter space, without densely sampling over the range.

The recovery of the individual parameters can be seen more clearly in Figure 5.13, relating to the marginalisation plots over the $\Delta\chi^2$ space. The analysis using the independent covariance matrix (denoted by the blue curve) fails to recover the two distinct parameter values. This is the expected behaviour due to the frequency resolution of the signal and the relative signal-to-noise ratio. From the Figure, it can be seen that the analysis with the time correlation fully accounted for was also unable to recover the correct values for each of the signal parameters but, interestingly, was capable of identifying that there was two signals present. Unfortunately the confidence intervals around the recovered values do not contain the true values of the signal parameters in each case. In other words, although the analysis with the time correlations provides

tighter constraints, in this example with low signal-to-noise, the independent analysis provides a better estimate for the signal parameters as although the parameter ranges are wider, they encompass the true values of the unknown parameters.

5.4 Investigation of the Correlation term in the Likelihood Expression

The analysis of the previous Section illustrated that the inclusion of the time correlations present in the data stream of the optimal TDI combination A, resulted in a narrower peak in the parameter recovery for a simple model of a signal containing two sinusoids. The marginalisation results show tighter constraints on the estimates for the signal parameters. In this Section, the Author will investigate this result further and seek to understand the origin of the improved parameter recovery, by analysing explicitly in terms of the individual covariances, the effect of the correlation term on the χ^2 relation for a specific simplified example.

Consider the simple example where the model contains a single parameter value (a) and the data stream is only composed of two data measurements ($t = 1, 2$). The noise realisations, given by the difference between the model and the measurements can, therefore, be described as,

$$\begin{aligned} J &= \text{data}(1) - \text{model}(1, a) \\ K &= \text{data}(2) - \text{model}(2, a) \end{aligned}$$

where the noise values are assumed to be drawn from Gaussian distributions with zero means and variances σ_1^2 and σ_2^2 respectively. The covariance matrix for the two correlated measurements is, therefore,

$$C = \begin{bmatrix} \sigma_1^2 & \sigma_{12}^2 \\ \sigma_{12}^2 & \sigma_2^2 \end{bmatrix}$$

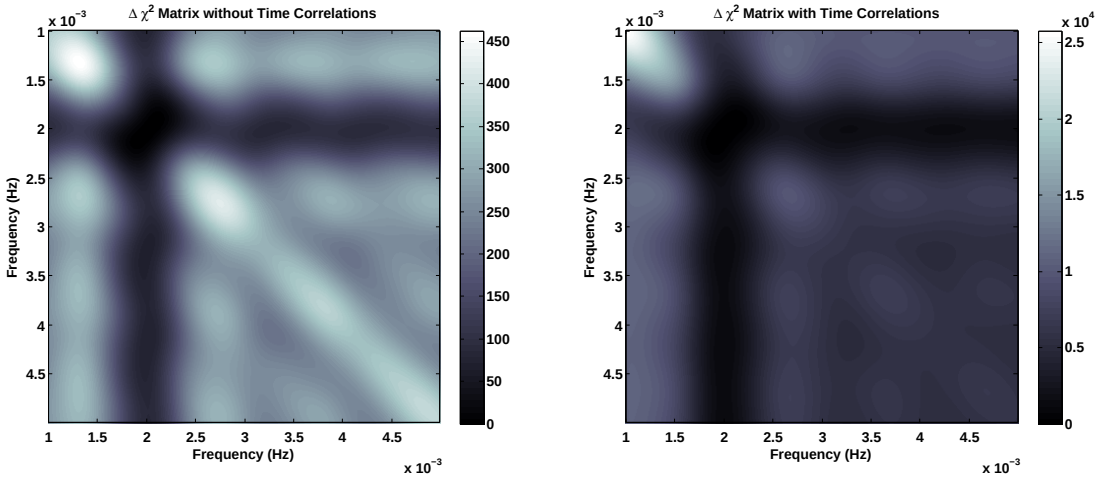

Figure 5.10: $\Delta\chi^2$ Surfaces for the Comparable Frequency Parameter Search, for independent and time correlated covariance matrices.

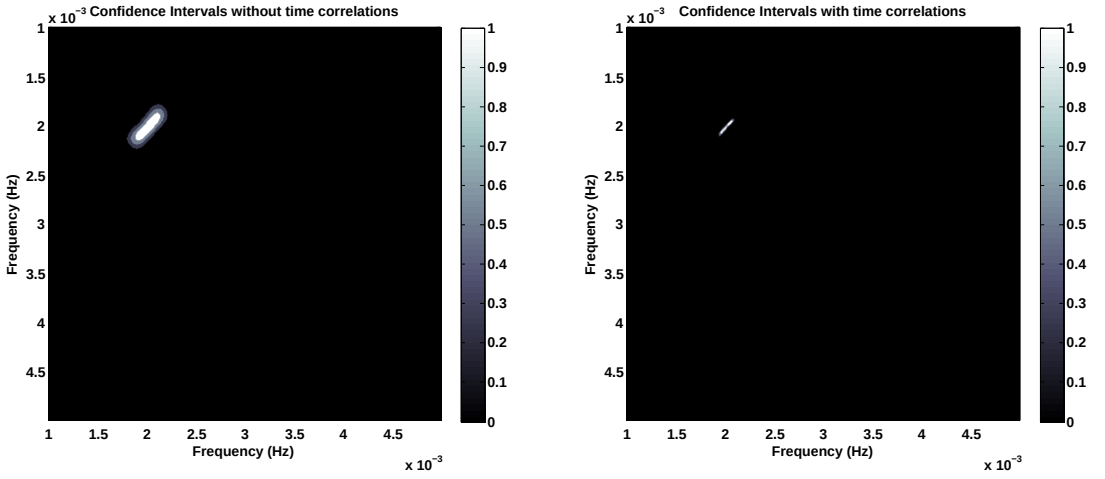

Figure 5.11: Confidence Invervals Plots for the Comparable Frequency Parameter Search, for independent and time correlated covariance matrices.

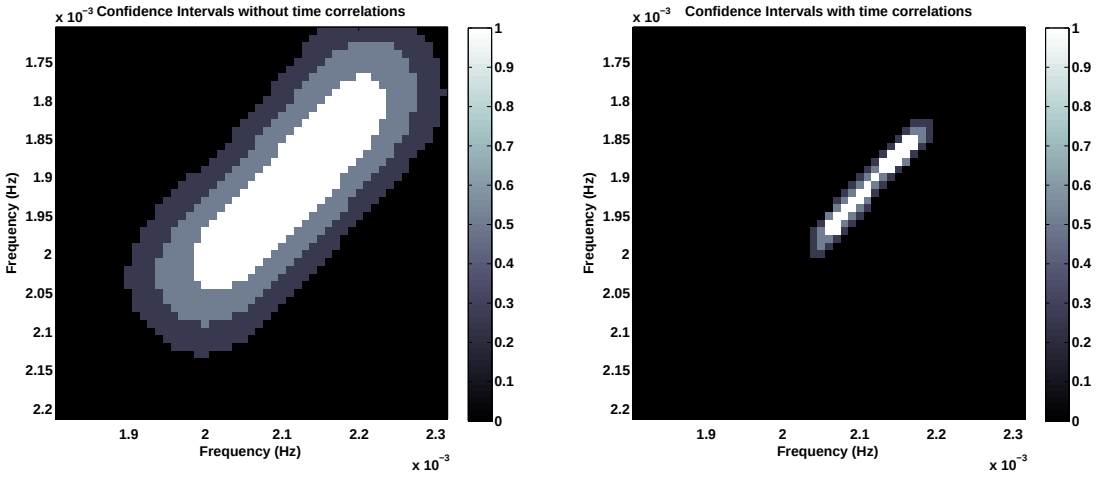

Figure 5.12: Confidence Interval plots for the Comparable Frequency Parameter Search, for independent and time correlated covariance matrices, which encompass the true values of the Signal Parameters (2×10^{-3}Hz, 2.01×10^{-3}Hz).

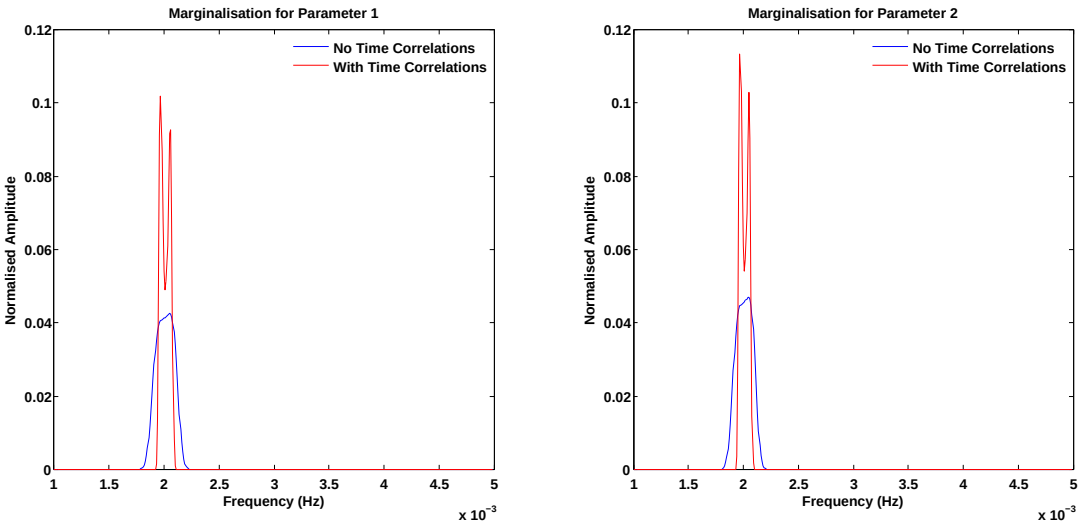

Figure 5.13: Marginalisation Plots for the Comparable Frequency Parameter Search, for independent and time correlated covariance matrices, describing the recovery of the two unknown frequency parameters. The frequency parameters of the true signal are 2×10^{-3}Hz and 2.01×10^{-3}Hz.

where σ_{12}^2 is the covariance between the measurement values. The inverse of the covariance matrix (C^{-1}) is defined as [61],

$$C^{-1} = \frac{1}{\sigma_1^2\sigma_2^2 - (\sigma_{12}^2)^2} \begin{bmatrix} \sigma_2^2 & -\sigma_{12}^2 \\ -\sigma_{12}^2 & \sigma_1^2 \end{bmatrix}.$$

The likelihood expression for the unknown parameter a is,

$$L(a) = \frac{1}{(2\pi)^{\frac{N}{2}}|C|^{\frac{1}{2}}} \exp\left[-\frac{1}{2}\chi^2(a)\right], \tag{5.14}$$

Expanding the χ^2 section of the likelihood expression explicitly,

$$\begin{aligned}
\chi^2(a) &= \sum_{i=1}^{2}(\text{data}(i) - \text{model}(i,a))^T[C^{-1}](\text{data}(i) - \text{model}(i,a)) \\
&= \begin{bmatrix} J & K \end{bmatrix} \left(\frac{1}{\sigma_1^2\sigma_2^2 - (\sigma_{12}^2)^2} \begin{bmatrix} \sigma_2^2 & -\sigma_{12}^2 \\ -\sigma_{12}^2 & \sigma_1^2 \end{bmatrix} \right) \begin{bmatrix} J \\ K \end{bmatrix} \\
&= \frac{1}{\sigma_1^2\sigma_2^2 - (\sigma_{12}^2)^2} \begin{bmatrix} J & K \end{bmatrix} \begin{bmatrix} \sigma_2^2 & -\sigma_{12}^2 \\ -\sigma_{12}^2 & \sigma_1^2 \end{bmatrix} \begin{bmatrix} J \\ K \end{bmatrix} \\
&= \frac{1}{\sigma_1^2\sigma_2^2 - (\sigma_{12}^2)^2} \begin{bmatrix} J\sigma_2^2 - K\sigma_{12}^2 & -J\sigma_{12}^2 - K\sigma_1^2 \end{bmatrix} \begin{bmatrix} J \\ K \end{bmatrix} \\
&= \frac{1}{\sigma_1^2\sigma_2^2 - (\sigma_{12}^2)^2} \left[J(J\sigma_2^2 - K\sigma_{12}^2) + K(-J\sigma_{12}^2 - K\sigma_1^2)\right] \\
&= \frac{1}{\sigma_1^2\sigma_2^2 - (\sigma_{12}^2)^2} \left[J^2\sigma_2^2 - 2JK\sigma_{12}^2 + K^2\sigma_1^2\right]
\end{aligned}$$

Note that the correlation coefficient is defined as $\rho = \frac{\sigma_{12}^2}{\sigma_1\sigma_2}$ and therefore the covariance of the measurements can be defined in terms of the individual standard deviations and the correlation coefficient, $\sigma_{12}^2 = \sigma_1\sigma_2\rho$. Substituting this into the above expression

gives,

$$\begin{aligned}\chi^2(a) &= \frac{1}{\sigma_1^2\sigma_2^2 - \sigma_1^2\sigma_2^2\rho^2}\left[J^2\sigma_2^2 - 2JK\sigma_1\sigma_2\rho + K^2\sigma_1^2\right] \\ &= \frac{1}{\sigma_1^2\sigma_2^2(1-\rho^2)}\left[J^2\sigma_2^2 - 2JK\sigma_1\sigma_2\rho + K^2\sigma_1^2\right] \\ &= \frac{1}{(1-\rho^2)}\left[\frac{J^2}{\sigma_1^2} + \frac{K^2}{\sigma_2^2} - \frac{2JK\rho}{\sigma_1\sigma_2}\right]. \end{aligned} \tag{5.15}$$

From the result of this expression, it can be clearly seen that the correlation coefficient ρ appears twice in the χ^2 relation - once in squared form and once on its own. The presence of time correlations in the model data streams are therefore able to directly influence the shape of likelihood surface. The sign and strength of the correlations in the data stream will affect the covariance terms, due to the presence of the unsquared ρ.

Applying the χ^2 expression containing the correlation terms to the likelihood expression shown in Equation 5.14, gives,

$$L(a) = \frac{1}{(2\pi)^{\frac{N}{2}}|C|^{\frac{1}{2}}}\exp\left[-\frac{1}{2}\frac{1}{(1-\rho^2)}\left[\frac{J^2}{\sigma_1^2} + \frac{K^2}{\sigma_2^2} - \frac{2JK\rho}{\sigma_1\sigma_2}\right]\right]. \tag{5.16}$$

And hence by taking the natural log of both sides of the above expression, the log likelihood relation is therefore,

$$\mathcal{L}(a) = \ln\frac{1}{(2\pi)^{\frac{N}{2}}|C|^{\frac{1}{2}}} - \frac{1}{2(1-\rho^2)}\left[\frac{J^2}{\sigma_1^2} + \frac{K^2}{\sigma_2^2} - \frac{2JK\rho}{\sigma_1\sigma_2}\right]. \tag{5.17}$$

From these results, it can clearly be seen that the inclusion of the correlation terms into the analysis directly affects the χ^2 part of the likelihood expression.

Note that if the correlation term ρ is zero, the more complex χ^2 expression, shown in Equation 5.15, reduces to the simple expression where the data measurements are independent from each other,

$$\chi^2_{ind}(a) = \frac{J^2}{\sigma_1^2} + \frac{K^2}{\sigma_2^2}$$

This is consistent with the results from the above procedure applied to an initially independent (diagonal) covariance matrix.

In summary, the above analysis has traced the effect of the non-zero covariance terms for the simple example where there are only two data measurements. The correlation between the measurements leads to correlation terms appearing as a scale factor on the normalised residuals (the $1-\rho^2$ term) and on the cross terms of the residuals themselves.

5.4.1 Simple Example

The overall effect of including or excluding the correlations can be investigated qualitatively by considering the simple example where the data values are drawn from the same distribution ($\sigma^2 = \sigma_1^2 = \sigma_2^2$) and are randomly identical, in other words, $J = K$ and hence,

$$J = (\text{data}(1) - \text{model}(1)) = (\text{data}(2) - \text{model}(2)).$$

The covariance between each of the data values is therefore $\sigma_{12}^2 = \sigma^2\rho$. Substituting these results into equation 5.15, simplifies the expression to

$$\begin{aligned}
\chi^2(a,b) &= \frac{1}{(1-\rho^2)}\left[\frac{2J^2}{\sigma^2} - \frac{2J^2\rho}{\sigma^2}\right] \\
&= \frac{1}{(1-\rho)(1+\rho)}\left[\frac{2J^2}{\sigma^2}(1-\rho)\right] \\
&= \frac{2J^2}{\sigma^2(1+\rho)},
\end{aligned}$$

and for the log-likelihood expression,

$$\begin{aligned}
\mathcal{L}(a) &= \ln\frac{1}{(2\pi)^{\frac{N}{2}}|C|^{\frac{1}{2}}} - \frac{1}{2(1-\rho^2)}\left[\frac{2J^2}{\sigma^2} - \frac{2J^2\rho}{\sigma^2}\right] \\
&= \ln\frac{1}{(2\pi)^{\frac{N}{2}}|C|^{\frac{1}{2}}} - \frac{J^2}{\sigma^2(1+\rho)}
\end{aligned}$$

Note that the first term on the right hand side of the above expression is not dependent on the individual data stream terms (i.e. $J(i)$) and will therefore be constant for each

measurement value.

Comparing the above expression to the more general log-likelihood relation shown in Equation 5.17, the squared correlation term on the normalised residual has cancelled out, by virtue of the two noise measurements having identically equal realisations of the same noise distribution. The remaining correlation term appears on the denominator of the χ^2 expression. Note that if the data measurements are highly correlated together ($\rho = 1$), the presence of the correlation term will increase the size of the denominator. If the data terms are highly correlated with each other but with an inverse relationship, termed *anti-correlated* ($\rho = -1$), the presence of the correlation term will have maximum effect, reducing the entire denominator to zero.

5.4.2 Discussion

The discussion in the above Section investigates the effect of non-zero covariance terms on the likelihood analysis. Analytically, the presence of the non-zero off-diagonal terms appear as correlation terms in the likelihood expression. The size of the normalised residuals will be affected by the size of the covariances between the signal measurements. As a consequence, the non-zero correlation term could also influence the size of the $\Delta\chi^2$ values, which describe the variations in the structure of the likelihood surface. Due to this, the size of the correlation terms will directly influence the features in the confidence intervals and marginalisation plots.

The important point to remember about the analysis in each case is that the individual optical bench data streams in the examples are identically equal. The time correlations are always present due to the construction of the TDI variables. The differences in the results for the independent and time correlated model signals come from the variations in the analysis; the absence or presence of the time correlations in the covariance matrix used in our expression for the likelihood.

In order to properly understand the overall effect of the correlation term, the Author will first discuss the implications of each occurrence individually, with respect to the χ^2 and $\Delta\chi^2$ relations and then as an overall effect, combining the individual effects

and investigating the influence the non-zero correlation terms will have on the results of the likelihood analysis.

Correlation in the Covariance terms

From the analysis of the previous Section, the presence of non-zero correlation terms was identified in the expression for the normalised residuals.

Consider the structure of the log-likelihood,

$$\mathcal{L}(a) = \text{constant} - \frac{1}{2}\chi^2.$$

As the first term in the log-likelihood is a constant, any changes in the χ^2 expression will directly affect the size of the log-likelihood expression.

If the data streams are not independent, then the χ^2 part of the likelihood description contains a non-zero $\frac{-2JK\rho}{\sigma_1\sigma_2}$ term, describing the covariances between the data values. The overall sign of this term is directly described by the type of correlation present.

For the simple case where the data streams are identical ($J = K$) and have the same variances ($\sigma_1^2 = \sigma_2^2 = \sigma^2$), if the correlation is highly positive, the χ^2 expression without the scale factors becomes,

$$\frac{J^2}{\sigma_1^2} + \frac{K^2}{\sigma_2^2} - \frac{2JK}{\sigma_1\sigma_2} \simeq 0.$$

In other words if the data streams values are approximately equal and the noise variances are equivalent then if the data measurements are highly positively correlated with each other ($\rho = 1$), the above expression will be close to zero.

Similarly, if the data streams are equal to each other but with opposing signs ($J = -K$) and they are highly anti-correlated ($\rho = -1$), the unscaled χ^2 expression will also be equal to zero, as the cross terms will be equal and opposite to the first two terms.

Note that in all other cases, when the individual data streams are not identically

equal, the cross term contribution will have less influence on the resultant size of the χ^2 expression.

Note that for a sinusoidal signal, there will be a number of occasions where the current timestamp value is similar to the values at other timestamps, due to the shape of the wave. Also as the noise streams for the TDI combinations are constructed from different timeshifted noise realisations, it is plausible that the noise data streams at a particular timestamp are approximately equal to a later timestamp.

Correlation as a Scale Factor on the Normalised Residuals

The results from the above examples have shown that the inclusion of the non-zero covariance terms in the likelihood analysis, will result in a χ^2 expression that includes a scale factor containing a correlation term ($\frac{1}{1-\rho^2}$). As the correlation term is squared, the scale factor expression will therefore be sensitive to the overall magnitude of the correlation.

Hence, if the correlations are highly positive or negative ($\rho \simeq -1, 1$), the scale factor will reduce to approximately zero on the denominator and will therefore dramatically increase the size of the χ^2 term.

Note that in the absence of non-zero covariances, the correlation term is zero, resulting in a scale factor of 1 and simplifying the likelihood expression to the independent case.

Overall effect of the Correlation term

The overall effect of the presence of the non-zero correlation terms in the likelihood analysis can be investigated, as previously discussed, by combining the individual effects on the χ^2 and $\Delta\chi^2$ relations.

If the data stream terms are highly correlated, either positively or negatively, then the scale factor term on the normalised residuals will be very large. Note that in the cases where the data streams are identically equal (or equal with opposing signs) the χ^2 expression reduces to zero and therefore the additional scaling effect of the scale factor

correlation term will have no effect. Note that in this case, the likelihood expression would be at a maximum.

From the results discussed in the previous Section, it is easy to see that the presence of a non-zero correlation term will directly affect the size of the χ^2 value, especially when the model template signals is close to the true signal. This will occur when the model parameter values are close to the true parameter values, but also when the time correlations are taken into account. As discussed in previous Sections, by accounting for the time correlations in the signals, the model templates are able to provide a better fit to the true signal data. This is in comparison to the model templates with the true signal parameter alone. The reappearance of identical equal noise realisations for the TDI combination A, results in covariances between the measurements that should be accounted for.

Note that if the size of the covariances between the measurements are relatively small compared to the variances, then the presence of the non-zero correlation terms will have the largest effect when the model template parameters are close to the true values. In this case, the difference between the data stream values is reduced and hence the effect of the correlation terms can be most clearly seen.

In summary, the linear correlation term will affect the amplitude of the likelihood values, while the squared correlation term scales the entire χ^2 relation and is dependant on the strength of the correlation. Therefore, the presence of a non-zero correlation term will influence the size of the χ^2 value. In other words, if the correlation of the data streams is constant with time, the presence of the correlation term will increase the value of the χ^2 term across the surface. If the correlation is time stamp dependent, then the size of the increase will depend on the individual data stream terms.

The implications of the correlation term for the $\Delta\chi^2$ values will therefore be dependant on the type of structure present in the likelihood surface. For example, for a maximal peak, the scale factor will multiply each of the points by the same amount, increasing the overall difference between them. In other words, the application of a scale factor to every result will increase the gradient ($\Delta\chi^2$) between them. The presence of

the correlation terms will also increase the $\Delta\chi^2$ values. In terms of the marginalisation plots, this effect will narrow the recovery peak with respect to an independant result. This result can be clearly seen in Figures 5.9 and 5.13.

Chapter 6

Possible Correlations in the MLDC LISA Data Stream

In the previous Chapters, the possibility of the LISA data streams being correlated with time has been investigated and the resultant effect on the recovery of signal parameters has been highlighted using toy model problems. The presence of the identical equal combination terms in the LISA data stream is the direct result of the time shifts applied to the individual optical bench measurements. It is therefore possible that the current LISA data sets that are used to test the viability and success of the current data analysis approaches could contain the time correlation terms. The presence of these terms in the data would invalidate any assumptions that the TDI combination data streams were uncorrelated at any given time stamp. Note that the A, E and T combinations are commonly used in Markov Chain Monte Carlo parameter search algorithms, as it is assumed that the combination data streams will be uncorrelated with time [49].

In the absence of live LISA data, the current data analysis approaches are currently being tested as part of a global data analysis effort, termed the Mock LISA Data Challenges (MLDC). In this final Chapter, the Author will briefly describe the background to the MLDC and using one of the data sets provided for the Challenges, investigate whether time correlations are observable for more realistic models of LISA data.

6.1 Mock LISA Data Challenges

At a meeting of the LISA International Science Team (LIST) in December 2005, the decision to organise a number of *Mock Data Challenges* was put into action. The Challenges would provide a focus for the development of LISA data analysis tools and foster collaborations within the international gravitational wave community. The results of the Challenges would demonstrate the technical readiness to recover valuable gravitational wave information from the complex LISA data stream.

The Mock LISA Data Challenge Taskforce was charged with the daunting task of designing the challenge problems and determining the criteria for the evaluation of the analysis. In other words, defining the benchmarks for the success or failure of the analysis methods and enabling comparisons to be drawn between them. The Challenges are designed to be blind tests, increasing in complexity with each new Round and defined to be challenges rather than direct contests to encourage collaborations [45, 57].

To assist the competitors, the Taskforce were also tasked with standardising the models of the LISA spacecraft and orbits, and providing generalised definitions of the waveforms for the gravitational wave sources. In other words, to enable direct comparisons between the results of the Challenges, the current LISA description was clarified in terms of the literature [62].

The structure of the LISA analysis can be defined in two distinct parts; first the simulation of the expected LISA data stream and then the analysis of the problem and the recovery of the gravitational wave source parameters. To faciliate the first part of the analysis, the Taskforce provided the Data Challenges in the form of TDI combination data streams, ulitising the two existing computational LISA data stream generators; Synthetic LISA created by Michelle Vallisneri [48] and LISA Simulator created by Neil Cornish and Louis Rubbo [53, 38].

To date, there have been three distinct rounds of Challenges, the challenge sets initially released approximately six months apart. The first Challenge set, released in July 2006, contained X, Y, Z data streams composed of noise contributions and either

a single gravitational wave signal or a small number of non overlapping multiple signals with unknown parameters [45]. The LISA data streams were defined in terms of the TDI 1.5 observables, corresponding to a static, orbiting array with armlengths equivalent to 5×10^6km or approximately 16.6 seconds. The optical bench measurements are constructed without laser noise contributions to ensure the absence of the terms in the data streams [63]. The signal classes were restricted to Galactic stellar-mass binaries and massive black hole (MBH) binary inspirals. The noises on each optical bench were defined to be Gaussian and stationary with no contributions from the galactic or extra-galactic foregrounds, removing the source confusion noise [57]. The noise contributions are therefore realised as a pseudo-random sequence of numbers relating to the instrumental noise from the optical and accelerator noises. Each simulator models the noise contribution using a different method; the LISA simulator generates independent Gaussian deviations in the frequency domain, multiplies them by $S^{\frac{1}{2}}(f)$, the one-sided spectral density of the respective noise contribution, and then Fourier Transforms the noise stream into the time domain. Conversely, Synthetic LISA generates the Gaussian random numbers in the time domain, creating a white noise data stream and then applies digital filters to obtain the desired spectral shape [63].

The desired outcome of the challenge was the confirmation that the complex LISA data stream can be tackled using the current data analysis techniques. To this end, the Taskforce also provided noise-free data streams of the gravitational wave signals, reflecting the characteristic shape of the expected signals over the length of the data streams.

The second and third Challenges build on the results of the first Challenge, describing more ambitious data analysis problems that involve the incorporation of more complex noise models and gravitational wave signals, for example, Extreme Mass Ratio Inspirals (EMRI), galactic foreground modelling, gravitational wave burst sources and stochastic backgrounds [57].

6.2 Investigating the MLDC Data Stream

A number of the current MLDC data analysis approaches utilise the optimal TDI combinations (i.e. A, E, T) to ensure that the data streams that are input into the complex search algorithms are uncorrelated [49, 57]. The ability of these algorithms to recover the correct gravitational wave signal parameters is reliant on the structures of the optimal TDI expressions to produce independent data streams. As shown in Chapter 4, the structure of the optimal combinations only ensures data stream independence for a given timestamp and hence the combination data streams will be subject to time correlations with respect to different time stamps. Note that it is possible that the effect of the time correlations in the live LISA data is small and would therefore only have a small effect on the recovery of the signal parameters. The further statistical analysis of the stream in recovering the parameters compensating for the effect of the small time correlations.

In order to investigate the strength of the time correlations in the noise contributions for the MLDC data, a data set was chosen from the first Challenge: the 1.2.1 dataset containing a MBH binary signal. Utilising the noise-free and full data streams in the Challenge data set, X, Y, Z noise data streams were created by subtracting the two data streams. These data streams will not contain any gravitational wave signal but describe the combined noise contributions at every time stamp for the 8-pulse TDI combinations. Using the form of the optimal combinations shown in Equation 3.11, new "uncorrelated" A, E and T data streams were constructed from the MLDC noise free data streams.

If the noise terms and hence the noise data streams are correlated in time, they should display non-zero correlation structure when time shifted with respect to each other. Using the definition of the correlation relation defined in terms of the expectation values of the data stream described in Equation 4.1, the results for the A, E, T combinations are shown in Figures 6.1 and 6.2. In this case, the correlation expression is calculated between the combination data stream with no time shifting applied, and the equivalent data stream with a timeshift of Δ. For example, for a timeshift of

$\Delta = 10$, the first timestamp of the timeshifted data stream is compared with the 11th timestamp value of the original data stream. To ensure that the data stream length is maintained throughout the calculation and that it contains characteristic values for the data stream, the unused values are appended to the bottom of the timeshifted data stream. In other words, the time stamps are cycled round relative to the current value of the time shift.

Although the noises sources present in the MLDC datastream are not white, the time correlations identified in Chapter 4 are only affected by certain time stamps of the data. The time stamps in question are defined by the arm lengths of the data which are much shorter than the data stream length and will therefore be unaffected by the cycled time stamps.

Figures 6.1 and 6.2 display the correlation coefficient calculated for a data stream of length 2097152, defined by the maximum length of the MLDC data streams, and time shift values up to $\Delta = 10000$. The top three plots in each figure describe the auto-correlation of the combination streams, between A, E and T respectively. The bottom plots relate to the cross-correlation between $A(t)$ and $E(t_\Delta)$, $A(t)$ and $T(t_\Delta)$, and E and $T(t_\Delta)$, where the t_Δ term represents the timeshifted time stamps of the respective data stream.

The results discussed in Chapter 4 indicated the presence of auto-correlation terms for a optical bench dependent noise term. There was also a cross-correlation presence for variations in the optical bench variances. For the optimal combinations, the non-zero off-diagonal terms present in the covariance matrix are negative for A and E but are positive for T. For the Mock LISA Data Challenges, the noise realisations defined with the same noise spectral densities and therefore the covariance matrix for the datasets should reflect the presence of the auto-correlations for all combinations.

It can be clearly seen that a number of plots in each Figure display non-zero correlations, specifically the auto-correlations for A and for E and the cross-correlation between the two data streams. The strength of the correlation amplitude at each timestamp relates directly to the presence of non-zero covariances in the data streams.

After the first few timestamps, the results from both simulators do not display any auto correlation for the T data stream and both Figures display structures consistent with rounding error for the cross-correlation plots of $A(t)$ and $T(t_\Delta)$, and for $E(t)$ and $T(t_\Delta)$, also indicating the presence of zero correlation. Looking at the first few timestamps in both Figures, the auto-correlation corresponding to zero time shift is equal to one, as expected for the normalised results.

The other non-zero values denote a brief sinusoidal shape within the first 32 timestamps, relating to the absence of some of the required time stamps in each data stream. In other words, for the data stream combinations constructed at the start of the data stream, the time stamp data relating to a single or double multiple of the armlengths are missing as they occur at timestamps that are earlier than the start of the datastream. Note that the auto-correlation at the zeroth timestamp will still equal one as the same timestamps are still present, however, the datastreams they describe will not be free from the laser noise contributions as some of the required data stream values are missing. The non-zero structure in the correlation plots is therefore the direct result of the missing optical bench values in the X, Y, Z data streams, rather than a reflection of a true change in the optimal combination correlation values.

Interestingly, the non-zero correlations shown in both Figures do not reflect the same structures; the LISA simulator results display a definite ringdown wavelike structure that oscillates around the central zero value, while the Synthetic LISA plots show a slow decrease in the correlation amplitude with increasing timeshift value. The cross-correlation plots between the A and E combinations also show different structures for each of the simulators; the LISA simulator with sinusoid variations beginning at a high positive correlation value, with the Synthetic LISA plot displays negative correlation that initially decreases as the timeshifting increases and then begins to increase again.

Looking at the shape of the decaying sinusoids in each Figure, it is possible that the non-zero correlations are reflecting the frequency cutoff applied to the individual noise spectra during their construction. In other words, the frequency cutoff applied to the noise spectrum of the simulators during the creation of the data stream time stamps

themself could have introduced the effect that is appearing as a slow sinsoidal variation in the time correlation plots [64]. The two simulators (LISA simulator and Synthetic LISA) used to produce the synthetic optical bench data use different techniques to model the optical bench measurements and the noise contributions, as discussed earlier in this Chapter, producing similar noise spectra from combinations of time and frequency domain data. The differences in the construction of these values and the lower frequency cutoffs of the noises could be the source of the differences between the non-zero structures in Figures 6.1 and 6.2.

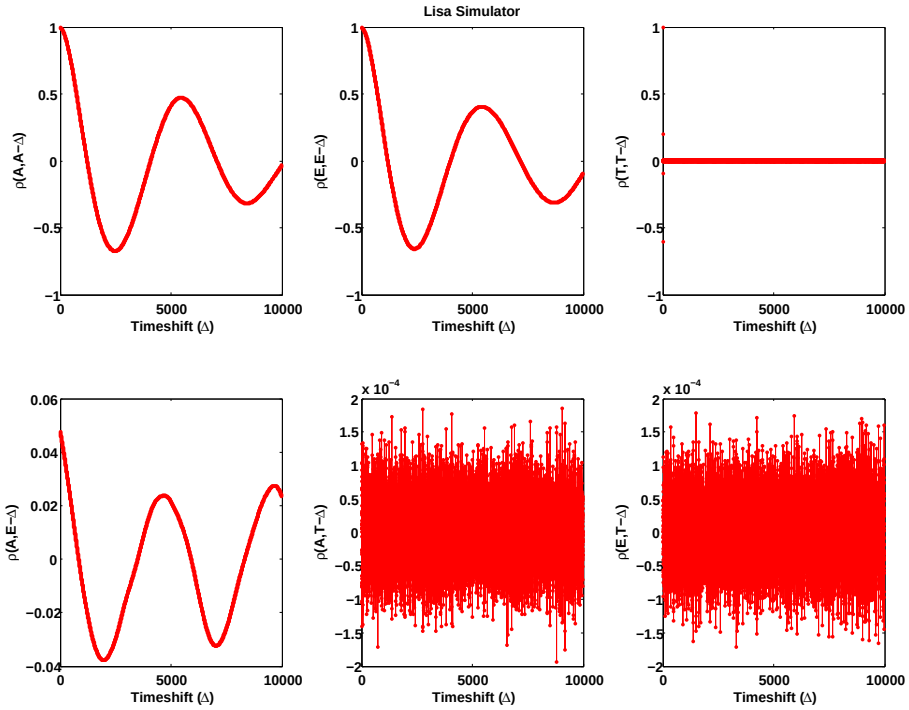

Figure 6.1: Time Correlation Plots for LISA Simulator. The first line describes the auto-correlations between the time stamps of the combinations A, E and T. The second row describes the cross-correlation between (A and E), (A and T) and (E and T) respectively. Total number of data time stamps = 2097152.

6.2.1 Conclusion

The realisations of the optimal TDI combinations constructed from the noise data stream for the first Mock LISA Data Challenge (1.2.1) display clear time dependent correlation structures between the A and E combinations. Specifically for the auto-

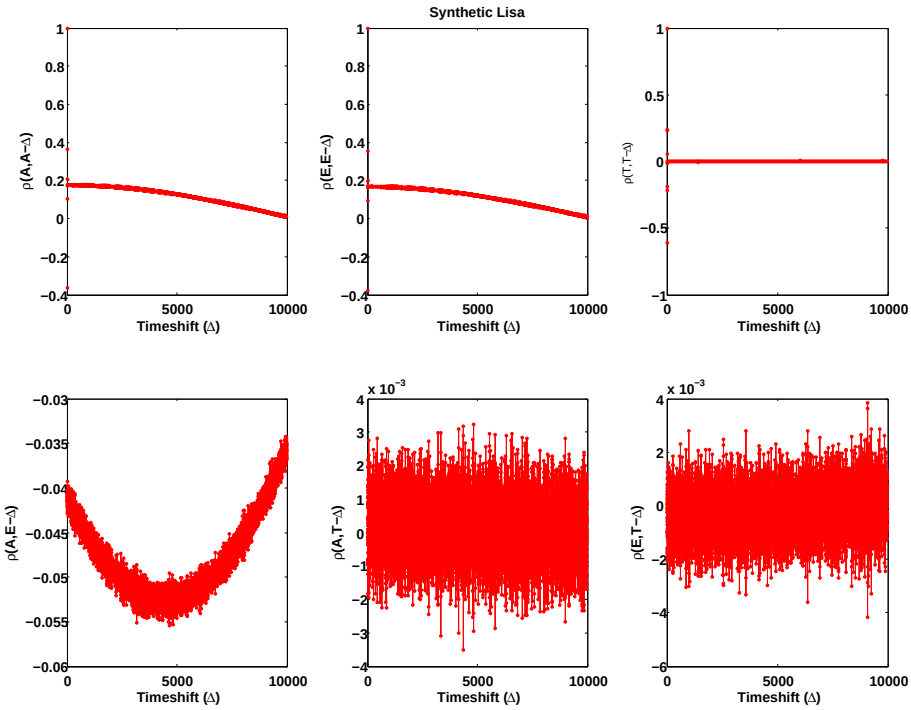

Figure 6.2: Time Correlation Plots for Synthetic LISA. The top line denoting the auto-correlation between the optimal combinations A, E and T, the second row describing the cross-correlations, between the optimal combinations created using the Synthetic LISA data streams, for (A and E), (A and T) and (E and T) respectively. Total number of data time stamps = 2097152.

correlation of A and of E, and the cross-correlations of A against E. The Challenge data sets relating to the LISA simulator [38] display sinusoidal structures, while the non-zero correlations corresponding to the Synthetic LISA [65] data sets slowly decrease over time.

In contrast to the toy models discussed in Chapter 4 where the gravitational signals were modelled as data streams containing two sinusoids with white noise contributions, the MLDC data sets have more realistic noise streams, reflecting the combinations of the different contributing noise spectra. The main contribution is the white phase optical and acceleration noises, where the acceleration noise is only defined to be white above 10^{-4}Hz and decreasing as $\frac{1}{f}$ below this limit, sometimes referred to as pink phase noise [63].

As previously discussed, the non-zero correlation structures appearing in Figures 6.1 and 6.2 might be the direct result of the differences in the relative construction methods employed by each of the simulators to model the LISA noise signals. The LISA simulator uses a one-sided spectral density multiplied by gaussian deviations in the Frequency domain which are then Fourier Transformed into the Time domain. The Synthetic LISA data streams are created in the Time domain, but are digital filtered to create the correct spectral shape. However each of the datastreams should be reflecting the same underlying noise distribution and therefore both methods should produce the same result. In this case, the differences in the correlation plots could solely be due to the underlying time correlations in the streams, the presence of which was confirmed analytically.

The data streams produced by the simulators will also be characterised by the selected frequency cut-offs that are applied to the noise spectra. The differences in each case could have resulted in the slowly varying sinusoidal signal discovered in the Figures. If this is the case, it is likely that this effect is swamping the correlation effect caused by the time covariances.

6.3 Eigenspace Solution to Correlations

The identification of the data stream terms for the optimal combinations involves the diagonalisation of the covariance matrix containing two terms relating to the variance and covariance of the α, β, γ combinations, described in Prince *et al* [30]. Romano and Woan [55] suggest an alternative method, involving the diagonalisation of a 6-by-6 covariance matrix relating to the permutations of the six optical bench data streams. In this case, there is no pre-combining of the data streams to remove the laser noise as the removal of the laser noise terms takes place during the diagonalisation of the covariance matrix. The laser noise removal is accomplished by identifying degenerate eigenvector solutions that are free from the laser noise variances.

For the 6-by-6 covariance matrix, the individual elements describe the covariances between the noise signals measured by each optical bench. The optical bench measurements are the sum of the noise contributions and a possible gravitational wave signal,

$$s_i(t) = p_i(t) + n_i(t) + h_i(t)$$

where $s_i(t)$ is the signal measured by the optical bench i at time stamp t, $p_i(t)$ is the laser noise contribution (spacecraft dependent), $n_i(t)$ is the optical bench noise contribution and $h_i(t)$ is the gravitational wave signal. The noise contributions can be simply described as the difference between the measured signal and the gravitational wave signal (i.e. $(s_i(t) - h_i(t))$). The element (i,j) in the covariance matrix at the current time stamp will therefore describe the covariance as

$$C_{ij} = \langle (s_i - h_i)(s_j - h_j) \rangle,$$

between the signal contributions $(n_i(t), p_i(t))$ and $(n_j(t), p_j(t))$, where i and j are the optical bench numbers.

In Romano and Woan [55], it is assumed that the laser frequency noise $p_i(t)$ is a

common noise term ($p(t) = p_i(t)$). The laser noise and the individual noise terms $n_i(t)$ are defined as gaussian distributed with zero mean and variances, and hence,

$$\langle n_i^2 \rangle = \langle n_j^2 \rangle \equiv \sigma_n^2$$
$$\langle p^2 \rangle \equiv \sigma_p^2$$

Note that in the case for a single sample of data from two detectors (i.e. s_1, s_2), the diagonal covariance terms (i.e. C_{ii}) will simplify to $\sigma_p^2 + \sigma_n^2$, while the off-diagonal terms will equal σ_p^2. For example,

$$C = \begin{pmatrix} (\sigma_p^2 + \sigma_n^2) & \sigma_p^2 \\ \sigma_p^2 & (\sigma_p^2 + \sigma_n^2) \end{pmatrix}$$

By diagonalising the covariance matrix, different eigenspace solutions can be found which correspond to the simplest descriptions of the individual detector signals. If one of the eigenvalues is only dependent on the variance of the individual noise contributions (σ_n^2), then the corresponding eigenvectors describe configurations of the contributing signals that are free from laser noise. In other words, by identifying eigenspace solutions that are free from the σ_p^2 variances, laser noise free combinations can be identified from the original covariance matrix without utilising the TDI combinations.

In this example, there are only two eigenvalues,

$$\lambda_+ = 2\sigma_p^2 + \sigma_n^2,$$
$$\lambda_\times = \sigma_n^2.$$

Although both eigenspace solutions provide simplified descriptions of the detector data, an interesting solution for LISA data analysis is the existance of the $\lambda_\times$ solution and its corresponding eigenvector,

$$e_- = \frac{1}{\sqrt{2}} \begin{pmatrix} 1 \\ -1 \end{pmatrix}$$

This eigenpair solution describes a unique way of combining the two detector data signals (s_1, s_2) that removes all of the laser noise.

By extending this idea to the more challenging task of a full LISA datastream, the noise covariance matrix relates to the individual variances of the noise terms and therefore at a single time stamp, the covariance matrix will take the form,

$$C = \begin{bmatrix} \sigma^2_{N_{11}} & \sigma^2_{N_{12}} & \dots & \sigma^2_{N_{16}} \\ \vdots & \ddots & & \vdots \\ \sigma^2_{N_{61}} & \sigma^2_{N_{62}} & \dots & \sigma^2_{N_{66}} \end{bmatrix}$$

where $\sigma^2_{N_ij}$ describes the covariance between the noise signals, composed from the respective laser noise and detector noise contributions, for optical benches i and j.

In this case, the eigenvalue solutions that are free from the laser noise will appear as degenerate solutions (relating to σ_n^2) within the eigenspace defined by the covariance matrix. Each of the related eigenvectors corresponds to a laser noise free combination of the LISA data stream that are independent not only at the current time stamp but also over the range of time stamps included in the analysis. Applying this technique to different covariance matrices would therefore enable laser noise free solutions to be found for any configuration of the LISA antenna (i.e. similar to TDI 1.5, TDI 2).

The presence of the time correlations could be accounted for the entire LISA data stream by investigating the recurrence of eigenvector structure with the covariance matrices described in Chapter 4, extended to the full length of the data stream.

Note that this technique relies on the construction of large covariance matrices as the overall size of the matrix is defined as the square of the total number of timestamps. For a full LISA simulation, the number of timestamps involved are very large and will prove to be difficult computationally to store and to diagonalise.

6.3.1 Patterns in the Eigenspace

A possible solution to the large covariance matrices needed to solve the direct diagonalisation technique could be to utilise the existing TDI combinations (i.e. X,Y,Z or

A,E,T) to simplify the diagonalisation. Note that as the A,E,T combinations discussed in Prince *et al* [30] are independent at the current time stamp, the recovery of the laser noise free TDI combinations for a large number of timestamps could be improved by diagonalising directly from the A, E and T data streams. In other words, the search for new TDI combinations that are independent in the large scale covariance matrix could be simplified by using the known TDI combinations as a starting point.

The TDI combinations (discussed in previous Chapters) of the LISA optical bench data produce data streams that are free from the laser noise components that would otherwise overwhelm any gravitational signal. Therefore, thinking of this in terms of the eigenspace defined by the different components of the signals, there are known combinations of the optical bench data streams (i.e. α,β,γ and X,Y,Z) that successfully remove the laser noise by identifying the equal and opposite laser noise terms. These combinations are the result of the interferometric solutions based on the geometric shape of the antenna. The recovery of laser noise free combinations using the eigenspace solutions suggested in Romano and Woan [55] provides a flexible and robust approach to dealing with a larger number of data stream time stamps by directly diagonalising the covariance matrix.

Applying the analysis to the covariance matrix defined in terms of the A, E, T expressions in Prince *et al*, the TDI combinations describe particular structures within the eigenvector space. For example, at the current time stamp, the 8-pulse A combination is composed of the 6-pulse combinations α and γ which are related in turn to particular optical bench terms. If the covariance matrix is described in terms of the data stream time stamps rather than the combinations at each time stamp (i.e. 6-by-6 rather than 3-by-3), the eigenvectors corresponding to the combination A in the eigenspace will therefore have non-zero values at the rows corresponding to particular optical benches.

For example, a 3-by-6 covariance matrix relating to the six optical bench terms and the three timestamps needed to supply the necessary terms to construct the combinations, the combination A will have a particular shape in the eigenvector space.

Thinking of this in terms of the optical bench terms, the individual values of the data stream that contribute to the construction of the A combination are different at each time stamp, but due to their geometric construction the same optical bench terms (ie. $y_{ij}(t), y_{ik}(t - L_j)$) are present. This means that in terms of the eigenvector space for a single timestamp (ensuring that A,E,T are eigenvectors for the space), for normalised eigenvectors the TDI combination will appear as a pattern of non-zero contributing terms (ie. between +1 and -1).

Extending this to a larger number of timestamps, the current value of the combination would still appear as a same pattern with the same signs and timestamp values. The extended covariance matrix would therefore contain repeating structure at different timestamps, relating directly to the reappearance of the same combination at different time stamps in the degenerate eigenspace. Similarly, different laser noise free combinations will appear as different repeating patterns in the degenerate eigenvector space. Therefore, the identification of repeating structure within this space will indicate the existence of a TDI combination for the LISA configuration.

6.3.2 Conclusions

The diagonalisation of the covariance matrix to recover TDI combinations involves a number of challenges; the matrix described either in terms of an existing combination (i.e. A, E, T) or the optical bench terms becomes difficult to store computationally for a large number of data stream values. The extension of the analysis to a large number of timestamps increases the size of the covariance matrix dramatically; the new matrix contains a matrix block of size 3-by-3 for A, E, T or 6-by-6 for the optical bench terms for each respective timestamp combination. The total number of time stamp blocks increases as the square of the number of time stamp values and therefore the side length of the entire covariance matrix is a linear multiple of the data stream size. The size of matrix required for a full years worth of LISA data is difficult to handle computationally; both in terms of the memory requirement and with respect to the large scale diagonalisation operation that is required.

The evaluation and manipulation of the matrix is difficult for a static and stationary LISA model, the extension of the analysis to the rotating LISA array will vary the structure in the covariance matrix, increasing the complexity of the matrix and the diagonalisation.

Within the computational restrictions, a number of covariance matrices containing the time correlation terms were diagonalised using the computational analysis program Maple (Version 10) [51]. Notably the results for the Prince *et al* analysis were recovered for a single time stamp covariance matrix of A, E, T. Unfortunately the optical bench and optimal combination analysis results did not display definite repeating structures over the limited range of possible time stamp ranges. The structures that were present for a single time stamp were lost during the extension to a larger number of time stamps and time correlations. The limitations on the computational analysis prevented the recovery of the ortho-normalised matrix for a timestamps greater than 50, inadequate for describing a data stream with a LISA armlength of approximately 16 timestamps.

In summary, the techniques described in Romano and Woan [55] could provide a method for directly removing the laser noise contributions and solving the independent data stream problem. This involves diagonalising a large covariance matrix related directly to the optical bench measurements and identifying the degenerate eigenvalues. The computer intensiveness could be surmounted by employing mathematical techniques to diagonalise the covariance matrix that utilise the symmetry and shape of the matrix (i.e. block Toeplitz) to simplify the procedure. If the patterns in the eigenvectors could be identified for the entire data stream, this might allow the laser noiseless TDI space to be described in terms of a few compact relations, similar to A, E, T.

Chapter 7

Overall Conclusions and Future Work

An important challenge for LISA data analysis is the removal of the laser noise contributions, to allow the confident detection of the gravitational wave signals. Time Delay Interferometry cancels out the laser noise contributions by identifying and time shifting the same realisations of the noise. Different TDI combinations are constructed from the individual optical bench measurements, each describing a different geometric configuration that removes the laser noise terms. A number of these combinations are based on existing interferometric solutions for detecting gravitational wave signals. For example, the X, Y and Z eight-pulse combinations discussed in Chapter 3 use a configuration based on the framework used by Michelson Interferometers. The laser noise free data streams produced by the TDI solutions are not independent with respect to each other, and hence further TDI combinations are constructed (i.e. A, E and T), that are orthogonal with respect to each other and use the initial combinations to ensure the laser noise cancellation.

As discussed in Chapter 4, the combination data streams constructed from the optimal combinations A,E,T are correlated in time. The construction of the six and eight pulse combinations, designed to remove the laser noise, introduces identically equal noise terms when recombined to create the optimal combinations. Hence, the data streams are only independent at the current time stamp of the data, the presence of identical noise realisations at different time stamps results in time correlations.

From the detailed analysis in Section 4.4, it was discovered that the non-zero auto- and cross-covariances are located at the points where the difference between the timestamps of the combinations are first and second multiples of the arm length size, for a static and stationary detector. The motion of the array changes the exact length of the arms at each timestamp and therefore introduces variations in the location of these points.

The non-zero elements of the covariance matrices can clearly be seen in Figures 4.2, 4.4 and 4.5. The non-zero auto-covariances relate to the inclusion of identical noise terms, while the cross-covariances, for the same timestamps, are zero when the noise variances are identical. This implies that for a optical bench dependent noise term with differing variances, that the data stream will contain noise correlations relating to the auto-covariances and the smaller cross-covariances.

The optimal combinations A, E and T are commonly used throughout the LISA data analysis community to ensure that the data streams that are used for likelihood analysis and signal recovery techniques are independent. In Chapter 5, the effect of using template models that assume that the signals are independent when the true signal was correlated in time was investigated and the presence of correlation terms in the normalised residuals were identified, using simple sinusoidal examples to simplify the analysis.

Within the likelihood expression, the correlation terms appear twice in the χ^2 relation, first as a scale factor, relating to $\frac{1}{1-\rho^2}$, and also with the cross covariance terms. The scale factor term has larger effect on the individual χ^2 values, increasing in its rate of growth in the presence of both a positive and a negative correlation. This results in a enhancement of the features on the likelihood surface, described in terms of $\Delta\chi^2$ and a narrower peak around the predicted signal parameter values. When the presence of the time correlations in the data stream are fully taken into account for the likelihood analysis of a toy problem consisting of a data stream containing two sinusoidal signals, they result in a tighter constraint on the signal parameters compared with the results from an independent analysis on the same time correlated data, when the signal-to-

noise is sufficiently high to recover the parameters successfully. This result can be seen clearly in the results plots in Section 5.2. Note that when the signal-to-noise is low, the independent results provide a more reliable estimate of the parameter values: the confidence intervals for the analysis when the time correlations have been taken into account provided tighter constraints but for the incorrect parameter values.

In Chapter 6, the effect of possible time correlations in the Mock LISA Data Challenge data produced by the LISA simulator and Synthetic LISA was investigated. The correlation analysis displayed clear non-zero correlations for the auto-correlation of A and E and the cross-correlations between the two combinations. The structures of the non-zero correlation values corresponding to the relative time shifts of the Challenge data are different for each generator. The LISA simulator displays sinusoidal variations, while Synthetic LISA shows a slow decrease in the correlation amplitude with increasing time shift value. Interestingly, both datasets display zero covariance for any combination involving the T combination. It is possible that the structure in these plots is the result of the frequency cutoff applied to the simulated data. Each simulator generates the optical and accelerator noise contributions to the LISA signal using a different method; these differences and the frequency cutoff applied to the data could explain why the two plots show different structures. If this is the case, the effect of the time correlations on the data stream could be comparatively small and is therefore being swamped by the existance of the larger noise contribution.

In conclusion, in order to accurately recover the signal parameters using the optimal combinations A, E and T, the time correlations present in the true signal data streams should be taken into account. The model templates with the time correlation terms provide a tighter constraint on the true signal parameters, than the results from independent model templates. The results in Chapter 4 show that the existing independent analysis could still be used provided that new combinations can be found that describe truly independent data streams. Completely independent combinations could be constructed by diagonalising the time correlated covariance matrix and simplified by identifying repeating structures in the eigenvectors.

Future work in this area could be to investigate the possibilities offered by parallel computing, to overcome the computational constraints of a single desktop machine. If this provided efficient diagonalisation of an optimally sized LISA covariance matrix (i.e. a size large enough to show repeating eigenvector structure), then new noise-free combinations could be found. These new TDI combinations constructed from the covariances between the optical bench measurements at each time stamp, would be independent with respect to each other at all time stamps.

A possible extension of the analysis discussed in Chapter 5, for the covariance matrix composed from the A, E and T combinations (discussed in Prince *et al* [30]), would be to investigate the effect of taking the time correlations into account for the current time stamp and propagating the effect out for the other time stamps. In other words, what effect on the likelihood expression would be observed if the covariances between the combination streams were properly accounted for at every time stamp, but the correlations introduced by the cross- and auto-covariances were still ignored.

Appendix A

Detailed Derivation of Wave Equation Solution For Einstein Equations

This Appendix contains a thorough treatment of the derivation of the wave equation solution for Einstein Equations in tensor notation, expanding on the discussions in Section 1.2. The notation used throughout follows the convention in Gravitation [11]. The Author also recommends the following texts for reference and further discussion [17, 8, 9].

The Einstein Equation relates the curvature of spacetime with the matter-energy distribution described by the Energy Momentum tensor $T_{\mu\nu}$.

$$G_{\mu\nu} = R_{\mu\nu} - \frac{1}{2}\eta_{\mu\nu}\mathcal{R}.$$

The Riemann tensor describes the curvature of the geometric structure in terms of Christoffel Symbols,

$$\begin{aligned} R_{\alpha\beta\gamma\delta} &= g_{\alpha\mu}R^{\mu}_{\beta\gamma\delta} \\ &= g_{\alpha\mu}[\Gamma^{\sigma}_{\beta\delta}\Gamma^{\mu}_{\sigma\gamma} - \Gamma^{\sigma}_{\beta\gamma}\Gamma^{\mu}_{\sigma\delta} + \Gamma^{\mu}_{\beta\delta,\gamma} - \Gamma^{\mu}_{\beta\gamma,\delta}], \end{aligned}$$

In Minkowski spacetime, the Christoffel symbols are all identically zero and therefore

the Riemann Christoffel tensor can be written as,

$$R_{\alpha\beta\gamma\delta} = g_{\alpha\mu}[\Gamma^{\mu}_{\beta\delta,\gamma} - \Gamma^{\mu}_{\beta\gamma,\delta}],$$

where the Christoffel symbols are defined as,

$$\Gamma^{\mu}_{\beta\delta} = \frac{1}{2} g^{\mu\nu}(g_{\beta\nu,\delta} + g_{\delta\nu,\beta} - g_{\beta\delta,\nu}).$$

Note also that in tensor notation a comma subscript denotes partial differentiation over an index,

$$A_{\alpha,\beta} = \frac{\partial}{\partial x^{\beta}} A_{\alpha}.$$

Note that in the absence of gravity, spacetime is geometrically flat but in the presence of a weak gravitational field, spacetime can be described as being *nearly flat*. Within this description the metric and the perturbations introduced by the gravitational waves are able to be clearly separated,

$$g_{\mu\nu} = \eta_{\mu\nu} + h_{\mu\nu} \tag{A.01}$$

where $h_{\mu\nu} << 1$. These coordinates are labelled *Nearly Lorentz Coordinates*. Note that in a flat (or assumed to be flat) spacetime, there is no divergence of the geometry and therefore the Christoffel symbols are identically zero. This *Linearised Theory* is a *weak-field approximation* to General Relativity, where spacetime is viewed as nearly Lorentzian, like Special Relativity. Within this theory, gravity is described using the curved-space formalism of General Relativity and can be modelled as a symmetric, second rank tensor field $\bar{h}_{\mu\nu}$ [11].

Hence the Riemann Curvature tensor can be simplified to first order as,

$$R_{\mu\delta\nu}{}^{\sigma} = R_{\mu\sigma} = \Gamma_{\mu\nu,\sigma}{}^{\sigma} - \Gamma_{\mu\sigma,\nu}{}^{\sigma}.$$

In terms of metric expressions,

$$R_{\mu\sigma} = \frac{1}{2} g^{\sigma\alpha}[g_{\mu\alpha,\nu\sigma} + g_{\nu\alpha,\mu\sigma} - g_{\mu\nu,\alpha\sigma} - g_{\mu\alpha,\sigma\nu} - g_{\sigma\alpha,\mu\nu} + g_{\mu\sigma,\alpha\nu}].$$

Expanding out the above expressions using equation A.01, describes the curvature tensor in terms of the perturbation h,

$$R^{\sigma}{}_{\mu\sigma\nu} = R_{\mu\sigma} = \frac{1}{2}[h^{\sigma}{}_{\nu,\mu\sigma} + h^{\alpha}{}_{\mu,\alpha\nu} - h_{\mu\nu,\alpha}{}^{\alpha} - h_{,\mu\nu}]. \tag{A.02}$$

Note that throughout linearised theory, the indices of $h_{\mu\nu}$ are raised and lowered with the Minkowski metric $\eta_{\mu\nu}$, rather than the general metric expression $g_{\mu\nu}$. Multiplication with the relevant metric term ($\eta^{\mu\nu}$) gives the corresponding curvature Scalar expression,

$$\mathcal{R} = \frac{\eta^{\mu\nu}}{2}[h^{\sigma}{}_{\nu,\mu\sigma} + h^{\sigma}{}_{\mu,\sigma\nu} - h_{\mu\nu,\sigma}{}^{\sigma} - h_{,\mu\nu}]. \tag{A.03}$$

Combining equations A.02 and A.03, the Einstein Equations can be written as,

$$\begin{aligned} G_{\mu\nu} &= \frac{1}{2}[h^{\sigma}{}_{\nu,\mu\sigma} + h^{\sigma}{}_{\mu,\sigma\nu} - h_{\mu\nu,\sigma}{}^{\sigma} - h_{,\mu\nu}] \\ &\quad -\frac{1}{4}\eta_{\mu\nu}\eta^{\alpha\beta}[h^{\sigma}{}_{\beta,\alpha\sigma} + h^{\sigma}{}_{\alpha,\beta\sigma} - h_{\alpha\beta,\sigma}{}^{\sigma} - h_{,\alpha\beta}]. \end{aligned}$$

Restructuring the indices and consolidating some of the terms, the Einstein tensor can be simplified to,

$$G_{\mu\nu} = \frac{1}{2}[h_{\mu\alpha,\nu}{}^{\alpha} + h_{\nu\alpha,\mu}{}^{\alpha} - h_{\mu\nu,\alpha}{}^{\alpha} - h_{,\mu\nu} - \eta_{\mu\nu}(h_{\alpha\beta}{}^{,\alpha\beta} - h_{,\beta}{}^{\beta})]. \tag{A.04}$$

At this stage, the expressions can be simplified by defining a *trace-reversed* perturbation $\bar{h}_{\mu\nu} = h_{\mu\nu} - \frac{1}{2}\eta_{\mu\nu}h$

$$G_{\mu\nu} = -\frac{1}{2}[\bar{h}_{\mu\nu,\alpha}{}^{\alpha} + \eta_{\mu\nu}\bar{h}_{\alpha\beta}{}^{,\alpha\beta} - \bar{h}_{\mu\alpha,\nu}{}^{\alpha} - \bar{h}_{\nu\alpha,\mu}{}^{\alpha}]. \tag{A.05}$$

The application of $\bar{h}$ does not change the underlying expression. This can be seen

mathematically by expanding out the terms in equation A.05 and working back to equation A.04.

Using the above description of the curvature tensors, the Einstein Equations are defined as,

$$\bar{h}_{\mu\nu,\alpha}{}^{\alpha} + \eta_{\mu\nu}\bar{h}_{\alpha\beta}{}^{,\alpha\beta} - \bar{h}_{\mu\alpha,\nu}{}^{\alpha} - \bar{h}_{\nu\alpha,\mu}{}^{\alpha} = 16\pi T_{\mu\nu}. \tag{A.06}$$

Note that the nearly flat coordinate system for which equation 1.2 holds is not unique. Different descriptions can be identified by carrying out particular coordinate transformations that will maintain the properties of the system. Although there is considerable coordinate freedom in the components of $h_{\alpha\beta}$, there is a firm constraint that the new coordination system must also behave as nearly Lorentzian. Within this limitation, there are two types of transform that can be applied to change the coordinate system. *Background Lorentz transformations* describe the application of a Lorentz "boost" of velocity along an axis direction, stretching the coordinate system in the direction of the velocity. *Gauge transformations* describe the application of a small vector ξ^{μ} to the coordinates x^{μ} without invalidating the assumption that the spacetime is nearly flat.

$$\xi_{\mu,\alpha}{}^{\alpha} = 0$$

These transformations would enable a coordinate system to be found that simplifies the Einstein Equations. For example, equation A.05 could be simplified if a coordinate system could be found for which,

$$\bar{h}^{\mu\nu}{}_{,\nu} = 0. \tag{A.07}$$

In other words, there is zero divergence of the metric perturbation terms. This approach is termed "finding the right *gauge* for the problem", analogous with similar procedures in electromagnetism. Note that the considerable coordinate freedom in the components of $h_{\alpha\beta}$ is termed *Gauge freedom*. It can be shown[1] that it is always possible to find a gauge that satisfies equation A.07, known as the *Lorentz Gauge Condition*.

[1] See Schutz [8] for further discussion.

The enforcement of the Lorentz gauge on Equation A.06 reduces the three left hand expressions to zero. Hence the simplified expression of the linearised Einstein Field Equations takes the form,

$$-h_{\mu\nu,\alpha}{}^{\alpha} = 16\pi T_{\mu\nu}.$$

From this expression, free space solutions of the Field Equations can be found, relating to,

$$\bar{h}_{\mu\nu,\alpha}{}^{\alpha} \equiv \eta^{\alpha\alpha}\bar{h}_{\mu\nu,\alpha\alpha} = 0. \tag{A.08}$$

The properties of this expression can be seen more clearly by writing out explicitly the individual terms. The Minkowski metric term $\eta^{\alpha\alpha}$ reduces to the vector expression $[-1\ 1\ 1\ 1]$.

The perturbation term $\bar{h}_{\mu\nu,\alpha\alpha}$ displays double differentiation over a repeated index, where $\alpha = 0 - 3$. The indices relate to the individual time and spatial coordinates of the matrix. Therefore the full expression can be written as,

$$(-\frac{\partial^2}{\partial t^2} + \nabla^2)\bar{h}_{\mu\nu} = 0. \tag{A.09}$$

The mathematical form of this equation satifies the properties of a *Wave Equation*.

The simplest solution to the linearised equation A.08 is the monochromatic, plane wave solution [11, 8].

$$\bar{h}_{\mu\nu} = \Re[A_{\mu\nu}\exp(ik_\alpha x^\alpha] \tag{A.010}$$

where $\Re[]$ denotes the Real part of the bracketed terms, A_α is the wave amplitude and k_α is the wave vector, which satisfy [17],

$$k_\alpha k^\alpha = 0$$

$$A_{\mu\alpha}k^\alpha = 0$$

In other words, the wave vector k is a null vector and the amplitude A is orthogonal

to k. These definitions are direct consequences of equation A.08 ($\bar{h}_{\mu\nu,\alpha}{}^{\alpha} = 0$) and the plane wave expression itself ($\bar{h}_{\mu}{}^{\alpha}{}_{,\alpha} = 0$).

Appendix B

Application of Bayes' theorem to the Bias of a Coin

This Appendix details the methodology and rationale underpinning Bayesian Probability Theory. The data from a simple coin tossing experiment is interpretated using Bayes' theorem and the results of each toss discussed in terms of the effect on the posterior and prior distributions, reflecting the degree of belief in a certain outcome. In this case, the desired outcome is defined to be the coin landing face up.

As discussed in Section 5.1, the change in the degree of belief for a particular outcome with the addition of new information is interpreted in terms of the prior probability distribution. The changes to the distribution can be interpreted in two different ways; firstly by investigating the effect of each of the experimental results on the prior distribution collectively, or secondly, by using the posterior distribution for the previous data value as the prior for the next one. Note that both approaches are equivalent.

Consider the probability of a coin landing heads side up (H). Bayes theorem can be written as,

$$\text{prob}(H|D,I) = \frac{\text{prob}(D|H,I).\text{prob}(H|I)}{\text{prob}(D|I)}.$$

where D are the observations of the coin flips. If the coin is unbiased then each observation is an independent event and is not influenced by the previous results. In

this situation, the joint pdf probability ($\text{prob}(D|H,I)$), the probability for the set of data is the product of the individual measurement probabilities ($\text{prob}(D_k|H,I)$).

$$\text{prob}(D|X,I) \propto \prod_{k=1}^{N} \text{prob}(D_k|X,I)$$

where D_k denotes the set of data, indexed by k.

Assuming a uniform distribution for the evidence term $\text{prob}(d|I)$, there is therefore equal probability of observing the measurement (d) based on the background information (I). Hence,

$$\text{prob}(H|D_k,I) \propto \text{prob}(D_k|H,I).\text{prob}(H|I).$$

The prior ($\text{prob}(H|I)$) describes the probability of observing a head (H) on the basis on the current knowledge about the coin (I). As the coin is two sided, there are only two possible outcomes of each flip. The bias (B) of the coin will determine the exact ratio of the outcomes. If you suspect that the coin might be biased, then you might assign equal probabilities to every option in the parameter space.

If the prior and evidence distributions are defined to be uniform over the same parameter ranges as the likelihood distribution, then the shape of the posterior distribution is directly related to the shape of the likelihood. In other words, the probability of the desired outcome based on the data is directly proportional to the probability of observing the particular data values assuming the outcome,

$$\text{prob}(B|D_k,I) \propto \text{prob}(D_k|B,I)$$

In this example, the unknown parameter is defined to be the bias (B) of the coin. As the data values are independent, the possibility of having R heads in N flips is described by a binominal distribution,

$$\text{prob}(R|H,I) \propto H^R(1-H)^{N-R}.$$

where the data term D contains, and is represented by, R heads.

The bias of the coin can be inferred from the data set by evaluating the posterior at discrete values over the parameter space. In this case, the limits of the parameter space are 0 and 1 ($0 \leq B \leq 1$). The parameter value of zero corresponds to only tail outcomes, while a value of one describes only heads. An unbiased coin will have the highest probability at $B = \frac{1}{2}$, reflecting a bias towards neither heads nor tails. The true location of the maximal peak in the posterior and the spread of the peak will determine what the bias estimate is for the data.

As previously mentioned, the posterior distribution can be worked out iteratively or retrospectively. The iterative method takes account of any previous data values by redefining the prior to be the posterior of the previous case. An uniform prior might be used in the first instance but after that the likelihood distribution would reflect the probability of the current data set value, modifying the prior that accounts for all of the previous values. The retrospective method accounts for all the data values at once, defining the likelihood on the basis of the total results for the sample with a uniform prior. To distinguish between them, the iterative terms will be subscripted with an i and the retrospective, with a r.

Now that all of the probability machinery is set up, consider the individual changes in the posterior as the coin is flipped.

- First flip is heads.
  - Substituting this value into the binormal distribution, the likelihoods for both methods are $\text{prob}(D|B, I)_{ir} \propto H^1$.
  - The posteriors are therefore $\text{prob}(B|D, I)_{ir} \propto H^1$.
- Second flip is heads.
  - The likelihood is $\text{prob}(D|B, I)_r \propto H^2$ and therefore the posterior is $\text{prob}(B|D, I)_r \propto H^2$.
  - Iteratively, the likelihood is proportional to the prior, which is equal to H^1, giving a posterior of $\text{prob}(B|D, I)_i \propto H^1 H^1 = H^2$.

- Third flip is tails.
  - The retrospective posterior is $\text{prob}(B|D,I)_r \propto H^2(1-H)^1$.
  - Iteratively, the prior describes the previous two results and is therefore H^2, while the likelihood only describes the current piece of data, relating to $(1-H)^1$, hence the posterior is $\text{prob}(B|D,I)_i \propto (1-H)^1(H^2) = (1-H)^1H^2$.
- If the Nth flip was heads, assuming that there had been $R-1$ heads previously,
  - Retrospectively, $\text{prob}(B|D,I)_r \propto H^R(1-H)^{N-R}$.
  - Iteratively, the prior is $H^{R-1}(1-H)^{((N-1)-(R-1))}$, the likelihood is H^1 and so

$$\begin{aligned}\text{prob}(B|D,I)_i &\propto H^{R-1}(1-H)^{((N-1)-(R-1))}H^1 \\ &\propto H^{R-1+1}(1-H)^{(N-1-R+1)} \\ &\propto H^R(1-H)^{N-R}\end{aligned}$$

Note that both methods will result in the same answer. This is unsurprising as they both describe the same data set and are subject to equivalent prior assumptions. Hence both approaches are equally valid and the choice can be made depending on the situation or personal preference.

Appendix C

Discussion of LISA notation

Throughout the LISA literature there are numerous notation and labelling conventions that have been adopted. In this Appendix, the author will clarify the differences between two of the prominent conventions, namely Tinto *et al* [35] (hereafter Tinto) and Shaddock [5]. They employ similar labeling systems but unfortunately not in the same way. In this thesis, the notation used is strongly influenced by Tinto [35]. In this Appendix, each of the conventions will be discussed in turn and any parallels highlighted between them.

C.1 Spacecraft Notation

Both conventions use the same spacecraft labels, 1, 2 and 3, and assign them in clockwise rotation, starting from the leftmost spacecraft, as shown in Figure C.1. The first difference between the conventions occurs in the method used to label the arm lengths between the spacecraft. Tinto continues to apply the $1, 2, 3$ labelling system, assigning the label to the arm opposite the spacecraft with the same number. In other words, arm 2 denotes the arm length between spacecraft 1 and 3. In the Shaddock notation, the arm length is designated by a subscript with two terms, the first corresponding to the transmitting bench and the second by the receiving optical bench. For example, the arm length between spacecraft 1 and 3 in a clockwise direction will be L_{31}.

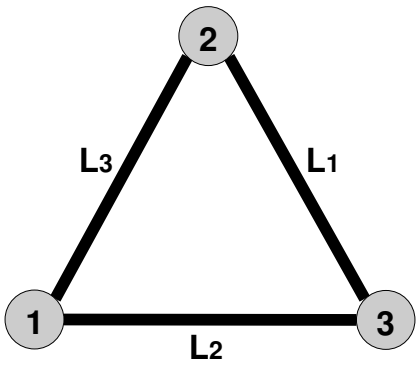

Figure C.1: Spacecraft and arm length labelling, following Tinto convention [4].

C.2 Optical bench Notation

Both authors describe the individual optical benches with subscript notation containing two terms, for example s_{ij}. In Tinto notation this subscript defines a signal that was transmitted by spacecraft k, travelled along armlength i (the first subscript number) and was received at spacecraft j (second subscript number). Note that the indexes i, j and k correspond to permutations of 1, 2 and 3. By contrast, the Shaddock notation follows the same convention as the arm lengths, where s_{ij} describes the signal that was transmitted by spacecraft i and received at j. A comparison between the optical bench labels in shown in Figure C.2.

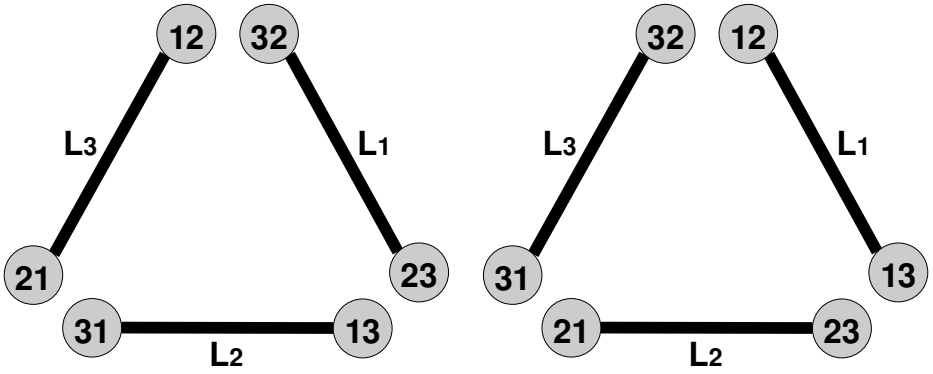

Figure C.2: Diagram of two conventions for spacecraft subscript labeling: Shaddock [5] notation is defined on the left, Tinto [4] notation on the right.

From Figure C.2, it can be noted that the labels for the two optical benches within

an individual spacecraft are the same in both notation conventions (i.e. spacecraft 1 contains optical benches 31 and 21). This can introduce confusion when comparing similar equations using the different notations. Note that without compensating for the differences in the notation the expressions related to recombinations of the datastreams will describe different situations.

In Tinto *et al* [44], (hereafter TSSA), a further notation convention for the optical benches is introduced. To distinguish between the terms relating directly to the optical bench and the laser light traveling down an arm and onto the optical bench. The benches themselves are labeled $1, 1^*, 2, 2^*, 3$ and 3^*. The labels relate to the spacecraft labeling system, while the superscript (*) is applied to the right optical bench in order to distinguish between the benches. In terms of the spacecraft themselves, the bench that transmits light in an anticlockwise direction round the configuration is termed the right hand bench (RHS).

For simplicity, the optical bench notation used throughout follows that of Tinto [35] and applies the notation to all terms relating to an bench. The optical bench motions are described in terms of the bench labels rather than the above notation (*). For example, the optical bench 1^* in TSSA notation corresponds to optical bench 21.

C.3 Time Delay Operator Notation

The notation convention for the time delay operator defined in equation 2.4 follows that of Tinto [35], describing the time delays in terms of arm lengths defined in units of time (L_k). The notational form for this operator is a subscript ($a_{ij,k}$), introduced in equation 2.4, where k relates to the relevant armlength label. This notation is commonly utilised in the literature due to its simplicity.

Shaddock [5] defines the time delay operator in terms of a expression D_{ij}, which follows the same subscript notation as the optical bench labeling system,

$$D_{ij}a(t) = a(t - \frac{L_{ij}}{c})$$

Note that both types of notation describe exactly the same time delay operator.

In summary, the notation used in both references describe the same antenna configuration; the only differences are in the labeling conventions.

Appendix D

Proof of Noise cancellation in Alpha Recombination

From [44, 4], the TDI combination α is defined to be:

$$\begin{aligned}\alpha &= y_{21} - y_{31} + y_{13,2} - y_{12,3} + y_{32,12} - y_{23,13} \\ &+\frac{1}{2}[(z_{23} - z_{13})_{,2} + (z_{23} - z_{13})_{,13} + (z_{31} - z_{21}) + (z_{31} - z_{21})_{,123} \\ &+(z_{12} - z_{32})_{,3} + (z_{12} - z_{32})_{,12}],\end{aligned}$$

The definitions of the inter- and intra-spacecraft measurements in terms of frequency modulations, where the lasers have a central frequency of ν_0 and the spacecraft are stationary with respect to each other are,

$$\begin{aligned}y_{ij_{RHS}} &= y_{ij}^{GW} + y_{ij}^{op} + C_{ik,i} - C_{ij} + [2\hat{n}_i \cdot \vec{\delta}_{ij} - \hat{n}_i \cdot \vec{\Delta}_{ij} - \hat{n}_i \cdot \vec{\Delta}_{ik,i}] \\ y_{ij_{LHS}} &= y_{ij}^{GW} + y_{ij}^{op} + C_{ik,i} - C_{ij} + [-2\hat{n}_i \cdot \vec{\delta}_{ij} + \hat{n}_i \cdot \vec{\Delta}_{ij} + \hat{n}_i \cdot \vec{\Delta}_{ik,i}] \\ z_{ij_{RHS}} &= C_{kj} - C_{ij} + 2\hat{n}_k \cdot (\vec{\delta}_{kj} - \vec{\Delta}_{kj}) + \mu_j \\ z_{ij_{LHS}} &= C_{kj} - C_{ij} - 2\hat{n}_k \cdot (\vec{\delta}_{kj} - \vec{\Delta}_{kj}) + \mu_j.\end{aligned}$$

The intra-spacecraft measurements are defined as differences in order to cancel the large fibre noise (μ_j),

$$\begin{aligned} z_{21} - z_{31} &= 2C_{31} - 2C_{21} + 2\hat{n}_3 \cdot (\vec{\delta}_{31} - \vec{\Delta}_{31}) + 2\hat{n}_2 \cdot (\vec{\delta}_{21} - \vec{\Delta}_{21}) \\ z_{32} - z_{12} &= 2C_{12} - 2C_{32} + 2\hat{n}_1 \cdot (\vec{\delta}_{12} - \vec{\Delta}_{12}) + 2\hat{n}_3 \cdot (\vec{\delta}_{32} - \vec{\Delta}_{32}) \\ z_{13} - z_{23} &= 2C_{23} - 2C_{13} + 2\hat{n}_1 \cdot (\vec{\delta}_{13} - \vec{\Delta}_{13}) + 2\hat{n}_2 \cdot (\vec{\delta}_{23} - \vec{\Delta}_{23}) \end{aligned}$$

Watch for the patterns in the notation to help ensure that the subscripts are correctly assigned. The RHS and LHS designations relate to the relative positions of the optical benches with respect to the spacecraft. Note that it is assumed that the arm lengths are the same in both directions (ie, $L_{31} = L_{32} = L_3$).

D.1 Laser Noise Cancellation

The α expression in terms of the laser noise contributions can be found by substituting in the related inter- and intra-spacecraft expressions. To clarify which terms are related to the different measurements, the expression has been split into α_y and $2\alpha_z$. Note that the factor of two corresponds to the multiplier of a half in the original α expression. Hence,

$$\begin{aligned} \alpha_{y_c} &= y_{21} - y_{31} + y_{13,2} - y_{12,3} + y_{32,12} - y_{23,13} \\ &= y_{21}^{GW} + y_{21}^{op} + C_{23,2} - C_{21} + [2\hat{n}_2 \cdot \vec{\delta}_{21} - \hat{n}_2 \cdot \vec{\Delta}_{21} - \hat{n}_2 \cdot \vec{\Delta}_{23,2}] \\ &\quad -(y_{31}^{GW} + y_{31}^{op} + C_{32,3} - C_{31} + [2\hat{n}_3 \cdot \vec{\delta}_{31} - \hat{n}_3 \cdot \vec{\Delta}_{31} - \hat{n}_3 \cdot \vec{\Delta}_{32,3}]) \\ &\quad +(y_{13,2}^{GW} + y_{13,2}^{op} + C_{12,12} - C_{13,2} + [2\hat{n}_1 \cdot \vec{\delta}_{13,2} - \hat{n}_1 \cdot \vec{\Delta}_{13,2} - \hat{n}_1 \cdot \vec{\Delta}_{12,12}]) \\ &\quad -(y_{12,3}^{GW} + y_{12,3}^{op} + C_{13,13} - C_{12,3} + [2\hat{n}_1 \cdot \vec{\delta}_{12,3} - \hat{n}_1 \cdot \vec{\Delta}_{12,3} - \hat{n}_1 \cdot \vec{\Delta}_{13,13}]) \\ &\quad +(y_{32,12}^{GW} + y_{32,12}^{op} + C_{31,123} - C_{32,12} + [2\hat{n}_3 \cdot \vec{\delta}_{32,12} - \hat{n}_3 \cdot \vec{\Delta}_{32,12} - \hat{n}_3 \cdot \vec{\Delta}_{31,123}]) \\ &\quad -(y_{23,13}^{GW} + y_{23,13}^{op} + C_{21,123} - C_{23,13} + [2\hat{n}_2 \cdot \vec{\delta}_{23,13} - \hat{n}_2 \cdot \vec{\Delta}_{23,13} - \hat{n}_2 \cdot \vec{\Delta}_{21,123}]) \end{aligned}$$

Rearranging the intra-spacecraft measurements in terms of the difference expressions, to simplify the total number of expressions, gives,

$$\begin{aligned}
2\alpha_{z_c} &= -(z_{13,2} + z_{13,13} + z_{21} + z_{21,123} + z_{32,3} + z_{32,12}) \\
&\quad +(z_{23,2} + z_{23,13} + z_{31} + z_{31,123} + z_{12,3} + z_{12,12}) \\
&= (z_{23} - z_{13})_{,2} + (z_{23} - z_{13})_{,13} + (z_{31} - z_{21}) + (z_{31} - z_{21})_{,123} \\
&\quad +(z_{12} - z_{32})_{,3} + (z_{12} - z_{32})_{,12} \\
&= -(z_{13} - z_{23})_{,2} - (z_{13} - z_{23})_{,13} - (z_{21} - z_{31}) - (z_{21} - z_{31})_{,123} \\
&\quad -(z_{32} - z_{12})_{,3} - (z_{32} - z_{12})_{,12}.
\end{aligned}$$

Substituting the intra-spacecraft differences into the expression gives,

$$\begin{aligned}
2\alpha_{z_c} &= -(2C_{23,2} - 2C_{13,2} + 2\hat{n}_1 \cdot (\vec{\delta}_{13} - \vec{\Delta}_{13})_{,2} + 2\hat{n}_2 \cdot (\vec{\delta}_{23} - \vec{\Delta}_{23})_{,2}) \\
&\quad -(2C_{23,13} - 2C_{13,13} + 2\hat{n}_1 \cdot (\vec{\delta}_{13} - \vec{\Delta}_{13})_{,13} + 2\hat{n}_2 \cdot (\vec{\delta}_{23} - \vec{\Delta}_{23})_{,13}) \\
&\quad -(2C_{31} - 2C_{21} + 2\hat{n}_3 \cdot (\vec{\delta}_{31} - \vec{\Delta}_{31}) + 2\hat{n}_2 \cdot (\vec{\delta}_{21} - \vec{\Delta}_{21})) \\
&\quad -(2C_{31,123} - 2C_{21,123} + 2\hat{n}_3 \cdot (\vec{\delta}_{31} - \vec{\Delta}_{31})_{,123} + 2\hat{n}_2 \cdot (\vec{\delta}_{21} - \vec{\Delta}_{21})_{,123}) \\
&\quad -(2C_{12,3} - 2C_{32,3} + 2\hat{n}_1 \cdot (\vec{\delta}_{12} - \vec{\Delta}_{12})_{,3} + 2\hat{n}_3 \cdot (\vec{\delta}_{32} - \vec{\Delta}_{32})_{,3}) \\
&\quad -(2C_{12,12} - 2C_{32,12} + 2\hat{n}_1 \cdot (\vec{\delta}_{12} - \vec{\Delta}_{12})_{,12} + 2\hat{n}_3 \cdot (\vec{\delta}_{32} - \vec{\Delta}_{32})_{,12})
\end{aligned}$$

Now that the relevant laser noise terms have been identified and properly timeshifted in each case, the laser noise terms for α as a whole can be separated as,

$$\begin{aligned}
\alpha_c &= C_{23,2} - C_{21} - C_{32,3} + C_{31} + C_{12,12} - C_{13,2} \\
&\quad -C_{13,13} + C_{12,3} + C_{31,123} - C_{32,12} - C_{21,123} + C_{23,13} \\
&\quad -C_{23,2} + C_{13,2} - C_{23,13} + C_{13,13} - C_{31} + C_{21} \\
&\quad -C_{31,123} + C_{21,123} - C_{12,3} + C_{32,3} - C_{12,12} + C_{32,12}
\end{aligned}$$

Rearranging the above expression to group the similar optical bench terms together, gives,

$$\begin{aligned}\alpha_c &= (-C_{21} - C_{21,123} + C_{21} + C_{21,123}) + (C_{31,123} - C_{31} - C_{31,123} + C_{31}) \\ &\quad +(-C_{32,3} - C_{32,12} + C_{32,3} + C_{32,12}) + (C_{12,12} + C_{12,3} - C_{12,3} - C_{12,12}) \\ &\quad +(-C_{13,2} - C_{13,13} + C_{13,2} + C_{13,13}) + (C_{23,2} + C_{23,13} - C_{23,2} - C_{23,13}) \\ &= 0\end{aligned}$$

In this form it is easy to see that all of the laser noise terms cancel out as expected.

D.2 Optical bench Cancellation

Following a similar procedure to the laser noise cancellation, the form of the optical bench terms for the inter-spacecraft measurements are,

$$\begin{aligned}y^{\Delta}_{ij_{RHS}} &= -n_i \cdot \Delta_{ij} - n_i \cdot \Delta_{ik,i} \\ y^{\Delta}_{ij_{LHS}} &= n_i \cdot \Delta_{ij} + n_i \cdot \Delta_{ik,i} \\ z^{\Delta}_{ij_{RHS}} &= n_k \cdot \Delta_{kj} \\ z^{\Delta}_{ij_{LHS}} &= -n_k \cdot \Delta_{kj}\end{aligned}$$

In terms of the isolated optical bench datastreams,

$$\begin{aligned}\alpha_{y_\Delta} &= -n_2 \cdot \Delta_{21} - n_2 \cdot \Delta_{23,2} \\ &\quad -n_3 \cdot \Delta_{31} - n_3 \cdot \Delta_{32,3} \\ &\quad -n_1 \cdot \Delta_{13,2} - n_1 \cdot \Delta_{12,12} \\ &\quad -n_1 \cdot \Delta_{12,3} - n_1 \cdot \Delta_{13,13} \\ &\quad -n_3 \cdot \Delta_{32,12} - n_3 \cdot \Delta_{31,123} \\ &\quad -n_2 \cdot \Delta_{23,13} - n_2 \cdot \Delta_{21,123}\end{aligned}$$

$$\begin{aligned}
\alpha_{z_\Delta} &= n_2 \cdot \Delta_{23,2} + n_2 \cdot \Delta_{23,13} \\
&\quad + n_3 \cdot \Delta_{31} + n_3 \cdot \Delta_{31,123} \\
&\quad + n_1 \cdot \Delta_{12,3} + n_1 \cdot \Delta_{12,12} \\
&\quad + n_1 \cdot \Delta_{13,2} + n_1 \cdot \Delta_{13,13} \\
&\quad + n_2 \cdot \Delta_{21} + n_2 \cdot \Delta_{21,123} \\
&\quad + n_3 \cdot \Delta_{32,3} + n_3 \cdot \Delta_{32,12}
\end{aligned}$$

Grouping the terms together by vector type, the full optical bench contribution is,

$$\begin{aligned}
\alpha_\Delta &= -n_1 \cdot \Delta_{13,2} - n_1 \cdot \Delta_{12,12} - n_1 \cdot \Delta_{12,3} - n_1 \cdot \Delta_{13,13} \\
&\quad + n_1 \cdot \Delta_{12,3} + n_1 \cdot \Delta_{12,12} + n_1 \cdot \Delta_{13,2} + n_1 \cdot \Delta_{13,13} \\
&\quad - n_2 \cdot \Delta_{21} - n_2 \cdot \Delta_{23,2} - n_2 \cdot \Delta_{23,13} - n_2 \cdot \Delta_{21,123} \\
&\quad + n_2 \cdot \Delta_{23,2} + n_2 \cdot \Delta_{23,13} + n_2 \cdot \Delta_{21} + n_2 \cdot \Delta_{21,123} \\
&\quad - n_3 \cdot \Delta_{31} - n_3 \cdot \Delta_{32,3} - n_3 \cdot \Delta_{32,12} - n_3 \cdot \Delta_{31,123} \\
&\quad + n_3 \cdot \Delta_{31} + n_3 \cdot \Delta_{31,123} + n_3 \cdot \Delta_{32,3} + n_3 \cdot \Delta_{32,12} \\
&= 0
\end{aligned}$$

Note that in each case, the terms with the same vector multiplier will cancel out, the intra-spacecraft measurements providing the same terms as the inter-spacecraft measurements but with opposite sign.

The remaining noise terms cannot be cancelled out using this type of reconstruction as the relevant terms only appear in the inter- and intra-spacecraft expressions a single time. The cancellation of the laser noise and optical bench terms were possible due to the presence of equal and opposite terms in the combination.

In summary, the construction of the α Sagnac combination from the datastreams will remove the laser frequency noise and also the movement of the optical benches. The other combinations of this form can be found by cyclical permutation of the indices ($i = 1, 2, 3$) and therefore each of the First Generation Sagnac combinations will also

have this property.

Appendix E

Calculation of Laser Noise Terms for Intra-spacecraft Measurements in Sagnac Combinations

The analysis of the correlations between the α, β, γ datasets relies on good knowledge of the laser noise contributions. The Sagnac Combinations have a number of laser noise terms that enter the full datastream with a factor of 0.5. This arises from the duplication of the laser noise terms with respect to the individual intra-spacecraft measurements. These are commonly described in terms of differences in order to cancel the fibre noise introducing each bench term twice which then requires the multiplication factor in order to match the strength of the laser noise terms from the inter-spacecraft measurements. The computation analysis of the correlations can be facilitated by the direct knowledge of the intra-spacecraft terms that are present in each combination.

Following the detail discussion of the noise cancellation in combination α in Appendix , it can be seen that the relevant laser noise terms α_z^c are,

$$\begin{aligned} \alpha_z^c &= -C_{23,2} + C_{13,2} - C_{23,13} + C_{13,13} - C_{31} + C_{21} \\ &\quad -C_{31,123} + C_{21,123} - C_{12,3} + C_{32,3} - C_{12,12} + C_{32,12} \end{aligned}$$

These terms were derived from the intra-spacecraft measurements described in terms of the difference between the benches. The relevant terms with respect to the other

Sagnac combinations β, γ can be computed by following a similar procedure.

The combinations in terms of the direct optical bench measurements are defined to be,

$$\begin{aligned}
\beta &= y_{32} - y_{12} + y_{21,3} - y_{23,1} + y_{13,23} - y_{31,21} \\
&\quad -\frac{1}{2}(z_{21,3} + z_{21,21} + z_{32} + z_{32,123} + z_{13,1} + z_{13,23}) \\
&\quad +\frac{1}{2}(z_{31,3} + z_{31,21} + z_{12} + z_{12,123} + z_{23,1} + z_{23,23}) \\
\gamma &= y_{13} - y_{23} + y_{32,1} - y_{31,2} + y_{21,31} - y_{12,32} \\
&\quad -\frac{1}{2}(z_{32,1} + z_{32,32} + z_{13} + z_{13,123} + z_{21,2} + z_{21,31}) \\
&\quad +\frac{1}{2}(z_{12,1} + z_{12,32} + z_{23} + z_{23,123} + z_{31,2} + z_{31,31})
\end{aligned}$$

Redefining the intra-measurements in term of the differences ($z_{21} - z_{31}$, $z_{32} - z_{12}$, $z_{13} - z_{23}$),

$$\begin{aligned}
\beta_z &= \frac{1}{2}[-(z_{21} - z_{31})_{,3} - (z_{21} - z_{31})_{,21} - (z_{32} - z_{12}) \\
&\quad -(z_{32} - z_{12})_{,123} - (z_{13} - z_{23})_{,1} - (z_{13} - z_{23})_{,23}] \\
\gamma_z &= \frac{1}{2}[-(z_{32} - z_{12})_{,1} - (z_{32} - z_{12})_{,32} - (z_{13} - z_{23}) \\
&\quad -(z_{13} - z_{23})_{,123} - (z_{21} - z_{31})_{,2} - (z_{21} - z_{31})_{,31}]
\end{aligned}$$

The laser noise contributions in terms of the intra-spacecraft differences are defined to be,

$$\tfrac{1}{2}(z_{21} - z_{31}) = C_{31} - C_{21}, \quad \tfrac{1}{2}(z_{32} - z_{12}) = C_{12} - C_{32}, \quad \tfrac{1}{2}(z_{13} - z_{23}) = C_{23} - C_{13}$$

So in terms of the combinations,

$$\begin{aligned}
\beta_z &= -(C_{31} - C_{21})_{,3} - (C_{31} - C_{21})_{,21} - (C_{12} - C_{32}) \\
&\quad -(C_{12} - C_{32})_{,123} - (C_{23} - C_{13})_{,1} - (C_{23} - C_{13})_{,23} \\
\gamma_z &= -(C_{12} - C_{32})_{,1} - (C_{12} - C_{32})_{,32} - (C_{23} - C_{13}) \\
&\quad -(C_{23} - C_{13})_{,123} - (C_{31} - C_{21})_{,2} - (C_{31} - C_{21})_{,31}
\end{aligned}$$

Note that the intra-spacecraft laser noise terms for each combination can also be determined from a single combination expression by cyclical permutation of the indices with $i = 1, 2, 3$.

For clarity, the individual optical bench terms and time stamps involved in the current realisation of the β datastream are shown in Table E.1. In this case, the arm lengths are defined to be static and equal to $L = 5$ and the current time value is described as $t = 0$.

Sign	Bench Number	Time Delay	Time Stamp
-1	31	L_3	-5
1	21	L_3	-5
-1	31	$L_1 + L_2$	-10
1	21	$L_1 + L_2$	-10
-1	12	0	0
1	32	0	0
-1	12	$L_1 + L_2 + L_3$	-15
1	32	$L_1 + L_2 + L_3$	-15
-1	23	L_1	-5
1	13	L_1	-5
-1	23	$L_2 + L_3$	-10
1	13	$L_2 + L_3$	-10

Table E.1: Intra-spacecraft Laser noise terms for Sagnac Combination β

Appendix F

Analysis of Laser Noise Cancellation in A,E,T Combinations

The use of the First Generation combinations to construct the uncorrelated combinations should ensure that the new combinations A, E, T are free from laser noise without the necessity for any extra recombinations of the data. The structure of the simpler combinations should have removed the laser noise terms. In this section, I will present an detailed analysis of the laser noise terms present in A and investigate the properties of the laser noise cancellation.

The laser noise terms related to the inter- and intra-spacecraft datastreams can be described in global terms as,

$$
\begin{aligned}
y_{ij_{RHS}} &= y_{ij}^{GW} + y_{ij}^{op} + C_{ik,i} - C_{ij} + [2\hat{n}_i \cdot \vec{\delta}_{ij} - \hat{n}_i \cdot \vec{\Delta}_{ij} - \hat{n}_i \cdot \vec{\Delta}_{ik,i}] \\
y_{ij_{LHS}} &= y_{ij}^{GW} + y_{ij}^{op} + C_{ik,i} - C_{ij} + [-2\hat{n}_i \cdot \vec{\delta}_{ij} + \hat{n}_i \cdot \vec{\Delta}_{ij} + \hat{n}_i \cdot \vec{\Delta}_{ik,i}] \\
z_{ij_{RHS}} &= C_{kj} - C_{ij} + 2\hat{n}_k \cdot (\vec{\delta}_{kj} - \vec{\Delta}_{kj}) + \mu_j \\
z_{ij_{LHS}} &= C_{kj} - C_{ij} - 2\hat{n}_k \cdot (\vec{\delta}_{kj} - \vec{\Delta}_{kj}) + \mu_j.
\end{aligned}
$$

Therefore in terms of laser noise,

$$\begin{aligned} y_{ij_c} &= C_{ik,i} - C_{ij} \\ z_{ij_c} &= C_{kj} - C_{ij} \end{aligned}$$

Note that the laser noise terms are general to both the LHS and RHS datasream expressions. The uncorrelated combinations derived by Prince *et al*[30], take the form,

$$\begin{aligned} A &= \frac{1}{\sqrt{2}}(\tilde{\gamma} - \tilde{\alpha}) \\ E &= \frac{1}{\sqrt{6}}(\tilde{\alpha} - 2\tilde{\beta} + \tilde{\gamma}) \\ T &= \frac{1}{\sqrt{3}}(\tilde{\alpha} + \tilde{\beta} + \tilde{\gamma}) \end{aligned}$$

where,

$$\begin{aligned} \alpha &= y_{21} - y_{31} + y_{13,2} - y_{12,3} + y_{32,12} - y_{23,13} \\ &\quad -\frac{1}{2}(z_{13,2} + z_{13,13} + z_{21} + z_{21,123} + z_{32,3} + z_{32,12}) \\ &\quad +\frac{1}{2}(z_{23,2} + z_{23,13} + z_{31} + z_{31,123} + z_{12,3} + z_{12,12}) \\ \beta &= y_{32} - y_{12} + y_{21,3} - y_{23,1} + y_{13,23} - y_{31,21} \\ &\quad -\frac{1}{2}(z_{21,3} + z_{21,21} + z_{32} + z_{32,123} + z_{13,1} + z_{13,23}) \\ &\quad +\frac{1}{2}(z_{31,3} + z_{31,21} + z_{12} + z_{12,123} + z_{23,1} + z_{23,23}) \\ \gamma &= y_{13} - y_{23} + y_{32,1} - y_{31,2} + y_{21,31} - y_{12,32} \\ &\quad -\frac{1}{2}(z_{32,1} + z_{32,32} + z_{13} + z_{13,123} + z_{21,2} + z_{21,31}) \\ &\quad +\frac{1}{2}(z_{12,1} + z_{12,32} + z_{23} + z_{23,123} + z_{31,2} + z_{31,31}) \end{aligned}$$

For clarity, the laser noise terms relating to the inter- and intra- spacecraft measurement are kept separate until the relative spacecraft terms are calculated. Rewriting the

relation for A in terms of the laser frequency noise in the inter-spacecraft measurements,

$$\begin{aligned}
\sqrt{2}A_y &= y_{13} - y_{23} + y_{32,1} - y_{31,2} + y_{21,31} - y_{12,32} \\
&\quad -(y_{21} - y_{31} + y_{13,2} - y_{12,3} + y_{32,12} - y_{23,13}) \\
&= (C_{12,1} - C_{13}) - (C_{21,2} - C_{23}) + (C_{31,13} - C_{32,1}) \\
&\quad -(C_{32,23} - C_{31,2}) + (C_{23,123} - C_{21,31}) - (C_{13,123} - C_{12,32}) \\
&\quad -(C_{23,2} - C_{21}) + (C_{32,3} - C_{31}) - (C_{12,12} - C_{13,2}) \\
&\quad +(C_{13,13} - C_{12,3}) - (C_{31,123} - C_{32,12}) + (C_{21,123} - C_{23,13})
\end{aligned}$$

And also for the intra-spacecraft datastreams,

$$\begin{aligned}
2\sqrt{2}A_z &= -(z_{32,1} + z_{32,32} + z_{13} + z_{13,123} + z_{21,2} + z_{21,31}) \\
&\quad +(z_{12,1} + z_{12,32} + z_{23} + z_{23,123} + z_{31,2} + z_{31,31}) \\
&\quad +(z_{13,2} + z_{13,13} + z_{21} + z_{21,123} + z_{32,3} + z_{32,12}) \\
&\quad -(z_{23,2} + z_{23,13} + z_{31} + z_{31,123} + z_{12,3} + z_{12,12}) \\
&= -(C_{12,1} - C_{32,1}) - (C_{12,32} - C_{32,32}) - (C_{23} - C_{13}) \\
&\quad -(C_{23,123} - C_{13,123}) - (C_{31,2} - C_{21,2}) - (C_{31,31} - C_{21,31}) \\
&\quad +(C_{32,1} - C_{12,1}) + (C_{32,32} - C_{12,32}) + (C_{13} - C_{23}) \\
&\quad +(C_{13,123} - C_{23,123}) + (C_{21,2} - C_{31,2}) + (C_{21,31} - C_{31,31}) \\
&\quad +(C_{23,2} - C_{13,2}) + (C_{23,13} - C_{13,13}) + (C_{31} - C_{21}) \\
&\quad +(C_{31,123} - C_{21,123}) + (C_{12,3} - C_{32,3}) + (C_{12,12} - C_{32,12}) \\
&\quad -(C_{13,2} - C_{23,2}) - (C_{13,13} - C_{23,13}) - (C_{21} - C_{31}) \\
&\quad -(C_{21,123} - C_{31,123}) - (C_{32,3} - C_{12,3}) - (C_{32,12} - C_{12,12})
\end{aligned}$$

Note that the factor of $\sqrt{2}$ relates to the ortho-normalisation factor for the vectors, while the factor of 2 is due to the relationship between the inter- and intra-spacecraft measurements in the Sagnac combinations.

Rearranging the expression to group the terms with the same optical bench gives,

$$\begin{aligned}
\sqrt{2}A_y &= C_{12,1} - C_{13} - C_{21,2} + C_{23} + C_{31,13} - C_{32,1} \\
&\quad -C_{32,23} + C_{31,2} + C_{23,123} - C_{21,31} - C_{13,123} + C_{12,32} \\
&\quad -C_{23,2} + C_{21} + C_{32,3} - C_{31} - C_{12,12} + C_{13,2} \\
&\quad +C_{13,13} - C_{12,3} - C_{31,123} + C_{32,12} + C_{21,123} - C_{23,13} \\
&= -C_{21,2} - C_{21,31} + C_{21} + C_{21,123} \\
&\quad +C_{31,13} + C_{31,2} - C_{31} - C_{31,123} \\
&\quad -C_{32,1} - C_{32,23} + C_{32,3} + C_{32,12} \\
&\quad +C_{12,1} + C_{12,32} - C_{12,12} - C_{12,3} \\
&\quad -C_{13} - C_{13,123} + C_{13,2} + C_{13,13} \\
&\quad +C_{23} + C_{23,123} - C_{23,2} - C_{23,13}
\end{aligned}$$

And for the intra-spacecraft laser noise measurements,

$$\begin{aligned}
2\sqrt{2}A_z &= [-C_{12,1} + C_{32,1} - C_{12,32} + C_{32,32} - C_{23} + C_{13} \\
&\quad -C_{23,123} + C_{13,123} - C_{31,2} + C_{21,2} - C_{31,31} + C_{21,31} \\
&\quad +C_{32,1} - C_{12,1} + C_{32,32} - C_{12,32} + C_{13} - C_{23} \\
&\quad +C_{13,123} - C_{23,123} + C_{21,2} - C_{31,2} + C_{21,31} - C_{31,31} \\
&\quad +C_{23,2} - C_{13,2} + C_{23,13} - C_{13,13} + C_{31} - C_{21} \\
&\quad +C_{31,123} - C_{21,123} + C_{12,3} - C_{32,3} + C_{12,12} - C_{32,12} \\
&\quad -C_{13,2} + C_{23,2} - C_{13,13} + C_{23,13} - C_{21} + C_{31} \\
&\quad -C_{21,123} + C_{31,123} - C_{32,3} + C_{12,3} - C_{32,12} + C_{12,12}]
\end{aligned}$$

$$
\begin{aligned}
2\sqrt{2}A_z &= [C_{21,2} + C_{21,31} + C_{21,2} + C_{21,31} - C_{21} - C_{21,123} - C_{21} - C_{21,123} \\
&\quad -C_{31,2} - C_{31,31} - C_{31,2} - C_{31,31} + C_{31} + C_{31,123} + C_{31} + C_{31,123} \\
&\quad +C_{32,1} + C_{32,32} + C_{32,1} + C_{32,32} - C_{32,3} - C_{32,12} - C_{32,3} - C_{32,12} \\
&\quad -C_{12,1} - C_{12,32} - C_{12,1} - C_{12,32} + C_{12,3} + C_{12,12} + C_{12,3} + C_{12,12} \\
&\quad +C_{13} + C_{13,123} + C_{13} + C_{13,123} - C_{13,2} - C_{13,13} - C_{13,2} - C_{13,13} \\
&\quad -C_{23} - C_{23,123} - C_{23} - C_{23,123} + C_{23,2} + C_{23,13} + C_{23,2} + C_{23,13}]
\end{aligned}
$$

Therefore the intra-spacecraft contributions for A are,

$$
\begin{aligned}
\sqrt{2}A_z &= [C_{21,2} + C_{21,31} - C_{21} - C_{21,123}] + [-C_{31,2} - C_{31,31} + C_{31} + C_{31,123}] \\
&\quad +[C_{32,1} + C_{32,32} - C_{32,3} - C_{32,12}] + [-C_{12,1} - C_{12,32} + C_{12,3} + C_{12,12}] \\
&\quad +[C_{13} + C_{13,123} - C_{13,2} - C_{13,13}] + [-C_{23} - C_{23,123} + C_{23,2} + C_{23,13}]
\end{aligned}
$$

Combining the laser noise expressions for both types, gives a total laser noise contribution of,

$$
\begin{aligned}
\sqrt{2}A &= \sqrt{2}(A_y + A_z) \\
&= [-C_{21,2} - C_{21,31} + C_{21} + C_{21,123}] + [C_{21,2} + C_{21,31} - C_{21} - C_{21,123}] \\
&\quad +[C_{31,13} + C_{31,2} - C_{31} - C_{31,123}] + [-C_{31,2} - C_{31,31} + C_{31} + C_{31,123}] \\
&\quad +[-C_{32,1} - C_{32,23} + C_{32,3} + C_{32,12}] + [C_{32,1} + C_{32,32} - C_{32,3} - C_{32,12}] \\
&\quad +[C_{12,1} + C_{12,32} - C_{12,12} - C_{12,3}] + [-C_{12,1} - C_{12,32} + C_{12,3} + C_{12,12}] \\
&\quad +[-C_{13} - C_{13,123} + C_{13,2} + C_{13,13}] + [C_{13} + C_{13,123} - C_{13,2} - C_{13,13}] \\
&\quad +[C_{23} + C_{23,123} - C_{23,2} - C_{23,13}] + [-C_{23} - C_{23,123} + C_{23,2} + C_{23,13}] \\
&= 0
\end{aligned}
$$

It can be easily seen that the intra-spacecraft measurements provide equal and opposite terms to the laser noise contributions from the inter-spacecraft datastreams. The inter-

ferometric structures that ensured that α, β, γ are free from laser noise are are present in construction of the optimal combinations. The Uncorrelated Noise combination A is therefore not subject to laser noise terms.

Appendix G

Glossary

Notation used in General Relativity Chapter

$A_{xx,xy}$	Gravitational wave polarisation.
$A^{TT}_{\mu\nu}$	Gravitational wave amplitude tensor.
$a(t)$	Scale factor.
e_{ij}	Polarisation Coordinate terms.
$\eta_{\mu\nu}$	Minkowski metric tensor.
f_0	Characteristic frequency of the GW.
f_{max}	Maximum Gravitational wave frequency.
F^{GW}_j	Gravitational wave field.
G	Newtonian Gravitational Constant.
$G_{\mu\nu}$	Einstein Tensor.
$g_{\mu\nu}$	Metric tensor.
Γ^i_{jk}	Christoffel symbol.
h	Dimensionless gravitational wave amplitude.
$h_{\mu\nu}$	Metric perturbation term (tensor-like).
$\bar{h}_{\mu\nu}$	Gravitational field term.
h^{TT}_{xx}	Tranverse Traceless gravitational perturbation.
H_0	Current value of the Hubble constant.
$H(t)$	Hubble Constant.
L	Path length of interferometric Gravitational Detector.

Λ^{α}_{β}	Lorentz Transform.
$M_{\odot}$	Mass of the Sun.
$\mathcal{R}$	Ricci Scalar.
$\frac{\Delta\nu}{\nu}$ Phase stability of laser.	
$R^{\alpha}_{\beta\mu\nu}$	Riemann Curvature Tensor.
$R_{\mu\nu}$	Ricci Tensor.
$\rho(t)$	Energy Density of the Universe.
$T_{\mu\nu}$	Energy-Momentum Tensor.
θ	Phase of a wave.
ξ_{μ}	Infinitesimal Coordinate Transforms.

Notation for LISA Chapters

S/C	Spacecraft.
ν_0	Central frequency for laser light.
$a_{ij,k}$	Time Delay operator $a_{ij,k} = a_{ij}(t - L_k)$.
p_{ij}	Local laser light.
$\vec{\delta_{ij}}$	Proof mass displacement.
$\vec{\Delta_{ij}}$	Optical bench displacement.
$s_{ij}(t)$	Phase Inter-spacecraft measurement.
	Measured time series of phase difference between local and received laser light. Time integral of $\nu_0 y_{ij}(t)$
$\tau_{ij}(t)$	Intra-spacecraft measurement (Phase).
	Time integral of $\nu_0 z_{ij}(t)$.
$s^{GW}_{ij}(t)$	Phase modulation introduced by Gravitational Waves.
$s^{op}_{ij}(t)$	Phase modulation introduced by Optical Path Noise.

$y_{ij}(t)$	Frequency Inter-spacecraft measurement. Fractional (or normalised by center frequency) Doppler series derived from reception at S/C 1 and transmission at S/C 2
$z_{ij}(t)$	Time series of the frequency fluctuations in the intra-spacecraft measurement.
$y_{ij}^{GW}(t)$	Time series of frequency modulation introduced by Gravitational Waves.
$y_{ij}^{laser}(t)$	Time series of frequency modulation introduced by Laser Noise.
$y_{ij}^{op}(t)$	Time series of frequency modulation introduced by fluctuations in the Optical Path.
$y_{ij}^{laser}(t)$	Time series of frequency modulation introduced by Acceleration Noise.
$C_{ij}(t)$	Time series of fractional frequency fluctuations originating in the laser source on optical bench ij.
$p_i(t)$	Random phase fluctuations in the laser source i. Time integral of $\nu_i C_{ij}(t)$.
L_i	Arm length of antenna, distance between two spacecraft.
$\dot{L}_i$	Velocity of arm length i.
$\hat{n}_i$	Unit vectors between the spacecraft, positive in anti-clockwise direction.
S_y	Power spectrum for laser link y_{ij}
S_y^{shot}	Shot Noise spectral density, for an individual laser link y_{ij}
S_y^{op}	Optical Path Noise spectral density, for an individual laser link y_{ij}
F_I^+	Detector beam pattern coefficients for Detector I with plus polarisation signal.
$F_{II}^\times$	Detector beam pattern coefficients for Detector II with cross polarisation signal.

θ_S	Source azimuthal angle in spherical polar coordinates (x-y plane).
ϕ_S	Source polar angle in spherical polar coordinates (defined from z-axis).
ψ_S	Polarisation angle of the source wavefront.
$\bar{\theta}(t)$	Azimuthal motion of LISA's centre-of-mass in ecliptic coordinates.
$\bar{\phi}(t)$	Polar motion of LISA's centre-of-mass.
$\bar{\theta}$	Initial Azimuthal motion of LISA's centre-of-mass in ecliptic coordinates (defined as a constant).
T	Period of LISA's orbit.
(x, y, z)	Unbarred coordinate system, relating to detector frame.
$(\bar{x}, \bar{y}, \bar{z})$	Unbarred coordinate system, relating to ecliptic frame.
$y_{I,II}(t)$	LISA datastream for Michelson Configuration.
$H_{I,II}(t, \theta)$	Gravitational Wave signal, as seen by the detector, for Michelson Configuration.
$n_{I,II}(t)$	Noise datastream for Michelson Configuration.
$h_{+,\times}(t)$	Polarisation of the Gravitational waves source for Michelson Configuration.
c	Speed of light in vacuum.

G.1 Quick Reference

Measurement	Frequency	Phase
Inter-spacecraft	y_{ij}	s_{ij}
Intra-spacecraft	z_{ij}	τ_{ij}
Laser Fluctuations	C_{ij}	p_{ij}

Parameter	LISA Default Value [27]
Armlength	5×10^9m
Laser Power	1 W
Laser Wavelength	1064nm
Telescope Diameter	0.3m
Optical Efficiency	0.3

Appendix H

Matlab Code

This Appendix contains the Matlab scripts used to produce the results discussed in Chapters 4 and 5.

The first script (aet_prince_mar08_L) identifies the A, E and T combination terms that will have non-zero covariance at a particular time stamp of the LISA data stream. The second script (noisereal_sin) uses the information about which terms are present at each time stamp to investigate the effect of the time correlations on the parameter recovery for a sinusoidal signal.

```
%Code name: aet_prince_mar08_L

%This code produces the results shown in Chapter 4.

%This code builds up a list of the bench time stamps present in each of the
time delay combinations A, E and T in Prince el al. The model of the lisa
arm lengths has been modified from static to allow different variations of
the distances between the spacecraft. From the descriptions of AET in terms
of the individual bench terms, the code runs over the list of all the
contributing bench terms for each combination at each time and determines
if any of the terms in either list are the same. Note that it does it for
the laser noise (p) and other noise (n) terms separately, as they contain
different number of terms. See Chapter 2 for more information.

%If a combination can be found, then the terms with have positive
covariance and it is added to the AET covariance matrix ( 3-by-3 blocks
corresponding to the auto and cross covariances of the combinations at the
same time stamp). Combining the results for the laser and other noise terms
gives a indication of the source of any non-zero structure appearing in the
matrix. And finally, these results are plotted to show the structure and
the results read out to file.


%**************************************************************************
**************

clear all;

timestamps=30;

lvar=1;

L=15;

Ldiff1=0;   % differences in the first time stamp for the Lerror for the
armlength
Ldiff2=0;
Ldiff3=0;

fid = fopen('/home/jen/grahamspaper/eigenfaces/work_sept08/cov_AET_Ls.txt',
'w+');
fid2 = fopen
('/home/jen/grahamspaper/eigenfaces/work_sept08/cov_AET_sym_Ls.txt', 'w+');

AET_p(1:18,1:4,1:3,1:timestamps)=0;
AET_n(1:18,1:4,1:3,1:timestamps)=0;

if lvar==0
Lerror(1,(1:2*timestamps))=0.0;
end

if lvar==1 %small scale variation
      error=[1 0 -1 0];

      err_diff=timestamps/length(error);

      Lerror=error;
      for i=1:2*err_diff
            Lerror=cat(2,Lerror,error);
      end
end
```

```
if lvar==2 %large scale variation - varying once within timest time stamps

num_sin=1;
      err_diff=timestamps/(num_sin*2);


      Lerror(1,1:(1*err_diff))=0;
      Lerror(1,((1*err_diff)+1):(2*err_diff))=1;
      Lerror(1,((2*err_diff)+1):(3*err_diff))=0;
      Lerror(1,((3*err_diff)+1):(4*err_diff))=1;


end
if lvar==3 % sine top hat variation the size of the timest

      for i=1:2*timestamps
      t(i)=(i-1);
      sin_err(i)=round(sin((2*pi*t(i))/(timestamps-2))); % the timest-1
means that the wavelength is slightly lower than the time range ie so that
there are zeros on both end od the sin wave
      end

      for i=1:2*timestamps
      Lerror(i)=sin_err(i);
      end

end

for i=1:timestamps
L1(1,i)=L+Lerror(i+Ldiff1);L1d=L1;
L2(1,i)=L+Lerror(i+Ldiff2);L2d=L2;
L3(1,i)=L+Lerror(i+Ldiff3);L3d=L3;
end

fid3= fopen('/home/jen/grahamspaper/eigenfaces/work_sept08/Llengths.txt',
'w+');

for i=1:timestamps
fprintf(fid3,'%d %d %d\n',L1(i),L2(i),L3(i));
end
fclose(fid3);


for t=1:timestamps;

time(t)=t-1;
time_str{t}=int2str(t);
time_cov(t)=3.5+3*(t-1);

%L=5;
%L1=L;L1d=L1;
%L2=L;L2d=L2;
%L3=L;L3d=L3;



sn1=0.8; sn2=0.9; sn3=1.0; sn4=1.1; sn5=1.2; sn6=1.3;

%sn1=1; sn2=sn1; sn3=sn1; sn4=sn1; sn5=sn1; sn6=sn1;
```

```
%error on the arm length


%first column=sign,second=bench,third=timestamp, fourth=sigma n for the
bench
%p_1 is the laser noise terms in the signal s_1, ie. s_1^{laser}.
%n_1 are the remaining noise terms.

%spacecraft dependent laser noise
      %p_1=[1,2,(-L3d+(time(t))),sn4;-1,1,time(t),sn1];  n_1=[1,1,time
(t),sn1];    %s_1=[1,2,-L3d;-1,1,0;1,31,0]; % ie 31=1=1
      %p_1d=[1,3,(-L2+(time(t))),sn5;-1,1,time(t),sn2];  n_1d=[1,2,time
(t),sn2];   %s_1d=[1,3,-L2;-1,1,0;1,21,0]; % ie 21=1'=2
      %p_2=[1,3,(-L1d+(time(t))),sn6;-1,2,time(t),sn3];  n_2=[1,3,time
(t),sn3];    %s_2=[1,3,-L1d;-1,2,0;1,12,0]; % ie 12=2=3
      %p_2d=[1,1,(-L3+(time(t))),sn1;-1,2,time(t),sn4];  n_2d=[1,4,time
(t),sn4];   %s_2d=[1,1,-L3;-1,2,0;1,32,0]; % ie 32=2'=4
      %p_3=[1,1,(-L2d+(time(t))),sn2;-1,3,time(t),sn5];  n_3=[1,5,time
(t),sn5];    %s_3=[1,1,-L2d;-1,3,0;1,23,0]; % ie 23=3=5
      %p_3d=[1,2,(-L1+(time(t))),sn3;-1,3,time(t),sn6];  n_3d=[1,6,time
(t),sn6];   %s_3d=[1,2,-L1;-1,3,0;1,13,0]; % ie 13=3'=6

%spacecraft dependent laser noise
      p_1=[1,2,(-L3d(t)+(time(t))),sn4;-1,1,time(t),sn1];  n_1=[1,1,time
(t),sn1];    %s_1=[1,2,-L3d;-1,1,0;1,31,0]; % ie 31=1=1
      p_1d=[1,3,(-L2(t)+(time(t))),sn5;-1,1,time(t),sn2];  n_1d=[1,2,time
(t),sn2];   %s_1d=[1,3,-L2;-1,1,0;1,21,0]; % ie 21=1'=2
      p_2=[1,3,(-L1d(t)+(time(t))),sn6;-1,2,time(t),sn3];  n_2=[1,3,time
(t),sn3];    %s_2=[1,3,-L1d;-1,2,0;1,12,0]; % ie 12=2=3
      p_2d=[1,1,(-L3(t)+(time(t))),sn1;-1,2,time(t),sn4];  n_2d=[1,4,time
(t),sn4];   %s_2d=[1,1,-L3;-1,2,0;1,32,0]; % ie 32=2'=4
      p_3=[1,1,(-L2d(t)+(time(t))),sn2;-1,3,time(t),sn5];  n_3=[1,5,time
(t),sn5];    %s_3=[1,1,-L2d;-1,3,0;1,23,0]; % ie 23=3=5
      p_3d=[1,2,(-L1(t)+(time(t))),sn3;-1,3,time(t),sn6];  n_3d=[1,6,time
(t),sn6];   %s_3d=[1,2,-L1;-1,3,0;1,13,0]; % ie 13=3'=6


%optical bench dependent laser noise numbering in tinto
      %p_1=[1,32,(-L3d+(time(t))),sn4;-1,31,time(t),sn1];  n_1=[1,1,time
(t),sn1];    %s_1=[1,2,-L3d;-1,1,0;1,31,0]; % ie 31=1=1
      %p_1d=[1,23,(-L2+(time(t))),sn5;-1,21,time(t),sn2];  n_1d=[1,2,time
(t),sn2];   %s_1d=[1,3,-L2;-1,1,0;1,21,0]; % ie 21=1'=2
      %p_2=[1,13,(-L1d+(time(t))),sn6;-1,12,time(t),sn3];  n_2=[1,3,time
(t),sn3];    %s_2=[1,3,-L1d;-1,2,0;1,12,0]; % ie 12=2=3
      %p_2d=[1,31,(-L3+(time(t))),sn1;-1,32,time(t),sn4];  n_2d=[1,4,time
(t),sn4];   %s_2d=[1,1,-L3;-1,2,0;1,32,0]; % ie 32=2'=4
      %p_3=[1,21,(-L2d+(time(t))),sn2;-1,23,time(t),sn5];  n_3=[1,5,time
(t),sn5];    %s_3=[1,1,-L2d;-1,3,0;1,23,0]; % ie 23=3=5
      %p_3d=[1,12,(-L1+(time(t))),sn3;-1,13,time(t),sn6];  n_3d=[1,6,time
(t),sn6];   %s_3d=[1,2,-L1;-1,3,0;1,13,0]; % ie 13=3'=6

%optical bench dependent laser noise numbering 1-6
      %p_1=[1,4,(-L3d+(time(t))),sn4;-1,1,time(t),sn1];  n_1=[1,1,time
(t),sn1];    %s_1=[1,2,-L3d;-1,1,0;1,31,0]; % ie 31=1=1
      %p_1d=[1,5,(-L2+(time(t))),sn5;-1,2,time(t),sn2];  n_1d=[1,2,time
(t),sn2];   %s_1d=[1,3,-L2;-1,1,0;1,21,0]; % ie 21=1'=2
      %p_2=[1,6,(-L1d+(time(t))),sn6;-1,3,time(t),sn3];  n_2=[1,3,time
(t),sn3];    %s_2=[1,3,-L1d;-1,2,0;1,12,0]; % ie 12=2=3
      %p_2d=[1,1,(-L3+(time(t))),sn1;-1,4,time(t),sn4];  n_2d=[1,4,time
(t),sn4];   %s_2d=[1,1,-L3;-1,2,0;1,32,0]; % ie 32=2'=4
```

```
      %p_3=[1,2,(-L2d+(time(t))),sn2;-1,5,time(t),sn5];  n_3=[1,5,time
(t),sn5];    %s_3=[1,1,-L2d;-1,3,0;1,23,0]; % ie 23=3=5
      %p_3d=[1,3,(-L1+(time(t))),sn3;-1,6,time(t),sn6];  n_3d=[1,6,time
(t),sn6];   %s_3d=[1,2,-L1;-1,3,0;1,13,0]; % ie 13=3'=6

      %z_21=[0.5,31,time(t),sn2;-0.5,21,time(t),sn1];
      %z_31=[0.5,21,time(t),sn1;-0.5,31,time(t),sn2];
      %z_12=[0.5,32,time(t),sn4;-0.5,12,time(t),sn3];
      %z_32=[0.5,12,time(t),sn3;-0.5,32,time(t),sn4];
      %z_23=[0.5,13,time(t),sn6;-0.5,23,time(t),sn5];
      %z_13=[0.5,23,time(t),sn5;-0.5,13,time(t),sn6];

      %C_31=[1,31,time(t),sn1];C_21=[1,21,time(t),sn2];C_12=[1,12,time
(t),sn3];C_32=[1,32,time(t),sn4];
      %C_23=[1,23,time(t),sn5];C_13=[1,13,time(t),sn6];

timeLs=[0 0 -1 0; 0 0 -1 0];
signLs=[-1 1 1 1; -1 1 1 1]; % this will change the sign of a laser noise
component to the opposite that it is beforehand

%halfLs=[0.5 1 1 1; 0.5 1 1 1]; % this is to add in the half factor on the
intra-spacecraft terms.

timeNs=[0 0 -1 0];
signNs=[-1 1 1 1];% this will change the sign of a laser noise component to
the opposite that it is beforehand

alpha_p(:,:,t)=cat(1,p_1d,(signLs.*p_1),(p_3d+(L2(t)*timeLs)),((signLs.*p_
2)+(L3(t)*timeLs)),(p_2d+((L1(t)+L2(t))*timeLs)),((signLs.*p_3)+((L1(t)+L3
(t))*timeLs)));
beta_p(:,:,t)=cat(1,p_2d,(signLs.*p_2),(p_1d+(L3(t)*timeLs)),((signLs.*p_3)
+(L1(t)*timeLs)),(p_3d+((L2(t)+L3(t))*timeLs)),((signLs.*p_1)+((L2(t)+L1
(t))*timeLs)));
gamma_p(:,:,t)=cat(1,p_3d,(signLs.*p_3),(p_2d+(L1(t)*timeLs)),((signLs.*p_
1)+(L2(t)*timeLs)),(p_1d+((L3(t)+L1(t))*timeLs)),((signLs.*p_2)+((L3(t)+L2
(t))*timeLs)));

alpha_n(:,:,t)=cat(1,n_1d,(signNs.*n_1),(n_3d+(L2(t)*timeNs)),((signNs.*n_
2)+(L3(t)*timeNs)),(n_2d+((L1(t)+L2(t))*timeNs)),((signNs.*n_3)+((L1(t)+L3
(t))*timeNs)));
beta_n(:,:,t)=cat(1,n_2d,(signNs.*n_2),(n_1d+(L3(t)*timeNs)),((signNs.*n_3)
+(L1(t)*timeNs)),(n_3d+((L2(t)+L3(t))*timeNs)),((signNs.*n_1)+((L2(t)+L1
(t))*timeNs)));
gamma_n(:,:,t)=cat(1,n_3d,(signNs.*n_3),(n_2d+(L1(t)*timeNs)),((signNs.*n_
1)+(L2(t)*timeNs)),(n_1d+((L3(t)+L1(t))*timeNs)),((signNs.*n_2)+((L3(t)+L2
(t))*timeNs)));

%alpha_z(:,:,t)=cat(1,((signNs.*C_23)+((L2)*timeNs)),((C_13)+((L2)
*timeNs)),((signNs.*C_23)+((L1+L3)*timeNs)),((C_13)+((L1+L3)*timeNs)),
((signNs.*C_31)),((C_21)),((signNs.*C_31)+((L1+L2+L3)*timeNs)),((C_21)+((L1
+L2+L3)*timeNs)),((signNs.*C_12)+((L3)*timeNs)),((C_32)+((L3)*timeNs)),
((signNs.*C_12)+((L1+L2)*timeNs)),((C_32)+((L1+L2)*timeNs)));

%beta_z(:,:,t)=cat(1,((signNs.*C_31)+((L3)*timeNs)),((C_21)+((L3)*timeNs)),
((signNs.*C_31)+((L2+L1)*timeNs)),((C_21)+((L2+L1)*timeNs)),((signNs.*C_
12)),((C_32)),((signNs.*C_12)+((L1+L2+L3)*timeNs)),((C_32)+((L1+L2+L3)
*timeNs)),((signNs.*C_23)+((L1)*timeNs)),((C_13)+((L1)*timeNs)),((signNs.
*C_23)+((L2+L3)*timeNs)),((C_13)+((L2+L3)*timeNs)));

%gamma_z(:,:,t)=cat(1,((signNs.*C_12)+((L1)*timeNs)),((C_32)+((L1)
*timeNs)),((signNs.*C_12)+((L3+L2)*timeNs)),((C_32)+((L3+L2)*timeNs)),
```

```
((signNs.*C_23)),((C_13)),((signNs.*C_23)+((L1+L2+L3)*timeNs)),((C_13)+((L1
+L2+L3)*timeNs)),((signNs.*C_31)+((L2)*timeNs)),((C_21)+((L2)*timeNs)),
((signNs.*C_31)+((L3+L1)*timeNs)),((C_21)+((L3+L1)*timeNs)));



%alpha_z(:,:,t)=cat(1,(signLs.*(z_13+(L2*timeLs))),(signLs.*(z_13+((L1+L3)
*timeLs))),(signLs.*(z_21)),(signLs.*(z_21+((L1+L2+L3)*timeLs))),(signLs.*
(z_32+(L3*timeLs))),(signLs.*(z_32+((L1+L2)*timeLs))),(z_23+((L2)*timeLs)),
(z_23+((L1+L3)*timeLs)),(z_31),(z_31+((L1+L2+L3)*timeLs)),(z_12+((L3)
*timeLs)),(z_12+((L1+L2)*timeLs)));

%beta_z(:,:,t)=cat(1,(signLs.*(z_21+(L3*timeLs))),(signLs.*(z_21+((L2+L1)
*timeLs))),(signLs.*(z_32)),(signLs.*(z_32+((L1+L2+L3)*timeLs))),(signLs.*
(z_13+(L1*timeLs))),(signLs.*(z_13+((L2+L3)*timeLs))),(z_31+((L3)*timeLs)),
(z_31+((L2+L1)*timeLs)),(z_12),(z_12+((L1+L2+L3)*timeLs)),(z_23+((L1)
*timeLs)),(z_23+((L2+L3)*timeLs)));

%gamma_z(:,:,t)=cat(1,(signLs.*(z_32+(L1*timeLs))),(signLs.*(z_32+((L3+L2)
*timeLs))),(signLs.*(z_13)),(signLs.*(z_13+((L1+L2+L3)*timeLs))),(signLs.*
(z_21+(L2*timeLs))),(signLs.*(z_21+((L3+L1)*timeLs))),(z_12+((L1)*timeLs)),
(z_12+((L3+L2)*timeLs)),(z_23),(z_23+((L1+L2+L3)*timeLs)),(z_31+((L2)
*timeLs)),(z_31+((L3+L1)*timeLs)));




%abg_p(:,:,1,t)=alpha_p(:,:,t);abg_p(:,:,2,t)=beta_p(:,:,t);abg_p(:,:,3,t)
=gamma_p(:,:,t);

%abg_n(:,:,1,t)=alpha_n(:,:,t);abg_n(:,:,2,t)=beta_n(:,:,t);abg_n(:,:,3,t)
=gamma_n(:,:,t);

%concatenating AET from alpha,beta,gamma_p.
neg_alpha_p(:,:,t)=alpha_p(:,:,t);
%neg_alpha_z(:,:,t)=alpha_z(:,:,t);
neg_beta_p(:,:,t)=beta_p(:,:,t);
%neg_beta_z(:,:,t)=beta_z(:,:,t);
for i=1:size(alpha_p,1)
neg_alpha_p(i,1,t)=-1*neg_alpha_p(i,1,t);
%neg_alpha_z(i,1,t)=-1*neg_alpha_z(i,1,t);
neg_beta_p(i,1,t)=-2*neg_beta_p(i,1,t);
%neg_beta_z(i,1,t)=-2*neg_beta_z(i,1,t); %taking care of the factor of 2
end

%A_p=cat(1,gamma_p,gamma_z,neg_alpha_p,neg_alpha_z);
%E_p=cat(1,alpha_p,alpha_z,neg_beta_p,neg_beta_z,gamma_p,gamma_z);
%T_p=cat(1,alpha_p,alpha_z,beta_p,beta_z,gamma_p,gamma_z);

A_p=cat(1,gamma_p,neg_alpha_p);
E_p=cat(1,alpha_p,neg_beta_p,gamma_p);
T_p=cat(1,alpha_p,beta_p,gamma_p);

%A_z=cat(1,gamma_z,neg_alpha_z);
%E_z=cat(1,alpha_z,neg_beta_z,gamma_n);
%T_z=cat(1,alpha_z,beta_z,gamma_z);
```

```
AET_p(1:size(A_p,1),:,1,t)=A_p(:,:,t);AET_p(1:size(E_p,1),:,2,t)=E_p
(:,:,t);AET_p(1:size(T_p,1),:,3,t)=T_p(:,:,t);

%concatenating AET from alpha,beta,gamma_n.
neg_alpha_n(:,:,t)=alpha_n(:,:,t);
neg_beta_n(:,:,t)=beta_n(:,:,t);
      for i=1:size(alpha_n,1)
      neg_alpha_n(i,1,t)=-1*neg_alpha_n(i,1,t);
      neg_beta_n(i,1,t)=-2*neg_beta_n(i,1,t);
      end

A_n=cat(1,gamma_n,neg_alpha_n);
E_n=cat(1,alpha_n,neg_beta_n,gamma_n);
T_n=cat(1,alpha_n,beta_n,gamma_n);

AET_n(1:size(A_n,1),:,1,t)=A_n(:,:,t);AET_n(1:size(E_n,1),:,2,t)=E_n
(:,:,t);AET_n(1:size(T_n,1),:,3,t)=T_n(:,:,t);

end
      %cov_p(min(alpha_p(:,3)),:max(alpha_p(:,3)),1:3,1:timestamps)=0;

for i=1:timestamps
for j=1:timestamps
for g=1:3
for h=1:3
      cov_sym{i,j}='0';
      cov_p_sym{g,h,i,j}='0';
cov_p(g,h,i,j)=0.0;
cov_n(g,h,i,j)=0.0;
end
end
end
end
jj=1;ii=1;
for i=1:timestamps
for j=1:timestamps

      for g=1:3
      for h=1:3

      for k=1:size(AET_n,1)
      for m=1:size(AET_n,1)

            if (AET_n(k,2,g,i)==AET_n(m,2,h,j)) && (AET_n(k,2,g,i)~=0)
            if AET_n(k,3,g,i)==AET_n(m,3,h,j)
                  %cov_n(abs(abg_n(k,3,i,j)),abg_n(k,2,i,j),i)=abg_n
(k,1,i,j)*abg_n(m,1,i,j);#
            %cov_n(g,h,i,j)=1;
            %cov_n(g,h,i,j)=cov_n(g,h,i,j)+1;
            cov_n(g,h,i,j)=cov_n(g,h,i,j)+(AET_n(k,4,g,i)*(AET_n(k,1,g,i)
*AET_n(m,1,h,j)));

            %cov_n_sym{g,h,i,j}='n';

            covlist_n(jj,1)=AET_n(k,2,g,i);
            covlist_n(jj,2)=AET_n(k,3,g,i);
            covlist_n(jj,3)=i;
            covlist_n(jj,4)=AET_n(k,1,g,i);
            jj=jj+1;
            end
            end
```

```
      end
      end


      for k=1:size(AET_p,1)
      for m=1:size(AET_p,1)

            if (AET_p(k,2,g,i)==AET_p(m,2,h,j)) && (AET_p(k,2,g,i)~=0)
            if AET_p(k,3,g,i)==AET_p(m,3,h,j)
            %cov_p(g,h,i,j)=1;
            %cov_p(g,h,i,j)=cov_p(g,h,i,j)+100;
            %cov_p(g,h,i,j)=cov_p(g,h,i,j)+(100*(AET_p(k,1,g,i)*AET_p
(m,1,h,j)));
            %cov_p(g,h,i,j)=cov_p(g,h,i,j)+(AET_p(k,4,g,i)*(AET_p(k,1,g,i)
*AET_p(m,1,h,j)));
            cov_p(g,h,i,j)=cov_p(g,h,i,j)+(100*(AET_p(k,1,g,i)*AET_p
(m,1,h,j)));
            cov_p_sym{g,h,i,j}='p';
            covlist_p(ii,1)=AET_p(k,2,g,i);
            covlist_p(ii,2)=AET_p(k,3,g,i);
            covlist_p(ii,3)=i;
            covlist_p(ii,4)=AET_p(k,1,g,i);
            ii=ii+1;
            end
            end
      end
      end
            %cov_pn(1,1,i,j)=cov_p(1,1,i,j)+cov_n(1,1,i,j);
      end
      end


end
end

for i=1:timestamps
for j=1:timestamps

      for g=1:3
      for h=1:3

            cov_pn(g,h,i,j)=cov_p(g,h,i,j)+cov_n(g,h,i,j);

      end
      end


end
end

      Cov_p_1(1:(3*timestamps),1:(3*timestamps))=0;

Cov_p_1(1:3,1:3)=cov_p(:,:,1,1);
for i=1:timestamps
      for j=1:timestamps
            Cov_p_1((((i-1)*3)+1):((i-1)*3)+3,(((j-1)*3)+1):(((j-1)*3)+3))
=cov_p(:,:,j,i);
      end
end

      Cov_pn_1(1:(3*timestamps),1:(3*timestamps))=0;
```

```
Cov_pn_1(1:3,1:3)=cov_pn(:,:,1,1);
for i=1:timestamps
      for j=1:timestamps
            Cov_pn_1((((i-1)*3)+1):((i-1)*3)+3,(((j-1)*3)+1):(((j-1)*3)+3))
=cov_pn(:,:,j,i);
      end
end

      Cov_n_1(1:(3*timestamps),1:(3*timestamps))=0;

Cov_n_1(1:3,1:3)=cov_n(:,:,1,1);
for i=1:timestamps
      for j=1:timestamps
            Cov_n_1((((i-1)*3)+1):((i-1)*3)+3,(((j-1)*3)+1):(((j-1)*3)+3))
=cov_n(:,:,j,i);
      end
end

Cov_p=Cov_p_1(:,:);
Cov_n=Cov_n_1(:,:);
Cov_pn=Cov_pn_1(:,:);

for i=1:timestamps
for j=1:timestamps

for ii=1:3
for jj=1:3

      if Cov_pn(((3*(i-1))+ii),(3*(j-1)+jj))~=0
            cov_n_sym{ii,jj,i,j}=[int2str(Cov_pn(((3*(i-1))+ii),(3*(j-1)
+jj))),'*n '];
      else
            cov_n_sym{ii,jj,i,j}='0 ';
      end
end
end
end
end

%concatenating the covariance matix together for the symbolic matrix
for j=1:timestamps
for i=1:3

      if i==1 && j==1
      C_sym_all=char(cov_n_sym(:,i,:,j));
      else
      C_sym_all=cat(2,C_sym_all,char(cov_n_sym(:,i,:,j)));
      end
end
end




figure(1);
imagesc(Cov_pn);colormap(bone);axis square

%[V,D]=eig(Cov_pn);

for i=1:length(Cov_n)
```

```
for j=1:length(Cov_n)
      if(j==length(Cov_n))
            fprintf(fid, '%d\n',Cov_n(i,j));
        else
            fprintf(fid, '%d ',Cov_n(i,j));
        end
end
end

fclose(fid);

for i=1:size(C_sym_all,1)
fprintf(fid2,'%s \n',C_sym_all(i,:));
end

fclose(fid2);

figure(2);
imagesc(Cov_pn);colormap(bone);axis square;xlabel('Time
stamps','FontSize',12,'FontWeight','bold');Ylabel('Time
stamps','Fontsize',12,'FontWeight','bold');set
(gca,'FontSize',12,'FontWeight','bold','XTick',time_cov,'XTickLabel',time_s
tr,'XGrid','on','YTick',time_cov,'YTickLabel',time_str,'YGrid','on')
%figure(3);
%imagesc(Cov_pn(19:21,4:6));colormap(gray);axis square;set
(gca,'XTickLabel',{'A(2)';'E(2)';'T(2)'},'YTick',[1,2,3],'YTickLabel',{'A
(7)';'E(7)';'T(7)'});colorbar('EastOutside','Box','on','XLim',[-0.5
1.5],'YTick',[-12 -8 -4 -3 -2 -1 0 1 2 3 4 8 12]);

%figure(4);subplot(1,2,1);imagesc(V);xlabel('V');colormap(bone);
%subplot(1,2,2);imagesc(D);xlabel('D');colormap(bone);
```

```
%Code name: noisereal_sin

%Code produces the results described in Chapter Five.

%This code builds on the analysis in script: aet_prince_mar08_L.

%A data signal is created using two sinusoids and a noise stream, created
from the optical bench terms present at each combination time stamp and
then performs a parameter search following that discussed in Chapter Five,
and then outputs the results to file.

%*******************************************

clear all;

timen=1000; % number of timestamps
timen_ex=0; % adding some on the end of the timestamps, so when the noise
is worked out there are no end effects.

m1=400; %number of models of each frequency , total model number=m^2
m2=400;

m1_flow=0.0015; %lowest frequency for models
m1_fhi=0.0025;

m2_flow=0.0015; %lowest frequency for models
m2_fhi=0.0025;

%opening files for saving data
fid = fopen('/home/jen/grahamspaper/eigenfaces/cov_notime.txt', 'w+');
fid2 = fopen('/home/jen/grahamspaper/eigenfaces/cov_time.txt', 'w+');
fid3 = fopen('/home/jen/grahamspaper/eigenfaces/conf_notime.txt', 'w+');
fid4 = fopen('/home/jen/grahamspaper/eigenfaces/conf_time.txt', 'w+');

fid5 = fopen('/home/jen/grahamspaper/eigenfaces/parameters.txt','w+');

fprintf(fid5,'%d\n',timen);
fprintf(fid5,'%d\n',m1);
fprintf(fid5,'%d\n',m2);
fprintf(fid5,'%d\n',m1_flow);
fprintf(fid5,'%d\n',m1_fhi);
fprintf(fid5,'%d\n',m2_flow);
fprintf(fid5,'%d\n',m2_fhi);

%true data variables
freq1=0.002
A1=1e-21;
freq2=0.0021
A2=1.1e-21;
c=3e8;

fprintf(fid5,'%d\n',freq1);
fprintf(fid5,'%d\n',freq2);
fprintf(fid5,'%d\n',A1);
fprintf(fid5,'%d\n',A2);

%variances for the noises
S_laser=1e-26; %value taken from grahamspaper
S_shot=5.3e-38;
S_pm=2.5e-48;
S_op=1.8e-37;
```

```
%var_noise=S_pm+S_op+S_shot;

var_noise=1e-42;

fprintf(fid5,'%d\n',var_noise);

%armlength size
L=15;
L1=L;L1d=L1;
L2=L;L2d=L2;
L3=L;L3d=L3;

fprintf(fid5,'%d\n',L);

%creating gaussian noise streams for each spacecraft/optical bench

noiseload=load('/home/jen/grahamspaper/eigenfaces/noise.txt', 'r');
noiserand(1:timen,1)=noiseload(1:timen,1);
noiserand(1:timen,2)=noiseload(1:timen,2);
noiserand(1:timen,3)=noiseload(1:timen,3);
noiserand(1:timen,4)=noiseload(1:timen,4);
noiserand(1:timen,5)=noiseload(1:timen,5);
noiserand(1:timen,6)=noiseload(1:timen,6);

      for i=1:(timen+timen_ex)
      laser(i,1)=(randn*sqrt(S_laser));
      laser(i,2)=(randn*sqrt(S_laser));
      laser(i,3)=(randn*sqrt(S_laser));

      %noise(i,1)=(randn*sqrt(var_noise));
      %noise(i,2)=(randn*sqrt(var_noise));
      %noise(i,3)=(randn*sqrt(var_noise));
      %noise(i,4)=(randn*sqrt(var_noise));
      %noise(i,5)=(randn*sqrt(var_noise));
      %noise(i,6)=(randn*sqrt(var_noise));

      noise(i,1)=(noiserand(i,1)*sqrt(var_noise));
      noise(i,2)=(noiserand(i,2)*sqrt(var_noise));
      noise(i,3)=(noiserand(i,3)*sqrt(var_noise));
      noise(i,4)=(noiserand(i,4)*sqrt(var_noise));
      noise(i,5)=(noiserand(i,5)*sqrt(var_noise));
      noise(i,6)=(noiserand(i,6)*sqrt(var_noise));

      end


%creating combined noise datastream for A,E,T

%fid = fopen('/home/jen/grahamspaper/eigenfaces/cov_aet.txt', 'w+');
%fid2 = fopen('/home/jen/grahamspaper/eigenfaces/cov_aet_sym.txt', 'w+');

AET_p(1:18,1:4,1:3,1:timen)=0;
AET_n(1:18,1:4,1:3,1:timen)=0;

for t=1:(timen+timen_ex);

      time(t)=t-1;
      time_str{t}=int2str(time(t));
      time_cov(t)=3.5+3*(t-1);
```

```
%sn1=0.8; sn2=0.9; sn3=0.9; sn4=1; sn5=1; sn6=0.8;

sn1=var_noise; sn2=sn1; sn3=sn1; sn4=sn1; sn5=sn1; sn6=sn1;

      %first column=sign,second=bench,third=timestamp, fourth=sigma n for
the bench

      p_1=[1,32,(-L3d+(time(t))),sn4;-1,31,time(t),sn1];  n_1=[1,1,time
(t),sn1];    %s_1=[1,2,-L3d;-1,1,0;1,31,0]; % ie 31=1=1
      p_1d=[1,23,(-L2+(time(t))),sn5;-1,21,time(t),sn2];  n_1d=[1,2,time
(t),sn2];   %s_1d=[1,3,-L2;-1,1,0;1,21,0]; % ie 21=1'=2
      p_2=[1,13,(-L1d+(time(t))),sn6;-1,12,time(t),sn3];  n_2=[1,3,time
(t),sn3];    %s_2=[1,3,-L1d;-1,2,0;1,12,0]; % ie 12=2=3
      p_2d=[1,31,(-L3+(time(t))),sn1;-1,32,time(t),sn4];  n_2d=[1,4,time
(t),sn4];   %s_2d=[1,1,-L3;-1,2,0;1,32,0]; % ie 32=2'=4
      p_3=[1,21,(-L2d+(time(t))),sn2;-1,23,time(t),sn5];  n_3=[1,5,time
(t),sn5];    %s_3=[1,1,-L2d;-1,3,0;1,23,0]; % ie 23=3=5
      p_3d=[1,12,(-L1+(time(t))),sn3;-1,13,time(t),sn6];  n_3d=[1,6,time
(t),sn6];   %s_3d=[1,2,-L1;-1,3,0;1,13,0]; % ie 13=3'=6

      C_31=[1,31,time(t),sn1];C_21=[1,21,time(t),sn2];C_12=[1,12,time
(t),sn3];C_32=[1,32,time(t),sn4];
      C_23=[1,23,time(t),sn5];C_13=[1,13,time(t),sn6];

      timeLs=[0 0 -1 0; 0 0 -1 0];
      signLs=[-1 1 1 1; -1 1 1 1]; % this will change the sign of a laser
noise component to the opposite that it is beforehand


      timeNs=[0 0 -1 0];
      signNs=[-1 1 1 1];% this will change the sign of a laser noise
component to the opposite that it is beforehand

      alpha_p(:,:,t)=cat(1,p_1d,(signLs.*p_1),(p_3d+(L2*timeLs)),((signLs.
*p_2)+(L3*timeLs)),(p_2d+((L1+L2)*timeLs)),((signLs.*p_3)+((L1+L3)
*timeLs)));
      beta_p(:,:,t)=cat(1,p_2d,(signLs.*p_2),(p_1d+(L3*timeLs)),((signLs.
*p_3)+(L1*timeLs)),(p_3d+((L2+L3)*timeLs)),((signLs.*p_1)+((L2+L1)
*timeLs)));
      gamma_p(:,:,t)=cat(1,p_3d,(signLs.*p_3),(p_2d+(L1*timeLs)),((signLs.
*p_1)+(L2*timeLs)),(p_1d+((L3+L1)*timeLs)),((signLs.*p_2)+((L3+L2)
*timeLs)));

      alpha_n(:,:,t)=cat(1,n_1d,(signNs.*n_1),(n_3d+(L2*timeNs)),((signNs.
*n_2)+(L3*timeNs)),(n_2d+((L1+L2)*timeNs)),((signNs.*n_3)+((L1+L3)
*timeNs)));
      beta_n(:,:,t)=cat(1,n_2d,(signNs.*n_2),(n_1d+(L3*timeNs)),((signNs.
*n_3)+(L1*timeNs)),(n_3d+((L2+L3)*timeNs)),((signNs.*n_1)+((L2+L1)
*timeNs)));
      gamma_n(:,:,t)=cat(1,n_3d,(signNs.*n_3),(n_2d+(L1*timeNs)),((signNs.
*n_1)+(L2*timeNs)),(n_1d+((L3+L1)*timeNs)),((signNs.*n_2)+((L3+L2)
*timeNs)));


      alpha_z(:,:,t)=cat(1,((signNs.*C_23)+((L2)*timeNs)),((C_13)+((L2)
*timeNs)),((signNs.*C_23)+((L1+L3)*timeNs)),((C_13)+((L1+L3)*timeNs)),
((signNs.*C_31)),((C_21)),((signNs.*C_31)+((L1+L2+L3)*timeNs)),((C_21)+((L1
+L2+L3)*timeNs)),((signNs.*C_12)+((L3)*timeNs)),((C_32)+((L3)*timeNs)),
((signNs.*C_12)+((L1+L2)*timeNs)),((C_32)+((L1+L2)*timeNs)));
```

```
      beta_z(:,:,t)=cat(1,((signNs.*C_31)+((L3)*timeNs)),((C_21)+((L3)
*timeNs)),((signNs.*C_31)+((L2+L1)*timeNs)),((C_21)+((L2+L1)*timeNs)),
((signNs.*C_12)),((C_32)),((signNs.*C_12)+((L1+L2+L3)*timeNs)),((C_32)+((L1
+L2+L3)*timeNs)),((signNs.*C_23)+((L1)*timeNs)),((C_13)+((L1)*timeNs)),
((signNs.*C_23)+((L2+L3)*timeNs)),((C_13)+((L2+L3)*timeNs)));

      gamma_z(:,:,t)=cat(1,((signNs.*C_12)+((L1)*timeNs)),((C_32)+((L1)
*timeNs)),((signNs.*C_12)+((L3+L2)*timeNs)),((C_32)+((L3+L2)*timeNs)),
((signNs.*C_23)),((C_13)),((signNs.*C_23)+((L1+L2+L3)*timeNs)),((C_13)+((L1
+L2+L3)*timeNs)),((signNs.*C_31)+((L2)*timeNs)),((C_21)+((L2)*timeNs)),
((signNs.*C_31)+((L3+L1)*timeNs)),((C_21)+((L3+L1)*timeNs)));
      %abg_p(:,:,1,t)=alpha_p(:,:,t);abg_p(:,:,2,t)=beta_p(:,:,t);abg_p
(:,:,3,t)=gamma_p(:,:,t);

      %abg_n(:,:,1,t)=alpha_n(:,:,t);abg_n(:,:,2,t)=beta_n(:,:,t);abg_n
(:,:,3,t)=gamma_n(:,:,t);

      %concatenating AET from alpha,beta,gamma_p.
      neg_alpha_p(:,:,t)=alpha_p(:,:,t);
      neg_alpha_z(:,:,t)=alpha_z(:,:,t);
      neg_beta_p(:,:,t)=beta_p(:,:,t);
      neg_beta_z(:,:,t)=beta_z(:,:,t);
      for i=1:size(alpha_p,1)
      neg_alpha_p(i,1,t)=-1*neg_alpha_p(i,1,t);
      neg_alpha_z(i,1,t)=-1*neg_alpha_z(i,1,t);
      neg_beta_p(i,1,t)=-2*neg_beta_p(i,1,t);
      neg_beta_z(i,1,t)=-2*neg_beta_z(i,1,t); %taking care of the factor of
2
      end

      A_p=cat(1,gamma_p,gamma_z,neg_alpha_p,neg_alpha_z);
      E_p=cat(1,alpha_p,alpha_z,neg_beta_p,neg_beta_z,gamma_p,gamma_z);
      T_p=cat(1,alpha_p,alpha_z,beta_p,beta_z,gamma_p,gamma_z);

      %A_p=cat(1,gamma_p,neg_alpha_p);
      %E_p=cat(1,alpha_p,neg_beta_p,gamma_p);
      %T_p=cat(1,alpha_p,beta_p,gamma_p);

      A_z=cat(1,gamma_z,neg_alpha_z);
      E_z=cat(1,alpha_z,neg_beta_z,gamma_n);
      T_z=cat(1,alpha_z,beta_z,gamma_z);

      AET_p(1:size(A_p,1),:,1,t)=A_p(:,:,t);AET_p(1:size(E_p,1),:,2,t)=E_p
(:,:,t);AET_p(1:size(T_p,1),:,3,t)=T_p(:,:,t);

      %concatenating AET from alpha,beta,gamma_n.
      neg_alpha_n(:,:,t)=alpha_n(:,:,t);
      neg_beta_n(:,:,t)=beta_n(:,:,t);
            for i=1:size(alpha_n,1)
            neg_alpha_n(i,1,t)=-1*neg_alpha_n(i,1,t);
            neg_beta_n(i,1,t)=-2*neg_beta_n(i,1,t);
            end

      A_n=cat(1,gamma_n,neg_alpha_n);
      E_n=cat(1,alpha_n,neg_beta_n,gamma_n);
      T_n=cat(1,alpha_n,beta_n,gamma_n);

      AET_n(1:size(A_n,1),:,1,t)=A_n(:,:,t);AET_n(1:size(E_n,1),:,2,t)=E_n
(:,:,t);AET_n(1:size(T_n,1),:,3,t)=T_n(:,:,t);
```

```
      end

      %now that i have identified which benches and times everything is at
- i am now going to get it to (hopefully) create a signal over time.
      A_sig(1:(timen+timen_ex))=0;
      E_sig(1:(timen+timen_ex))=0;
      T_sig(1:(timen+timen_ex))=0;

blah(1:(timen+timen_ex))=0;

      k=1;
      for j=1:(timen+timen_ex) %timestamps
      for i=1:size(A_n,1)      % running over the number of noise
realisations that contribute
      if A_n(i,3,j)>0 && A_n(i,3,j)<=(timen+timen_ex)

            %A_sig(A_n(i,3,j))=A_sig(A_n(i,3,j))+(A_n(i,1,j)*noise(A_n
(i,3,j),A_n(i,2,j)));
            A_sig(j)=A_sig(j)+(A_n(i,1,j)*noise(A_n(i,3,j),A_n(i,2,j)));

%A_sig(A_n(i,3,j))=(A_n(i,1,j)*noise(A_n(i,3,j),A_n(i,2,j)));
      A_sig_1(k,j)=(A_n(i,1,j)*noise(A_n(i,3,j),A_n(i,2,j)));
      k=k+1;

blah(A_n(i,3,j))=blah(A_n(i,3,j))-A_n(i,1,j);
      end
      end
      end

      for j=1:(timen+timen_ex)
      for i=1:size(E_n,1)

            if E_n(i,3,j)>0 && E_n(i,3,j)<=(timen+timen_ex)
                  E_sig(E_n(i,3,j))=E_sig(E_n(i,3,j))+(E_n(i,1,j)*noise(E_n
(i,3,j),E_n(i,2,j)));
            end
            if T_n(i,3,j)>0 && T_n(i,3,j)<=(timen+timen_ex)
                  T_sig(T_n(i,3,j))=T_sig(T_n(i,3,j))+(T_n(i,1,j)*noise(T_n
(i,3,j),T_n(i,2,j)));
            end

      end
      end

      j=1;
      for i=1:timen
            A_noise(j)=A_sig(i);
            j=j+1;
      end

%creating the covariance matrix

cov_p(1:timen,1:timen)=0.0;
cov_n(1:timen,1:timen)=0.0;

for i=1:timen
for j=1:timen


      for k=1:size(A_n,1)
      for n=1:size(A_n,1)
```

```
            if (A_n(k,2,i)==A_n(n,2,j)) && (A_n(k,2,i)~=0)
            if A_n(k,3,i)==A_n(n,3,j)
                  %cov_n(abs(abg_n(k,3,i,j)),abg_n(k,2,i,j),i)=abg_n
(k,1,i,j)*abg_n(m,1,i,j);#
            %cov_n(g,h,i,j)=1;
            %cov_n(g,h,i,j)=cov_n(g,h,i,j)+1;
            cov_n(i,j)=cov_n(i,j)+(A_n(k,4,i)*(A_n(k,1,i)*A_n(n,1,j)));

            end
            end
      end
      end
end
end

%     Cov_n_1(1:(3*timen),1:(3*timen))=0;

%Cov_n_1(1:3,1:3)=cov_n(:,:,1,1);
%for i=1:timen
%     for j=1:timen
%           Cov_n_1((((i-1)*3)+1):((i-1)*3)+3,(((j-1)*3)+1):(((j-1)*3)+3))
=cov_n(:,:,j,i);
%     end
%end


for i=1:timen
for j=1:timen


      for k=1:size(A_p,1)
      for n=1:size(A_p,1)

            if (A_p(k,2,i)==A_p(n,2,j)) && (A_p(k,2,i)~=0)
            if A_p(k,3,i)==A_p(n,3,j)
                  %cov_n(abs(abg_n(k,3,i,j)),abg_n(k,2,i,j),i)=abg_n
(k,1,i,j)*abg_n(m,1,i,j);#
            %cov_n(g,h,i,j)=1;
            %cov_n(g,h,i,j)=cov_n(g,h,i,j)+1;
            cov_p(i,j)=cov_p(i,j)+(A_p(k,4,i)*(A_p(k,1,i)*A_p(n,1,j)));

            end
            end
      end
      end
end
end

Cov_n=cov_n(:,:)+cov_p(:,:);

%creating the true data signal

      for i=1:timen
        t(i)=i;

        sin1(i)=(A1*sin((2*pi*freq1*t(i)))); %creating two sin waves with
different frequencies
        sin2(i)=(A2*sin((2*pi*freq2*t(i))));

      data(i)=sin1(i)+sin2(i)+A_noise(i);
```

```
      data_test(i)=sin1(i)+sin2(i)+(cov_n(1,1)/var_noise)*noise(i,1); % to
check for freq_dependences between signal with ordinary noise(noise) and
correlated noise(A_noise)
      end

% quick fft to see if i can still see the signal above the noise

      data_fft=fft(data);

      fft_uplim = 0.1*(t(2)-t(1));

      fft_length = (length(data)/2);

      for i=1:fft_length+1
            fft_freqs(i) = 0.0+((i-1)*(fft_uplim/fft_length));
      end

      datatest_fft=fft(data_test);

      fft_uplim_test = 0.5*(t(2)-t(1));

      fft_length_test = (length(data_test)/2);

      for i=1:fft_length+1
            fft_freqs_test(i) = 0.0+((i-1)*
(fft_uplim_test/fft_length_test));
      end

      figure(7);plot(fft_freqs,abs(data_fft(1:fft_length+1)),'.-');
      figure(8);plot(fft_freqs_test,abs(datatest_fft(1:fft_length_test+
1)),'.-');

%running over different model values
ii=1;
    for k=1:m1
    for j=1:m2
        mfreq1(j)=m1_flow+((j-1)*((m1_fhi-m1_flow)/m1));
        mfreq2(k)=m2_flow+((k-1)*((m2_fhi-m2_flow)/m2));

        for i=1:timen
            %m_t(i)=t(i-1)+(i/timesp);
            %msin1(i,j)=A1*sin((2.0*pi*mfreq1(j)*m_t(i)));
            msin1(i)=A1*sin(2.0*pi*mfreq1(j)*t(i));
            msin2(i)=A2*sin((2.0*pi*mfreq2(k)*t(i)));

            model(i,1,j,k)=msin1(i)+msin2(i); % creating the model values
(size= timesn x m x m)

            model_freqs(1,ii)=mfreq1(j); % keeping track of the different
frequencies for the models
            model_freqs(2,ii)=mfreq2(k);
        end
ii=ii+1;
    end
    end

%calculating the covariance matrices

for i=1:timen
for j=1:timen
```

```
            cov1(i,j)=0;
            cov2(i,j)=0;

      if(i~=j)
            cov1(i,j)=0.0*Cov_n(i,j);
      end
      if(i==j)
            cov1(i,j)=Cov_n(i,j);
      end
            cov2(i,j)=Cov_n(i,j);

      if(cov1(i,j)~=0)
      sqrtcov1(i,j)=sqrt(cov1(i,j));
      else
      sqrtcov1(i,j)=0;
      end

      if(cov2(i,j)~=0)
      sqrtcov2(i,j)=sqrt(cov2(i,j));
      else
      sqrtcov2(i,j)=0;
      end
end
end

detcov1=abs(det(cov1));
detcov2=abs(det(cov2));

invcov1=inv(cov1);
invcov2=inv(cov2);

%calculating chisqlihood

%working out the data minus the models for each timeseries and model.
for k=1:m1
for j=1:m2
for i=1:timen
dmm(i,1,j,k)=(data(i)-model(i,1,j,k));
end
end
end

for k=1:m1
for j=1:m2
      num_m(j)=j;

      %chisq1b(j,k)=log(1/(((2*pi)^(timen/2))*(detcov1)^(timen)))+(-0.5*
(transpose(dmm(:,1,j,k))*(-1.*invcov1))*dmm(:,1,j,k));
      %chisq2b(j,k)=log(1/(((2*pi)^(timen/2))*(detcov2^timen)))+(-0.5*
(transpose(dmm(:,1,j,k))*(-1.*invcov2))*dmm(:,1,j,k));

      %chisq1(j,k)=-log(((2*pi)^(timen/2)))-log((detcov1)^(timen))+(-0.5*
(transpose(dmm(:,1,j,k))*(-1.*invcov1))*dmm(:,1,j,k));
      %chisq1(j,k)=-log(((2*pi)^(timen/2)))-log((detcov1))+(-0.5*(transpose
(dmm(:,1,j,k))*(-1.*invcov1))*dmm(:,1,j,k));
      %chisq2(j,k)=-log((detcov2))+(-0.5*(transpose(dmm(:,1,j,k))*(-1.
*invcov2))*dmm(:,1,j,k));

      %chisq1(j,k)=(1/(((2*pi)^(timen/2))*sqrt(detcov1)))*exp(-0.5*
(transpose(dmm(:,1,j,k))*(-1.*invcov1))*dmm(:,1,j,k));
      %chisq2(j,k)=(1/(((2*pi)^(timen/2))*sqrt(detcov2)))*exp(-0.5*
```

```
(transpose(dmm(:,1,j,k))*(-1.*invcov2))*dmm(:,1,j,k));

      chisq1a(j,k)=(transpose(dmm(:,1,j,k))*(invcov1))*dmm(:,1,j,k);
      chisq2a(j,k)=(transpose(dmm(:,1,j,k))*(invcov2))*dmm(:,1,j,k);
end
end
min_chisq1=min(min(chisq1a));
min_chisq2=min(min(chisq2a));

%note that what i'm working out is a chi-squared relation (data-model)^2/(2
*sigma^2)
%so below is actually delta chi squared.
for k=1:m1
for j=1:m2
      chisq1(j,k)=(chisq1a(j,k)-min_chisq1);
      chisq2(j,k)=(chisq2a(j,k)-min_chisq2);
end
end

%Working out confidence regions

for k=1:m1
for j=1:m2

if (chisq1(j,k)<=2.3)
      conf1(j,k)=1.0;
elseif (chisq1(j,k)<=6.17 && chisq1(j,k)>2.3)
      conf1(j,k)=0.5;
elseif (chisq1(j,k)<=11.8 && chisq1(j,k)>6.17)
      conf1(j,k)=0.25;
else
      conf1(j,k)=0.0;
end

if (chisq2(j,k)<=2.3)
      conf2(j,k)=1.0;
elseif (chisq2(j,k)<=6.17 && chisq2(j,k)>2.3)
      conf2(j,k)=0.5;
elseif (chisq2(j,k)<=11.8 && chisq2(j,k)>6.17)
      conf2(j,k)=0.25;
else
      conf2(j,k)=0.0;
end

end
end


figure(1);imagesc(conf1);title('conf1');colormap(bone);
figure(2);imagesc(conf2);title('conf2');colormap(bone);

%printing out to a file

for i=1:length(chisq1)
for j=1:length(chisq1)
      if(j==length(chisq1))
                  fprintf(fid, ' %d\n',chisq1(i,j));
            fprintf(fid2, ' %d\n',chisq2(i,j));
            fprintf(fid3, ' %d\n',conf1(i,j));
            fprintf(fid4, ' %d\n',conf2(i,j));
        else
```

```
                fprintf(fid, ' %d',chisq1(i,j));
            fprintf(fid2, ' %d',chisq2(i,j));
            fprintf(fid3, ' %d',conf1(i,j));
            fprintf(fid4, ' %d',conf2(i,j));
        end
end
end

fclose(fid);fclose(fid2);fclose(fid3);fclose(fid4);fclose(fid5);









% identifying the maximum/best estimate of the chisqlihoods

min_l1=min(chisq1);
min_l11=min(min_l1);
[min_1a min_1b]=find(chisq1==min_l11);

%finding the runner up (ie second best estimate)
min1_2nd=min_l1(1);
for i=1:length(min_l1)
      if min_l1(i)>min1_2nd & min_l1(i)~=min_l11
            min1_2nd=min_l1(i);
      end
end
[min_1a_2nd min_1b_2nd]=find(chisq1==min1_2nd);

min_l2=min(chisq2);
min_l22=min(min_l2);
[min_2a min_2b]=find(chisq2==min_l22);

%finding the runner up (ie second best estimate) for the second chisqlihood
min2_2nd=min_l2(1);
for i=1:length(min_l2)
      if min_l2(i)>min2_2nd & min_l2(i)~=min_l22
            min2_2nd=min_l2(i);
      end
end
[min_2a_2nd min_2b_2nd]=find(chisq2==min2_2nd);

%graph scaling
gs=mfreq1(1);

%changing the frequency values into strings for the axes and legend.
mfreq1_str=num2str(transpose(mfreq1));

%basic plots of the chisqlihoods
figure(3);plot(mfreq1,chisq1,'.-');title('cov=diagonal');xlabel
('frequency');ylabel('Log Likelihood');  legend([mfreq1_str]);%set
(gca,'XTickLabel',mfreq1_str);
figure(4);plot(mfreq1,chisq2,'.-');title('cov=time covs');xlabel
('frequency');ylabel('Log Likelihood'); legend([mfreq1_str]);
```

```
%Fancy plots of chisqihoods: 3D surfaces and imagesc.
figure(5);
%subplot(2,1,1);
%surf(mfreq1,mfreq1,chisq1*1e20);
%colormap(bone);view(-35,45);xlabel('frequency');ylabel('Frequency');zlabel
('Log chisqlihood x1e20');colorbar;title(['snr=',snr2_str,' A1=',A1_str,'
A2=',A2_str,' N=',N_str]);
%%set(gca,'XTick',[0.1,0.2,0.3,0.4,0.5],'XTickLabel',mfreq1
_str);%'Ytick',mfreq1,'YTickLabel',mfreq1_str);
%subplot(2,1,2);
imagesc(mfreq2,mfreq1,chisq1);xlabel('frequency');ylabel('frequency');title
('chi-sq - No time covariances');
%rectangle('Position',[freq1-0.5*gs,freq2-0.5*gs,1*gs,1
*gs],'EdgeColor','r');
%rectangle('Position',[freq2-0.5*gs,freq1-0.5*gs,1*gs,1
*gs],'EdgeColor','r');colormap(bone);
%rectangle('Position',[mfreq1(min_1a(1))-0.25*gs,mfreq1(min_1a(2))-0.25
*gs,0.5*gs,0.5*gs],'EdgeColor','b');
%rectangle('Position',[mfreq1(min_1b(1))-0.25*gs,mfreq1(min_1b(2))-0.25
*gs,0.5*gs,0.5*gs],'EdgeColor','b');

%rectangle('Position',[mfreq1(min_1a_2nd(1))-0.25*gs,mfreq1(min_1a_2nd(2))-
0.25*gs,0.5*gs,0.5*gs],'EdgeColor','g');
%rectangle('Position',[mfreq1(min_1b_2nd(1))-0.25*gs,mfreq1(min_1b_2nd(2))-
0.25*gs,0.5*gs,0.5*gs],'EdgeColor','g');

figure(6);
%subplot(2,1,1);
%surf(mfreq1,mfreq1,chisq2*1e20);
%colormap(bone);view(-35,45);xlabel('frequency');ylabel('Frequency');zlabel
('Log chisqlihood x1e20');colorbar;title(['snr=',snr2_str,' A1=',A1_str,'
A2=',A2_str,' N=',N_str]);
%subplot(2,1,2);
imagesc(mfreq1,mfreq2,chisq2);xlabel('frequency');ylabel('frequency');title
('chi-sq - With time covariances');
%rectangle('Position',[freq1-0.5*gs,freq2-0.5*gs,1*gs,1
*gs],'EdgeColor','r');
%rectangle('Position',[freq2-0.5*gs,freq1-0.5*gs,1*gs,1
*gs],'EdgeColor','r');colormap(bone);
%rectangle('Position',[mfreq2(min_2a(1))-0.25*gs,mfreq2(min_2a(2))-0.25
*gs,0.5*gs,0.5*gs],'EdgeColor','b');
%rectangle('Position',[mfreq2(min_2b(1))-0.25*gs,mfreq2(min_2b(2))-0.25
*gs,0.5*gs,0.5*gs],'EdgeColor','b');

%rectangle('Position',[mfreq2(min_2a_2nd(1))-0.5*gs,mfreq2(min_2a_2nd(2))-
0.5*gs,1*gs,1*gs],'EdgeColor','g');
%rectangle('Position',[mfreq2(min_2b_2nd(1))-0.5*gs,mfreq2(min_2b_2nd(2))-
0.5*gs,1*gs,1*gs],'EdgeColor','g');
```

Bibliography

[1] Jacqui Toher, Copyright. Picture created using AutoCAD 2009, 2008.

[2] NASA, Copyright. Picture Credit, 2008.

[3] Shane L. Larson. Online Sensitivity Curve Generator, 2008.

[4] F. B. Estabrook, M. Tinto, and J. W. Armstrong. Time-Delay Analysis of LISA Gravitational Wave Data: Elimination of Spacecraft Motion Effects. *Phys. Rev. D*, 62(4):042002, Jul 2000.

[5] D. A. Shaddock. Operating LISA as a Sagnac Interferometer. *Phys. Rev. D*, 69(2):022001, January 2004.

[6] The LIGO Scientific Collaboration: B. Abbott. LIGO: The Laser Interferometer Gravitational-Wave Observatory. *ArXiv e-prints*, November 2007.

[7] J. Hough and S. Rowan. Gravitational Wave Detection by Interferometry (Ground and Space). *Living Reviews in Relativity*, 3:3–+, June 2000.

[8] Bernard F. Schutz. *A First Course in General Relativity*. Cambridge University Press, 2002.

[9] S. W. Hawking and W. Israel, editors. *300Years of Gravitation*. Cambridge University Press, 1989.

[10] Scott Dodelson. *Modern Cosmology*. Academic Press, 2003.

[11] Kip S. Thorne, Charles W. Misner, and John A. Wheeler. *Gravitation (Physics Series)*. W. H. Freeman, September 1973.

[12] P. Coles, editor. *The Icon Critical Dictionary of The New Cosmology*. Icon Books, 1998.

[13] Norman Gray. Honours Course in General Relativity. 2006.

[14] G. Hinshaw, J. L. Weiland, R. S. Hill, N. Odegard, D. Larson, C. L. Bennett, J. Dunkley, B. Gold, M. R. Greason, N. Jarosik, E. Komatsu, M. R. Nolta, L. Page, D. N. Spergel, E. Wollack, M. Halpern, A. Kogut, M. Limon, S. S. Meyer, G. S. Tucker, and E. L. Wright. Five-Year Wilkinson Microwave Anisotropy Probe (WMAP) Observations: Data Processing, Sky Maps, and Basic Results. *ArXiv e-prints*, 803:0732, March 2008.

[15] M. Hendry and G. Woan. Gravitational Astrophysics. *Astronomy & Geophysics*, 48:1.10–1.17, 2007.

[16] John Veitch. *Applications of Markov Chain Monte Carlo Methods to Continuous Gravitational Wave Data Analysis*. PhD Thesis, University of Glasgow, 2007.

[17] I. Ciufolini, V.Gorini, U. Moschella, and P. Fré, editors. *Gravitational Waves*. Series in High Energy Physics, Cosmology and Gravitation. Institute of Physics Publishing, 2001.

[18] B. W. Carroll and D. A. Ostlie. *An Introduction to Modern Astrophysics*. Addison-Wesley, 1996.

[19] S. A. Hughes. Untangling the Merger History of Massive Black Holes with LISA. *Mon. Not. R. Astron. Soc.*, 331:805–816, April 2002.

[20] R. A. Hulse and J. H. Taylor. Discovery of a Pulsar in a Binary System. *Astrophys. J.*, 195:L51–L53, January 1975.

[21] Scott A. Hughes. A Brief Survey of LISA Sources and Science. *AIP Conf. Proc.*, 873:13–20, 2006.

[22] M. Tinto and S. V Dhurandhar. Time-Delay Interferometry. *Living Rev. Relativity*, 8(4), 2005.

[23] Curt Cutler and Theocharis A. Apostolatos and Lars Bildsten and Lee Samuel Finn and Eanna E. Flanagan and Daniel Kennefick and Dragoljubov M. Markovic and Amos Ori and Eric Poisson and Gerald Jay Sussman and Kip S. Thorne. The Last Three Minutes: Issues in Gravitational Wave Measurements of Coalescing Compact Binaries. *Physical Review Letters*, 70:2984, 1993.

[24] LIGO Scientific Collaboration. Search for Gravitational Waves from Binary Black Hole Inspirals in LIGO Data. *Physical Review D*, 73:062001, 2006.

[25] Hideki Asada and Toshifumi Futamase. Post-Newtonian Approximation. *Progress of Theoretical Physics*, 128:123, 1997.

[26] M. J. Benacquista, J. DeGoes, and D. Lunder. A Simulation of the LISA Data Stream from Galactic White Dwarf Binaries. *Classical and Quantum Gravity*, 21:S509, 2004.

[27] S. L. Larson. LISA: A Modern Astrophysical Observatory. 2005. Prepared for 33rd SLAC Summer Institute on Particle Physics (SSI 2005): Gravity in the Quantum World and the Cosmos, Menlo Park, California, 25 Jul - 5 Aug 2005.

[28] T Tanaka. Gravitational Waves from Extreme Mass-Ratio Inspirals. *Journal of Physics: Conference Series*, 120(3):032001 (7pp), 2008.

[29] A. A. Michelson and E. W. Morley. On the Relative Motion of the Earth and the Luminiferous Ether. *American Journal of Science*, 34:333–345, 1887.

[30] T. A. Prince, M. Tinto, S. L. Larson, and J. W. Armstrong. LISA Optimal Sensitivity. *Phys. Rev. D*, 66(12):122002, December 2002.

[31] Laser Interferometer Gravitational Wave Observatory Website. http://www.ligo.caltech.edu/, 2008.

[32] VIRGO Website. http://www.virgo.infn.it/, 2008.

[33] GEO600 Website. http://geo600.aei.mpg.de/, 2008.

[34] TAMA Website. http://tamago.mtk.nao.ac.jp/, 2008.

[35] J. W Armstrong, F. B Estabrook, and M. Tinto. Time-Delay Interferometry for Space-Based Gravitational Wave Searches. *Astrophys. J.*, 527(1):814–826, December 1999.

[36] M. Tinto, F.B. Estabrook, and J.W. Armstrong. Time-Delay Interferometry and LISA's Sensitivity to Sinusoidal Gravitational Waves. Technical report, Pasadena, U.S.A., 2002.

[37] C. Cutler. Angular Resolution of the LISA Gravitational Wave Detector. *Phys. Rev. D*, 57:7089–7102, June 1998.

[38] N. J. Cornish and L. J. Rubbo. LISA Response Function. *Phys. Rev. D*, 67(2):022001, January 2003.

[39] Massimo Tinto, F. B. Estabrook, and J. W. Armstrong. Time-Delay Interferometry For LISA. *Phys. Rev. D*, 65(8):082003, Apr 2002.

[40] Andrzej Krolak, Massimo Tinto, and Michele Vallisneri. Optimal Filtering of the LISA Data. *Physical Review D*, 70:022003, 2004.

[41] Max Planck Institut für Quantenoptics. LISA: Pre-Phase A Report, December 1995. 1996.

[42] Louis J. Rubbo, Neil J. Cornish, and Olivier Poujade. Forward Modeling of Space-Borne Gravitational Wave Detectors. *Phys. Rev. D*, 69:082003, 2003.

[43] Shane L. Larson, William A. Hiscock, and Ronald W. Hellings. Sensitivity Curves for Spaceborne Gravitational Wave Interferometers. *Phys. Rev. D*, 62(6):062001, Aug 2000.

[44] M. Tinto, D. A. Shaddock, J. Sylvestre, and J. W. Armstrong. Implementation of Time-Delay Interferometry for LISA. *Phys. Rev. D*, 67(12):122003, June 2003.

[45] K. A. Arnaud and S. Babak and J. G. Baker and M. J. Benacquista and N. J. Cornish and C. Cutler and S. L. Larson and B. S. Sathyaprakash and M. Vallisneri and A. Vecchio and J.-Y. Vinet. The Mock LISA Data Challenges: An Overview. *AIP Conf. Proc.*, 873:619–624, 2006.

[46] Shane L. Larson, William A. Hiscock, and Ronald W. Hellings. Sensitivity Curves for Spaceborne Gravitational Wave Interferometers. *Physical Review D*, 62:062001, 2000.

[47] Michele Vallisneri. Geometric Time Delay Interferometry. *Phys. Rev. D*, 72, 2005.

[48] M. Vallisneri. Synthetic LISA: Simulating Time Delay Interferometry in a Model LISA. *Phys. Rev. D*, 71, 2005.

[49] C. Röver, A. Stroeer, E. Bloomer, N. Christensen, J. Clark, M. Hendry, C. Messenger, R. Meyer, M. Pitkin, J. Toher, R. Umstätter, A. Vecchio, J. Veitch, and G. Woan. Inference on Inspiral Signals using LISA MLDC Data. *Classical and Quantum Gravity*, 24:521–+, October 2007.

[50] Weisstein, Eric W. MathWorld - A Wolfram Web Resource, 2008.

[51] MapleSoft. Maple 10 Mathematical Software, 2007.

[52] Alberto Vecchio. Private Communication, September 2006.

[53] N.J. Cornish, L.J. Rubbo and O. Poujade. The LISA Simulator, www.physics.montana.edu/LISA/.

[54] Alexander Stroeer. Private Communication, July 2006.

[55] J. D. Romano and G. Woan. Principal Component Analysis for LISA: The Time Delay Interferometry Connection. *Phys. Rev. D*, 73(10):102001–+, May 2006.

[56] Mathworks Ltd. MATLAB R2007a, 2007.

[57] K A Arnaud and S Babak and J G Baker and M J Benacquista and N J Cornish and C Cutler and L S Finn and S L Larson and T Littenberg and E K Porter and M Vallisneri and A Vecchio and J.-Y. Vinet. An Overview of the Second Round of the Mock LISA Data Challenges. 2007.

[58] Sivia, D. S. *Data Analysis: A Bayesian Tutorial (Oxford Science Publications)*. Oxford University Press, July 1996.

[59] Louis Lyons. *A Practical Guide to Data Analysis for Physical Science Students*. Cambridge University Press, Cambridge, 1991.

[60] Phil Gregory. *Bayesian Logical Data Analysis for the Physical Sciences*. Cambridge University Press, New York, NY, USA, 2005.

[61] Woan, Graham. *The Cambridge Handbook of Physics Formulas*. Cambridge University Press, 2000.

[62] Mock LISA Data Challenge Taskforce. Document for Challenge 1. August 2006.

[63] K. A. Arnaud and S. Babak and J. G. Baker and M. J. Benacquista and N. J. Cornish and C. Cutler and S. L. Larson and B. S. Sathyaprakash and M. Vallisneri and A. Vecchio and J.-Y. Vinet. A How-To for the Mock LISA Data Challenges. *AIP Conf. Proc.*, 873:625–632, 2006.

[64] Patrick Sutton. Private Communication, November 2008.

[65] Michele Vallisneri. Synthetic LISA, http://www.vallis.org/syntheticlisa/.

Index